ISBN 978-82-326-1752-4 (printed version)
ISBN 978-82-326-1753-1 (electronic version)
ISSN 1503-8181

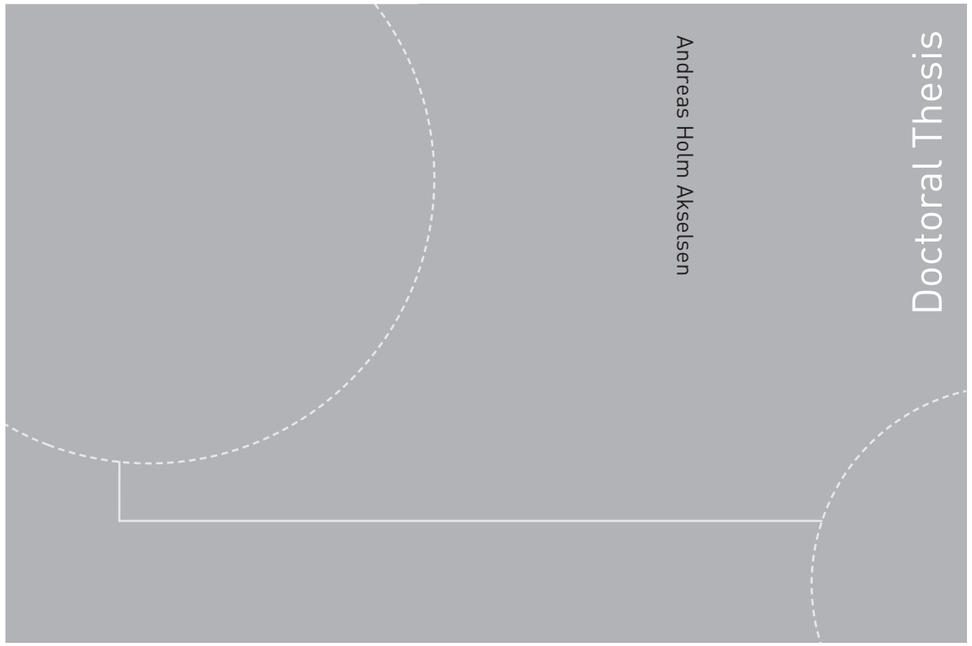

Doctoral theses at NTNU, 2016:207

Andreas Holm Akselsen

Efficient Numerical Methods for Waves in One-Dimensional Two-Phase Pipe Flows

NTNU
Norwegian University of
Science and Technology

NTNU
Norwegian University of
Science and Technology
Faculty of Engineering
Science and Technology
Department of Energy and Process Engineering

NTNU
Norwegian University of
Science and Technology

Doctoral theses at NTNU, 2016:207

NTNU

Andreas Holm Akselsen

Efficient Numerical Methods for Waves in One-Dimensional Two-Phase Pipe Flows

Thesis for the degree of Philosophiae Doctor

Trondheim, August 2016

Norwegian University of Science and Technology
Faculty of Engineering
Science and Technology
Department of Energy and Process Engineering

NTNU
Norwegian University of
Science and Technology

NTNU
Norwegian University of Science and Technology

Thesis for the degree of Philosophiae Doctor

Faculty of Engineering
Science and Technology
Department of Energy and Process Engineering

ISBN 978-82-326-1752-4 (printed version)
ISBN 978-82-326-1753-1 (electronic version)
ISSN 1503-8181

Doctoral theses at NTNU, 2016:207

Printed by Skipnes Kommunikasjon as

Abstract

This thesis is aimed at improving simulation efficiency for stratified-wavy gas-liquid flows. Towards this goad, the simpler nature of *incompressible* two-phase flows is utilized for predicting hydraulic wave dynamics, both through theoretical analysis and numerical simulation. Numerical methods proposed for the incompressible two-fluid model include

- a hybridization of a finite volume method with analytical roll-wave profile solutions,
- a Method of Characteristics and finite volume hybridizations thereof, and
- a linearized Riemann solver (Roe scheme.)

Theoretical analyses based on the same model further the understanding of Kelvin-Helmholtz stability in stratified pipe flows and provide a comprehensive account of how the flow stability predictions of numerical simulators depend on model discretization. Kelvin-Helmholtz/von Neumann analysis is shown to be a valuable support tool for choosing numerical scheme and simulation parameters. Finally, a dual grid scheme is proposed which enables us to extend the computational benefits of incompressible flow models to compressible systems. The dual grid scheme effectively decouples the length scales and numerical CFL restrictions of hydraulic (incompressible) waves from that of acoustic (compressibility) waves. Efficiency is observed to be improved by several orders of magnitude for a wide range of simulation cases.

Preface

Work on this thesis started in August 2012 at the Department of Energy and Process Engineering, the Norwegian University of Science and Technology, and was completed in late June, 2016. The main supervisor has been Professor Ole Jørgen Nydal (NTNU). Professor Zhilin Yang from Statoil has been the co-supervisor.

This PhD was financed by the Faculty of Engineering Science and Technology at NTNU in connection with the Multiphase Flow Assurance Center (FACE.) FACE was a research cooperation between IFE, NTNU and SINTEF running from 2007 to 2014 [3].

Acknowledgements

I wish to express my gratitude to my supervisor Ole Jørgen Nydal for giving me the opportunity to work with this topic, and for giving me the freedom to pursue new ideas. His friendly, generous and helpful demeanour will always be appreciated.

I would also like to heartily thank Tore Flåtten for his forthcomingness and eagerness to discuss topics of a technical nature. Tore's considerable knowledge and generous feedback has helped me through some of the rougher periods of this enterprise.

My colleagues, Tor K. Kjeldby, Ivar E. Smith, Heiner Schümann, Andrea A. Shmueli, Mariana J.C. Diaz Arias and Kontorbamse, also deserve my warmest gratitude. I am thankful not only for the knowledge and insight that we have exchanged over the years, but also on a personal level for the support shown, the good times shared and for them seeming impervious to my moaning.

Lastly, I would be at a loss without the support and encouragement from my family. Some day I will actually thank them for it.

Trondheim, June 2016

Andreas H. Akselsen

Contents

Nomenclature

Latin symbols

$\mathcal{A}$	Cross-sectional area (parameter)	m^2
a, A	Cross-section field area	m^2
C	Wave celerity	$\mathrm{m\,s^{-1}}$
$\hat{c}$	Complex (linear) wave celerity	$\mathrm{m\,s^{-1}}$
c	Shock velocity	$\mathrm{m\,s^{-1}}$
D	Interior diameter (parameter)	m
R	Interior radius (parameter)	m
$\boldsymbol{f}, \boldsymbol{F}$	Flux vector; $\boldsymbol{f} = (q_\ell, j)^T$	
g_x, g_y	Gravitational acceleration ($\boldsymbol{g} = g_x\boldsymbol{i} + g_y\boldsymbol{j}$) (parameter)	$\mathrm{m\,s^{-2}}$
$h, H, \mathcal{H}$	Height of the interface in the pipe cross section	m
i	Imaginary unit	
j, J	(Specific) momentum (difference) flux; (3.12b)	$\mathrm{kg\,m^{-3}\,s^{-2}}$
$p, \mathcal{P}$	Pressure	$\mathrm{kg\,m^{-1}\,s^{-2}}$
Δp	$\Delta p_k = \langle p \rangle_k - p_{\mathrm{i},k}$	$\mathrm{kg\,m^{-1}\,s^{-2}}$
q, Q	Volumetric flow rate; $q_k = a_k u_k$	$\mathrm{m^3\,s^{-1}}$
$\mathcal{Q}$	Mixture flow rate (parameter); (3.11b)	$\mathrm{m^3\,s^{-1}}$
s_k	Momentum source; (3.2)	$\mathrm{kg\,s^{-2}}$
$s, S, \mathcal{S}$	(Specific) momentum (difference) source; (3.12c)	$\mathrm{kg\,m^{-4}\,s^{-2}}$
t	Time	s
u, U	Fluid velocity	$\mathrm{m\,s^{-1}}$
$\boldsymbol{v}, \boldsymbol{V}$	Mathematically conservative variable vector; $\boldsymbol{v} = (a_\ell, [\rho u]_{\mathrm{g}}^{\ell})^T$	
x, X	Axial position	m
y	Normal coordinate (normal to x)	m

Greek Symbols

γ	Interphase half-angle	–
$\delta\phi$	Perturbation of ϕ	–

θ	Pipe inclination, positive above datum (parameter)	$-$
$\varkappa$	Eq. (3.16)	$\mathrm{kg\,m^{-4}\,s^{-1}}$
$\lambda^{\pm}$	Eigenvalues (3.15)	$\mathrm{m\,s^{-1}}$
ρ	Density (parameter)	$\mathrm{kg\,m^{-3}}$
σ	Perimeter length	m
τ	Skin friction	$\mathrm{kg\,m^{-1}\,s^{-2}}$
ϕ, Φ	Dummy variable	

Annotations

$\prime$	$\Phi' = \frac{\mathrm{d}\Phi}{\mathrm{d}A_\ell}$
*	$\phi^* = \frac{\phi_\ell}{a_\ell} + \frac{\phi_\mathrm{g}}{a_\mathrm{g}}$
$-, +$	Left, right side of shock
g	Gas
i	(At) interphase
k	Generic phase: $k \in \{\mathrm{g}, \ell\}$
ℓ	Liquid
L, R	Left, right states of Riemann problem
r	Relative to wave (using relative fluid velocities.)

Encasements

$[\cdot]^{\ell}_{\mathrm{g}}$	$(\cdot)_\ell - (\cdot)_\mathrm{g}$
$[\cdot]^{+}_{-}$	$(\cdot)^+ - (\cdot)^-$
$\overline{\phi}$	Ensemble average
$\langle\phi\rangle$	Cross-section field average

Chapter 1

Introduction

1.1 Background

The term 'multiphase flow' was introduced in a dynamic sense by Soo in in 1965 [76] for flows containing fields of particles, bubbles or droplets. In addition to the dynamics found in single-phase flows, multiphase flows harbour a rich variety of phenomena though the vast range of topological phase configurations possible. Multiphase dynamics are often encountered in industrial contexts; in heat and cooling processes and during fluid collection and transport. The nuclear industry was the first to drive the development towards *dynamic* modelling of multiphase flows [37]. These models were aimed towards water-steam cooling systems for ensuring process stability [18]. Accident simulation and damage control are also important usages which entail prediction of quick pressure transients.

Advances in multiphase modelling were quickly absorbed into simulators for large-scale gas-oil-water transport systems after the rise of the off-shore petroleum industry [23]. Such tools are essential for flow assurance, flow efficiency, production optimization, feasibility and profitability studies, equipment sizing and safety control [70]. Many other industries, such as chemical production facilities and renewable energy suppliers, also benefit from multiphase flow modelling, for example were heat exchangers [51] and boiling and condensation processes [61] are concerned. Another example is CO2 capture and storage [5, 1]. A large portion of research within applied mathematics today is focused towards multiphase flow problems [2].

Flow Regimes and Stability

Multiphase pipe flow is characterised by a wide variety of flow regimes. Each flow regime is identified by the flow patterns it exhibits. Observed pressure drops

and shear stresses differ strongly from one regime to another as a result of the topologically different flow patterns. These differences have made it necessary to model individual flow regimes separately.

Flow fields will be separated in near-horizontal pipelines if fluid velocities are moderate. This is called the *stratified* flow regime and is the regime towards which this thesis is focused. Two types of mechanisms alter this flow pattern. Terrain topography and bends and dips in the pipeline can cause liquid accumulation, particularly if the flow is to some extent driven by gravity. Accumulating liquid may then block the pipe cross-section, forming a liquid plug which results in intermittent flow. Alternatively, if the velocity difference between the stratified flow fields are sufficiently great, hydrodynamic flow instabilities occur [57]. Waves then begin to grow. Wave crests will eventually span the cross-section if the growth is sufficient. Otherwise, wave breaking and turbulence stabilize the waves. Interphase stability, structural stability and slug stability will determine whether stratified flow persists of if a *slugging flow regime* ensues [10, 12].

Slugging flow is an intermitted flow pattern consisting of sequential liquid slugs followed by elongated bubbles. If the gas rate is sufficiently increased then gas will begin to occupy the pipe centre, push liquid out towards the pipe walls. This flow pattern is known as *annular* flow. Also increasing the liquid flow rate, the flow pattern will turn into a chaotic blend of liquid-gas flow structures known as *churn flow.* Should the amount of liquid far exceed the amount of gas, a fully dispersed *bubble flow* regime appears. Here, small bubbles propagate through a continuous liquid phase. Figure 1.1 presents a schematic of the different flow regimes in horizontal pipes. Figure 1.2 portrays, also schematically, what is known as a flow map. Flow maps show which flow patterns are expected as a function of flow rates for a specific pipeline configuration and set of fluid properties.

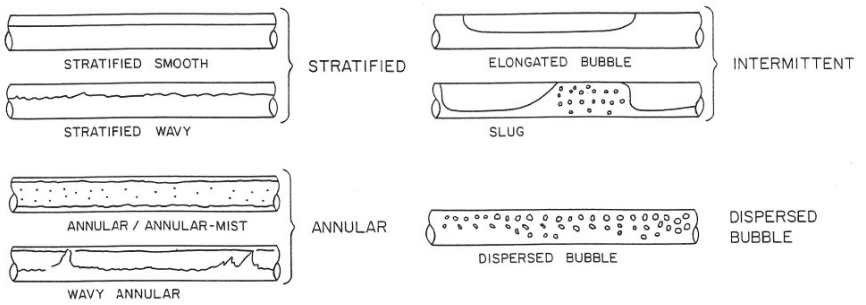

Figure 1.1: Flow patterns in horizontal pipes. Image source: [46].

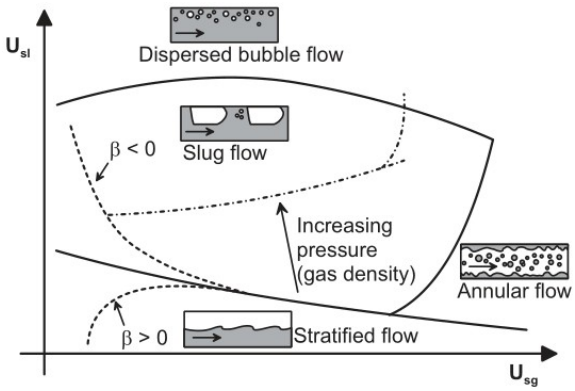

Figure 1.2: Flow map for horizontal pipes. Image source: [58]. β is here the pipe inclination.

Modelling and Simulation

Mathematical *modelling* consists of formulating an equation set which represent, or approximates, a part of nature. Important features of a model are

- that it gives a fair representation of the physical system,
- that it is used in a range where its assumptions and approximations are valid,
- that it provides *unique* solutions,
- that it is simple enough to simulate and
- that it is *closed* (all variables and functions are well-defined.)

Models of conservation laws typically consist of a set of partial differential equations combined with algebraic closures. We often make a distinction between *mechanistic* and *phenomenological* modelling strategies. Mechanistic models are derivatives from some fundamental mechanical or thermodynamic principles, combined with meaningful approximations. These are usually *conservation* principles (the local conservation of mass, momentum and energy.) Phenomenological models approach the problem from the opposite direction, seeking equation sets which directly approximate dynamics observed in nature. The latter modelling strategy tends to be more *intrusive*, but usually offers a more direct route for obtaining the descried model response. Phenomenological models should still be made consistent with fundamental principles, though they are not derived directly therefrom.

Simulation involves the numerical techniques used for solving those differential equation sets which constitutes a model. Aspects of *simulation* includes ensuring that the simulation algorithms are

- *efficient* (requiring only an acceptable number of CPU computations,)
- *accurate* (generating good approximations to exact model solutions) and
- *robust* (reliable in that a meaningful result will be found.)

The focus of this thesis will mainly be towards *simulation*.

Existing Models and Codes for Transient Multiphase Pipe Flows

One-dimensional transport models dominate when it comes to simulation of macroscale transport systems. This still seem to be the trend for the years to come, despite the increase in available computational power through the digital age. The majority of transient codes are based on the so-called *two-fluid model* [78, 77, 44, 29, 28, 67], which originates from an averaging of the conservation equations across individual flow fields over the pipe cross-section. A mass, a momentum and an energy equation then emerges for each flow field. This is the model implemented in the nuclear codes TRACE [26], RELAP [42] and CATHARE [30, 11]. Popular codes based on the two-fluid model in the petroleum community include OLGA [13], LedaFlow [20] and PeTra [59] (now cannibalized by OLGA.) The two-fluid model is also used in the academic codes TRIOMPH and MAST [45, 17, 16] where it has been shown capable of predicting a natural transition to slug flow from out of hydrodynamic instabilities.

Another commonly used multiphase transport model is the *drift flux* model, obtained by summing together the momentum equations of the two-fluid model [67]. This model resolves some of the issues related to the two-fluid model by being unconditionally hyperbolic and having a conservative equation form, but it requires additional closure relations to distinguish the velocity fields. Codes based on the drift flux model include TACITE [69], FlowManager [41] and COMPAS [85].

These are but a few of the codes and models which have used for multiphase transport predictions. In additions to transient flow models, there exists a large number of steady state model and point models not mentioned here (see e.g. [23] and the references within.)

1.2 Motivation and Objectives

Wave dynamics plays a central role in the smooth-stratified to wavy-stratified to slugging flows regimes. Surface waves will persist in stratified flow if the flow conditions are such that a flat interphase is inherently unstable. These will grow until they are stabilized by non-linear effects, or until they breach the pipe cross-section and cause slug formations. Hydrodynamic slugging is therefore strongly related

to the history and evolution of dynamic waves. Waves form a transition mechanism which some flow models try to reproduce and others to mimic, for example through heuristic slug initiation routines. Further, wave structures tend to interact, both with each other and with the pipeline geometry. Other wave phenomena arise from boundaries and external sources, for example surges and void waves, pressure waves from valves, blockages, collapses and bursts, and wave-instability cycles as two parts of a pipeline system interact through acoustic and hydraulic waves travelling back and forth [53, 4, 40].

Wave interaction and evolution is not easily captured with phenomenological modelling. Phenomenologically modelled slugging is known to require additional information about the initial slug properties and also some ad-hoc mechanism to regulate the slugging frequency [43, 60].

Alternatively, predictions on wave growth and slugging can be made by utilizing the natural stability mechanisms inherent in the two-fluid model [56, 21, 16, 17]. This requires us to perform detailed simulations in order to obtain a correct macro-scale flow evolution, even though the details of individual waves are not of interest – it takes a lot of computer power. In industry-sized pipeline systems, like off-shore transport systems, this is not always a feasible option.

The objective of this thesis is to accurately and robustly simulate hydrodynamic flow phenomena and wave dynamics, yet at a manageable computational cost. To this end, new methods, techniques and simulation strategies for the stratified-to-slugging regime of near-horizontal flows will be developed.

Chapter 2

Summary to Papers

The objective outlined in the previous section has been approached from various directions. Paper I, II, III and VI are aimed directly towards simulation efficiency. A dual grid methodology is proposed in Paper I and VI to the relax resolution restrictions normally afflicting explicit implementations of the two-fluid model. Paper II explores the possibility of combining analytical modelling of non-linear waves with an object-oriented simulation strategy. More conventional schemes are proposed in Paper III, tailored to efficiently detect the onset of linear instability and predict the non-linear wave regime that ensues.

Paper IV and V are directed towards applied theory. The analysis presented in Paper V aids in finding a discretization and discretization parameters which accurately and efficiently predicts hydrodynamic instabilities. This analysis also highlights important connections between discretization parameters and predictive capability. Paper IV seeks to extend our understanding of the roll-wave flow regime and when we can expect transition to slugging flow.

The papers and some of the literature which inspired them are depicted in Figure 2.1.

The following articles are presented in the order in which they were written.

Paper I ‘Applying Multiple Grids to a Multi-Field Model - The Resolution Requirements of Individual Fields in the Two-Fluid Model for 1D Pipe Flow’

This is the first of two papers investigating the use of double numerical grids for simulating the two-fluid model. A gas-liquid two-grid discretization was implemented in the SLUGGIT computer code [55, 54, 68]. The two-grid method was shown to have a great efficiency potential. At the same time it was seen that coupling the information contained

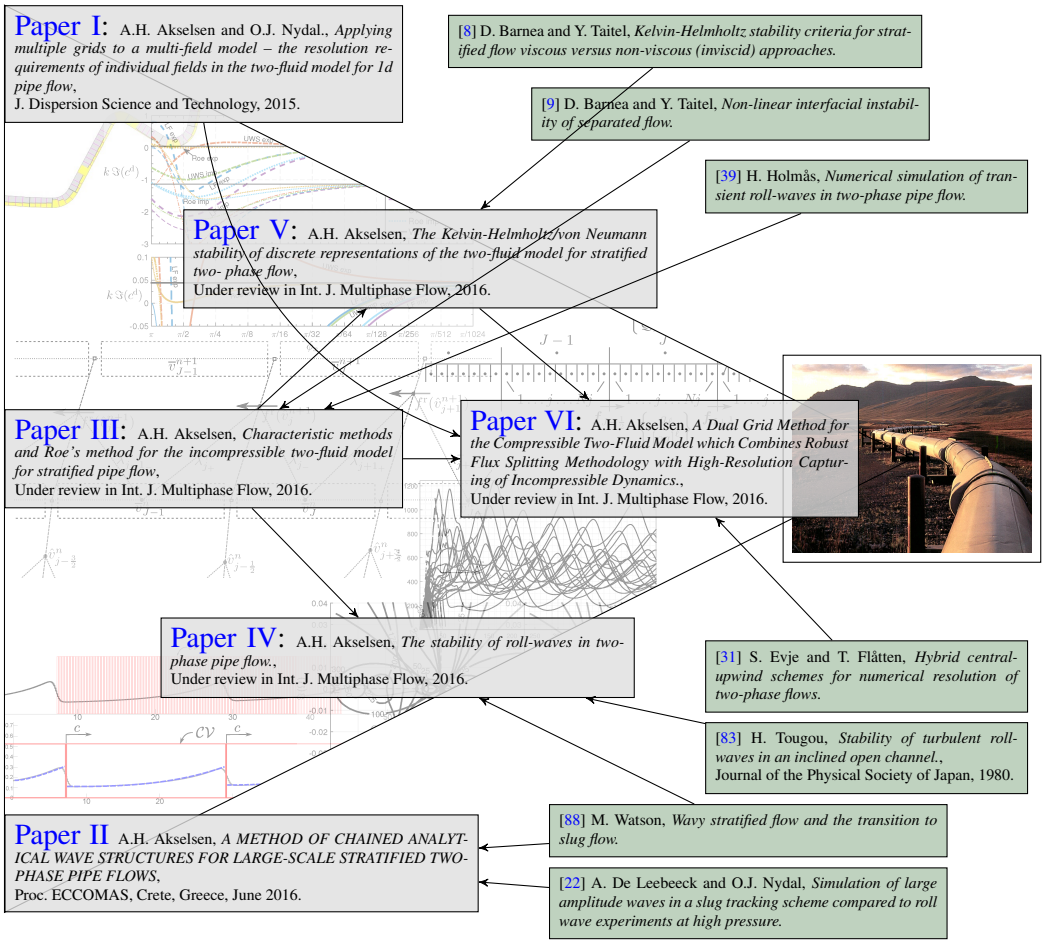

Figure 2.1: Scientific papers; development and inspiration.

in each grid is not trivial; grid-dependent disturbances were observed to be projected from the larger grid down onto the smaller one.

Paper II 'A METHOD OF CHAINED ANALYTICAL WAVE STRUCTURES FOR LARGE-SCALE STRATIFIED TWO-PHASE PIPE FLOWS'

This method was based on a simulation concept from De Leebeeck and Nydel [22], who used computational objects to simulate roll-waves, and on the analytical roll-wave solutions of Dressler [27] and Watson [88]. Rather than adding intermittent solitary wave objects onto an otherwise plane flow field, as in [22], the idea in Paper II is to simulate the wave regime as a continuing chain of wave objects. These objects are generalizations of steady wave solutions (section 3.9,) and a single computational element constitutes a wave crest. Thus, a detailed representation of the wavy flow regime should be made computationally affordable also for large scale pipeline systems. Although reproducing the flow dynamics, true efficiency was eluded due to the effort required in searching for and integrating the profile solutions.

Paper III 'CHARACTERISTIC METHODS AND ROE'S METHOD FOR THE INCOMPRESSIBLE TWO-FLUID MODEL FOR STRATIFIED PIPE FLOW.'

This paper is a search for efficient schemes for the incompressible two-fluid model. Inspired by Watson's model investigated in Paper II, and by the simulations performed by Holmås in [39], focus was placed on numerical techniques based on the eigenstructure of the incompressible two-fluid model. A Roe scheme and several schemes based on the Method of Characteristics were proposed. These schemes are original to the author's knowledge, some utilizing moving-grid techniques.

Paper IV 'THE STABILITY OF ROLL-WAVES IN TWO-PHASE PIPE FLOW'

This paper was a separate endeavour, written alongside Paper III. Inspired by Watson's roll-wave solutions [88], the goal of this project was to obtain linear stability expressions capable of determining whether a wavy flow regime can persist, or if the slugging flow will be encountered. It was however found that many modes of instability exist. These require computationally expensive mapping. Still, the analysis pursues a fundamentally different approach to flow regime prediction and was therefore included as a paper.

Paper V 'THE KELVIN-HELMHOLTZ/VON NEUMANN STABILITY OF DISCRETE

REPRESENTATIONS OF THE TWO-FLUID MODEL FOR STRATIFIED TWO-PHASE FLOW'

This paper examines the well-known Kelvin-Helmholtz stability of the two-fluid model and the von Neumann analyses sometimes applied to discrete representations thereof. The origin of this paper was an examination of the stability properties of the SLUGGIT code. It was discovered that the Kelvin-Helmholtz stability derivation could be undertaken in a way that conserves the underlying form and structure of the incompressible two-fluid model and which can be subjected to physical interpretation. Further, when highlighting the parallels to von Neumann analysis, it was seen that the two are sufficiently analogous for von Neumann results to be obtained directly from the Kelvin-Helmholtz expressions. This directly provides the stability properties of a wide family of discrete representations. Several features of numerical modelling were investigated in relation to stability prediction. The article advocates for use of linear theory as a tool for choosing discretization scheme and parameters, and for analysing and interpreting the predictions that these schemes provide.

A preliminary version of this paper was also presented at the 9th International Conference on Multiphase Flow (ICMF,) May 22 to 27, 2016 in Florence, Italy. The restricted content of this proceedings article makes it easier to read and so it is included among the appendices.

Paper VI 'A DUAL GRID METHOD FOR THE COMPRESSIBLE TWO-FLUID MODEL WHICH COMBINES ROBUST FLUX SPLITTING METHODOLOGY WITH HIGH-RESOLUTION CAPTURING OF INCOMPRESSIBLE DYNAMICS'

This final paper is a return to the investigations of Paper I. Using the techniques and the understanding acquired in the papers previous, an accurate and efficient method for simulating compressible flows is described. This method effectively avoids the problem of disturbances which originate from the grid projection, observed in Paper I. As opposed distinguished the grid models based on whether the grid equations pertain to the gas or the liquid field, the new method distinguishes grid models based on compressibility. The Hybrid Central-Upwind flux splitting scheme of Evje and Flåtten [31] is used in combination with the Roe scheme from Paper III. This effectively decouples the hydraulic spatial scales from the acoustic ones. The resulting scheme, at

least when compared to explicit schemes, improves computational efficiency by several orders of magnitude in a wide range of flow problem.

Additional Texts Three texts have been included in Appendix B. First, the conference paper related to Paper V. Second, a summary of the Biberg friction model [15] used in the tests of Paper III-VI. Third, a rigid pipe–flexible joint structural pipeline model, developed 'on the side.'

An ICMF conference paper [24] has also been co-authored during this Phd.

Chapter 3

New and Old Theory on Stratified Two-Phase Pipe Flows

This chapter contains the most important theory used and derived throughout this work. Some parts comes from the literature. Other parts are original contributions.

The two-fluid model is presented in section 3.1 and simplified into a model for stratified flow, and finally for incompressible stratified flow (section 3.3 and 3.4.) Next, stability is considered for plane stratified flow in section 3.5 and 3.6. We then move on to examine the non-linear flow that ensues. Discontinuities and shocks are studied in section 3.7 and 3.8. Finally, the roll-wave solutions, which appear frequently in the submitted papers, are presented and investigated further – this in section 3.9. The chapter finishes, in section 3.10, by informally examining the two-fluid model it relation to stability, hyperbolicy and well-posedness. These are topics which have spawned controversy in the multiphase community for many years.

3.1 The Two-Fluid Model

Thorough derivation of the Two-Fluid model can be found in many pieces of literature, for example [78, 77, 44, 29, 28, 67]. The model will here merely be presented, although these model equations are rudimentarily recovered when studying the momentum conservation through a shock later in section 3.8. This will suffice by way of model derivation.

The field equations for field k of the two-fluid model may for any flow topology

be written

$$\partial_t a_k \langle \overline{\rho} \rangle_k + \partial_x a_k \langle \overline{\rho u} \rangle_k = 0, \tag{3.1a}$$

$$\partial_t a_k \langle \overline{\rho u} \rangle_k + \partial_x a_k \left\langle \overline{\rho u^2} + \overline{p} \right\rangle_k - \langle \overline{p} \rangle_{\mathrm{i},k} \, \partial_x a_k = \langle \overline{s} \rangle_k \,, \tag{3.1b}$$

$$a_\ell + a_\mathrm{g} = \mathcal{A}(x), \tag{3.1c}$$

with momentum sources

$$\langle \overline{s} \rangle_\ell = -\sigma_k \, \langle \overline{\tau} \rangle_{\mathrm{w},k} + \sigma_\mathrm{i} \, \langle \overline{\tau} \rangle_{\mathrm{w,i}} - a_\ell \, \langle \overline{\rho} \rangle_\ell \, g_x, \tag{3.2a}$$

$$\langle \overline{s} \rangle_\mathrm{g} = -\sigma_\mathrm{g} \, \langle \overline{\tau} \rangle_{\mathrm{w},k} - \sigma_\mathrm{i} \, \langle \overline{\tau} \rangle_{\mathrm{w,i}} - a_\mathrm{g} \, \langle \overline{\rho} \rangle_\mathrm{g} \, g_x. \tag{3.2b}$$

g is here the gravitational acceleration and $g_x = g \sin\theta$, $g_y = g \cos\theta$ if θ is the pipe inclination, positive above datum. The phase areas a_k and perimeters σ are illustrated in Figure 3.1 for the case of stratified flow. Bars $\overline{\phi}$ indicate the ensemble or statistical average. It is used to convert the micro-scale chaotic turbulent flow structures into a coherent macro-scale representation. Angular brackets $\langle \phi \rangle_k$ indicate the average over the cross-section area, $\langle \phi \rangle_{\mathrm{w},k}$ over the pipe wall perimeter and $\langle \phi \rangle_{\mathrm{i},k}$ over the interface perimeter of field k. We will in this thesis consider two-field gas-liquid flows only and use symbolic indexation $k \in \{\ell, \mathrm{g}\}$ where ℓ pertains to the liquid field and g to the gas field.

Density fluctuations in the mass transport are dealt with by redefining the mean fluid velocity on the basis of momentum:

$$\overline{u} \equiv \overline{\rho u} / \overline{\rho}. \tag{3.3}$$

The momentum convection term is commonly rewritten into a form computable with averaged variables combined with closure relations. We write

$$\left\langle \overline{\rho u^2} \right\rangle_k = \Gamma \, \langle \overline{\rho} \rangle_k \, \langle \overline{u} \rangle_k^2 + \left\langle \overline{\rho \, (u - \overline{u})^2} \right\rangle_k ,$$

where the *shape factor*

$$\Gamma = \frac{\langle \overline{\rho}_k \overline{u}_k^2 \rangle}{\langle \overline{\rho} \rangle_k \, \langle \overline{u} \rangle_k^2}$$

and the second term is the average Reynolds stresses. Definition (3.3) has been used to reduce the Reynolds stress term. The shape factor Γ accounts of the effect that the statistical flow profile has on the non-linear convection term. Average Reynolds stresses account for the turbulent accelerations. The latter is commonly merged with the viscous shear stresses terms and modelled from there.

Modelling of the shape factor and, in particular, the Reynolds stresses is the subject of an enormous amount of literature and research – it falls outside of the

scope of this thesis. In what follows we shall disregard the shape factor (is it fairly small for turbulent flows[1] and straight-forward to include.) We will also assume the Reynolds stresses to be represented through the friction closures. This understood, we will drop the bar notation, remembering the statistical perspective of the flow. Angular brackets will also be dropped for the fluid velocities, interface pressure and shear stresses as variations in these are disregarded.

3.2 Geometric relationships

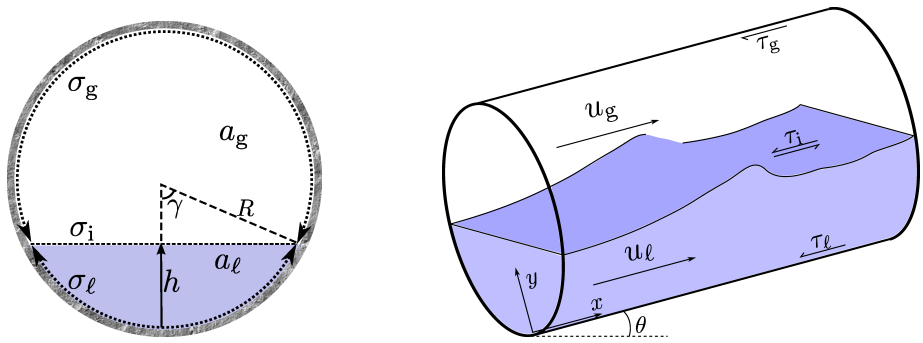

Figure 3.1: Pipe geometry and flow variables.

The circular pipe geometry enters into the modelling through the relationship between the level height h, the specific areas a_k and the perimeter lengths σ_k and σ_i. These are listed below:

$$\begin{aligned}
\gamma &= \arccos(1 - h/R) & \frac{\mathrm{d}\gamma}{\mathrm{d}h} &= \gamma' = 1/(R\sin\gamma) \\
h &= \mathcal{H}(a_\ell) = R(1-\cos\gamma), & \frac{\mathrm{d}h}{\mathrm{d}a_\ell} &= \mathcal{H}'(a_\ell) = 1/(2R\sin\gamma), \\
a_\ell &= \mathcal{A}_\ell(h) = R^2(\gamma - {}^1\!/_2\sin 2\gamma), & \frac{\mathrm{d}a_\ell}{\mathrm{d}h} &= \mathcal{A}_\ell{}'(h) = 2R\sin\gamma,
\end{aligned} \tag{3.4}$$

$$\sigma_\ell = 2R\gamma, \quad \sigma_g = 2R(\pi - \gamma), \quad \sigma_i = 2R\sin\gamma.$$

All geometric properties can be written as explicit expressions in h, though the

[1] $\Gamma = 2.0$ in single phase laminar flows and $1.04 \leq \Gamma \leq 1.11$ in single phase fully developed turbulent flows [89, p. 180].

same is not true for the volume fractions. Biberg's approximation [14]

$$\gamma \approx \pi\alpha_\ell + \left(\frac{3\pi}{2}\right)^{1/3}\left(1 - 2\alpha_\ell + \alpha_\ell^{1/3} - \alpha_{\mathrm{g}}^{1/3}\right) - 0.005\,\alpha_\ell\alpha_{\mathrm{g}}(\alpha_{\mathrm{g}} - \alpha_\ell)\left(1 + 4\left(\alpha_\ell^2 + \alpha_{\mathrm{g}}^2\right)^2\right)$$

is however very accurate and is commonly used within simulation routines. R is here the pipe inner radius, γ the interface half-angle and $\alpha_k = a_k/\mathcal{A}$ the volume fraction.

The pressure at the cross-sectional centroid (centre of gravity) of field k hydrostatically corresponds to the mean pressure in that field. Computing the height $\langle h\rangle_k$ of the centroid of $\mathcal{A}_k$ is a straight-forward exercise. Having done this, it is found that

$$\langle h\rangle_\ell = \frac{1}{a_\ell}\int_0^{\gamma_{\mathrm{i}}} h\frac{\mathrm{d}A}{\mathrm{d}\gamma}\,\mathrm{d}\gamma = R - \frac{2}{3}\frac{R^3}{a_\ell}\sin^3\gamma_{\mathrm{i}} \tag{3.5a}$$

and

$$\langle h\rangle_{\mathrm{g}} = \frac{1}{a_{\mathrm{g}}}\int_{\gamma_{\mathrm{i}}}^{\pi} h\frac{\mathrm{d}A}{\mathrm{d}\gamma}\,\mathrm{d}\gamma = R + \frac{2}{3}\frac{R^3}{a_{\mathrm{g}}}\sin^3\gamma_{\mathrm{i}}. \tag{3.5b}$$

Figure 3.2 shows the respective average heights; the location of the centre of gravity in a pipe is not much different from what it would be in a channel or duct, where

$$\text{channel/duct:} \qquad \langle h\rangle_\ell = h/2, \qquad \langle h\rangle_{\mathrm{g}} = (D+h)/2. \tag{3.6}$$

3.3 Level Height Formulation of the Two-Fluid Model

We separate the axial pressure, designated to the interface pressure p_{i}, from the common hydrostatic approximation of the normal pressure distribution:

$$\langle p\rangle_k \cong p_{\mathrm{i},k} + \Delta p_k(h), \tag{3.7}$$

where

$$\Delta p_k = \rho_k g_y(h - \langle h\rangle_k). \tag{3.8}$$

The point of making this separation is that that the hydrostatic pressure difference Δp depends only on the lever height h. It is important to note that (3.7) entails a

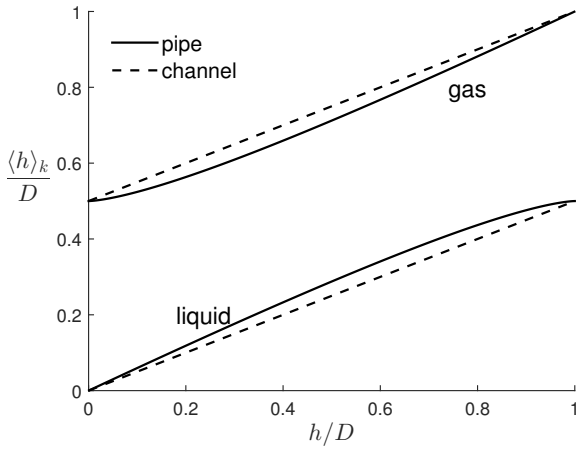

Figure 3.2: Centres of gravity; equations (3.5), (3.6).

long wavelength assumption as we are disregarding the effect that acceleration in the normal direction has on the pressure.

Provided the model is differentiable locally, we may then write the pressure terms of the momentum equation (3.1b) as

$$\partial_x a_k \langle p\rangle_k - p_{\mathrm{i},k}\partial_x a_k = \partial_x a_k \Delta p_k + a_k \partial_x p_{\mathrm{i},k} = (a_k \Delta p_k)'\partial_x h + a_k \partial_x p_{\mathrm{i},k},$$

where $\phi' = \frac{\mathrm{d}\phi}{\mathrm{d}h}$. Inserting (3.5) and the expressions for γ', a_ℓ' and h from (3.4), we find for the liquid phase

$$\begin{aligned}(a_\ell \Delta p_\ell)' &= \rho_\ell g_y \left[a_\ell + a_\ell' h - R a_\ell' + 2R^3\left(\sin^3\gamma\right)'\right] \\ &= \rho_\ell g_y \left[a_\ell + 2R^2 \sin\gamma(1-\cos\gamma) - 2R^2\sin\gamma + 2R^3\sin^2(\gamma)\cos(\gamma)\,\gamma'\right] \\ &= \rho_\ell g_y a_\ell,\end{aligned}$$

and thus

$$\partial_x a_\ell \langle p\rangle_\ell - p_{\mathrm{i},\ell}\partial_x a_\ell = a_\ell \partial_x p_{\mathrm{i},\ell} + a_\ell \rho_\ell g_y \partial_x h. \tag{3.9a}$$

A similar procedure applied to the gas phase reveals

$$\partial_x a_\mathrm{g} \langle p\rangle_\mathrm{g} - p_{\mathrm{i},\mathrm{g}}\partial_x a_\mathrm{g} = a_\mathrm{g} \partial_x p_{\mathrm{i},\mathrm{g}} + a_\mathrm{g} \rho_\mathrm{g} g_y \partial_x h. \tag{3.9b}$$

Finally, the pressure $p_{\mathrm{i},k}$ at the interphase is modelled from the densities alone, $p_{\mathrm{i},k} = \mathcal{P}_k(\rho_k)$, ignoring temperature influences. We also disregard the surface tension so that the interphase pressures encountered from either field are one and the same: $p_{\mathrm{i},\ell} = p_{\mathrm{i},\mathrm{g}} = p_\mathrm{i}$.

Put together, the two-fluid model now reads

$$\partial_t(\rho a)_k + \partial_x(\rho a u)_k = 0, \tag{3.10a}$$
$$\partial_t(\rho a u)_k + \partial_x\left(\rho a u^2\right)_k + a_k \partial_x p_\mathrm{i} + g_y \rho_k a_k \partial_x h = s_k, \tag{3.10b}$$
$$a_\ell + a_\mathrm{g} = \mathcal{A}(x), \tag{3.10c}$$
$$p_\mathrm{i} = \mathcal{P}_\mathrm{g}(\rho_\mathrm{g}) = \mathcal{P}_\ell(\rho_\ell). \tag{3.10d}$$

3.4 The Incompressible Two-Fluid Model

Acoustic waves are often of little or no importance for the development of stratified flows, provided the fluids advect slowly compared with the speed of sound [39, 66]. This enables us to reduce the two-fluid model (3.10) further by assuming incompressibility. The resulting model has a lower rank, a simpler eigenstructure and a conservative equation form (albeit not for the physically conserved variables.)

The incompressible two-equation model is obtained by reducing the momentum equations (3.10b) with their respective mass equations (3.10a) and eliminating the pressure term between them, resulting in

$$\partial_t \boldsymbol{v} + \partial_x \boldsymbol{f} = \boldsymbol{s}, \tag{3.11a}$$
$$\begin{pmatrix} a_\ell + a_\mathrm{g} \\ q_\ell + q_\mathrm{g} \end{pmatrix} = \begin{pmatrix} \mathcal{A}(x) \\ \mathcal{Q}(t) \end{pmatrix}, \tag{3.11b}$$

with mathematically conserved variables and fluxes

$$\boldsymbol{v} = \begin{pmatrix} a_\ell \\ [\rho\, u]_\mathrm{g}^\ell \end{pmatrix}, \qquad \boldsymbol{f} = \begin{pmatrix} q_\ell \\ j \end{pmatrix}, \qquad \boldsymbol{s} = \begin{pmatrix} 0 \\ s \end{pmatrix}.$$

Symbols for the flux and source components have here been defined and are

flow rate: $$q_k = a_k u_k, \tag{3.12a}$$

'momentum' flux: $$j = \tfrac{1}{2}\left[\rho\, u_\ell^2\right]_\mathrm{g}^\ell + [\rho]_\mathrm{g}^\ell\, g_y h, \tag{3.12b}$$

'momentum' source: $$s = -\,[\rho]_\mathrm{g}^\ell\, g_x - \left[\frac{\tau\sigma}{a}\right]_\mathrm{g}^\ell + \tau_\mathrm{i}\sigma_\mathrm{i}\left(\frac{1}{a_\ell} + \frac{1}{a_\mathrm{g}}\right), \tag{3.12c}$$

with

$$[\cdot]_\mathrm{g}^\ell = (\cdot)_\ell - (\cdot)_\mathrm{g}.$$

We will refer to the second equation component of (3.11a) as a 'momentum' equation, although it really imposes the conservation of a specific momentum difference. The right hand functions $\mathcal{A}$ and $\mathcal{Q}$ of the algebraic identities (3.11b) are

parametric. The latter has been obtained by summing the two mass equations and applying the former.

This is the form of the incompressible two-fluid model as found in e.g. [39, 88, 47, 66], sometimes referred to as a 'no-pressure-wave model.' The author found this system to have a fairly simple quasi-linear form which he utilized in Paper II, III and V, and a nice orthogonal form used for the Method of Characteristics in Paper III. These forms will be presented shortly. Among the citations presented, only Keyfitz [52] and Wangensteen [87] seem to work with the quasi-linear form of an incompressible two-fluid model, though they choose a much more complicated formulation. The orthogonal forms are among the references seen used by Crowley [19] and Barnea and Taitel [9], though they too use a different, unnecessarily approximate form.

System (3.11) can be written in quasi linear form

$$\left(\partial_t + \frac{\partial \boldsymbol{f}}{\partial \boldsymbol{v}}\partial_x\right)\boldsymbol{v} = \boldsymbol{s} \tag{3.13}$$

in terms of a Jacobian

$$\frac{\partial \boldsymbol{f}}{\partial \boldsymbol{v}} = \frac{1}{\rho^*}\begin{pmatrix} (\rho u)^* & 1 \\ \varkappa^2 & (\rho u)^* \end{pmatrix} \tag{3.14}$$

whose eigenvalues are

$$\lambda^{\pm} = \frac{(\rho u)^* \pm \varkappa}{\rho^*}. \tag{3.15}$$

A new variable

$$\varkappa = \sqrt{\rho^* \left[\rho\right]_{\mathrm{g}}^{\ell} g_y \mathcal{H}' - \frac{\rho_\ell \rho_{\mathrm{g}}}{a_\ell a_{\mathrm{g}}}(u_{\mathrm{g}} - u_\ell)^2}. \tag{3.16}$$

has here been introduced along with the operator

$$\phi^* = \frac{\phi_\ell}{a_\ell} + \frac{\phi_{\mathrm{g}}}{a_{\mathrm{g}}}.$$

The determinant of our Jacobian is

$$\det \frac{\partial \boldsymbol{f}}{\partial \boldsymbol{v}} = \frac{\left((\rho u)^*\right)^2 - \varkappa^2}{\rho^{*2}} = \frac{\left(\rho u^2\right)^* - \left[\rho\right]_{\mathrm{g}}^{\ell} g_y \mathcal{H}'}{\rho^*}. \tag{3.17}$$

Figure 3.3 illustrates the information travelling directions of subcritical ($\lambda^+\lambda^- < 0$) and supercritical ($\lambda^+\lambda^- > 0$) states. The information travelling direction is important numerically, for example for designing good upwind schemes or choosing

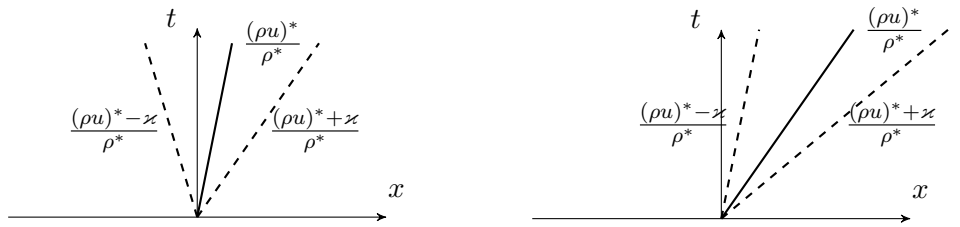

(a) subcritical (b) supercritical

Figure 3.3: Characteristic directions.

appropriate boundary conditions.

Finally, let us look at the orthogonal form of (3.11). We may diagonalize (3.13) with left eigenvectors, as follows:

$$\frac{\partial \boldsymbol{f}}{\partial \boldsymbol{v}} = \mathbb{L}^{-1}\Lambda\mathbb{L}, \tag{3.18}$$

where

$$\mathbb{L} = \begin{pmatrix} \boldsymbol{\ell}^+ \\ \boldsymbol{\ell}^- \end{pmatrix}, \qquad \boldsymbol{\ell}^\pm = \begin{pmatrix} 1 & \pm 1/\varkappa \end{pmatrix}, \qquad \Lambda = \begin{pmatrix} \lambda^+ & 0 \\ 0 & \lambda^- \end{pmatrix}. \tag{3.19}$$

Inserting (3.18) into (3.13) and multiplying by $\mathbb{L}$ from the left gives an orthogonal system

$$\boldsymbol{\ell}^\pm \frac{\mathrm{d}\boldsymbol{v}}{\mathrm{d}t} = \boldsymbol{\ell}^\pm \boldsymbol{s}, \qquad \text{along } \frac{\mathrm{d}x}{\mathrm{d}t} = \lambda^\pm. \tag{3.20}$$

Equation (3.20) expresses how the state $\boldsymbol{v}$ changes along the two paths $\int \lambda^+ \mathrm{d}t$ and $\int \lambda^- \mathrm{d}t$. A new state is formed at the intersection of these two paths from the information travelling along each. For information in one part of the system to reach another part it must travel along one of these paths, forwards in time. Figure 3.4 illustrates the range of influence and the range of dependency of some point $\boldsymbol{z}$ (Characteristic paths are assumed straight in the figure, which is a fair approximation for minute disturbances on an otherwise uniform state.)

3.5 Kelvin-Helmholtz Stability

It is well known that the two-fluid model (be it (3.1), (3.10) or (3.11)) retains the mechanisms which initiates hydrodynamic instability, commonly known as Kelvin-Helmholtz instability. A large number of linear analyses have been published over the years, usually looking into how various modelling terms are affect

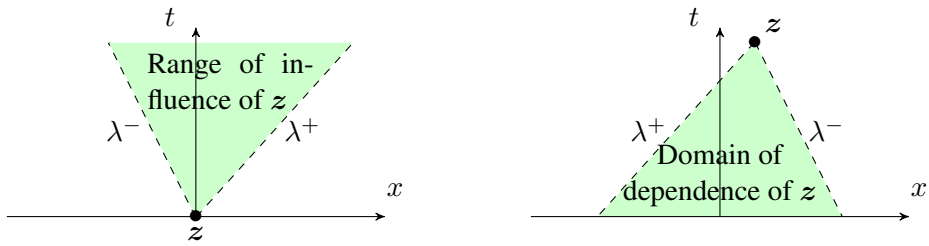

Figure 3.4: Information influence and dependence range in our hyperbolic system (3.11).

stability [57, 12, 63, 8, 50, 72, 6, 71, 64, 34]. Linear analysis gives an algebraic stability criterion which is useful for modelling and for flow prediction tools. The criterion derived in this section is commonly referred to as the *viscous* Kelvin-Helmholtz (VKH) criterion due to the presence of the momentum source term which contains shear stresses (not to be confused with second order differential terms in the two-fluid model.)

The VKH criterion will now quickly be derived through a route somewhat different than the one normally taken. It is a simplified version of the derivation presented in Paper V.

We start by expressing the system in a frame of reference relative to perturbation wave, translating with celerity C. If the celerity C is constant then this is equivalent to replacing all fluid velocities u_k with relative velocities

$$u_{k,\mathrm{r}} = u_k - C.$$

Expressing all functions with a reference relative to the perturbation wave

$$\tilde{\phi}(x - Ct, t) = \phi(x, t),$$

the model (3.11a) becomes

$$\partial_t \tilde{\boldsymbol{v}} + \partial_x \tilde{\boldsymbol{f}}_{\mathrm{r}} = \tilde{\boldsymbol{s}}. \tag{3.21}$$

Subscript 'r' indicates the relative frame; that all fluid velocities u_k are to be replaced with $u_{k,\mathrm{r}} = u_k - C$. We now perturb a uniform steady state $\boldsymbol{V}$[2], designated upper-case symbols, with a small disturbance wave $\delta\tilde{\boldsymbol{v}}$. Linearized about $\boldsymbol{V}$, (3.21) reads

$$\left(\partial_t + \frac{\partial \boldsymbol{F}_{\mathrm{r}}}{\partial \boldsymbol{V}}\partial_x - \frac{\partial \boldsymbol{S}}{\partial \boldsymbol{V}}\right)\delta\tilde{\boldsymbol{v}} = 0. \tag{3.22}$$

[2]The state $\boldsymbol{V}$ could also be non-uniform provided the perturbation wavelengths are much smaller than the length scales of the flow state [71].

Every term in (3.22) equals zero individually at the state of neutral VKH stability because the steady state is independent of the perturbation. The celerity C, which is the chosen translation velocity of our coordinate frame, ensures $\partial_t\,\delta\tilde{\boldsymbol{v}} = 0$.[3] This leaves us with the five equations,

$$\mathrm{d}\boldsymbol{F}_\mathrm{r} = 0, \qquad \mathrm{d}S = 0 \tag{3.23}$$

and the two identities (3.11b). Equations (3.23) express the term-by-term equilibrium of the two-fluid model (3.11) in the relative frame at neutral stability.

System (3.23)+(3.11b) may be solved for $\{A_\ell, A_\mathrm{g}, U_\ell, U_\mathrm{g}, C\}$, for example as follows: The first flux component equation $\mathrm{d}F_{\mathrm{r},1} = 0$ (and (3.11b)) reveals that the relative flow rates are constant;

$$Q_{k,\mathrm{r}} = A_k U_{k,\mathrm{r}} = \mathrm{const.} \tag{3.24}$$

This links all velocities to A_ℓ and C. The condition $\mathrm{d}S = 0$ then relates C to A_ℓ. S is in VKH analyses normally expressed as a function of volumetric flow rates $S = \mathcal{S}(A_\ell, Q_\ell, Q_\mathrm{g})$. The chain rule then yields $\mathrm{d}S = S'\,\mathrm{d}A_\ell = 0$, where

$$S' = \frac{\mathrm{d}S}{\mathrm{d}A_\ell} = \frac{\partial\mathcal{S}}{\partial A_\ell} + \frac{\partial\mathcal{S}}{\partial Q_\ell}\frac{\mathrm{d}Q_\ell}{\mathrm{d}A_\ell} + \frac{\partial\mathcal{S}}{\partial Q_\mathrm{g}}\frac{\mathrm{d}Q_\mathrm{g}}{\mathrm{d}A_\ell} = \frac{\partial\mathcal{S}}{\partial A_\ell} + \left(\frac{\partial\mathcal{S}}{\partial Q_\ell} - \frac{\partial\mathcal{S}}{\partial Q_\mathrm{g}}\right)C. \tag{3.25}$$

$\mathrm{d}S = 0$ then entails

$$C = \frac{\frac{\partial\mathcal{S}}{\partial A_\ell}}{\frac{\partial\mathcal{S}}{\partial Q_\mathrm{g}} - \frac{\partial\mathcal{S}}{\partial Q_\ell}}. \tag{3.26}$$

Finally, the second flux equation $\mathrm{d}F_{\mathrm{r},2} = \mathrm{d}J_\mathrm{r} = J_\mathrm{r}'\,\mathrm{d}A_\ell = 0$ fixes A_ℓ and the state of neutral VKH stability. Imposing (3.24), we find that this condition reads

$$J_\mathrm{r}' = \frac{\mathrm{d}J_\mathrm{r}}{\mathrm{d}A_\ell} = [\rho]_\mathrm{g}^\ell\, g_y\mathcal{H}' - \left(\rho\, U_\mathrm{r}^2\right)^* = 0, \tag{3.27}$$

$J_\mathrm{r}' < 0$ resulting in wave growth. A more detailed and precise presentation of VKH stability is given in Paper V.

In fact, it is shown in Paper V that the wave growth and decay, even of a viscous two-fluid model, is governed by a simple *dispersion equation* containing these exact terms, namely

$$\mathrm{i}kJ_\mathrm{r}' - S' = 0, \tag{3.28}$$

k being the wavenumber. The celerity C of *neutral* VKH stability (3.26) is here replaced by a *complex* celerity $\hat{c}$ in J_r' and S', and (3.28) is solved for $\hat{c}$; one finds two solutions

$$\hat{c} = b_1 \pm \sqrt{b_1^2 - b_0}$$

[3] somewhat simplified; there will be a superpositioning of perturbation waves which individually obeys $\partial_t\,\delta\tilde{\boldsymbol{v}} = 0$.

with

$$b_1 = \frac{1}{\rho^*}\left((\rho U)^* + \frac{1}{2}\frac{\mathrm{i}}{k}\left(\mathcal{S}_{Q_\ell} - \mathcal{S}_{Q_\mathrm{g}}\right)\right), \qquad b_0 = -\frac{1}{\rho^*}\left(J' + \frac{\mathrm{i}}{k}\mathcal{S}_{A_\ell}\right).$$

We will refer to the wave with the greater absolute value as the *fast wave*, terming the other the *slow wave*. Wave perturbations are proportional to $\exp(-\mathrm{i}k\hat{c}t)$, meaning that a positive imaginary component in $\hat{c}$ results in perturbation growth while a negative imaginary component results in perturbation decay. (At neutral stability $\Im(\hat{c}) = 0$ and $\Re(\hat{c}) = C$. The terms in (3.28) are then orthogonal and seen to give (3.26) and (3.27).)

Note that the VKH condition (3.26)–(3.27) for neutral stability is independent of the wavenumber k. Indeed, this has been pointed out by many authors before, for example by Jones and Prosperetti [50] for a generalized first-order formulation of the two-fluid model. These authors and others have pointed to this fact as a flaw in the two-fluid model, showing that the model of only first-order differential equations is incomplete. However, we see from (3.28) that the rate of growth or decay anywhere but at the state of neutral stability is wavenumber dependent. The observed wavelength distribution in an unstable flow will thus not be uniform.

Two-fluid models containing higher order differential terms will have wavenumber dependences also in the condition of neutral stability [72, 8, 64, Paper V].

3.6 Eigenstructure and Stability

As we should expect, the eigenvalues (3.15) remains consistent after a Galilean transformation in that

$$\lambda^\pm_\mathrm{r} = \lambda^\pm(U_k \to U_{k,\mathrm{r}}) = \lambda^\pm - C.$$

Considering the determinant (3.17), the condition for neutral stability (3.27) is seen to be related directly to the relative eigenvalues through

$$J'_\mathrm{r} = -\rho^* \det\frac{\partial \boldsymbol{F}_\mathrm{r}}{\partial \boldsymbol{V}} = -\rho^* \lambda^+_\mathrm{r}\lambda^-_\mathrm{r}, \tag{3.29}$$

the final equality being a general feature of linear algebra. Indeed, solving $\det\frac{\partial \boldsymbol{F}_\mathrm{r}}{\partial \boldsymbol{V}} = 0$ is a common route for determining the von Neumann stability of discrete two-fluid model representations [62, 71, 34], although the relation to the Kelvin-Helmholtz stability has to the authors knowledge not been noted before Paper V. The last equality reveals that *VKH stability coincides with hydraulically critical flow in the*

frame of a perturbation. Depending on the sign of $(\rho U_\mathrm{r})^*$, we find

$$\text{Neutral VKH criterion:} \qquad \lambda_\mathrm{r}^{\pm} = 0, \qquad \left(\lambda_\mathrm{r}^{\mp} = 2\frac{(\rho U_\mathrm{r})^*}{\rho^*}.\right) \tag{3.30}$$

The eigenvalues $\lambda^{\pm}$ do of course not depend on the source term S, although the *relative* eigenvalues $\lambda_\mathrm{r}^{\pm} = \lambda^{\pm} - C$ and the VKH stability criterion do through (3.26). In the case of inviscid flow (flow without shear stresses) we have $S \equiv 0$. The wave celerity C will then not be prescribed by (3.26) and the equations (3.23) can be satisfied at any hyperbolic flow state. In other words, a perturbation wave in any inviscid state will neither grow nor decay for as long at the two-fluid model remains hyperbolic; $\lambda^{\pm} \in \mathbb{R}$. In fact, from (3.28), or simply by contemplating the *meaning* of eigenvalues, we see that the inviscid perturbation celerities and the eigenvalues are one and the same;

$$\hat{c}\big|_{S\equiv 0} = \lambda^{\pm}. \tag{3.31}$$

From (3.31), or (3.29), we see that the inviscid celerity must turn complex if the eigenvalues do. Inspecting the eigenvalues (3.15), the '*inviscid* Kelvin-Helmholtz' (IKH) criterion may thus be written

$$\text{Neutral IKH criterion:} \qquad \varkappa = 0. \tag{3.32}$$

The 'growth' that ensues from IKH instability is thus not well-defined as the equation system turns non-hyperbolic; the initial value problem is ill-posed. In contrast, the VKH offers a region of hyperbolic wave growth in between (3.30) and (3.32). An interpretation of why the two-fluid model loses hyperbolicity will be presented later in section 3.10.

A plot from Paper V is shown in Figure 3.5. The parametric plot depicts the complex celerity $\hat{c}$ under increasing gas rates Q_g, other parameters being unchanged. The real component of $\hat{c}$ is the perturbation wave celerity; the velocity with which a disturbance propagates in the system. The imaginary component governs the rate of exponential growth ($\Im(\hat{c}) > 0$) or decay ($\Im(\hat{c}) < 0$.) Volume fractions, flow rates and friction state derivatives are computed from the VKH neutrally stable state. Then, all but the gas rates are kept constant. Multiple graphs of reducing source strengths ('source weight') are shown to indicate what happens as viscosity is reduced – the VKH criterion does not converge towards the IKH criterion, but the growth rate in between the two tends towards zero. A region of hyperbolic wave growth (assumed and marked 'well-posed'[4]) is seen in the λ^+

[4]Model 'well-posedness' is formally a considerable claim, though it is often used in the presented literature to describe models which are hyperbolic or models whose growth is bounded (e.g. due to included surface tension.) We try to avoid such terminology in this text.

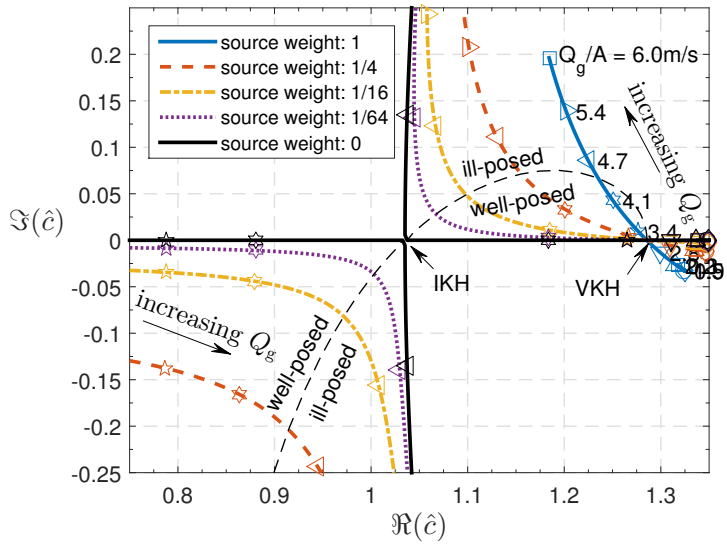

Figure 3.5: Parametric plot of complex celerity $\hat{c}$: $\delta\hat{\boldsymbol{v}} \propto \exp(-ik\hat{c}t)$ under increasing gas flow rates. 'Source weights' indicate multiplication factors to the source $\mathcal{S}$, demonstrating how the stability behaviour evolves as the model approaches the inviscid limit. The annotations 'VKH' and 'IKH' indicate the sates of neutral VKH and IKH stability, respectively. See also Figure 3.7.

wave for all graphs with a non-zero source weight. At source weight zero (inviscid model,) no growth or decay occurs until the model looses its hyperbolicity ('ill-posed').

Figure 3.6 shows a demonstration of how the model and the relative characteristic paths respond as flow rates are increased. The VKH stability condition can be understood in terms of the relative characteristic paths and whether or not they straddle the ordinate ((a)–(c).) IKH instability occurs as the two paths overlap, $\lambda_{\mathrm{r}}^{+} = \lambda_{\mathrm{r}}^{-}$ ((c)–(e),) at which point the two-fluid model is linearly degenerate. IKH instability in an inviscid model, which is where it makes sense to talk about IKH stability, entails $\lambda_{\mathrm{r}}^{+} = \lambda_{\mathrm{r}}^{-} = 0$ and $C = (\rho U)^*/\rho^*$ ((f).) Figure 3.6e somewhat dramatically indicates the change to complex eigenvalues and the transition to an elliptic two-fluid model. What actually happens at this point is a topic which has received some attention from mathematicians (e.g. [52, 32, 25],) but no good physical interpretation is known to the author.

References to the sketched characteristic paths of Figure 3.6 are given within Figure 3.7, relating these paths to the mode of stability. As the gas rate increases, the initially stable flow (a) passes the VKH stability criterion (b) ($\Im(\hat{c}) = 0$) and

turns kinematically unstable (c). Further increasing the gas rates excites the wave growth until the the model turns elliptic, (d)–(e), spawning dynamic growth where the two-fluid model constitutes an ill-posed initial value problem.

In contrast to the friction model used in Figure 3.5, which was the Biberg model [15] described in the Biberg model summery, a simpler friction model due to Taitel and Dunkler [80] has been used in Figure 3.7 and in the sections that follow:

$$\left\{\begin{array}{ll} \tau_k = {}^1\!/_2\, f_{\mathrm{c},k}\, \rho_k u_k |u_k|, & \tau_\mathrm{i} = {}^1\!/_2\, f_{\mathrm{c,i}}\, \rho_\mathrm{g} (u_\mathrm{g} - u_\ell)|u_\mathrm{g} - u_\ell|, \\ f_{\mathrm{c},k} = 0.046 \left(\dfrac{u_k d_k}{\nu_k}\right)^{-0.2}, & f_{\mathrm{c,i}} \leftarrow \left(\dfrac{f_{\mathrm{c,i}}}{f_{\mathrm{c,g}}}\right) f_{\mathrm{c,g}}, \\ d_\ell = 4\, a_\ell / \sigma_\ell, & d_\mathrm{g} = 4\, a_\mathrm{g} / (\sigma_\ell + \sigma_\mathrm{i}). \end{array}\right\} \tag{3.33}$$

Two different flow states, with different interfacial friction factors $f_{\mathrm{c,i}}/f_{\mathrm{c,g}}$, are presented. The former, in Figure 3.7a, is the most normal case. Here, the critical wave speed C is greater than the characteristic drift velocity $(\rho U)^*/\rho^*$ so that $(\rho U_\mathrm{r})^* < 0$ at neutral VKH stability. This is the case depicted in the path posts of Figure 3.6. The interphasial friction multiplier is here $f_{\mathrm{c,i}}/f_{\mathrm{c,g}} = 15$ and the uniform flow state is $H = 0.2d$, $\mathcal{Q}/\mathcal{A} = 4.5\,\mathrm{m/s}$. Note however that the neutral VKH wave celerity given by (3.26) is arbitrarily dependent on the friction model and unrelated to the two-fluid model. We can therefore envisage that a friction model producing $C < (\rho U)^*/\rho^*$ so that $(\rho U_\mathrm{r})^* > 0$. Even $(\rho U_\mathrm{r})^* = 0$ is possible, so that no hyperbolic growth region exists. In fact, $(\rho U_\mathrm{r})^* > 0$ can be achieved with the friction model (3.33) if the interphasial friction is sufficiently reduced; $f_{\mathrm{c,i}}/f_{\mathrm{c,g}} = 1.5$ and the flow state $H = 0.2d$, $\mathcal{Q}/\mathcal{A} = 4.5\,\mathrm{m/s}$ is depicted in Figure 3.7b. As we see, also the 'slow' wave can, at least theoretically, be the driver of flow instabilities. We will look further into what this means for the flow development in section 3.9.

3.7 Discontinuity, Weak Solutions and the Riemann Problem

Discontinuities form a natural component of hyperbolic conservation laws [82]. They may persist from initial or boundary conditions, or form naturally through the evolution of strongly non-linear systems. Discontinuities force us to locally weaken our notion of what the *solution* to a differential problem constitutes. Weak solutions are founded around the principle that discontinuous solutions must retain some conservation property in an integral sense – see e.g. [75]. Importantly, weak, discontinuous solutions are not invariant to mathematical transformations of the

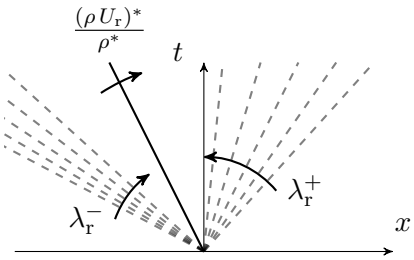

(a) VKH stable (wave decay.)
IKH neutrally stable (no decay.)
(3.11) is hyperbolic.

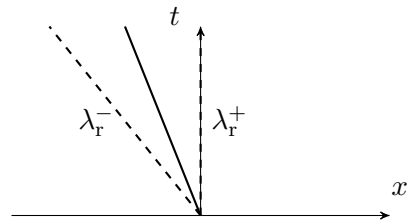

(b) VKH and IKH neutrally stable (no decay.)
(3.11) is hyperbolic.

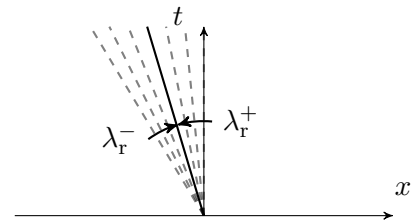

(c) VKH unstable (wave growth)
IKH neutrally stable (no decay)
(3.11) is hyperbolic.

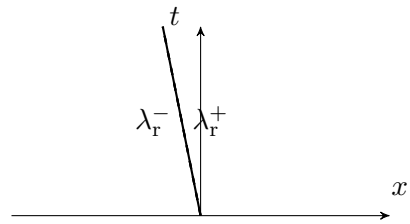

(d) VKH unstable (wave growth.)
IKH neutrally stable (no decay.)
(3.11) is parabolic.

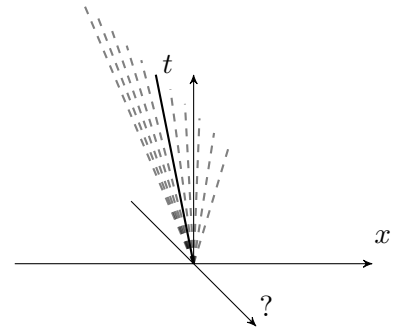

(e) VKH and IKH unstable (wave growth.) (3.11) is elliptic.

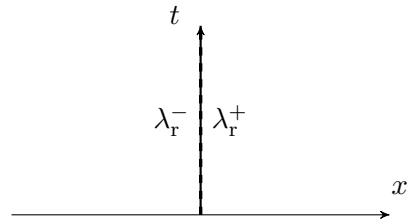

(f) Inviscid flow model (no friction terms.)
VKH stability not active.
IKH neutrally stable (no decay.)
(3.11) is parabolic.

Figure 3.6: Characteristic directions *relative to the celerity of a perturbation wave*. $(\rho U_r)^* \leq 0$

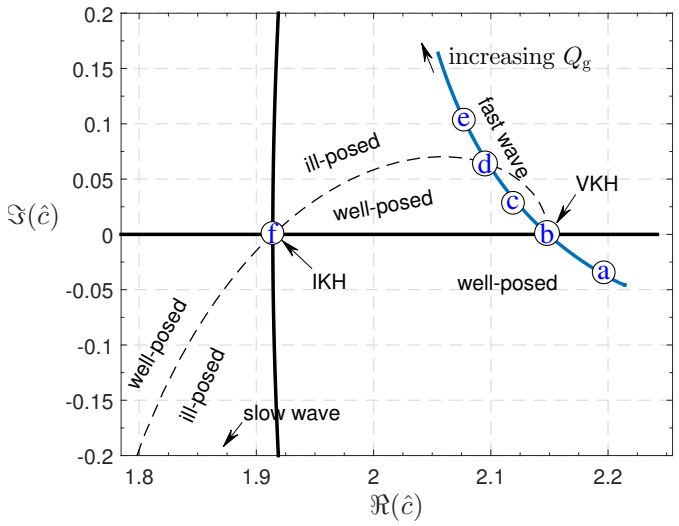

(a) $(\rho U_r)^* \leq 0$.
Friction model (3.33), $f_{c,i}/f_{c,g} = 15.0$ and state parameters $H = 0.2d$, $\mathcal{Q}/\mathcal{A} = 4.5\,\mathrm{m/s}$.
Labels refer to the characteristic path sketches of Figure 3.6.

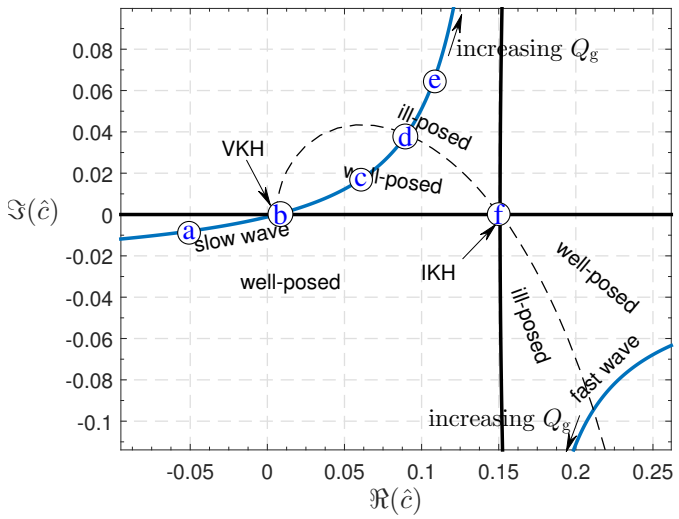

(b) $(\rho U_r)^* \geq 0$.
Friction model (3.33), $f_{c,i}/f_{c,g} = 1.5$ and state parameters $H = 0.2d$, $\mathcal{Q}/\mathcal{A} = 3.4\,\mathrm{m/s}$.
Labels refer to the characteristic path sketches of Figure 3.6, *but with the x-axes reversed and the $+/-$ eigenvalues swapped.*

Figure 3.7: $\hat{c}$-plots. $\delta\tilde{\boldsymbol{v}} \propto \exp(-\mathrm{i}k\hat{c}t)$.

equation system because transformations based on the chain rule require differentiability. Rigorous derivations of weak solutions typically consider the inviscid limit of a viscous system, but forming solutions based on conservation and entropy principles is a simpler route. This will be demonstrated in section 3.8.

The Riemann problem is fundamental for the construction of weak solutions for conservation laws. Its solution reveals the essential wave structures of hyperbolic systems. Further, it plays en key role in the Godunov family of numerical methods, such as in linearized Riemann solvers (Roe schemes.) We write the Riemann problem

$$\left\{ \begin{array}{c} \partial_t \boldsymbol{v} + \partial_x \boldsymbol{f} = 0, \\ \boldsymbol{v}(x<0,0) = \boldsymbol{v}_{\mathrm{L}}, \quad \boldsymbol{v}(x>0,0) = \boldsymbol{v}_{\mathrm{R}} \end{array} \right\}, \tag{3.34}$$

where $\boldsymbol{v}$ and $\boldsymbol{f}$ are some vector functions. The solution of (3.34) is built from a number of shocks, rarefaction waves and contact discontinuities equalling up to the number of differential equations. This solution exists and is unique provided the jump in initial data is 'sufficiently small' (Lax's theorem; see e.g. [38, pp. 194-196].)

Fundamental thermodynamic principles must be kept in mind when considering shock solutions, even if the system considered is isothermal or isentropic. In particular, the entropy production should never become negative. Such considerations result in the Lax entropy principle requiring a shock with velocity c, originating from any particular λ-characteristic and connecting left state $\boldsymbol{v}^-$ to right state $\boldsymbol{v}^+$, to satisfy

$$\lambda(\boldsymbol{v}^+) < c < \lambda(\boldsymbol{v}^-) \tag{3.35}$$

in order to be physical [38, pp. 180-187]. If not satisfied, the 'shock' should really be a rarefaction wave, or it is a contact discontinuity ($\lambda(\boldsymbol{v}^+) = c = \lambda(\boldsymbol{v}^-)$.)

Figure 3.8 indicates how the form of the solution of (3.34) will depend on the characteristic slopes of the left and right states. If we look at a two-equation system, (3.11) for example, then the solution of (3.34) will at most consist of a left, right and intermediate state connected by two waves. The waves are either rarefaction waves, shocks satisfying the Lax entropy condition (3.35), or contact discontinuities. We will observe a shock in the $\pm$-wave if $\lambda^{\pm}(\boldsymbol{v}_{\mathrm{L}}) > \lambda^{\pm}(\boldsymbol{v}_{\mathrm{R}})$, a rarefaction wave if $\lambda^{\pm}(\boldsymbol{v}_{\mathrm{L}}) < \lambda^{\pm}(\boldsymbol{v}_{\mathrm{R}})$ and a contact discontinuity if $\lambda^{\pm}(\boldsymbol{v}_{\mathrm{L}}) = \lambda^{\pm}(\boldsymbol{v}_{\mathrm{R}})$.[5]

[5]The characteristic field resulting in the last family of waves is said to be *linearly degenerate* while the characteristic fields resulting in either of the other two wave families are said to be *genuinely non-linear*.

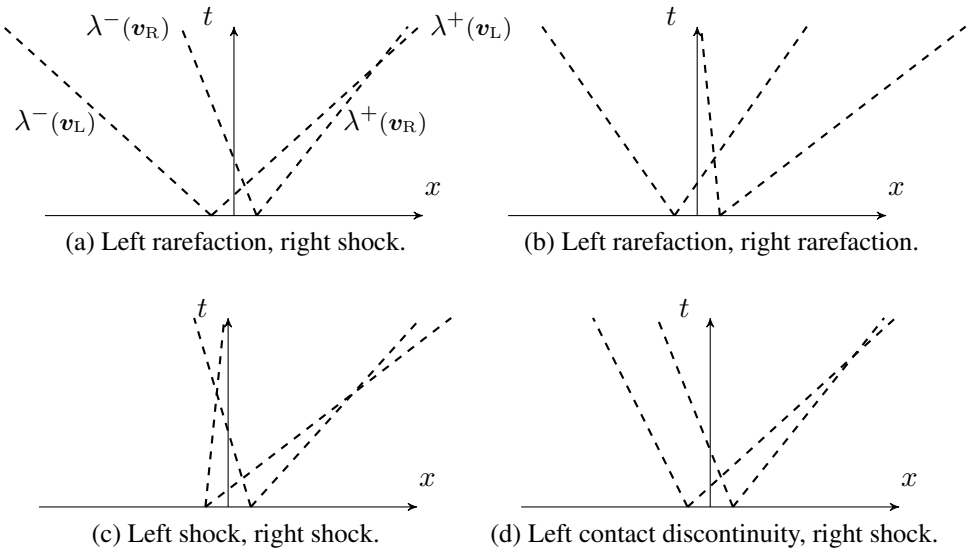

(a) Left rarefaction, right shock.

(b) Left rarefaction, right rarefaction.

(c) Left shock, right shock.

(d) Left contact discontinuity, right shock.

Figure 3.8: Example forms of the solution to the Riemann problem (3.34).

Figure 3.9a shows an example of how the characteristic paths may interact across a discontinuity. The figure shows a Riemann problem with initially stationary fluids and a greater liquid fraction on the left side. This figure is generated from the Method of Characteristics scheme presented in Paper III which discretely integrates (3.20). Data points are computable where the characteristic curves intersect. Level heights shown in Figure 3.9b are triangular (barycentric) interpolations through the line $t = 0.1$. The case simulated is that of free-surface flow $\rho_\mathrm{g} = 0$ (the shallow water equations), for which the analytical solutions (also shown) can be found in [38].

3.8 Shocks

Perhaps the simplest shock condition for the incompressible two-fluid model is derived from the system form (3.11). This is the shock condition used in, e.g., [88, 49, 48] and Paper II, III and IV. It is of course also the shock condition which a numerical scheme based on (3.11) will obey.

Consider a shock connecting a left state $\boldsymbol{v}^-$ at x^- to a right state $\boldsymbol{v}^+$ at x^+. Integrate, in a moving frame, (3.11a) thinly over the shock, from $x_\mathrm{r}^- = x^- - ct$ to $x_\mathrm{r}^+ = x^+ - ct$. Either applying Leibniz' rule $\int_{x_\mathrm{r}^-}^{x_\mathrm{r}^+} \frac{\partial}{\partial t}\phi \,\mathrm{d}x = \frac{\mathrm{d}}{\mathrm{d}t}\int_{x_\mathrm{r}^-}^{x_\mathrm{r}^+} \phi \,\mathrm{d}x - c\,[\phi]_-^+$, or applying a Galilean transformation to the x-axis, $x \to x - ct$, then yields the

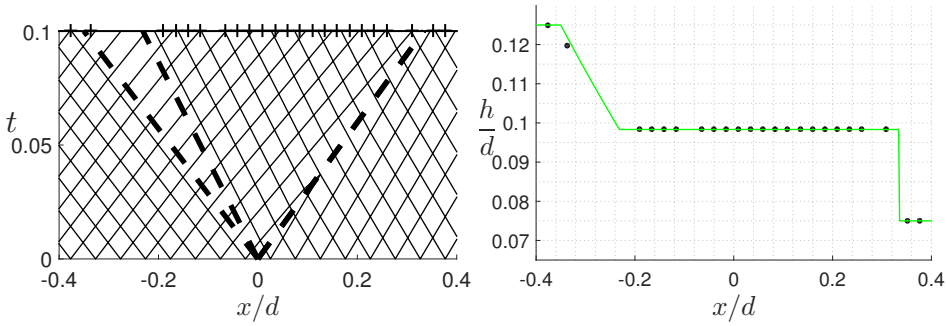

(a) Characteristic paths

(b) Level height at $t = 0.1$, simulation vs. analytical solution.

Figure 3.9: The Riemann problem with an initial discontinuity at $(0, 0)$.
Left: Rarefaction wave. Right: Shock.
Computed with the Method of Characteristics scheme presented in Paper III which discretely integrates (3.20).

shock condition

$$[\boldsymbol{f}_{\mathrm{r}}]_{-}^{+} = 0. \tag{3.36}$$

Our collection of difference notations has here been extended to include

$$[\cdot]_{-}^{+} = (\cdot)^{+} - (\cdot)^{-},$$

and any term whose integrand remains finite has vanished in the limit $[x_{\mathrm{r}}]_{-}^{+} \to 0^{+}$.[6] The first component of (3.36) is the same as in the stability analysis, i.e., (3.24): that the volumetric flows are preserved. The second component reads

$$[j_{\mathrm{r}}]_{-}^{+} = \left[\tfrac{1}{2}\left[\rho u_{\mathrm{r}}^2\right]_{\mathrm{g}}^{\ell} + [\rho]_{\mathrm{g}}^{\ell}\, g_y h\right]_{-}^{+} = 0, \tag{3.37}$$

which is recognised as a Bernoulli invariant.

The shock condition (3.37) seems reasonable, but it deserves some further consideration! It was pointed out in section 3.7 that shock conditions are not mathematically invariant to variable transformations. We note that the chain rule has been applied when deriving (3.11) from (3.1), both in the level height formulation of (3.10b) and in recovering the final conservative equation form. The chain rule requires differentiability locally and so these operations alter the shock invariants. Put bluntly, condition (3.37) is not momentum conserving; it conserves $[\rho u]_{\mathrm{g}}^{\ell}$.

[6] Transient terms remain finite in the moving frame if the frame follows the shock exactly. Source terms are assumed always finite.

To illustrate the difference between a shock in (3.1) and one in (3.11), consider for simplicity the conservative and the non-conservative formulations of the shallow water equations

$$\begin{pmatrix} h \\ hu_\ell \end{pmatrix}_t + \begin{pmatrix} hu_\ell \\ hu_\ell^2 + \frac{1}{2} g_y h^2 \end{pmatrix}_x = \mathbf{0}, \quad \begin{pmatrix} h \\ u_\ell \end{pmatrix}_t + \begin{pmatrix} hu_\ell \\ \frac{1}{2} u_\ell^2 + g_y h \end{pmatrix}_x = \mathbf{0}, \tag{3.38}$$

respectively. Mathematically, the two are equivalent if the flow is smooth. The incompressible two-fluid model turns into the latter non-conservative equation set if $\rho_\mathrm{g} = 0$ and the cross-section is rectangular. They then also yield the same shock conditions.[7] Shock conditions from (3.38) again appear as the invariance of the relative fluxes. Eliminating the shock velocity c between the respective mass and momentum equations, we express the respective Hogouiot loci

$$u_\ell^+ = u_\ell^- \pm [h]_-^+ \sqrt{\frac{g_y}{2}\left(\frac{1}{h^+} + \frac{1}{h^-}\right)}, \quad u_\ell^+ = u_\ell^- \pm [h]_-^+ \sqrt{\frac{2\, g_y}{h^+ + h^-}} \tag{3.39}$$

for the two model formulations. These functions respectively map possible right pairs (h^+, u_ℓ^+) provided a left state (h^-, u_ℓ^-). The functions are graphed in Figure 3.10 for two left states $(h^-, u_\ell^-) = (0.5, 1.0)$ and $(0.1, 1.0)$. As we see, the two model formulations are not equivalent when it comes to shocks. The differences are however small provided the shock height is moderate relative to the level heights. (Only a branch of each locus obeys the Lax entropy principle (3.35).)

The reminder of this section will be devoted to deriving a new shock condition which is momentum conserving. This has not been done in either of the papers presented or in any of the literature known to the author. It is an exercise which provides some additional insight.

Consider again a thin control volume moving with the shock front, as sketched for the gas phase in Figure 3.11. The linear momentum equation can, from Reynolds' transport theorem, be written

$$\boldsymbol{F}_k^\mathrm{ext} = \int\limits_{\mathcal{V}_k} \frac{\partial \rho \boldsymbol{u}}{\partial t}\, \mathrm{d}V + \oint\limits_{\mathcal{A}_k} \rho \boldsymbol{u}(\boldsymbol{u}\cdot\boldsymbol{n})\, \mathrm{d}A = \frac{\mathrm{d}}{\mathrm{d}t} \int\limits_{\mathcal{V}_{k,\mathrm{r}}(t)} \rho \boldsymbol{u}\, \mathrm{d}V + \oint\limits_{\mathcal{A}_{k,\mathrm{r}}(t)} \rho \boldsymbol{u}(\boldsymbol{u}_\mathrm{r}\cdot\boldsymbol{n})\, \mathrm{d}A \tag{3.40}$$

[7] We noted that shock condition (3.37) upholds a Bernoulli invariant. In, e.g., [79] one finds that the change in energy through a shock in the shallow-water equations can be written

$$\lim_{[x]_-^+ \to 0^+} \frac{\mathrm{d}E}{\mathrm{d}t} = q_{\ell,\mathrm{r}} \left[\tfrac{1}{2} u_{\ell,\mathrm{r}}^2 + g_y h\right]_-^+,$$

which equals zero precisely with the shock condition (3.37), $\rho_\mathrm{g} = 0$. This shock is therefore *isentropic*. Shocks which are momentum conserving and entropy-valid obey $\lim \frac{\mathrm{d}E}{\mathrm{d}t} < 0$.

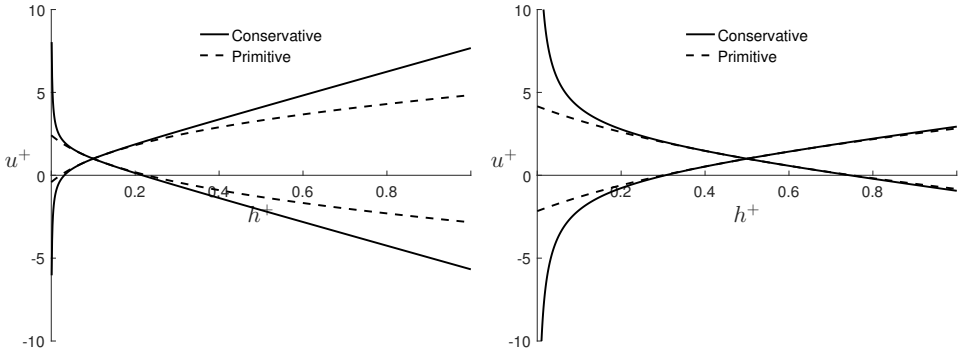

(a) $h^- = 0.1$ (b) $h^- = 0.5$

Figure 3.10: The Hogouiot loci (3.39): shock curves of the conservative and primitive variable shallow water equations (3.38). $u_\ell^- = 1$, $g_y = 10$.

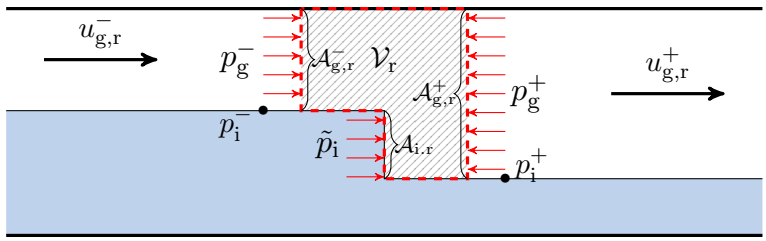

Figure 3.11: Sketch of a shock control volume for the gas phase. (Liquid phase similar.)

where the net external force is

$$\boldsymbol{F}_k^{\text{ext}} = -\oint_{\mathcal{A}_{k,\text{r}}} p\,\boldsymbol{n}\,\mathrm{d}A - \int_{\Sigma_{k,\text{r}}} \boldsymbol{\tau}_\text{w}\,\mathrm{d}A + \int_{\mathcal{V}_{k,\text{r}}} \rho\,\boldsymbol{g}\,\mathrm{d}V.$$

Again, provided integrands remain finite (which they are in the relative frame,) all volumetric integrals disappear because $\mathcal{V}_{k,\text{r}} \to \emptyset$ as $[x_\text{r}]_-^+ \to 0$. The remaining terms are

$$\begin{aligned}\oint_{\mathcal{A}_{k,\text{r}}} (\rho\boldsymbol{u}\boldsymbol{u}_\text{r} + p\mathbb{I})\cdot\boldsymbol{n}\,\mathrm{d}A &= \left(\int_{\mathcal{A}_{k,\text{r}}^-} - \int_{\mathcal{A}_{k,\text{r}}^+}\right)(\rho u u_\text{r} + p)\,\mathrm{d}A \pm \int_{\mathcal{A}_{\text{i},\text{r}}} p\,\mathrm{d}A \\ &= \left[a_k\left\langle\overline{\rho u u_\text{r}} + \overline{p}\right\rangle_k\right]_-^+ - \langle\tilde{p}_\text{i}\rangle\,[a_k]_-^+ = 0, \end{aligned} \tag{3.41}$$

where $\langle\tilde{p}_\text{i}\rangle$ is some ill-defined mean pressure over the shock itself. It reflects the non-conservative form of the two-fluid model (3.1). Let's try modelling it simply

$$\langle\tilde{p}_\text{i}\rangle = \frac{1}{2}\left(p_\text{i}^+ + p_\text{i}^-\right). \tag{3.42}$$

Note that (3.42) only affects the momentum transfer *between* phases – the modelling choice here will not alter the net momentum conservation over the shock. Inserting the hydrostatic pressure model (3.7) into (3.41) and eliminating $[p_\text{i}]_-^+$ now yields

$$\left[\frac{\left[a\left\langle\overline{\rho u u_\text{r}} + \Delta p\right\rangle\right]_-^+}{a^+ + a^-}\right]_\text{g}^\ell = 0, \tag{3.43a}$$

or, expressed in terms of the shock celerity,

$$c = \left[\frac{\left[a\left\langle\overline{\rho u^2}\right\rangle + a\,\langle\Delta p\rangle\right]_-^+}{a^+ + a^-}\right]_\text{g}^\ell \Bigg/ \left[\frac{\left[a\,\langle\overline{\rho u}\rangle\right]_-^+}{a^+ + a^-}\right]_\text{g}^\ell. \tag{3.43b}$$

The shock condition from the mass equation will be the same as in (3.36), namely

$$\left[a_k\left\langle\overline{\rho u_{k,\text{r}}}\right\rangle\right]_-^+ = 0. \tag{3.44a}$$

Expressed in terms of c,

$$c = \frac{\left[a_\ell\left\langle\overline{\rho u_\ell}\right\rangle\right]_-^+}{\left[a_\ell\left\langle\overline{\rho}\right\rangle\right]_-^+}. \tag{3.44b}$$

Again we consider locally incompressible flow. As expected, (3.43) and (3.44) reduces to shock conditions for the conservative shallow water equations when $\rho_\text{g} =$

0 and the geometry is that of a channel. Eliminating c between (3.43b) and (3.44b) once again generates a second order polynomial which, when solved, provides the Hogouiot locus relating u_ℓ^+ to h^+ for any prescribed left state (h^-, u_ℓ^-). Figure 3.12 shows such loci for the momentum conservative shock compared to the shock condition (3.36). The pipe geometry is used with the hydrostatic pressure closure (3.8) and centroid heights (3.5). As demonstrated earlier, the difference is small if the shocks are small relative to the level heights, but can be more substantial otherwise. Figure 3.13 shows the difference which the two shock formulations manifests on Watson's roll-wave solution presented later in section 3.9. Small roll-waves are affected little. Watson himself noted in [88] that (3.37) 'is not strictly valid through a discontinuity but the errors are small for weak shocks.' This fact seems to have been forgotten since.

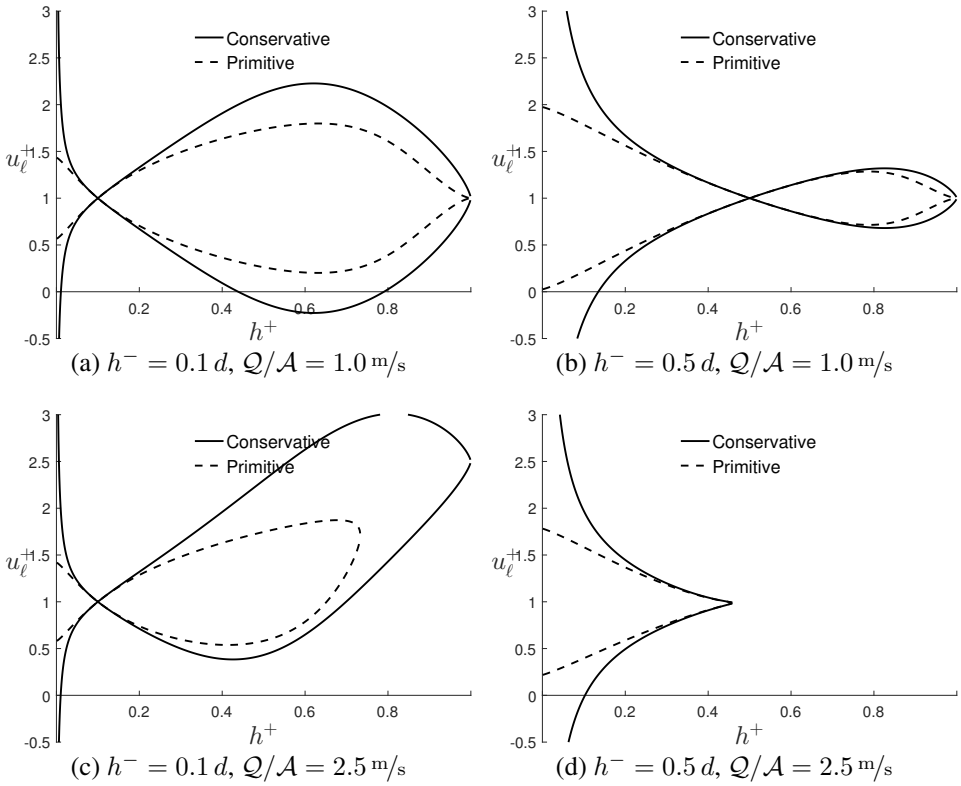

(a) $h^- = 0.1\,d$, $\mathcal{Q}/\mathcal{A} = 1.0\,\mathrm{m/s}$ (b) $h^- = 0.5\,d$, $\mathcal{Q}/\mathcal{A} = 1.0\,\mathrm{m/s}$

(c) $h^- = 0.1\,d$, $\mathcal{Q}/\mathcal{A} = 2.5\,\mathrm{m/s}$ (d) $h^- = 0.5\,d$, $\mathcal{Q}/\mathcal{A} = 2.5\,\mathrm{m/s}$

Figure 3.12: Hogouiot loci in two-phase pipe flow; Momentum conservative shock formulation (3.43) vs. (3.37).
$u_\ell^- = 1.0\,\mathrm{m/s}$; $\rho_\ell = 1\,000\,\mathrm{kg/m^3}$, $\rho_\mathrm{g} = 50\,\mathrm{kg/m^3}$, $d = 0.1\,\mathrm{m}$, $\theta = 0°$.

Notice finally that if we divide (3.41) by the shock length and revert the usual Galilean transformation, $x \to x + ct$, then we recover the original momentum equation (3.1b) of the two-fluid model ('assuming' continuity.) Source terms should be reinstated as volume integrals are divided by an infinitesimal length and turn into cross-section averages. We can therefore view (3.40) and (3.41) by way of a rudimentary derivation of the two-fluid model momentum equation.

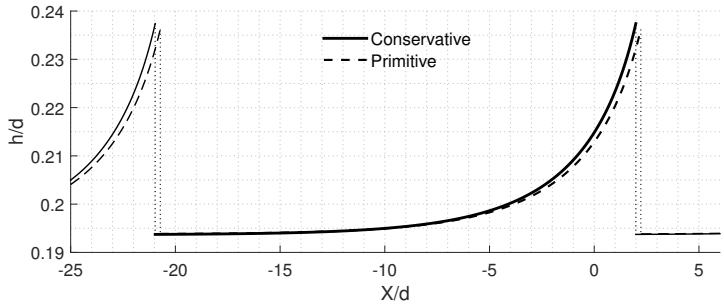

Figure 3.13: Comparison of roll-wave profiles using (3.43) vs. (3.37). State cf. Figure 3.14a.

3.9 Roll-Waves

The roll-wave solutions presented in this section were first presented by Watson in [88]. They are based on the same type of steady, stepwise exponential solutions derived for free-surface flows by Thomas [81] and Dressler [27]. These in turn were inspired by the profile solutions of hydraulic jumps found by Brass already in 1868. Viscous continuous solution, similar to Dressler's [27], have been provided by Johnson [47]. Solutions containing turbulent closures have been provided by Richard and Gavrilyuk [74]. The latter showed good profile agreement with experimental data.

Roll-waves, often called 'bores' by hydraulic engineers, are essentially hydraulic jumps in a moving frame. Fairly regular trains of roll-waves are frequently observed in nature, for example on the pavement of a slightly sloped street when it rains. Roll-waves constitute a central element in the wavy flow regime of two-phase flows. They tend to grow from out of a linear instability until they are stabilized by non-linear mechanisms. Waves can breach the pipe cross-section if the non-linear stabilization is insufficient, or if the waves interact with each other or the pipe geometry in an agitating manner. This can then result in the formation of slugs.

If a linearly growing wave is stabilized, it will eventually obtain a steady celerity $\hat{c} \to C \in \mathbb{R}$. The 'steady state' $\boldsymbol{V}$ that then emerges is steady in the relative frame $X_\mathrm{r} = x - C\,t$. It is now a function of X_r; $\boldsymbol{V} = \boldsymbol{V}(X_\mathrm{r})$. Assuming no disturbances, (3.21) now reads

$$\frac{\mathrm{d}\boldsymbol{F}_\mathrm{r}}{\mathrm{d}X_\mathrm{r}} = \boldsymbol{S}. \tag{3.45}$$

As with the VKH criterion in section 3.5, the mass component of (3.45) yields

$$\mathrm{d}Q_{\ell,\mathrm{r}} = 0,$$

and therefore (3.24) applies also now; the relative flow rates, often called the 'progressive discharges', are constant. The velocities are then single-variable functions $U_k = Q_{k,\mathrm{r}}/A_k + C$, and so are all else. Rearranged, the momentum component of (3.45) reads

$$\mathrm{d}X_\mathrm{r} = \frac{\mathrm{d}J_\mathrm{r}}{S}, \tag{3.46}$$

which is the profile equation of steady roll-waves. Assuming monotone profiles, we may again express this profile equation in terms of some state variable. $J_\mathrm{r}' = \frac{\mathrm{d}J_\mathrm{r}}{\mathrm{d}A_\ell}$, subject to (3.24), is already derived in (3.27), section 3.5. Integrated, the profile of a roll-wave is inversely expressed as

$$X_\mathrm{r}(H) = H_0 + \int_{H_0}^{H} \frac{J_\mathrm{r}'}{\mathcal{H}'S}\,\mathrm{d}h. \tag{3.47}$$

We have here chosen the level height H as the integration variable since A_ℓ is an explicit function of H while the inverse is not true (section 3.2.)

In the literature known to the author, roll-wave solutions generated from (3.47) are always convex, as in Figure 3.13. The shock condition is then a *fast* wave, generated for the intersection between $\lambda^+(\boldsymbol{V}^-)$ and $\lambda^+(\boldsymbol{V}^+)$ if the flow direction is positive. However, we found in section 3.6 and Figure 3.7b that also slow wave instabilities can be observed, at least theoretically, if provided with the right friction closures. The slow roll-wave that grows out from this instability is graphed in Figure 3.14b and observed to be concave. Both these flow cases have been simulated with the Roe scheme, using 512 cells. Data points from the steady profile to which these simulations converged are plotted atop the graphs of the analytical solutions. These overlap precisely.

Figure 3.14 also shows the numerator and denominator functions appearing in the profile solution (3.47) (equations (3.12c) and (3.27)) graphed. The functional value of $J_\mathrm{r} - J_\mathrm{r}^-$, the roots of which constitutes the shock condition (3.37), is

also shown. These graphs are similar to graphs presented by Johnson in [47] for the convex profile. The slow concave wave profile is seen to be organized about different roots than the fast convex one.

Both J_r' and S have a root within the height span of a roll-wave. These roots must coincide for the profiles to be integrable. The point at which they coincide is commonly termed the *critical point* H_0: $J_r'(H_0) = S(H_0) = 0$. Indeed, considering the eigenvalues in (3.29), we see that H_0 really is the hydraulically critical point in the relative reference frame.

Figure 3.15 shows the relative characteristic curves as they appear in the convex and concave roll-waves. As noted earlier in view of Figure 3.7, the convex roll-wave grows from out of the fast linear wave and so the wave front shock is that from the interaction between $\lambda^+(\boldsymbol{V}^+)$ and $\lambda^+(\boldsymbol{V}^-)$. Conversely, the concave roll-wave grows from out of the slow linear wave with the shock generated from the $\lambda^-(\boldsymbol{V}^+)$, $\lambda^-(\boldsymbol{V}^-)$ interaction. Both these shocks obey the Lax entropy condition (3.35).

VKH stability is an integral part of the roll-wave solutions. The critical point corresponds to a state of VKH neutral stability (3.27), and this point must exist for a for a steady shock front to exist and for roll-wave solutions to exist.[8] Expressed inversely, the VKH state of neutral stability *is* a critical point H_0. *Every* point is therefore a critical point in a neutrally stable uniform flow – we may imagine a zero-amplitude roll-wave or an infinite number of zero-wavelength roll-waves. Since there can be no profile inclination in a uniform flow we get $\mathrm{d}S = 0$ (Equation (3.23).) (3.24) also holds.

3.10 Hyperbolicity, the Ailments of the Two-Fluid Model and a Heuristic Diagnosis

A more general and informal discussion will be presented in this last section of the theoretical chapter.

We have so far only mentioned the conditionally hyperbolic nature of the two-fluid model. Vanishing model hyperbolicity has been a point of controversy with the two-fluid model after first being recognized by Gidaspow [35, 36]. Since then, it has been the subject of much study. Numerous contributors have tried to mend the model (e.g. [72, 8, 6, 73, 71, 34, 64, 63] and references within,) though these

[8] To see the former we may consider that $J_r' < 0$ constitutes subcritical flow and $J_r' > 0$ supercritical flow (Equation (3.29),) and that a shock can only form to bridge one of each. In between the profile functions are smooth so that critical point $J_r' = 0$ must exist; a condition corresponding the the VKH condition (3.27).

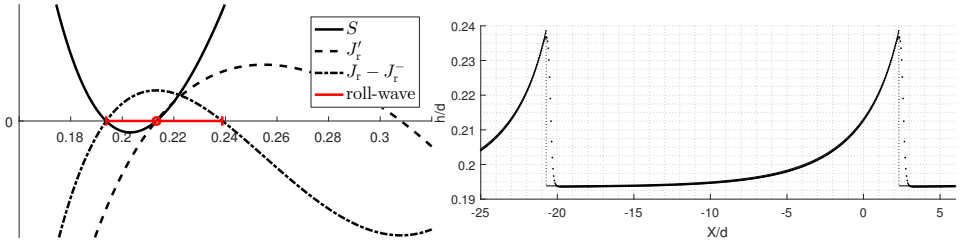

(a) Fast, convex roll-wave. $\mathcal{Q}/\mathcal{A} = 4.5\,\mathrm{m/s}$, $f_{\mathrm{c,i}}/f_{\mathrm{c,g}} = 15$

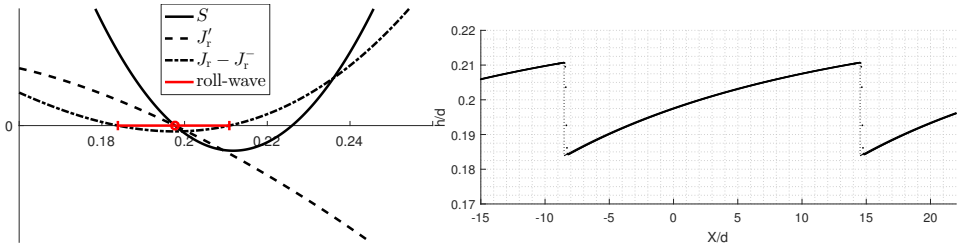

(b) Slow, concave roll-wave. $\mathcal{Q}/\mathcal{A} = 3.4\,\mathrm{m/s}$, $f_{\mathrm{c,i}}/f_{\mathrm{c,g}} = 1.5$

Figure 3.14: Left: Scaled terms appearing in profile equation (3.47) and the shock (3.37) as function of h/D. Red lines mark the range of the particular roll-wave solution. Markers are placed at H_0.
Right: Wave profiles; analytical integration of (3.47) (solid line) and numerical simulation of (3.11) with the Roe scheme of Paper III with 512 grid cells per wave (dot markers.) The analytical and simulated profiles are overlapping. $X(H_0) = 0$. $H_{\text{uniform flow}} = 0.2\,d$, $\rho_\ell = 1\,000\,\mathrm{kg/m^3}$, $\rho_\mathrm{g} = 50\,\mathrm{kg/m^3}$, $d = 0.1\,\mathrm{m}$, $\theta = 1°$. Wavelength $= 23\,d$.

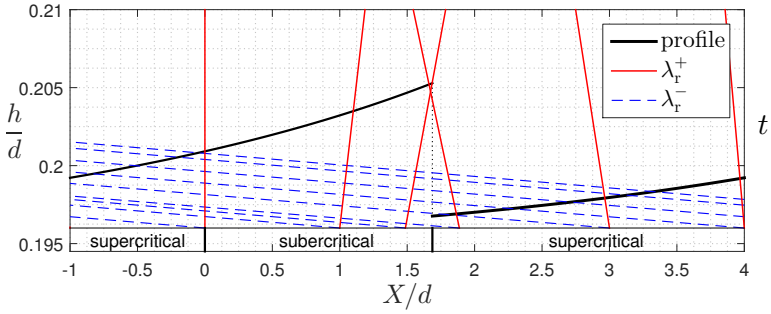

(a) Convex roll-wave. $\mathcal{Q}/\mathcal{A} = 4.5\,\mathrm{m/s}$, $f_{c,i}/f_{c,g} = 15$

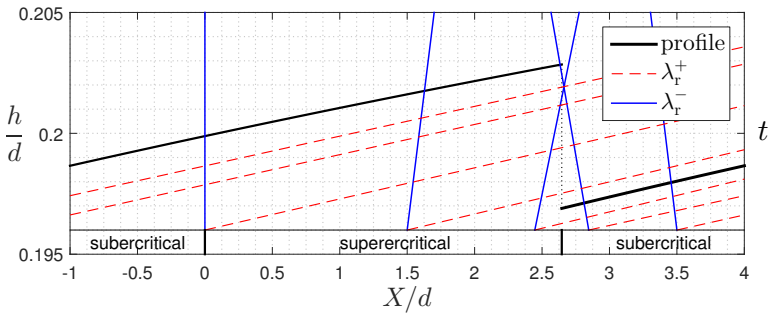

(b) Concave roll-wave. $\mathcal{Q}/\mathcal{A} = 3.4\,\mathrm{m/s}$, $f_{c,i}/f_{c,g} = 1.5$

Figure 3.15: Characteristic curves relative to a roll-wave solution. Wavelength $= 5\,d$ – other states as in Figure 3.14. Time axes of the characteristic curves are scaled for visibility.

usually approach the problem indirectly, proposing model extensions and then examining the resulting model properties. Mathematically oriented analyses have been provided to interpret ill-posedness in the two-fluid model [25, 52, 32], though these provide little by way of a physical interpretation.

Let us try to get a better understanding of what ails the two-fluid model. Complex eigenvalues originate from the volume fraction characteristics. Because the acoustic characteristics of (3.10) are well-behaved [65, 84, 33] it is sufficient to study incompressible flows. The condition for real eigenvalues is then $\varkappa^2 \geq 0$.

Consider the original two-fluid model (3.1) without compressibility. The most basic modelling assumptions leading to ill-posedness in (3.1) are

$$\langle p \rangle_\ell = \langle p \rangle_{\mathrm{g}} = \langle p \rangle_{\mathrm{i},k} = \langle p \rangle, \tag{3.48}$$

which makes sense for example in vertical annular flows. The model resulting from assumption (3.48) is often called the Wallis model after first being put forth in [86]. Let us also disregard friction and gravity altogether: $s_k \equiv 0$. The momentum equation (3.1b) now reads

$$\partial_t \rho_k u_k + \partial_x \big(\tfrac{1}{2} \rho_k u_k^2 + \langle p \rangle \big) = 0. \tag{3.49}$$

Integrating, we obtain two Bernoulli-type equations

$$\partial_t \varphi_k + \frac{u_k^2}{2} + \frac{\langle p \rangle}{\rho_k} = \text{const.}, \tag{3.50}$$

where $\partial_x \varphi_k = u_k$. Let us do now what we have already done a number of times – let us consider a uniform flow state $\boldsymbol{V}$ with a tiny perturbation on it. Again we move our reference frame so that it follows the perturbation. For the uniform flow field to have real eigenvalues we must choose

$$U_\ell = U_{\mathrm{g}} = U.$$

Equation (3.50) and Figure 3.16 conceptually illustrates the phenomenon of *Bernoulli suction*. Continuity enforces a velocity difference which should excite a pressure difference (create suction at the interphase.) It is the same type of acceleration induced pressure field seen, for instance, in a Laval nozzle or atop an airfoil. Consider the following remarks:

Remark 1. *If the interphase is affected by the indicated radial pressure gradient then any perturbation is unstable. This unconditional instability may very well be physical and has been referred to as both 'interphasial instability' and 'dynamic instability' [7, 10, 72, 18]*

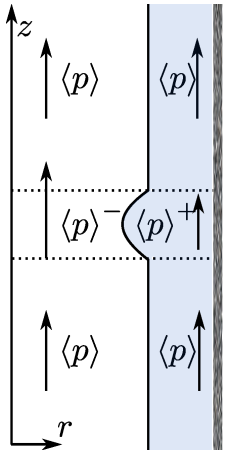

Figure 3.16: Bernoulli suction in annular flow.

Remark 2. *The instability is local.*

The local nature of Bernoulli suction makes this instability mechanism independent of perturbation wavelength, though the instability slowness (from a fluid transport/inertia perspective) is reduced with shortened wavelengths. Thus, an infinite wavenumber becomes infinitely unstable, as seen from stability analysis.[9] This has motivated researchers to introduce surface tension and axial viscosity terms into the two-fluid model [72, 8, 34].

In terms of axial drag forces, we see in the Wallis model (3.49) something analogous to D'Alambert's paradox as the pressure is recovered behind the perturbation. Physically, at high Reynolds numbers, we would not recover the pressure behind steep perturbations and these would then experience considerable drag. Consequently, high-wavenumber unstable structures are destroyed, forming capillary waves and ripples on the annular interphase. Because they are then unable to grow, the annular flow should turn stable in a statistical sense [7].

So how does the model ill-posedness fit into this? Let us alter our perspective slightly and consider the following cheeky claim:

> The inherent interphasial instability noted above is *not* of itself the problem with the two-fluid model, but that the model *lacks the mechanisms with which to enforce it.*

In view of the Wallis model (3.49) we see that

Remark 3. *the instability sketched in Figure 3.16 directly contradicts the model assumptions* (3.48).

[9] (3.31): Growth frequency $\omega = \Im(\hat{c})\, k = \lambda^{\pm} k \propto k$.

Uniform pressures are assumed though the cross-section in the Wallis model. This means that the model pressure observed in the perturbation will be something other than we would see in, say, a single-phase nozzle.[10] Anyway, we find that any perturbation forcing $u_\mathrm{g} \neq u_\ell$ produces complex eigenvalues and instability ($\hat{c} = \lambda^\pm$ from (3.31).)

Further, we again note that

Remark 4. *the Bernoulli suction is local – it is not felt by the points in the neighbourhood outside of the perturbation.*

At any point outside of the perturbation the information travels along the relative path $\frac{\mathrm{d}x_\mathrm{r}}{\mathrm{d}t} = \lambda^\pm_\mathrm{r} = 0$ (Figure 3.6f in light of Figure 3.4,) i.e., it does not travel at all. There is no acceleration and, more importantly, no axial pressure field to tell the neighbourhood that the perturbation demands fluid with which to grow. A solution which satisfies the differential equation system could therefore not maintain itself through time and would have to be 'enforced'. In this way, time makes up a dimension analogous to space – a two-dimensional elliptic system.

From a physical perspective, the instability outlined above should be maintained through a three-dimensional pressure field which is non-uniform radially and protrudes out in the axial directions.[11] The axial extension of the pressure field is present in the original formulation of the momentum equation (3.1b) through the term $-p_{\mathrm{i},k}\partial_x a_k$. However, the assumption (3.48) denies this term any spatial extent and so we lose hyperbolicity. We modelled the interphasial pressure difference Δp_k in (3.10) and (3.11), but in the localized hydrostatic manner (3.8). The dimensional extension is then retained only through the level height gradient $\partial_x h$, which provides us with only conditional hyperbolicity. Imagining the picture in Figure 3.16 with a full three dimensional pressure field, we would expect Δp_k to be proportional both to the curvature of the interphase and to the dynamic pressure $\frac{1}{2}\rho_k U^2$. A hydrostatic pressure field would come in addition in horizontal flows.

All fantastication aside, how do the hyperbolizating and regularization attempts found in literature alter the structure of our model? First, let us consider the level height term (3.8). It essentially imposes shallow water wave dynamics on our system [90]. The perturbation, without the suction effect, will now disperse. The level height term therefore counteracts the localness of the Bernoulli suction. In fact, it imposes a simple balance; if the suction is not sufficient to withstand the

[10] Of course, two-fluid models exist which solves field pressures individually, retaining hyperbolicity – for example the Saurel-Abgrall model (see e.g. [33].)

[11] The imaginary components of the model eigenvalues reflect, in some philosophical sense, the lacking radial dimension or the lack of axial extension in the model.

wave dispersion (say, if the suction atop a tiny perturbation is less than the pressure difference on its sides,) then it will move and communicate with its neighbourhood. This balance is observed in $\varkappa$, (3.16). Consider again the *inviscid* flow model ($S \equiv 0$), whose perturbation wave celerities are $\hat{c} = \lambda^{\pm}$, eigenvalues given in (3.15). When real, there will be a positive and a negative celerity of equal magnitude about a constant drift $(\rho U)^*/\rho^*$. As long as these waves disperse they will neither grow nor decay. Increasing the fluid velocity difference (the suction) will effectively reduce the speed with which these perturbation waves disperse away from the original perturbation, relative to the drift. At some fluid velocity difference (suction) they become stationary (Figure 3.6f) with $\varkappa = 0$ and $\hat{c}_{\mathrm{r}} = \lambda_{\mathrm{r}}^{\pm} = 0$. This critical state can be interpreted as a perfect balance between the weight of the perturbation and the suction atop it. Further suction tips the balance and enforces local dynamic growth.

As mentioned before, the influence of the level height term is to provide dispersion which generates a region of hyperbolic, *neutrally stable* flow. Hyperbolic *wave growth* comes from out of the non-linear friction sources. This mechanism is well known from shallow water theory and is founded in the way in which a perturbation will alter the net force balance, causing fluid acceleration.

Chapter 4

Achievements, Concluding Remarks and Recommendations

Ideas related to efficient simulation of stratified two-phase flows have been explored within this thesis. Hydrodynamic flows have been shown to pose many challenges, towards which the following contributions have been made (in the presented order):

i Work was devoted to debugging and performing case studies with the EPT slug tracking code 'SLUGGIT' during the initial stages of this PhD.

ii A dual grid scheme was implemented into the SLUGGIT code. This scheme implementation was used to demonstrate the potential of dual grid methods with regard to simulation efficiency. Challenges related to disturbances from grid projection were documented. (Paper I.)

iii A structural pipeline model was playfully developed (Appendix B, p. 177.)

iv A conceptually novel approach for simulation of wave dynamics and the wavy flow regime has been derived. This approach demonstrated that transient wave dynamics can be reproduced with a quasi-analytical approach, using steady profile solutions. Watson's steady-state roll-wave solutions [88] were here generalized into a semi-transient stretching and contracting frame. (Paper II.)

v The eigenstructure of the incompressible two-fluid modes has been derived and studied. On this basis, a non-simplified Method of Characteristics was formulated. Various hybridizations combining the Method of Characteristics and the Finite Volume Method were also conceived for the incompressible two-fluid model. (Paper III.)

vi An approximate Riemann solver (Roe scheme) for the incompressible two-fluid model was proposed. (Paper III.)

vii The performance of the characteristic schemes and the Roe scheme was evaluated up against analytical flow stability criteria and roll-wave solutions. A strong accuracy dependence on the CFL-number was demonstrated. (Paper III.)

viii The linear stability of Watson's non-linear steady roll-wave solutions was investigated theoretically and compared to the roll-wave stability observed in simulation. (Paper IV.)

ix A new derivation of the Kelvin-Helmholtz stability conditions was presented and provided with physical interpretations. This analysis was then related to discrete representations of the two-fluid model, and the essential difference between differential and discrete models outlined. It was demonstrated that the analysis can aid with choices regarding the numerical scheme and the simulation parameters. Fundamental relationships between discretization and wave stability prediction were also demonstrated. (Paper V.)

x The flux-splitting method [31] was incorporated into a dual-grid framework. A dual-grid method was proposed which significantly improves the efficiency of explicit simulations. The method was demonstrated to avoid the projection errors observed earlier as information is exchanged between spatial scales. (Paper IV.)

xi Fundamental relationships between the eigenstructure of the incompressible two-fluid model and linear flow stability were outlined. (section 3.5–3.6)

xii A new momentum conserving shock condition for the incompressible two-fluid model was proposed. (section 3.8.)

xiii The existence of concave roll-wave profile solutions was documented. (section 3.9.)

xiv An informal, physical view on the conditional hyperbolicity of the two-fluid model was presented (section 3.10.)

Broadly speaking, the most important concept of this thesis is to utilize incompressible flow modelling for simulation and theoretical analyses of hydraulic waves.

The strategy of incorporating analytical approximations of naturally occurring wave structures seems to be feasible. Intuitively, this holds a potential for computational efficiency. More modelling of the analytical approximations does however appear to be required in order to reach such a potential, possibly using explicit expressions to approximate wave profiles. Good models of turbulence and wave-breaking are required for any analytical approach to better reflect experimental observations, both in simulation and in stability analysis.

'Safer' approaches are probably found among more conventional numerical techniques. Both numerical (Paper III, VI) and theoretical (Paper V) investigations have shown that the onset of linear hydrodynamic instability can be detected fairly accurately on coarse regular grids if the applied scheme is constructed appropriately. In particular, characteristic methods and explicit upwind methods with a (characteristic) CFL number close to unity does a good job with linear instabilities. Non-linear wave dynamics imposes additional requirements to robustness. Schemes based purely on the Method of Characteristics are not suited for strongly non-linear flows as this method lacks the necessary conservation properties. Work also remains to understand the numerical properties of the characteristic–finite volume method hybridizations, in particular with respect to dynamic grids. These schemes should be refined further.

The dual-grid methodology, in combination with flux splitting techniques, has been proven capable of numerically decoupling the resolution requirements of hydraulic and acoustic scales. Efficiency benefits of this approach, as compared to explicit single-grid schemes, are apparent, particularly when factoring in the improved accuracy due to longer explicit time steps. Generalization of the dual-grid methodology is however still lacking; the incompressible model and the flux splitting approach [31] due to Evja and Flåtten are prescribed only for the two-equation model (3.11) and the four-equation model (3.1), respectively. How higher order models (containing more flow field, energy equations, etc.) would be incorporated into this method has not been considered.

Perhaps the most pressing challenges ahead concerning wavy flows are modelling aspects. The two-fluid model seems to be incomplete, and good one-dimensional closures for strongly non-linear flows are still wanting. This has generally been understood for a long time now; three-dimensional physics have been disregarded in order to obtain a quicker one-dimensional flow model. We are now struggling to recover these physics.

Bibliography

[1] Special report on carbon dioxide capture and storage. Technical report, IPCC, CAMBRIDGE UNIVERSITY PRESS, Cambridge, United Kingdom and New York, USA, 2005.

[2] *European Congress on Computational Methods in Applied Sciences and Engineering (ECCOMAS)*, Crete, Greece, June 2016. https://www.eccomas2016.org/proceedings/.

[3] The Multiphase Flow Assurance and Innovation Centre -final report-. Published at http://www.forskningsradet.no/prognett-sfi/Artikkel/FACE__Multiphase_Flow_Assurance_Innovation_Centre/1224067030430, 2016.

[4] A. H. Akselsen and O. J. Nydal. Sumulation of unstable two-pase flows in long risers. Master's thesis, NTNU, Trondheim, Norway, June 2012.

[5] P. Aursand, M. Hammer, S. T. Munkejord, and Ø. Wilhelmsen. Pipeline transport of CO2 mixtures: Models for transient simulation. *International Journal of Greenhouse Gas Control*, 15:174 – 185, 2013.

[6] S. Banerjee. Separated flow models. ii. higher order dispersion effects in the averaged formulation. *International Journal of Multiphase Flow*, 6(3):241 – 8, 1980/06/.

[7] D. Barnea. Stability analysis of annular flow structure, using a discrete form of the 'two-fluid model'. *International Journal of Multiphase Flow*, 17(6):705 – 16, 1991/11/.

[8] D. Barnea and Y. Taitel. Kelvin-Helmholtz stability criteria for stratified flow viscous versus non-viscous (inviscid) approaches. *International Journal of Multiphase Flow*, 19(4):639 – 649, 1993.

[9] D. Barnea and Y. Taitel. Non-linear interfacial instability of separated flow. *Chemical Engineering Science*, 49(14):2341 – 2349, 1994.

[10] D. Barnea and Y. Taitel. Interfacial and structural stability of separated flow. *International Journal of Multiphase Flow*, 20(supplissue):387 – 414, 1994/08/.

[11] F. Barre and M. Bernard. The CATHARE code strategy and assessment. *Nuclear Engineering and Design*, 124(3):257 – 84, 1990/12/.

[12] K. Bendiksen and M. Espedal. Onset of slugging in horizontal gas-liquid pipe flow. *International Journal of Multiphase Flow*, 18(2):237 – 247, 1992.

[13] K. H. Bendlksen, D. Malnes, R. Moe, and S. Nuland. Dynamic two-fluid model olga. theory and application. *SPE Production Engineering*, 6(2):171 – 180, 1991.

[14] D. Biberg. An explicit approximation for the wetted angle in two-phase stratified pipe flow. *Canadian Journal of Chemical Engineering*, 77(6):1221 – 1224, 1999.

[15] D. Biberg. A mathematical model for two-phase stratified turbulent duct flow. *Multiphase Science and Technology*, 19(1):1 – 48, 2007.

[16] M. Bonizzi, P. Andreussi, and S. Banerjee. Flow regime independent, high resolution multi-field modelling of near-horizontal gas-liquid flows in pipelines. *International Journal of Multiphase Flow*, 35(1):34 – 46, 2009.

[17] M. Bonizzi and R. Issa. On the simulation of three-phase slug flow in nearly horizontal pipes using the multi-fluid model. *International Journal of Multiphase Flow*, 29(11):1719 – 47, 2003/11/.

[18] J. A. Boure, A. E. Bergles, and L. S. Tong. Review of two-phase flow instability. *Nuclear Engineering and Design*, 25(2):165 – 92, 1973/07/.

[19] C. J. Crowley, G. B. Wallis, and J. J. Barry. Validation of a one-dimensional wave model for the stratified-to-slug flow regime transition, with consequences for wave growth and slug frequency. *International Journal of Multiphase Flow*, 18(2):249 – 271, 1992.

[20] T. J. Danielson, K. M. Bansal, B. Djoric, E.-D. Duret, S. T. Johansen, and Ø. Hellan. Testing and qualification of a new multiphase flow simulator. In *Proc. Offshore Technology Conference, 2-5 May, Houston, Texas, USA*, 2011.

[21] T. J. Danielson, K. M. Bansal, B. Djoric, D. Larrey, S. T. Johansen, A. De Leebeeck, and J. Kjolaas. Simulation of slug flow in oil and gas

pipelines using a new transient simulator. In *Proc. Offshore Technology Conference, 30 April-3 May, Houston, Texas, USA*. Offshore Technology Conference, 2012.

[22] A. De Leebeeck and O. Nydal. Simulation of large amplitude waves in a slug tracking scheme compared to roll wave experiments at high pressure. *International Journal of Multiphase Flow*, 36(1):40 – 50, 2010.

[23] H. Dhulesia and D. Lopez. Critical evaluation of mechanistic two-phase flow pipeline and well simulation models. In *SPE Annual Technical Confrence and Exhibition*, pages 393–402, oct. 1996.

[24] M. Diaz, A. Akselsen, and O. Nydal. Experiments on Severe Slugging in a S-Riser System with Viscous Liquids. 2013.

[25] T. N. Dinh, R. R. Nourgaliev, and T. G. Theofanous. Understanding the ill-posed two-fluid model. In *The 10th International Topical Meeting on Nuclear Reactor Thermal Hydraulics*, Seoul, Korea, October 2003.

[26] Division of Risk Assessment and Special Projects Office of Nuclear Regulatory Research U. S. Nuclear Regulatory Commission, Washington, DC. *TRACE V5.0 THEORY MANUAL Field Equations, Solution Methods, and Physical Models*.

[27] R. Dressler. Mathematical solution of the problem of rollwaves in inclined open channels. *Communications on Pure and Applied Mathematics*, 2:149 – 194, 1949/06/.

[28] D. A. Drew. Mathematical modeling of two-phase flow. *Annual Review of Fluid Mechanics*, 15:261 – 291, 1983.

[29] D. A. Drew and S. L. Passman. *Theory of multicomponent fluids*. Applied mathematical sciences. Springer, New York, 1999.

[30] P. Emonot, A. Souyri, J. L. Gandrille, and F. Barré. Cathare-3: A new system code for thermal-hydraulics in the context of the NEPTUNE project. *Nuclear Engineering and Design*, 241(11):4476 – 4481, 2011. 13th International Topical Meeting on Nuclear Reactor Thermal Hydraulics (NURETH-13).

[31] S. Evje and T. Flåtten. Hybrid central-upwind schemes for numerical resolution of two-phase flows. *Mathematical Modelling and Numerical Analysis*, 39(2):253 – 73, 2005/03/.

[32] A. Fitt. Numerical and analytical solution of ill-posed systems of conservation laws. *Applied Mathematical Modelling*, 13(11):618 – 631, 1989.

[33] T. Flåtten. *Hybrid Flux Splitting Schemes for Numerical Resolution of Two-Phase Flows*. PhD thesis, NTNU, September 2003.

[34] W. D. Fullmer, V. H. Ransom, and M. A. Lopez De Bertodano. Linear and nonlinear analysis of an unstable, but well-posed, one-dimensional two-fluid model for two-phase flow based on the inviscid Kelvin-Helmholtz instability. *Nuclear Engineering and Design*, 268:173 – 184, 2014.

[35] D. Gidaspow. Modeling of two phase flow. In *Proc. of the fifth International Hest Transfer Conference, September 3-September 7, 1974, Keidanrenkaikan Building, Tokyo. Round Table Discussions*. [Tokyo] : Japan Society of Mechanical Engineers, 1974.

[36] D. Gidaspow. Multiphase flow and fluidization. *Journal of Fluid Mechanics*, 287:405 – 405, 1995.

[37] F. H. Harlow and J. E. Welch. Numerical calculation of time-dependent viscous incompressible flow of fluid with free surface. *Physics of Fluids*, 8(12):2182 – 2189, 1965.

[38] H. Holden and N. H. Risebro. *Front tracking for hyperbolic conservation laws*. Applied mathematical Sciences (Book 152). Springer, New York, Berlin, Heidelberg, 2002. Autre tirage : 2007 (2nd corr. printing).

[39] H. Holmås. Numerical simulation of transient roll-waves in two-phase pipe flow. *Chemical Engineering Science*, 65(5):1811 – 25, 2010/03/01.

[40] K. Holmås, G. Gahr Lunde, G. Setyadi, P. Angelo, and G. Rudrum. Prediction of liquid surge waves at ormen lange. In *Proc. 16th International Conference on Multiphase Production Technology, 12-14 June, Cannes, France*. BHR Group, 2013.

[41] K. Holmås and A. Løvli. FlowManager^{TM}Dynamic: A multiphase flow simulator for online surveillance, optimization and prediction of subsea oil and gas production. In *BHR*, Cannes, 2011. Flow Management Systems, FMC Technologies, Norway.

[42] Information Systems Laboratories, Inc., Rockville, Maryland, Idaho. *RELAP5/MOD3.3 code manual volume I: code structure, system models and solution methods*, December 2001.

[43] K. Ioannou, M. Widener, S. Kashou, and D. Estanga. Terrain slugging in a subsea tieback: When predictions fail. In *8th North American Conference on Multiphase Technology, 20-22 June, Banff, Alberta, Canada*, pages –. BHR Group, 2012.

[44] M. Ishii and T. Hibiki. *Thermo-Fluid Dynamics of Two-Phase Flow*. SpringerLink : Bücher. Springer New York, 2010.

[45] R. Issa and M. Kempf. Simulation of slug flow in horizontal and nearly horizontal pipes with the two-fluid model. *International Journal of Multiphase Flow*, 29(1):69 – 95, 2003/01/.

[46] S. Johansen, T. Ytrehus, and K. Einarsrud. Modeling of Multiphase Flows. Compendium of PhD course EP8404, Multiphase Flow Modeling,Norwegian University of Science and Technology.

[47] G. Johnson. *A Study of Stratified Gas-Liquid Pipe Flow*. PhD thesis, Univ. Oslo, 2005. dr. scient.

[48] G. Johnson, J. Nossen, and A. Bertelsen. A comparison between experimental and continuous theoretical roll waves in horizontal and slightly inclined pipes at high pressure. pages 643 – 655, Barcelona, Spain, 2005.

[49] G. W. Johnson, A. F. Bertelsen, and J. Nossen. A mechanistic model for roll waves for two-phase pipe flow. *AIChE Journal*, 55(11):2788 – 2795, 2009.

[50] A. Jones and A. Prosperetti. On the suitability of first-order differential models for two-phase flow prediction. *International Journal of Multiphase Flow*, 11(2):133 – 48, 1985/03/. first-order differential models;two-phase flow prediction;stability features;one-dimensional two-phase flow models;first-order derivatives;drag effects;wavenumber;.

[51] S. Kakac and B. Bon. A review of two-phase flow dynamic instabilities in tube boiling systems. *International Journal of Heat and Mass Transfer*, 51(3-4):399 – 433, 2008.

[52] B. Keyfitz. Lack of hyperbolicity in the two-fluid model for two-phase incompressible flow. *Discrete and Continuous Dynamical Systems – Series B*, 3(4):541–563, Nov. 2003.

[53] T. Kjeldby, R. Henkes, and O. Nydal. Lagrangian slug flow modeling and sensitivity on hydrodynamic slug initiation methods in a severe slugging case. *International Journal of Multiphase Flow*, 53:29 – 39, 2013.

[54] T. K. Kjeldby. *Lagrangian three-phase slug tracking methods*. PhD thesis, Norwegian University of Science and Technology, 2013.

[55] J. Kjølaas. *Plug propagation in multiphase pipelines: Modeling and small scale experiments*. PhD thesis, Norwegian University of Science and Technology. Department of Energy and Process Engineering, Trondheim, May 2007.

[56] J. Kjolaas, A. De Leebeeck, and S. Johansen. Simulation of hydrodynamic slug flow using the LedaFlow slug capturing model. pages 365 – 383, Cannes, France, 2013.

[57] E. S. Kordyban and T. Ranov. Mechanism of slug formation in horizontal two-phase flow. *Transactions of the ASME. Series D, Journal of Basic Engineering*, 92(4):857 – 64, 1970/12/.

[58] O. Kristiansen and O. Nydal. *Experiments on the transition from stratified to slug flow in multiphase pipe flow*. PhD thesis, Norwegian University of Science and Technology. Department of Energy and Process Engineering, Trondheim, 2004.

[59] M. Larsen, E. Hustvedt, P. Hedne, and T. Straume. Petra: A novel computer code for simulation of slug flow. *Proceedings - SPE Annual Technical Conference and Exhibition*, Pi:965 – 976, 1997.

[60] C. Lawrence, Z. G. Xu, P. Andersson, H. Eiding, L. Hovden, J. Henriksson, S. Henriksen, S. Dayarathna, T. Haugset, T. Ruden, and B. Hu. Validation of a physically-based model for slug initiation and evolution in hydrodynamic slug flow. In *17th International Conference on Multiphase Production Technology, 10-12 June, Cannes, France*. BHR Group, 2015.

[61] M. S. Lee, V. Aute, A. Riaz, and R. Radermacher. A review on direct two-phase, phase change flow simulation methods and their applications. In *International Refrigeration and Air Conditioning Conference*, 2012.

[62] J. Liao, R. Mei, and J. F. Klausner. A study on the numerical stability of the two-fluid model near ill-posedness. *International Journal of Multiphase Flow*, 34(11):1067 – 1087, 2008.

[63] P. Y. Lin and T. J. Hanratty. Prediction of the initiation of slugs with linear stability theory. *International Journal of Multiphase Flow*, 12(1):79 – 98, 1986.

[64] M. Lopez-de Bertodano, W. Fullmer, and A. Vaidheeswaran. One-dimensional two-equation two-fluid model stability. *Multiphase Science and Technology*, 25(2-4):133 – 167, 2013.

[65] R. W. Lyczkowski, D. Gidaspow, C. W. Solbrig, and E. D. Hughes. Characteristics and stability analyses of transient one-dimensional two-phase flow equations and their finite difference approximations. *Nuclear Science and Engineering*, 66(3):378 – 396, 1978.

[66] J. M. Masella, Q. H. Tran, D. Ferre, and C. Pauchon. Transient simulation of two-phase flows in pipes. *International Journal of Multiphase Flow*, 24(5):739 – 755, 1998.

[67] S. T. Munkejord. *Analysis of the two-fluid model and the drift-flux model for numerical calculation of two-phase flow*. PhD thesis, The Norwegian University of Science and Technology, 2005.

[68] O. J. Nydal and S. Banerjee. Dynamic slug tracking simulations for gas-liquid flow in pipelines. *Chem. Eng. Comm.*, 141-142:13–39, 1996.

[69] C. L. Pauchon, H. Dhulesia, G. B. Cirlot, and J. Fabre. Tacite: a transient tool for multiphase pipeline and well simulation. volume Pi, pages 311 – 326, New Orleans, LA, USA, 1994.

[70] P. Pickering, G. Hewitt, M. Watson, and C. Hale. The prediction of flows in production risers – truth & myth? Published online, http://www.feesa.net, 2001.

[71] H. Pokharna, M. Mori, and V. H. Ransom. Regularization of two-phase flow models. *J. Comput. Phys.*, 134(2):282–295, July 1997.

[72] J. D. Ramshaw and J. A. Trapp. Characteristics, stability, and short-wavelength phenomena in two-phase flow equation systems. *Nuclear Science and Engineering*, 66(1):93 – 102, 1978.

[73] F. Renault and O. J. Nydal. Influence of dynamic pressure terms on stratified two-phase flow stability : Presented at the 5th international conference on multiphase flow, yokohama, japan, may 30-june 4, 2004. 2004.

[74] G. L. Richard and S. L. Gavrilyuk. A new model of roll waves: Comparison with brock's experiments. *Journal of Fluid Mechanics*, 698:374 – 405, 2012.

[75] S. Salsa. *Partial Differential Equations in Action : From Modelling to Theory*. Universitext. Springer-Verlag Italia Milano, Milano, 2008.

[76] S. Soo. Dynamics of multiphase flow systems. *Industrial and Engineering Chemistry – Fundamentals*, 4(4):426 – 433, 1965.

[77] S. Soo. *Multiphase Fluid Dynamics*. Taylor & Francis, 1983.

[78] S. Soo. *Particulates And Continuum-Multiphase Fluid Dynamics: Multiphase Fluid Dynamics*. Taylor & Francis, 1989.

[79] J. J. Stoker. The formation of breakers and bores the theory of nonlinear wave propagation in shallow water and open channels. *Communications on Pure and Applied Mathematics*, 1(1):1–87, 1948.

[80] Y. Taitel and A. Dukler. A model for predicting flow regime transitions in horizontal and near horizontal gas-liquid flow. *AIChE Journal*, 22(1):47 – 55, 1976/01/.

[81] H. A. Thomas. The propagation of waves in steep prismatic conduits. In *Hydraulics Conf.*, pages 214–229, Carnegie Institute of Technology, Pittsburgh, 1939.

[82] E. F. Toro. *Riemann solvers and numerical methods for fluid dynamics : a practical introduction*. Springer, Berlin, New York, 1997.

[83] H. Tougou. Stability of turbulent roll-waves in an inclined open channel. *Journal of the Physical Society of Japan*, 48(3):1018 – 23, 1980/03/.

[84] I. Toumi and A. Kumbaro. An approximate linearized riemann solver for a two-fluid model. *Journal of Computational Physics*, 124(2):286 – 300, 1996/03/15.

[85] J. S. B. van Zwieten. Towards advanced one-dimensional numerical models for multiphase flow in pipelines. Technical report, Delft University of Technology, 2013. In Reports of the Delft Institute of Applied Mathematics, ISSN 1389-6520.

[86] G. B. Wallis. *One-dimensional two-phase flow*. McGraw-Hill, 1969.

[87] T. Wangensteen. *Mixture-Slip Flux Splitting for the numerical computation of 1D two phase flow*. PhD thesis, NTNU, September 2010.

[88] M. Watson. Wavy stratified flow and the transition to slug flow. In C. Fairhurst, editor, *Multi-phase Flow – Proceedings of the 4th International Conference*, pages 495–512, Cranfield, UK, 1989.

[89] F. White. *Fluid Mechanics*. McGraw-Hill series in mechanical engineering. McGraw-Hill, 2008.

[90] G. Whitham. *Linear and Nonlinear Waves*. Wiley, 1974.

Appendix A

Papers

PAPER I

Applying Multiple Grids to a Multi-Field Model - The Resolution Requirements of Individual Fields in the Two-Fluid Model for 1D Pipe Flow

Andreas H. Akselsen and Ole Jørgen Nydal

Published in
Journal of Dispersion Science and Technology

Is not included due to copyright

PAPER II

A METHOD OF CHAINED ANALYTICAL WAVE STRUCTURES FOR LARGE-SCALE STRATIFIED TWO-PHASE PIPE FLOWS

Andreas H. Akselsen

Presented and included in proceedings of
The VII European Congress on Computational Methods in Applied Sciences and Engineering (ECCOMAS)
Crete Island, Greece, 5-10 June 2016
https://www.eccomas2016.org/proceedings/

ECCOMAS Congress 2016
VII European Congress on Computational Methods in Applied Sciences and Engineering
M. Papadrakakis, V. Papadopoulos, G. Stefanou, V. Plevris (eds.)
Crete Island, Greece, 5–10 June 2016

A METHOD OF CHAINED ANALYTICAL WAVE STRUCTURES FOR LARGE-SCALE STRATIFIED TWO-PHASE PIPE FLOWS (ECCOMAS CONGRESS 2016)

A.H. Akselsen[1]

[1]Department of Energy and Process Engineering, Norwegian University of Science and Technology
Kolbjørn Hejes v. 1B, 7491 Trondheim, Norway
e-mail: andreas.h.akselsen@ntnu.no

Keywords: Chained Analytical Waves; Roll-Waves; Two-Phase Flow; Pipe Flow; Two-Fluid Model

Abstract. *Pipeline transport systems can span vast distances, making finely resolved simulation techniques computationally unaffordable. This article examines the use of analytical steady wave solutions in a dynamic simulation framework as a technique for obtaining physical wave dynamics in a flow regime simulator without discretising individual wave structures. A scheme based on this principle is presented wherein a family of steady roll-waves profile solutions is generalised to allow for a dynamic profile evolution. These solutions are then implemented into a finite volume scheme where a wave solution constitutes a single dynamic grid cell. Waves interact dynamically to construct a wave regime evolving in time. Predictions on flow development are compared with finely resolved direct numerical simulations on fixed grids. Steady wave solutions, once subjected to coordinate stretching, behaves appropriately in the dynamic frame, predicting the regime development in time, the wave coalescences and the final steady state or slug transition.*

1 INTRODUCTION

1.1 Review

Roll-wave trains are periodic occurrences of moving hydraulic jumps and constitutes a shallow-water flow regime in both channels and pipes. The wave dynamic of this flow regime is important in two-phase pipe flows as it affect the momentum exchange between phases, and because it may initiate the transition to a slugging flow.

Profile solutions of steady-state hydraulic jumps in open channels was published by Brass already in 1868.

Thomas [17] presented, in 1937 and 1939, a family of explicit, mechanistic, free surface roll-wave solutions using a reference system relative to the waves through a moving belt analogy.

Dressler [7] later formalised these profile solutions into a closed form composed of trains of piecewise monotonic solutions connected by shocks. He formulated conservation conditions for these shocks. Dressler also went on to prove the uniqueness of these solutions through entropy considerations, and to also construct viscous, continuous profile solutions. Thomas and Dressler both showed, by different means, that some amount of friction was a necessary requirement for the formation of roll-waves.

Miya et. al. [14] went on to derive similar profile solutions for gas-liquid channel flows, also including shape factors for the velocity profiles. They further investigated the pressure distribution and compared the profile solutions to experimental data.

Watson [18] reformulated the gas-liquid solution for flow in pipes. This model had a form similar to that for channel flow, but with a geometrical complexity making it unsuited for analytical integration. Algebraically explicit profile solutions are therefore unavailable for pipe flow. The increased complexity of these equations also makes solution uniqueness difficult to prove; this was instead assumed.

Johnson et. al. [11, 10] continued the work on discontinuous and viscous continuous roll-wave models for stratified pipe flow. They constructed a database system for retrieving profile solutions at given flow conditions. In [12], Johnson et. al. compare high-pressure, upward inclined pipe flow experiments to the continuous roll-wave model to find good agreement.

Comparisons between roll-wave experiments and predictions from finely resolved numerical representations have been made by multiple authors. For instance, Holmås [9] compared a pseudospectral representation (using fast Fourier transformation) of the incompressible two-fluid pipe flow model with the above cited experiments of Johnson. The Biberg model [2] for pre-integrated turbulent shear and velocity profiles was here incorporated.

Similar comparisons were made by Cao et. al. [5], including $k - \varepsilon$ turbulent closures to their Riemann solver + MUSCL method. They report good agreement with the experimental data of Brock's [3] after the $k - \varepsilon$ extension.

Richard and Gavrilyuk [15] extended Dressler's roll-wave solutions to account for turbulent shear and dissipation. Reynolds' stresses are here related to enstrophy in the wave, providing wave-breaking as a model extension. Very good agreement with Brock's experimental data was found [3], appropriately breaking off the sharp wave tip of the Dressler solutions.

In the work of Brook et. al. [4], the solutions of Dressler were compared to roll-wave simulation results of the shallow water equations using a second order Godunov method.

A final work worth mentioning in relation to these steady wave solutions is Lahey's piece on dispersed bubbly pipe flow [13]. Here, void waves were analysed using non-linear theory, finding similar sets of structures and profile solutions.

In regard to the method principle, some ideas have been drawn from the work of De Leebeeck

and Nydal [6]. They presented a phenomenological model treating large waves as a fixed-length choke object and used object oriented programming to simulate intermittent occurrences of such wave representations.

1.2 Aim

The aim in this work is to whether solutions for steady wave trains can be used in modelling dynamically evolving wavy flows. Will a set of spurious analytical waves merge and adjust to a 'fully developed' flow pattern? Does the method have potential for use in engineering simulator tools?

The concept is tested through a method based on the principle of singleton wave solutions in the frame of a finite volume method. Predicting the development of a *flow regime* in long pipeline simulations is usually more important than predicting individual waves. We need therefore not demand exact conformity with the base model, but that the appropriate statistical development is ensured and that predictions on regime transition are reliable. Similar methods can be devised for any type of regime flow where reasonably steady intermittent structures appear.

1.3 Introduction to a method of dynamically chained analytical wave structures

In this article, the steady state solutions presented by the aforementioned authors will be generalised and introduced into a dynamic, computational framework for simulating transient wave development. (The term 'steady state' will here refere to solutions which are steady in a reference system moving with constant translation velocity.) For ease of reference, the resulting method will be dubbed *the method of chained analytical waves,* CAW for short.

The concept of the CAW method is presented in Figure 1.1 with explanations in the caption. It consists of four basic steps:

i) A profile and shock celerity reconstruction from the average state properties in a relative reference system.

ii) Integrating the average wave properties in time using fluxes and sources obtained from the chained profiles.

iii) Letting the wave objects move according to the shock celerities.

iv) Reconstructing the profiles and shock celerities anew from the new average properties.

The two-fluid model is presented in Section 2. A conservative finite volume method for dynamic cells is then presented in Section 3.1, with the average volume equations in Section 3.1.1 and the shock conditions in Section 3.1.2. The analytical wave model is found in Section 3.2, with the general profile equations presented in Section 3.2.2. Section 3.3 deals with selecting a wave profile from the family of profile solutions on the basis of the average properties. Putting these pieces together, Section 3.4 presents the simulation routine.

Figure 1.2 illustrates the main difference between the CAW method and conventional, fine-gridded CFD methods, namely the much greater number of grid cells required by the latter. The numerical stability of both types of solution methods will be restricted by CFL-type criteria which limit the length of the time integration step in proportion to the grid cell lengths. Consequently, the CAW method should be capable of remaining stable while using significantly longer time steps, at a time scale better suited for wave dynamics.

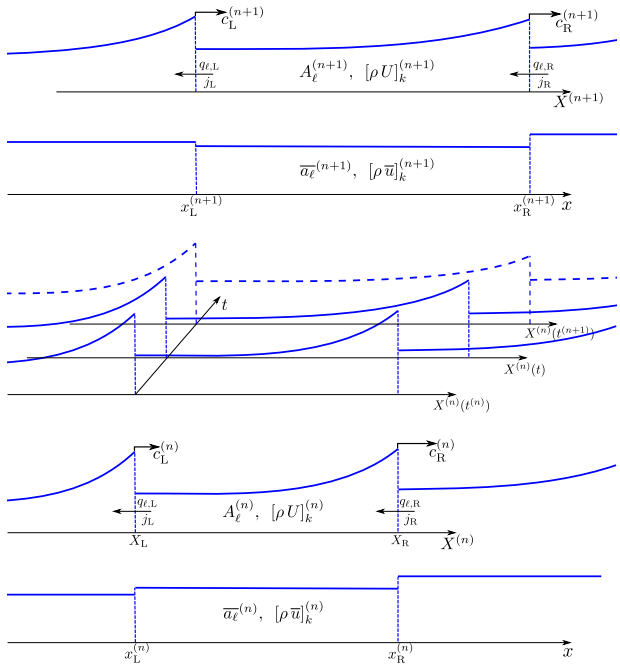

Figure 1.1: Principle illustration.
• Bottom: Available average state $\overline{\boldsymbol{\psi}}$
• 2nd from bottom: Adopt a reference system relative to the wave. Reconstruct the waves with the analytical wave model and determine the shock celerities and the flux exchanges between waves (Section 3.2-3.3.)
• Middle: Integrate in time using the fluxes and shock speeds obtained at $t^{(n)}$ from the analytical wave regime. Allow the wave to stretch and contract in the strip $t \in \left[t^{(n)}, t^{(n+1)}\right\rangle$, (Section 3.1.)
• 2nd from top and top: The time integration provides the average state $\overline{\boldsymbol{\psi}}^{(n+1)}$ at time $t^{(n+1)}$, and the cycle repeats for the new time step.

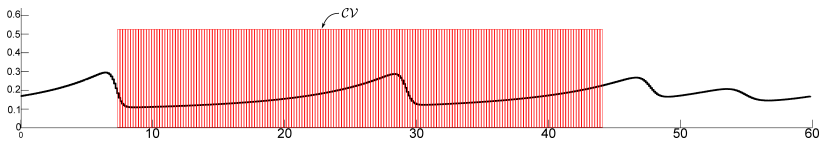

(a) Conventional capturing simulation with a fine, stationary grid – 500 grid cells.

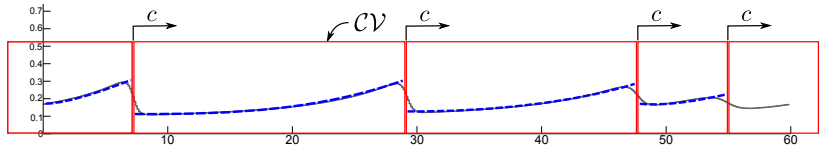

(b) Chained analytical wave simulation – 4 grid cells.

Figure 1.2: Control volumes

2 THE TWO-FLUID MODEL

In addition to the presence of a gas, the complication of a pipe geometry is a key difference between the explicit shallow water roll-wave solutions of Dressler and the numerically computed pipe flow solutions of Watson – Figure 2.1 shows a schematic. The pipe introduces new

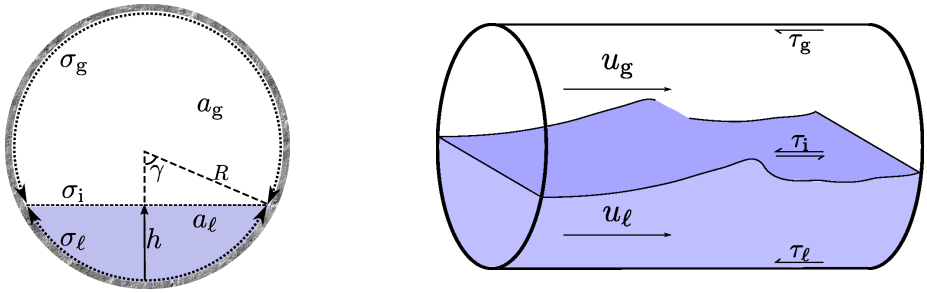

Figure 2.1: Pipe cross-section

geometric variables such as the level height h, partial cross-section areas a_k and perimeter length σ_k for the gas ($k = \mathrm{g}$) and liquid ($k = \ell$) phases. These are all algebraically interchangeable through a geometric function $a_\ell = \mathcal{A}_\ell(h)$:

$$\mathcal{A}_\ell(h) = R^2\left(\gamma - {}^1\!/_2 \sin 2\gamma\right), \qquad \sigma_\ell = 2R\gamma,$$
$$\mathcal{A}'_\ell = \frac{\mathrm{d}\mathcal{A}_\ell}{\mathrm{d}h} = \sigma_\mathrm{i}, \qquad \sigma_\mathrm{g} = 2R\left(\pi - \gamma\right),$$
$$\gamma = \arccos\left(1 - h/R\right), \qquad \sigma_\mathrm{i} = 2R\sin\gamma.$$

Though expressions of the same property, the level height h is beat suited as an independent modelling variable as a_k and σ_k are explicit functions in h, whereas the inverse is not true. R is here the pipe inner radius and γ the interface half-angle. Subscript 'i' indicates the gas-liquid interface.

The compressible, isothermal, four-equation two-fluid model for stratified pipe flow results from an averaging of the conservation equations across the cross-sectional area and is commonly written

$$\partial_t\left(a\rho\right)_k + \partial_x\left(a\rho u\right)_k = 0, \tag{2.1a}$$
$$\partial_t\left(a\rho u\right)_k + \partial_x\left(a\rho u^2\right)_k + a_k\partial_x p_\mathrm{i} + a_k\rho_k g\cos\theta\,\partial_x h = s_k, \tag{2.1b}$$

where phase subscript $k \in \{\mathrm{g}, \ell\}$. p_i is the interface pressure, coupled to the fluid densities ρ_k by some equation of state.

The phase properties represent cross-sectional averages in each field, and, together, the two last left-hand terms in the momentum equation represents a hydrostatic approximation to the average pressures over the cross-section. A flat, fully turbulent velocity profile is here assumed.

The numerical treatment of the pressure term is a key issue in simulating the two-fluid model. It introduces sonic characteristics and stability restrictions. In this work, as well as in most of those hereto cited, pressure issues are numerically sidestepped by assuming both phases to be

incompressible. This eliminates the sonic characteristics while the system still retains its conditionally hyperbolic nature. It also allows for a conservative, two-equation system formulation. The interfacial pressure, essentially linking the momentum equations of each phase, is eliminated by first reducing each momentum equation by their respective mass equations, and then divided each by their respective specific areas a_k. Subtracting one from the other, the pressure term is eliminated. The resulting conservation equations reads

$$\partial_t \boldsymbol{\psi} + \partial_x \boldsymbol{f} = \boldsymbol{s} \tag{2.2a}$$

with

$$\boldsymbol{\psi} = \begin{pmatrix} a_\ell \\ [\rho u]^\ell_{\mathrm{g}} \end{pmatrix}, \qquad \boldsymbol{f} = \begin{pmatrix} q_\ell \\ j \end{pmatrix}, \qquad \boldsymbol{s} = \begin{pmatrix} 0 \\ s \end{pmatrix}. \tag{2.2b}$$

Flux and source component symbols have here been introduced and are

$$q_k = a_k u_k, \qquad j = \left[\rho \frac{u^2}{2}\right]^\ell_{\mathrm{g}} + w_y\, h, \tag{2.2c}$$

$$s = -w_x - \left[\frac{\tau\sigma}{a}\right]^\ell_{\mathrm{g}} + \tau_{\mathrm{i}}\sigma_{\mathrm{i}}\left(\frac{1}{a_\ell} + \frac{1}{a_{\mathrm{g}}}\right), \tag{2.2d}$$

and phase differencing operation $[\cdot]^\ell_{\mathrm{g}} = (\cdot)_\ell - (\cdot)_{\mathrm{g}}$ which will be used throughout. The algebraic relations

$$a_\ell + a_{\mathrm{g}} = \mathcal{A}, \qquad q_\ell + q_{\mathrm{g}} = \mathcal{Q}, \tag{2.2e}$$

close the model. This is essentially the same formulation as used by Holmås in [9]. $\mathcal{A}$ may in general be a parametric function of x and $\mathcal{Q}$ of t, though they are here treated as constants. The second relation in (2.2e) is obtained from adding together the two mass equations (2.1a) and applying the first relation. Specific weight terms, also parametric, are

$$w_x = [\rho]^\ell_{\mathrm{g}}\, g \sin\theta, \qquad w_y = [\rho]^\ell_{\mathrm{g}}\, g \cos\theta,$$

with g being the gravitational acceleration and θ the pipe inclination angle, positive above datum. The friction model τ_k is based on the rather simple Taitel and Dukler model [16] for turbulent flow, quickly summarised below:

$$\begin{aligned} &\tau_k = {}^1\!/_2\, C_{\mathrm{f},k}\, \rho_k u_k |u_k|, && \tau_{\mathrm{i}} = {}^1\!/_2\, C_{\mathrm{f,i}}\, \rho_{\mathrm{g}} (u_{\mathrm{g}} - u_\ell)|u_{\mathrm{g}} - u_\ell|, \\ &C_{\mathrm{f},k} = 0.046\, Re_k^{-0.2}, && Re_k = (ud/\nu)_k, \\ &d_\ell = 4\, a_\ell/\sigma_\ell, && d_{\mathrm{g}} = 4\, a_{\mathrm{g}}/(\sigma_\ell + \sigma_{\mathrm{i}}). \end{aligned}$$

The interfacial friction factor is $C_{\mathrm{f,i}} = m_{\mathrm{x}} \max\{C_{\mathrm{f,g}}, 0.014\}$ where m_{x} is a crude model parameter employed by numerous authors in order to achieve $C_{\mathrm{f,i}} > C_{\mathrm{f,g}}$ as observed experimentally. ν is the kinematic viscosity.

A study on how m_{x} affect the wave regime was carried out in [11] and will not be repeated here. Instead, m_{x} is rather arbitrarily given the value $m_{\mathrm{x}} = 5.0$. The choice of m_{x} affects the range of flow conditions in which the stable roll-wave regime is observed.

3 A METHOD OF CHAINED ANALYTICAL WAVE STRUCTURES

Details of the CAW method are described in this section. The process of averaging the base equation system (2.2) into movable, stretching and contracting control volumes is described in Subsection 3.1, while details of the wave model are described in Subsection 3.2. Finally, a routine description is given in Subsection 3.4.

Readers who are foremost interested in the method principle (as presented in the introductory section) may skip past the method details presented here and still gather an impression from the results section that follows.

3.1 A finite volume method framework

3.1.1 Average volume equations

A control volume is placed over a wave, as illustrated in Figure 1.2b. Integration of (2.2a) is performed across the control volume, first in space from the left shock at x_{L} to the right one at x_{R}, and then in time from the present time t_n to the next time level t_{n+1}:

$$\int_{t_n}^{t_{n+1}} \int_{x_{\mathrm{L}}(t)}^{x_{\mathrm{R}}(t)} \left(\partial_t \boldsymbol{\psi} + \partial_x \boldsymbol{f} - \boldsymbol{s}\right) \mathrm{d}x \, \mathrm{d}t = 0. \tag{3.1}$$

Using Leibniz' rule, the first transient term evaluates to

$$\int_{x_{\mathrm{L}}(t)}^{x_{\mathrm{R}}(t)} \partial_t \boldsymbol{\psi} \, \mathrm{d}x = \partial_t \big(\Delta x \overline{\boldsymbol{\psi}}\big) - \left[c\,\boldsymbol{\psi}\right]_{\mathrm{L}}^{\mathrm{R}} \tag{3.2}$$

where $c = \frac{\mathrm{d}x}{\mathrm{d}t}$ is the control volume border velocity, chosen equal to the shock speed of the wave front discontinuity, such that the control volume follows the wave front. $\Delta x(t) = x_{\mathrm{R}}(t) - x_{\mathrm{L}}(t)$ is the wavelength, and the notation for evaluating the left-right difference $[\cdot]_{\mathrm{L}}^{\mathrm{R}} = (\cdot)_{\mathrm{R}} - (\cdot)_{\mathrm{L}}$ is adopted. The bar will indicate the cell average and is defined

$$\overline{\phi}(t) = \frac{1}{\Delta x(t)} \int_{x_{\mathrm{L}}(t)}^{x_{\mathrm{R}}(t)} \phi(x,t) \, \mathrm{d}x. \tag{3.3a}$$

Also introducing the temporal average $\langle \cdot \rangle^{(n)}$,

$$\langle \phi(x) \rangle^{(n)} = \frac{1}{\Delta t} \int_{t_n}^{t_{n+1}} \phi(x,t) \, \mathrm{d}t \tag{3.3b}$$

with $\Delta t = t_{n+1} - t_n$, the integral equation (3.1) is cast as

$$\big(\Delta x \overline{\boldsymbol{\psi}}\big)^{(n+1)} = \big(\Delta x \overline{\boldsymbol{\psi}}\big)^{(n)} + \Delta t \left\langle \Delta x \overline{\boldsymbol{s}} - \left[\boldsymbol{f}_{\mathrm{r}}\right]_{\mathrm{L}}^{\mathrm{R}} \right\rangle^{(n)}, \tag{3.4}$$

where the flux terms have been made relative to the shock propagation, i.e., $\boldsymbol{f}_{\mathrm{r}} = (q_{\ell,\mathrm{r}}, j_{\mathrm{r}})^T = \boldsymbol{f} - c\boldsymbol{\psi}$. Relative notation will be adopted throughout to indicate when fluxes are relative a moving frame. The mass and momentum fluxes of the relative frame are key variables and are therefore emphasised:

$$q_{\ell,\mathrm{r}} = a_\ell \left(u_\ell - c\right), \qquad\qquad j_{\mathrm{r}} = \left[\rho u \left(\frac{u}{2} - c\right)\right]_{\mathrm{g}}^{\ell} + h w_y. \tag{3.5}$$

It is important to note that Equation (3.4) is still exact.

In case of a first order time integration, $\langle\cdot\rangle^{(n)}$ simply evaluates to

$$\langle\cdot\rangle^{(n)} \xrightarrow{\text{explicit}} (\cdot)^{(n)}, \qquad \langle\cdot\rangle^{(n)} \xrightarrow{\text{implicit}} (\cdot)^{(n+1)}.$$

Explicit time integration $\langle\cdot\rangle^{(n)} \to (\cdot)^{(n)}$ is used in the CAW method. Equation (3.4) then reads

$$\begin{aligned}
(\Delta x\overline{a_\ell})^{(n+1)} &= (\Delta x\overline{a_\ell})^{(n)} - \Delta t \left[q_{\ell,\mathrm{r}}^{(n)}\right]_{\mathrm{L}}^{\mathrm{R}}, \\
\left(\Delta x \left[\rho\overline{u}\right]_{\mathrm{g}}^{\ell}\right)^{(n+1)} &= \left(\Delta x \left[\rho\overline{u}\right]_{\mathrm{g}}^{\ell}\right)^{(n)} + \Delta t \left(\Delta x\overline{s} - \left[j_{\mathrm{r}}\right]_{\mathrm{L}}^{\mathrm{R}}\right)^{(n)}.
\end{aligned}$$

3.1.2 Shock conditions

The coordinate translation velocity $C(H)$ may dynamically vary over a wave as it stretches or contracts, meaning that celerity c adhere to the shocks themselves rather to a wave as a whole. A shock must obey the condition that the relive fluxes $\boldsymbol{f}_{\mathrm{r}} = (q_{\ell,\mathrm{r}}, j_{\mathrm{r}})^T$ are shock invariant.[1]

Following a shock front $i + \frac{1}{2}$, the common notation for a left and right discontinuity limit is adopted, namely $\phi^- = \phi_{\mathrm{R},i}$ and $\phi^+ = \phi_{\mathrm{L},i+1}$. The conservation conditions $j_{\mathrm{r}}^- = j_{\mathrm{r}}^+$ and $q_{\ell,\mathrm{r}}^- = q_{\ell,\mathrm{r}}^+$ imply $J_{\mathrm{r}}(h^-, q_{\ell,\mathrm{r}}, c) = J_{\mathrm{r}}(h^+, q_{\ell,\mathrm{r}}, c)$. Subtracting $\frac{1}{2}\rho_k c$ on both sides illustrates that this condition corresponds to maintaining a Bernoulli invariant

$$\left[\left[\tfrac{1}{2}\rho\,(u-c)^2\right]_{\mathrm{g}}^{\ell} + w_y\, h\right]_{-}^{+} = 0, \tag{3.6}$$

where $[\cdot]_-^+ = (\cdot)^+ - (\cdot)^-$. This is the jump condition similar to that presented by Watson [18]. Solving for c yields

$$c = \frac{\left[\rho\,[u^2/2]_-^+\right]_{\mathrm{g}}^{\ell} + w_y\,[h]_-^+}{\left[\rho\,[u]_-^+\right]_{\mathrm{g}}^{\ell}}.$$

Conservation of the relative discharge $q_{\ell,\mathrm{r}}$ can be archived through the model choice of $Q_{\ell,\mathrm{r}}(H)$ – see Section 3.2.3.

Once the shock celerities and the integral values (3.4) have been computed, the control volume borders are translated according to $x_{i+\frac{1}{2}}^{(n+1)} = x_{i+\frac{1}{2}}^{(n)} + \Delta t\, c_{i+\frac{1}{2}}^{(n)}$. New wavelengths $\Delta x_i^{(n+1)} = x_{i+\frac{1}{2}}^{(n+1)} - x_{i-\frac{1}{2}}^{(n+1)}$ yield the new average states $\overline{\psi}_i^{(n+1)} = \left(\Delta x\overline{\psi}\right)_i^{(n+1)} / \Delta x_i^{(n+1)}$. A wave sketch with the discussed variable is presented in Figure 3.1.

3.2 An analytical wave model

A local coordinate system $X(x,t)$, moving with celerity $C(x)$, is defined

$$X^{(n)} = x - C^{(n)}t, \qquad \begin{aligned} x_{\mathrm{L}} \le x \le x_{\mathrm{R}}, \\ t_n \le t < t_{n+1}, \end{aligned}$$

[1] To see that both components of $\boldsymbol{f}_{\mathrm{r}}$ are invariants across a shock, let C be the shock speed c and evaluate (3.7a) over an infinitely narrow integral. All but $\boldsymbol{f}_{\mathrm{r}}^+ - \boldsymbol{f}_{\mathrm{r}}^-$ disappears.

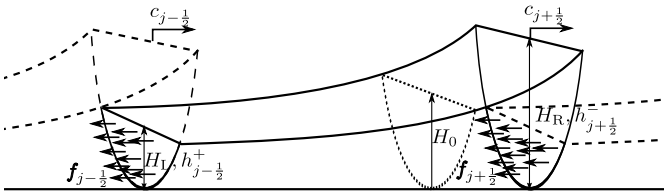

Figure 3.1: A sketch of a wave solution interacting in a wave train.

where $C^{(n)}$ is generally a function of x, but constant in a steady wave train. Next, translated variables are introduced as $\Phi(X,t) = \phi(x,t)$, reserving upper-case characters for these. Equations (2.2) are now recast in the relative coordinates, yielding

$$\partial_t \boldsymbol{\Psi} + \partial_X \boldsymbol{F}_{\mathrm{r}} + \boldsymbol{\Psi} \partial_X C = \boldsymbol{S}, \tag{3.7a}$$

$$A_\ell + A_{\mathrm{g}} = \mathcal{A}, \qquad Q_\ell + Q_{\mathrm{g}} = \mathcal{Q}, \tag{3.7b}$$

with $\boldsymbol{F}_{\mathrm{r}} = \boldsymbol{F} - C\boldsymbol{\Psi} = (Q_{\ell,\mathrm{r}}, J_{\mathrm{r}})^T$ being the fluxes with relative velocities. $Q_{\ell,\mathrm{r}}$ and J_{r} are of course similar to (3.5) with moving-frame variables.

Note that a non-conservative term $\boldsymbol{\Psi}\partial_X C$ has arisen to represent coordinate stretching. It manifests as a source term because changes in the space within which $\boldsymbol{\psi}$ is conserved are invisible from the stretching reference system.

System (3.7) may also be written in the form of a relative Jacobian $\mathbb{B}_{\mathrm{r}} = \frac{\partial \boldsymbol{F}}{\partial \boldsymbol{\Psi}} - C\mathbb{I}$, i.e.,

$$\left(\partial_t + \mathbb{B}_{\mathrm{r}} \partial_x\right) \boldsymbol{\Psi} = \boldsymbol{S} \tag{3.8}$$

where

$$\mathbb{B}_{\mathrm{r}} = \frac{1}{\rho^*} \begin{pmatrix} (\rho\, U_{\mathrm{r}})^* & 1 \\ \kappa^2 & (\rho\, U_{\mathrm{r}})^* \end{pmatrix}$$

and

$$\kappa = \sqrt{\frac{\rho^* w_y}{\mathcal{A}'_\ell} - \frac{\rho_\ell \rho_{\mathrm{g}}}{A_\ell A_{\mathrm{g}}} \left(U_{\mathrm{g}} - U_\ell\right)^2}. \tag{3.9}$$

Here, the intrinsic weighting operation

$$\phi^* = \frac{\phi_\ell}{A_\ell} + \frac{\phi_{\mathrm{g}}}{A_{\mathrm{g}}}$$

makes its first appearance as an useful shorthand. Eigenvalues of (3.2) are

$$\lambda^{\pm}_{\mathrm{r}} = \frac{(\rho\, U_{\mathrm{r}})^* \pm \kappa}{\rho^*}. \tag{3.10}$$

3.2.1 The steady profile equation

The profile equation for steady roll-waves are time-invariant, non-stretching solutions of (3.7), i.e., $\partial_t \boldsymbol{\Psi} = \boldsymbol{0}$, $\partial_X C = 0$. Equation (3.7a) then directly yields

$$\frac{\mathrm{d}Q_{\ell,\mathrm{r}}}{\mathrm{d}X} = 0, \qquad\qquad \frac{\mathrm{d}J_{\mathrm{r}}}{\mathrm{d}X} = S,$$

where the first result implies that $Q_{\ell,\mathrm{r}}$, and therefore also $Q_{\mathrm{g,r}}$, are constant. Applying the chain rule $\frac{\mathrm{d}J_\mathrm{r}}{\mathrm{d}X} = \frac{\mathrm{d}J_\mathrm{r}}{\mathrm{d}H}\frac{\mathrm{d}H}{\mathrm{d}X}$ to the second result yields

$$X' = \frac{J'_\mathrm{r}}{S}, \qquad \text{(steady wave)}. \tag{3.11a}$$

This is the profile equation, inverted. The level height H has been chosen as integration variable and so

$$\phi' = \frac{\mathrm{d}\phi}{\mathrm{d}H}$$

has been defined. Imposing $Q_{k,\mathrm{r}} = \mathrm{const}$, the profile numerator is found to be

$$J'_\mathrm{r} = \frac{\mathrm{d}J_\mathrm{r}}{\mathrm{d}H} = w_y - \mathcal{A}'_\ell \left(\rho\, U_\mathrm{r}^2\right)^* . \tag{3.11b}$$

Relative velocities are of course $U_{k,\mathrm{r}} = U_k - C$. The dynamic frame of the source does not cause any changes as compared to (2.2d), i.e.,

$$S = -w_x - \left[\frac{\mathcal{T}\Sigma}{A}\right]_\mathrm{g}^\ell + \mathcal{T}_\mathrm{i}\Sigma_\mathrm{i}\left(\frac{1}{A_\ell} + \frac{1}{A_\mathrm{g}}\right). \tag{3.11c}$$

All terms appearing in (3.11a) are functions of H alone.

For the formation of a steady solution to be possible, i.e., for $\partial_t \boldsymbol{\Psi} \to 0$, the roots of J'_r and S must coincide in what is known as the 'critical point' H_0: $J'_\mathrm{r}(H_0) = S(H_0) = 0$. The wave height increases monotonically with the region $H < H_0$ being hydraulically supercritical ($\mathrm{sgn}\lambda^- = \mathrm{sgn}\lambda^+$) and $H > H_0$ being subcritical ($\mathrm{sgn}\lambda^- \neq \mathrm{sgn}\lambda^+$). This is the profile equation similar to that presented by Watson [18] (alternatively Johnson in [10].)

The well-known 'viscous Kelvin-Helmholtz' criterion for marginal flow stability [1] can easily be inferred directly from the profile equation (3.11) as a zero-amplitude roll-wave. Even a zero-amplitude wave must contain a critical point H_0. By uniformity, all points in a marginally stable plane flow are critical points. In addition, for the wave to remain at zero amplitude, S in (3.11a) must be at an equilibrium with respect to H. Consequentially, the viscous Kelvin-Helmholtz criterion, as presented in [1], may simply be written

$$S = 0, \qquad S' = 0, \qquad J'_\mathrm{r} = 0.$$

The first condition is the hold-up equation, providing the steady, waveless stratified state. The second condition determines the critical wave speed while the third forms the criterion of marginal stability. In this way, viscous, stratified stability theory is a natural component of the wave profile solution; breaking wave solutions does not exist unless the uniformly plane stratified flow solution is unstable.

3.2.2 The stretching profile equation

In contrast to the steady wave solution, $\boldsymbol{\Psi}$ is here still a function of time, and C and $Q_{\ell,\mathrm{r}}$ are generally not constant within a wave. The state $\boldsymbol{\Psi}$ is however still approximated as a single variable function in H. For this to be reasonable, the time variation is assumed slow and relatable to the average properties and fluxes. Thus, time dependency is included only indirectly through locally parametric state averages $\boldsymbol{\Phi}(X,t) \to \boldsymbol{\Phi}\big(H(X,t); \overline{\boldsymbol{\psi}}(t), \boldsymbol{f}_\mathrm{L}(t), \boldsymbol{f}_\mathrm{R}(t)\big)$ and differentiated as a

single variable function.

$C(H; c_{\mathrm{L}}, c_{\mathrm{R}})$ and $Q_{\ell,\mathrm{r}}(H; q_{\ell,\mathrm{L}}, q_{\ell,\mathrm{R}})$ are modelled locally within the wave to remain globally continuous – Section 3.2.3. These should evolve towards constant values as the steady state solution (3.11a) is approached. Phase velocities are given directly from $U_k = Q_{k,\mathrm{r}}/A_k + C$, with $Q_{\mathrm{g,r}} = Q_{\mathrm{m}} - AC - Q_{\ell,\mathrm{r}}$.

The derivative of the state $\mathbf{\Psi} = \left(A_\ell, [\rho\, U]_{\mathrm{g}}^{\ell}\right)^T$, with respect to the single variable H, is

$$\mathbf{\Psi}' = \begin{pmatrix} 1 \\ -\left(\rho\, U_{\mathrm{r,adj}}\right)^* \end{pmatrix} \mathcal{A}'_\ell, \tag{3.12}$$

where the adjusted relative velocities

$$U_{k,\mathrm{r,adj}} = U_{k,\mathrm{r}} - \frac{Q'_{\ell,\mathrm{r}} - A_\ell C'}{\mathcal{A}'_\ell} = U_k - \frac{Q'_\ell}{\mathcal{A}'_\ell} \tag{3.13}$$

have been introduced. Equation (3.8) may now be written

$$\left(\mathbf{\Psi}'\partial_t + \mathbb{B}_{\mathrm{r}}\mathbf{\Psi}'\partial_x\right) H = \begin{pmatrix} 0 \\ S - S_{\mathrm{trans}} \end{pmatrix}, \tag{3.14}$$

where S_{trans} is an artificial source representation of rest terms $\rho^* \left(\partial_t Q_{\ell,\mathrm{r}} + A_\ell \partial_t C\right)$ from the slow transient – it will be discussed shortly. Eliminating $\partial_t H$ between the two equation components of (3.14), one obtains the stretchable inversed profile equation

$$X' = \frac{J'_{\mathrm{r,adj}}}{S - S_{\mathrm{trans}}}, \tag{3.15}$$

with

$$J'_{\mathrm{r,adj}} = w_y - \mathcal{A}'_\ell \left(\rho\, U^2_{\mathrm{r,adj}}\right)^*. \tag{3.16}$$

Note that if the flow has reached a steady state in which $[q_{\ell,\mathrm{r}}]_{\mathrm{L}}^{\mathrm{R}} = [c]_{\mathrm{L}}^{\mathrm{R}} = 0$, then both $Q_{\ell,\mathrm{r}}$ and C are constants (see Section 3.2.3.) One has from (3.13) that $J'_{\mathrm{r,adj}} = J'_{\mathrm{r}}$ and (3.15) becomes identical to the steady discontinuous solutions (3.11), provided $S_{\mathrm{trans}} \to 0$.

A truly steady wave in which $S_{\mathrm{trans}} = 0$ and $\partial_t \mathbf{\Psi} = 0$ also implies that the roots of J'_{r} and S coincide at the critical point H_0, as explained in Section 3.2.1. In evolving waves, on the other hand, the roots of $J'_{\mathrm{r,adj}}$ and S will not coincide perfectly. The quite simple means of making the profile integrable is here to let the S_{trans} term, representing the transient residual, provide the degree of freedom needed for accomplishing the double root. S_{trans} is made a spatial constant within each wave, expressing the discrepancy between the two roots. Precisely, $S_{\mathrm{trans}} = S(H_0)$ where H_0 is the root of $J'_{\mathrm{r,adj}}$.

Johnson et. al. [10] chose the friction multiplier m_{x} such that the double root was achieved, rather than using an artificial source term. The present approach was chosen in order to make the method independent of the friction closure.

Note that if second order differential terms are to be included into the profile model, for instance turbulent shear terms as in [12], the profile may no longer be monotonic and the variable inversion $H(X) \to X(H)$ no longer possible.

3.2.3 Modelling 'in the small' – $Q_{\ell,\mathrm{r}}(H)$ and $C(H)$

In this section the choices for the modelled discharge rate $Q_{\ell,\mathrm{r}}$ and translation velocity C are discussed. These choices then directly govern the transient $\partial_t A_\ell$ in the strip $[t_n, t_{n+1}\rangle$ through the mass equation in (3.7a).

$Q_{\ell,\mathrm{r}}$ and C are made globally continuous and locally linear in their individual variable ξ, that is

$$\phi = \phi_{\mathrm{L}} + [\phi]_{\mathrm{L}}^{\mathrm{R}} \frac{\xi_\phi - \xi_{\phi,\mathrm{L}}}{[\xi_\phi]_{\mathrm{L}}^{\mathrm{R}}}, \qquad \phi \in \{Q_{\ell,\mathrm{r}}, C\}. \tag{3.17}$$

The ξ's are chosen as

$$\xi_{Q_{\ell,\mathrm{r}}} = A_\ell^{3/2} \left(\mathcal{A}'_\ell\right)^{-1/2}, \qquad \xi_C = 1/A_\ell.$$

The choice for $\xi_{Q_{\ell,\mathrm{r}}}$ is motivated by the consideration that changes in $Q_{\ell,\mathrm{r}}$ should be consistent with the characteristic speeds (3.10), simplified in assuming $\rho_\ell \gg \rho_{\mathrm{g}}$ (the characteristics of the shallow water equations.)

ξ_C is chosen considering the adjusted relative liquid convection velocity $U_{\ell,\mathrm{r,adj}} = \big(Q_{\ell,\mathrm{r}} - A_\ell \frac{\mathrm{d}Q_{\ell,\mathrm{r}}}{\mathrm{d}A_\ell} - A_\ell^2 \frac{\mathrm{d}C}{\mathrm{d}A_\ell}\big)/A_\ell$ active in $J'_{\mathrm{r,adj}}$, seeking to make the influence of coordinate stretching uniform.

These sub-models do affect the wave dynamics notably, and better alternatives are likely to exist.

3.3 Finding the Correct Profile Solution

Expression (3.15) gives the inverse wave profile as function of H. The wave profile should be consistent with the average wave cell properties, i.e., wavelength, mass and momentum from the integral equations, that is

$$\left(1, \overline{a_\ell}, [\rho\overline{u}]_{\mathrm{g}}^{\ell}\right) = \frac{1}{\Delta x} \int_{h_{\mathrm{L}}}^{h_{\mathrm{R}}} \left(1, A_\ell, [\rho\, U]_{\mathrm{g}}^{\ell}\right) \frac{J'_{\mathrm{r,adj}}}{S - S_{\mathrm{trans}}}\, \mathrm{d}H. \tag{3.19}$$

These three conditions, together with the shock condition (3.6), are sufficient to uniquely determine the shock states $\{h^+, h^-, q_\ell, c\}_{i+\frac{1}{2}}$. A multi-dimensional root search algorithm is employed for the job. [2]

The momentum flux $j_{\mathrm{r,L}}$ through the left face of the control volume is computed $j_{\mathrm{r,L}} = J_{\mathrm{r}}(H_{\mathrm{L}}, q_{\ell,\mathrm{L}}, c_{\mathrm{L}})$, and similar for the right face. J_{r} will then remain globally continuous since c was defined in (3.6) to maintain the momentum invariant across shocks. Likewise, $Q_{\ell,\mathrm{r}}$ is globally continuous from (3.17). Finally, the average source term is

$$\overline{s} = \overline{S} = \frac{1}{\Delta x} \int_{h_{\mathrm{L}}}^{h_{\mathrm{R}}} S\, \frac{J'_{\mathrm{r,adj}}}{S - S_{\mathrm{trans}}}\, \mathrm{d}H.$$

The profile itself is then given by

$$X(h) = X_{\mathrm{L}} + \int_{h_{\mathrm{L}}}^{h} \frac{J'_{\mathrm{r,adj}}}{S - S_{\mathrm{trans}}}\, \mathrm{d}H; \quad h_{\mathrm{L}} \le h \le h_{\mathrm{R}}.$$

[2] The CAW method was programmed in the MATLAB language; built-in functions `integrate` and `fsolve` of version R2013b were used to evaluate (3.19) and to search for the roots, respectively.

Main conditions for a physical wave profile solution are

$$h_{\mathrm{L}} < H_0 < h_{\mathrm{R}} \tag{3.20a}$$
$$J'_{\mathrm{r,adj}} > 0, \qquad H > H_0 \tag{3.20b}$$
$$S - S_{\mathrm{trans}} > 0, \qquad H > H_0 \tag{3.20c}$$
$$J'_{\mathrm{r,adj}} < 0, \qquad H < H_0 \tag{3.20d}$$
$$S - S_{\mathrm{trans}} < 0, \qquad H < H_0 \tag{3.20e}$$
$$C < U_\ell, \qquad h_{\mathrm{L}} < H < h_{\mathrm{R}} \tag{3.20f}$$

Further details on the conditional nature of S, J'_{r} and the shock relation (3.6) is provided in [11, 10]. Conditions (3.20a) and (3.20b) imply that h_{R} must be less than the upper root of $J'_{\mathrm{r,adj}}$, at which $\frac{\mathrm{d}H}{\mathrm{d}X} \to \infty$. Likewise, (3.20a) and (3.20e) implies that h_{L} must be greater than the lower root of $S - S_{\mathrm{trans}}$, at which $\frac{\mathrm{d}H}{\mathrm{d}X} \to 0$.

3.4 Simulation routine

A simultaneous and a sequential solver approach will presently be described. The main distinction is that the simultaneous procedure requires the solution of one $4 \times N$-dimensional profile problem every time step, N being the number of waves, while the sequential procedure requires the solution of N three-dimensional problems.

3.4.1 Simultaneous solver

Each wave in a wave train will provide a shock front (jump) and append four variables (h^+, h^-, $q_{\ell,\mathrm{r}}$ and c) to the system. The shock condition (3.6) couples the individual profiles such that the profile of one wave is mutually dependent on the profile of its neighbouring waves. The number of variables in the coupled system is four times the number of distinct shocks i.e., $\{h^+, h^-, q_{\ell,\mathrm{r}}, c\}_{i+\frac{1}{2}}$, $i = 1 \ldots N$.
Figure 3.2 provides an algorithmic illustration of the simulation procedure.

3.4.2 Sequential solver

If, on the other hand, the wave solutions are decoupled by instead using the wave velocities from the previous time step, the chained wave system will consist of separate three-dimensional single-wave problems with the variables $\{h_{\mathrm{L}}, h_{\mathrm{R}}, q_{\mathrm{r},\ell,\mathrm{L}}\}_i$. $Q^{(n)}_{\ell,\mathrm{r}}$ from (3.17) may be constructed using the old differences $[q_\ell]^{\mathrm{R}(n-1)}_{\mathrm{L}}$ together with $q^{(n)}_{\mathrm{r},\ell,\mathrm{L}}$. An algorithmic illustration is given in Figure 3.3. The downside of a sequential procedure is that it is prone to numerical oscillations due to the lag in celerity information. Under-relaxation of c, performed in the manner $c^{(n)} := rc^{(n-1)} + (1-r)\, c^{(n)}$, r being the relaxation factor, is an effective way of stabilising the sequential routine. Measures like reducing the time step and iterating on the next time level also improve stability, though these measures also reduce the simulation efficiency.

3.5 Implementation and management

The CAW simulator programme is implemented using object oriented programming with wave and shock objects arranged sequentially in a linked list. All flow objects are also linked to the main pipe object holding properties like pipe inclination and diameter, gathered relative to

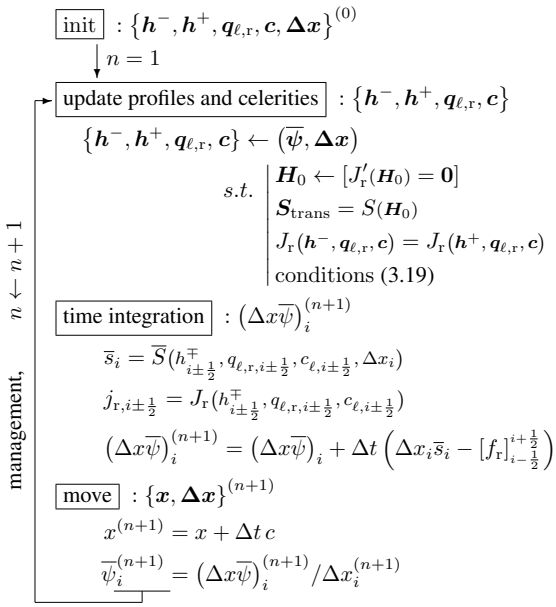

Figure 3.2: Simulation procedure. Profiles solved simultaneously. Time index (n) dropped. Vectors indicate collected shock data.

the flow objects' positions during runtime.

The CAW method requires an initial set of wavelengths. This must either be supplied as user input or retrieved from direct simulations (Section 4.)
Wave mergers, or coalescences, are identified from the collision of shocks or the diminishment of the shock height. In such events, two wave objects must merge. Mergers involve compounding the conserved integral properties into a new single wave object which covers the same spatial interval.

4 VALIDATION: WAVE CAPTURING THROUGH FINE DISCRETISATION

For validation, the target equations (2.2) are also solved through direct discretisation on a fixed uniform grid.

A number of the simpler common schemes were tested. Out of these, the simplest alternative, an explicit, non-staggered, first order upwind (or donor cell) scheme was preferred on the basis of simplicity. This is used for in all numerical comparisons with the number of grid cells equalling 3000 and the liquid-based CFL number equalling 0.5. For completeness, the discretised equations are presented in (4.1):

$$a_{\ell,i}^{(n+1)} = a_{\ell,i}^{(n)} - \frac{\Delta t}{\Delta x}\left(q_i^{(n)} - q_{i-1}^{(n)}\right), \tag{4.1a}$$

$$u_{\ell,i}^{(n+1)} = \left(\rho_\ell + \rho_{\mathrm{g}} \frac{a_{\ell,i}^{(n+1)}}{a_{\mathrm{g},i}^{(n+1)}}\right)^{-1} \times \left[\frac{\rho_{\mathrm{g}}\, \mathcal{Q}}{a_{\mathrm{g},i}^{(n+1)}} + \left[\rho\, u_i^{(n)}\right]_{\mathrm{g}}^{\ell} - \frac{\Delta t}{\Delta x}\left(j_i^{(n)} - j_{i-1}^{(n)}\right) + s_i^{(n)}\right], \tag{4.1b}$$

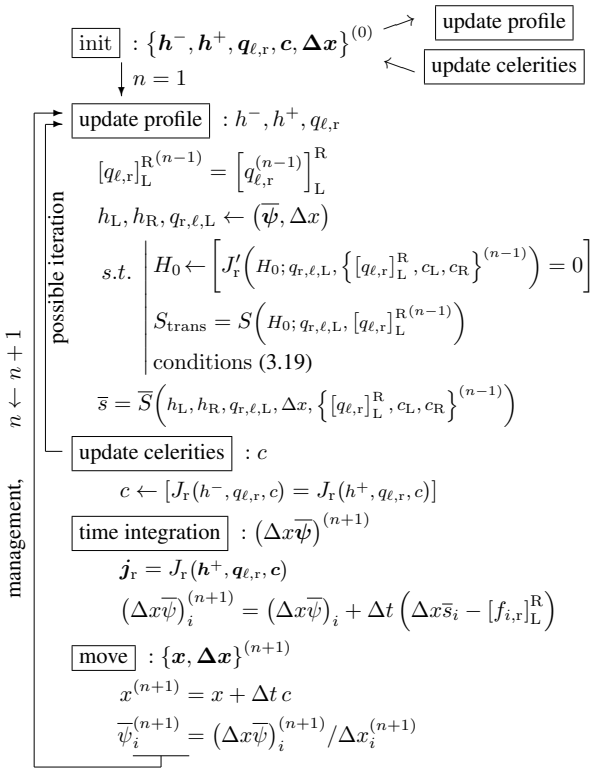

Figure 3.3: Simulation procedure. Profiles solved sequentially. Time index (n) dropped. Vectors indicate collected shock data.

with q_ℓ and j given in (2.2c) and s in (2.2d). Simulations performed with (4.1) will simply be referred to as 'direct simulations' in the following discussion.

Although the direct simulations are finely resolved, one should keep in mind that they too are associated with inaccuracies from numerical diffusion and dispersion.

5 NUMERICAL EXPERIMENTS

This work contains a large number of parameters. In the interest of briefness the parameters listed in Table 1 will remain fixed for all numerical experiments. Fluid parameters correspond to air-water flow in atmospheric conditions. Boundary conditions are made periodic (cyclic) for all test cases.

ρ_ℓ	998	$\mathrm{kg/m^3}$
ρ_g	1.205	$\mathrm{kg/m^3}$
ν_ℓ	1.005E-6	$\mathrm{m^2/s}$
ν_g	1.50E-5	$\mathrm{m^2/s}$
m_x	5.0	–
d	0.078	m
$q_\ell^{(0)}/\mathcal{A}$	0.25	$\mathrm{m/s}$

Table 1: Fixed parameters.

5.1 Simulations where the initial CAW profiles are used as the initial conditions for the direct simulation.

The first set of simulations are presented in Figure 5.1. Here, CAW simulations consist of two waves with initial length $\Delta x^{(0)} = 10\,d$ and $\Delta x^{(0)} = 20\,d$. A direct simulation runs alongside the CAW simulation in each case. Initial conditions in the direct simulations are taken as point values of the initial profile solution of the CAW. At $t > 0$ the two simulation methods run independent of each other. Initial superficial velocities of the gas phase are $q_\mathrm{g}^{(0)}/\mathcal{A} = 10.0\,\mathrm{m/s}$ in Subfigure (a) and (b), and $q_\mathrm{g}^{(0)}/\mathcal{A} = 11.0\,\mathrm{m/s}$ in Subfigure (c). The mixture rate remains unchanged from its initial value through all cases, that is $\mathcal{Q} \equiv q_\ell + q_\mathrm{g} = q_\ell^{(0)} + q_\mathrm{g}^{(0)}$.

Subfigure (a) shows the profile development in a one degree upwards inclined pipe. Wave profiles remain similar throughout the simulation, and wave coalescence occurs in close proximity in time and space. The predicted rate at which the shorter wave is eaten by the longer one is seen to differ more as the distance between wave fronts decreases. This feature may be caused by the diffusive properties of the simple direct simulation scheme, or it can be caused by an increase in the artificial source S_trans required to maintain the quasi-steady approximation in the CAW method. A third possible explanation for the slight discrepancy is that the sub-models of Section 3.2.3 are not optimal.

In Subfigure (b), the pipe inclination is one degree downwards. This manifests in higher waves and faster coalescence. (Waves pass the periodic boundaries many times in between snapshots.) The rate of coalescence is still greater in Subfigure (c), where the gas rates have been increased. The wave resulting from this wave merger is unstable, which from a modelling perspective can be interpreted at the formation of a momentary slug. In the direct simulation, this is seen as numerical instability; a sudden exponential and non-physical growth at the wave

tip (also occurring in Figures 5.3,) leading to a simulation breakdown. In the CAW simulation, the instability is manifested in that no single monotone profile solution fitting the average properties exists.

Figure 5.2 presents the time evolution of the artificial source term S_{trans} for the two stable cases, Figure 5.1a and b. S_{trans} is largest initially and just before and just after a wave coalescence. The larger values of S_{trans} prior to a coalescence may contribute to the discrepancy in predicted celerities, as mentioned above. After coalescence, S_{trans} quickly diminishes towards zero, meaning that the solution becomes identical to the steady wave solution presented in Section 3.2.1.

5.2 Simulations where the initial conditions of the CAW simulation are collected from a developing direct simulation.

A similar case set-up is presented in Figures 5.3 and 5.4 with a horizontal pipe. These CAW simulations are initiated with the average wave properties gathered from an intrinsically developing direct simulation. The direct simulation was initially uniform apart from a tiny, pointwise random disturbance. Instantaneous data was then stored at $t = 30\,\text{s}$, before the growing waves began to break. Resetting the time to $t = 0$, CAW simulations are initiated by partitioning the direct simulation domain and averaging the properties within these partitions. The criterion for a wave partition is that it forms the midpoint between a local left peak and local right trough in liquid fraction. These wave are still developing, as can be seen from the initial profiles at $t = 0$. Figure 5.3 shows wave profile snapshots and Figure 5.4 displays the wavelengths development in time. Subfigures 5.3a and 5.4a present a simulation with sequentially computed CAW profiles (Section 3.4.2.) This simulation has been computed with a 90% under-relaxation when updating the wave celerities, keeping it numerically stable. The flow pattern evolves slowly and does not appear to be greatly affected by the considerable relaxation.

Subfigures 5.3b and 5.4b present this same test case when adopting the simultaneous solution procedure (Section 3.4.1.) Average states $\overline{\psi}$ are compared in Figure 5.5. The time and location of wave mergers are here in good agreement, keeping in mind the these simulations ran independently of each other before direct simulation waves started to break.

Finally, Figure 5.6 compares the two-wave development in a range of pipe inclinations, (a), for gravity driven flows, and, (b), for pressure driven flows.

5.3 Multiple waves in alternating pipe geometry

Finally, a larger simulation with multiple waves is performed in a snake-like pipe configuration. The pipeline geometry is shown in Table 2. $q_{\text{g}}^{(0)}/\mathcal{A} = 9\,\text{m/s}$. Periodic boundary conditions make this configuration continuous.

Pipe	1	2	3	4	5	6	7	8	9	10
θ	-.1°	-.3°	-.5°	-.3°	-.1°	.1°	.3°	.5°	.3°	.1°
L	10	10	20	10	10	10	10	20	10	10

Table 2: Pipeline geometry

In order to avoid disturbing the profile search routine, changes in pipe inclination are ac-

(a) $\theta = +1°$, $q_{\mathrm{g}}^{(0)}/\mathcal{A} = 10\,\mathrm{m/s}$.

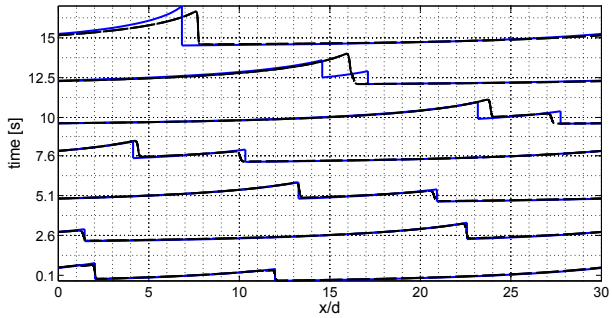

(b) $\theta = -1°$, $q_{\mathrm{g}}^{(0)}/\mathcal{A} = 10\,\mathrm{m/s}$.

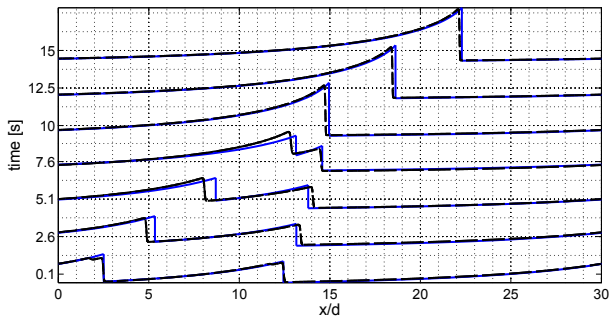

(c) $\theta = -1°$, $q_{\mathrm{g}}^{(0)}/\mathcal{A} = 11\,\mathrm{m/s}$.

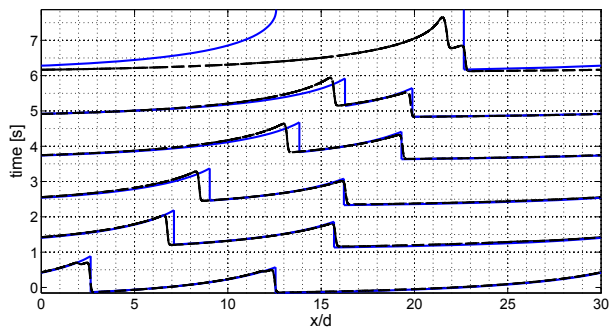

Figure 5.1: Double wave simulation using the simultaneous solution procedure. The initial state of the direct simulations is taken from the initial solutions of the analytical waves. Solid line: CAW, stippled line: direct simulation.
$\Delta x^{(0)} \in \{10\,d, 20\,d\}$. Wave heights H ranges from around $0.1\,d$ to $0.3\,d$ before coalescence. (Waves pass through boundaries many times between each profile visualisation.)

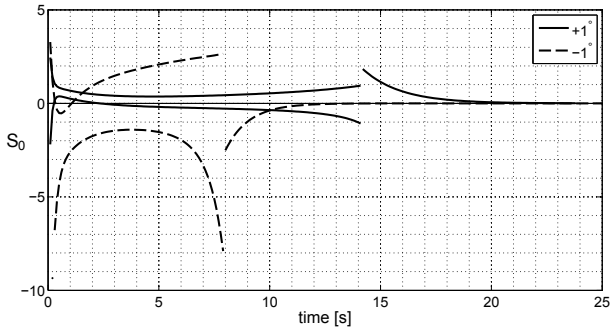

Figure 5.2: Artificial source S_{trans}. $q_{\text{g}}^{(0)}/\mathcal{A} = 10.0\,{}^{\text{m}}/_{\text{s}}$, $\theta = \pm 1°$, cf. Figure 5.1a and b.

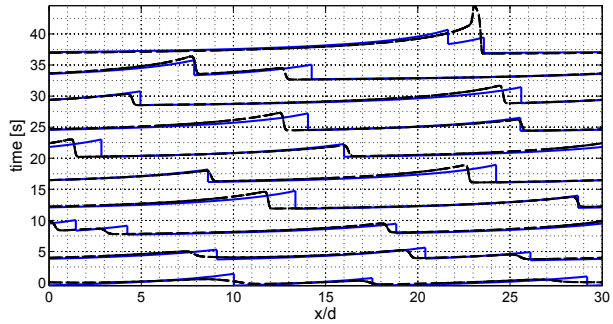

(a) Sequential procedure. 90% relaxation.

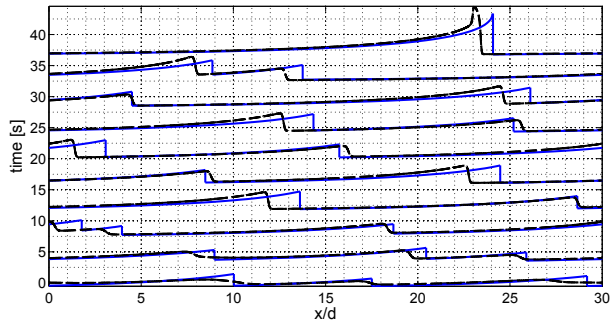

(b) Simultaneous procedure. (No relaxation.)

Figure 5.3: Profile development in time. The initial average states of the analytical wave simulation is computed by averaging partitions of a direct simulation at $t = 30\,\text{s}$. Solid line: CAW, stippled line: direct simulation.
$q_{\text{g}}^{(0)}/\mathcal{A} = 11\,{}^{\text{m}}/_{\text{s}}$, $\theta = 0°$.

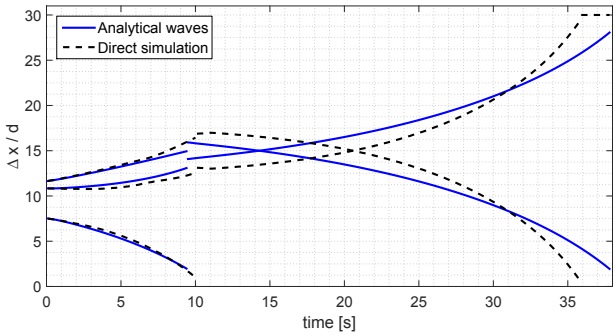

(a) Sequential procedure. $Q_{\ell,\mathrm{r}}(H)$ and $C(H)$, as per Section 3.2.3. 90% relaxation.

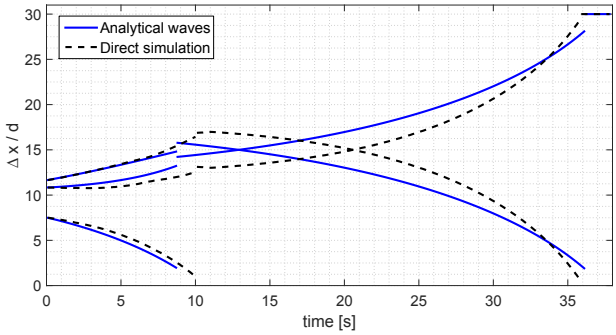

(b) Simultaneous procedure. $Q_{\ell,\mathrm{r}}(H)$ and $C(H)$, as per Section 3.2.3. (No relaxation.)

Figure 5.4: Wavelength development in time, presented as $\Delta x/d$. Cf. Figure 5.3.

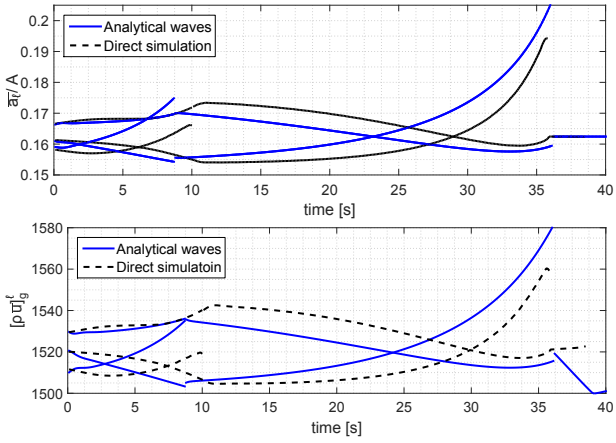

Figure 5.5: $\overline{a_\ell}/A$ and $[\rho\,\overline{u}]^{\ell}_{\mathrm{g}}$. Simultaneous procedure, cf. Figure 5.3b

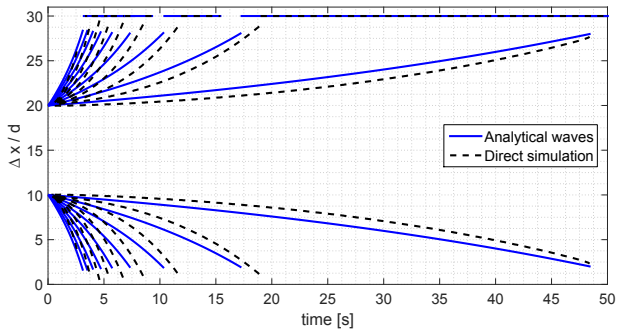

(a) No gas present. $\theta \in \{-1.5°, -2.0°, \ldots, -5.5°\}$ where the lengths of the curbed lines on the 'fan' decreases with increasing inclination.

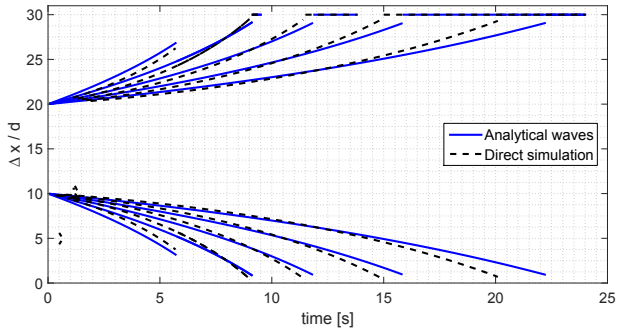

(b) $\theta = 0°$. $q_g^{(0)}/\mathcal{A} \in \{8\,\mathrm{m/s}, 9\,\mathrm{m/s}, \ldots, 12\,\mathrm{m/s}\}$ where the lengths of the curbed lines on the 'fan' decreases with increasing superficial gas velocity.

Figure 5.6: Wavelength plot. Simultaneous procedure.

counted for by approximating a constant inclination in the profile equation. This inclination is computed from the fraction of wave found within each pipe segment. CAW profiles will thus react instantaneously to the changing inclination, inertia being supplied only though the average state. The sequential solver (Figure 3.3) is used with 95% under-relaxation.

Figure 5.7 presents the time evolution from a 12-wave simulation in a 120 diameter long domain. The two predictions remain fairly consistent throughout the simulation. Alternating pipe inclinations are manifested as a wavy evolution in the wavelength plot, Figure 5.8.

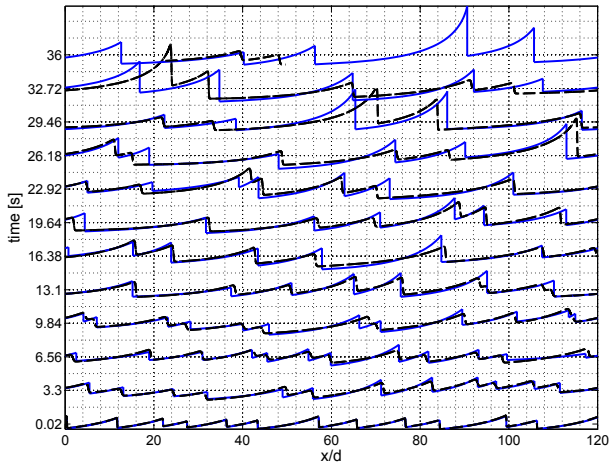

Figure 5.7: Multiple waves in the pipeline configuration of Table 2; profile evolution. Solid line: CAW, stippled line: direct simulation.

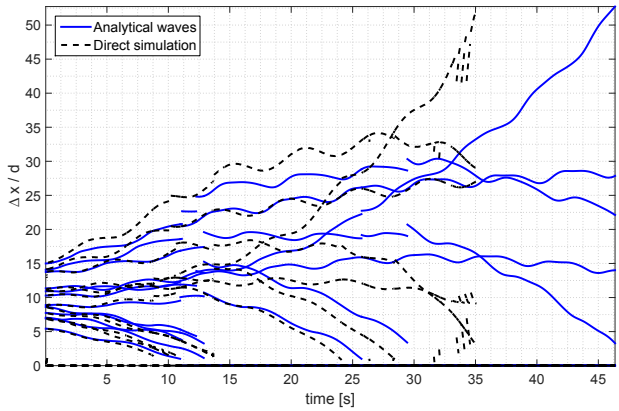

Figure 5.8: Multiple waves in the pipeline configuration of Table 2, cf. Figure 5.7; wavelength evolution.

The higher waves coalesce quicker in the capturing simulation than in the CAW during the later stages of the simulation, similar to what was observed in the two-wave simulations. Coalescence of the two highest waves takes place around $t = 35\,\mathrm{s}$ in the direct simulation, resulting

in an unstable wave and the subsequent simulation break-down. This happens about ten seconds later in the CAW simulation.

Average variables $\overline{\psi}$ are again plotted against time in Figure 5.9. Oscillations of these average variables are quite consistent, despite the significant under-relaxation of the sequential CAW solver.

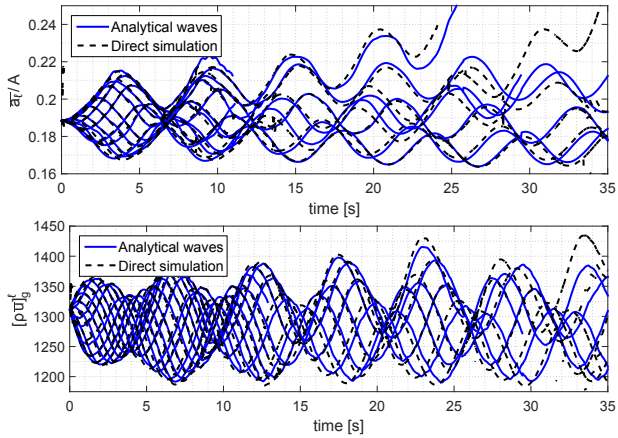

Figure 5.9: Average wave properties $\overline{\psi} = \langle \overline{a_\ell}, [\rho\,\overline{u}]_g^\ell \rangle$ cf. Table 2 and Figure 5.7

6 POTENTIAL AND EFFICIENCY

Tests presented in the previous section were of a basic nature, evaluating the main principle that analytical wave solutions would evolve appropriately if put into a dynamic frame. Obviously, the applicability such principles is tightly hinged on the degree to which defined structures (waves) are physically present.

Regarding efficiency, the bottleneck of the CAW method, as presented here, is the profile reconstruction of Section 3.3, implemented with a multi-dimensional root search algorithm. The main computational cost within this profile search routine is in turn the numerical profile integrations for retrieving average wave properties. Such costly routines can be acceptable only if that cost can be regained through significantly fewer cells and larger time steps. Simpler models, or profile approximations, which provide algebraically pre-integrable expressions would alleviate the computational cost significantly.

7 CONCLUSIONS

A simulation concept which takes advantage of naturally occurring flow structures has been presented and tested using a method of dynamically chained analytical waves. Results compare favourably with fully resolved direct simulations of the same state equation set.

In particular, the tested method seems capable of predicting wave speeds, wave evolution and wave coalescences with reasonable accuracy in time and space. The method shows the same stability behaviour as in the fully resolved simulations, and appears to be well adopted for the range of flow parameters within which the roll-wave phenomenon is set to occur. Prediction accuracy is likely to improve with further method development.

Predictions are made using vastly larger grid cells and time steps than what is required with conventional finite-volume methods. Still, better ways of searching for profile solutions seems to be necessary for the method to become truly efficient. The method also requires initial wavelengths as input. However, once some initial wavelengths have been given, or extracted from a direct simulation, the wave regime develops either towards an appropriate steady state or a flow regime transition.

Acknowledgements

This work is financed by The Norwegian University of Science and Technology (NTNU) as a contribution to the Multiphase Flow Assurance programme (FACE.) The author thanks Kontorbamse for the inspirational support.

REFERENCES

[1] D. Barnea and Y. Taitel. Interfacial and structural stability of separated flow. *International Journal of Multiphase Flow*, 20(supplissue):387 – 414, 1994/08/.

[2] D. Biberg. A mathematical model for two-phase stratified turbulent duct flow. *Multiphase Science and Technology*, 19(1):1 – 48, 2007.

[3] R.R. Brock. Development of roll-wave trains in open channels. *American Society of Civil Engineers, Journal of the Hydraulics Division*, 95(HY4):1401 – 1427, 1969.

[4] B.S. Brook, S.A.E.G. Falle, and T.J. Pedley. Numerical solutions for unsteady gravity-driven flows in collapsible tubes: evolution and roll-wave instability of a steady state. *Journal of Fluid Mechanics*, 396:223 – 56, 1999/10/10.

[5] Zhixian Cao, Penghui Hu, Kaiheng Hu, Gareth Pender, and Qingquan Liu. Modelling roll waves with shallow water equations and turbulent closure. *Journal of Hydraulic Research*, 0(0):1–17, 0.

[6] A. De Leebeeck and O.J. Nydal. Simulation of large amplitude waves in a slug tracking scheme compared to roll wave experiments at high pressure. *International Journal of Multiphase Flow*, 36(1):40 – 50, 2010.

[7] R.F. Dressler. Mathematical solution of the problem of rollwaves in inclined open channels. *Communications on Pure and Applied Mathematics*, 2:149 – 194, 1949/06/.

[8] D. Gidaspow. Multiphase flow and fluidization. *Journal of Fluid Mechanics*, 287:405 – 405, 1995.

[9] H. Holmås. Numerical simulation of transient roll-waves in two-phase pipe flow. *Chemical Engineering Science*, 65(5):1811 – 25, 2010/03/01.

[10] George W. Johnson, Arnold F. Bertelsen, and Jan Nossen. A mechanistic model for roll waves for two-phase pipe flow. *AIChE Journal*, 55(11):2788 – 2795, 2009.

[11] G.W. Johnson. *A Stuy of Stratified Gas-Liquid Pipe Flow*. PhD thesis, Univ. Oslo, 2005. dr. scient.

[12] G.W. Johnson, J. Nossen, and A.F. Bertelsen. A comparison between experimental and continuous theoretical roll waves in horizontal and slightly inclined pipes at high pressure. pages 643 – 655, Barcelona, Spain, 2005.

[13] Jr. Lahey, R.T. Void wave propagation phenomena in two-phase flow (kern award lecture). *AIChE Journal*, 37(1):123 – 35, 1991/01/.

[14] M. Miya, D.E. Woodmansee, and T.J. Hanratty. A model for roll waves in gas-liquid flow. *Chemical Engineering Science*, 26(11):1915 – 31, 1971/11/. liquid film;high speed gas flow;flow surges;roll waves;height;wall shear stress;gas pressure;mathematical model;.

[15] G.L. Richard and S.L. Gavrilyuk. A new model of roll waves: Comparison with brock's experiments. *Journal of Fluid Mechanics*, 698:374 – 405, 2012.

[16] Y. Taitel and A.E. Dukler. A model for predicting flow regime transitions in horizontal and near horizontal gas-liquid flow. *AIChE Journal*, 22(1):47 – 55, 1976/01/.

[17] H. A. Thomas. The propagation of waves in steep prismatic conduits. In *Hydraulics Conf.*, pages 214–229, Carnegie Institute of Technology, Pittsburgh, 1939.

[18] M. Watson. Wavy stratified flow and the transition to slug flow. In C.P. Fairhurst, editor, *Multi-phase Flow – Proceedings of the 4th International Conference*, pages 495–512, Cranfield, UK, 1989.

PAPER III

Characteristic Methods and Roe's Method for the Incompressible Two-Fluid Model for Stratified Pipe Flow

Andreas H. Akselsen

Under review in
The International Journal of Multiphase Flow

Characteristic Methods and Roe's Method for the Incompressible Two-Fluid Model for Stratified Pipe Flow

A.H. Akselsen*

Department of Energy and Process Engineering, Norwegian University of Science and Technology, Kolbjørn Hejes v. 1B, 7491 Trondheim, Norway

Abstract

This article examines the use of characteristic methods in stratified two-phase pipe flow simulations for obtaining non-dissipative flow predictions. A Roe scheme and several methods based on the principle of characteristics are presented for the two-fluid model. The main focus is finding numerically efficient ways of capturing wave dynamics and flow regime transitions through direct simulation. Characteristic methods offer the possibility of simulating hyperbolic systems without numerical dissipation. These methods do however lack certain fundamental conservation properties. Challenges related to information scattering and clustering in space and time, particularly around shocks, are also an issue in some method variants. Hybridisations with the finite volume method are proposed which overcome these shortcomings. All methods are compared, evaluating predictions on the onset of linear wave growth and simulations of non-linear, discontinuous roll-waves. The following observations are made: 1. Characteristic methods are excellent at predicting the onset of linear hydrodynamic instability, even with a small number of computational nodes. 2. Dissipative errors in finite volume methods and characteristic hybrids will be closely linked to the Courant number. The Roe scheme and the characteristic hybrids give very little dissipation error as the Courant number approaches unity. This then becomes a question of numerical stability. 3. Adapting dynamic grid cells, moving along with the characteristics information drift, greatly improves simulation efficiency by allowing for longer time steps. Dynamic grid cells are also useful for alleviating the need for interpolation in characteristic methods.

On the whole, the performance of the characteristic hybridisations are similar to that of the Roe scheme. Characteristic hybridisations perform somewhat better in predicting linear instability while the Roe scheme is better suited for the shock fronts found in the roll-wave flow regime. These method easily out-perform the more basic upwind and Lax-Friedrich schemes.

Keywords: two-phase; pipe-flow; two-fluid model; method of characteristics; Roe scheme

1. Introduction

The method of characteristics, henceforth abbreviated 'MOC', has been common amongst hydraulic engineers many years, particularly for calculations regarding sonic waves in long pipelines (waterhammer) [17, 16]. These are problems where the sonic information travels very fast on both directions compared to the convective velocity. The MOC does not suffer from numerical diffusion in the same way that finite difference, volume or element methods do, which makes it suitable for expressing the long-range sonic waves of pipe systems.

The method has also been used for multiphase pipe flow problems, such as for dispersed flows [6]. The non-dissipative nature of the method also makes it attractive in relation to surface wave phenomena. Crowley et. al. [7] and Barnea and Taitel [2, 1] simulated stratified two-phase pipe flow under simplifying assumptions using the MOC. They compared these results to analytical expressions from linear stability theory. The method was here chosen so that numerical diffusion would not artificially stabilise the flow.

Surface waves are a vital element in the evolution of stratified pipe flow. Characteristics methods are however uncommon in multiphase pipe flow simulation software, the reasons for which can by and large be boiled down to three shortcomings in the MOC:

1. The MOC does not provide a numerically conservative formulation. Numerical errors may then accumulate and manifest in the false appearance or disappearance of mass, momentum, energy, etc..
2. The distribution of numerical nodes in space and time turns irregular if the problem is strongly non-linear.
3. The method is generally not well-suited for handling discontinuities.

More common for simulating non-linear hyperbolic problems are Roe's approximate Riemann solvers [15], which

*Corresponding author
Email address: andreas.h.akselsen@ntnu.no (A.H. Akselsen)

are designed to provide solutions to a linearised shock problem.

Toumi and Kumbaro [20, 21] were amongst the first to formulate Roe schemes for compressible two-phase pipe flow models. The flow models represented by these schemes cannot be put in a conservative form; providing weak formulations of the non-conservative terms is a central feature of this work.

Flåtten and Munkejord [9] presented a strategy for constructing a Roe-average matrix without placing any requirements on the drift flux function. It need not even be an algebraic expression. This was used to provide a Roe matrix for the drift-flux model for two-phase flows.

A last method worth mentioning for simulating stratified two-phase pipe flow is Holmås' pseudospectral scheme [10]. Spectral methods are not included here as their application to non-periodic boundary problems in unclear.

The objective of this paper is the study and development of simple and efficient methods for simulating stratified pipe flows, focusing primarily on characteristic methods. An efficient method should be capable of both detecting the onset of hydrodynamic wave growth, and producing the wavy flow regime that ensues. Therefore, methods are tested up against analytical expressions for the onset of linear instability [1] and discontinuous roll-waves [22].

The structure of this article is as follows: The incompressible two-fluid model for stratified pipe flow is presented in Section 2. Theory for the construction of characteristic methods and finite volume methods are presented in Sections 3 and 4, respectively. A number of characteristics-based methods are presented in Section 5, sequentially focusing on remedying some of the issues associated with the characteristics approach. A Roe method has been developed and is presented in Section 6. These methods are then compared through the numerical experiments of Section 7, where the methods are tested in both the linear and non-linear wave regimes. Discussion and conclusions are given in Sections 8 and 9, respectively.

2. The Two-Fluid Model for Pipe Flow

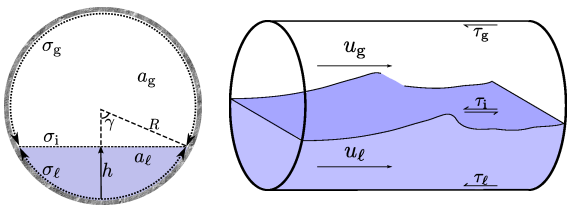

Figure 2.1: Pipe cross-section

Figure 2.1 illustrates the pipe geometry and some of the quantities appearing the two-fluid model. Field k, occupied by either gas $k = \mathrm{g}$ or liquid $k = \ell$, is segregated from the other field. Subscript i indicates the fluid interface. The circular pipe geometry itself enters into the modelling through the relation between the level height h, the specific areas a_k and the perimeter lengths σ_k and σ_i. These are algebraically interchangeable through a geometric function

$$h = \mathcal{H}(a_\ell). \tag{2.1}$$

Only the inverse of $\mathcal{H}$ is an explicit expression

$$\mathcal{H}^{-1}(h) = R^2\left(\gamma - {}^1\!/_2 \sin 2\gamma\right), \quad \gamma(h) = \arccos\left(1 - \frac{h}{R}\right),$$

but Biberg's approximation [4]

$$\begin{aligned}\mathcal{H}(a_\ell) &= R\left(1 - \cos\gamma\right),\\ \gamma \approx\ & \pi\alpha_\ell + \left(\frac{3\pi}{2}\right)^{1/3}\left(1 - 2\alpha_\ell + \alpha_\ell^{1/3} - \alpha_\mathrm{g}^{1/3}\right)\\ & - 0.005\,\alpha_\ell\alpha_\mathrm{g}\left(\alpha_\mathrm{g} - \alpha_\ell\right)\left(1 + 4\left(\alpha_\ell^2 + \alpha_\mathrm{g}^2\right)^2\right),\end{aligned}$$

is very accurate. R is here the pipe inner radius, γ the interface half-angle and $\alpha_k = a_k/\mathcal{A}$ is the phase fraction. The function derivative is $\mathcal{H}' = 1/\sigma_\mathrm{i}$ and the perimeter lengths are

$$\sigma_\ell = 2R\gamma, \qquad \sigma_\mathrm{g} = 2R\left(\pi - \gamma\right), \qquad \sigma_\mathrm{i} = 2R\sin\gamma.$$

The compressible, adiabatic, equal pressure four-equation two-fluid model for stratified pipe flow results from an averaging of the conservation equations across the cross-section area. The model is commonly written

$$\left(\rho_k a_k\right)_t + \left(\rho_k a_k u_k\right)_x = s_k^{\mathrm{mass}}, \tag{2.2}$$

$$\left(\rho_k a_k u_k\right)_t + \left(\rho_k a_k u_k^2\right)_x + a_k p_{\mathrm{i},x} + \rho_k g\cos\theta\, a_k h_x = s_k^{\mathrm{mom}}. \tag{2.3}$$

p_i is here the pressure at the interface, assumed the same for each phase as surface tension is neglected. h is the height of the interface from the pipe floor, and the term in which it appears originates from approximating a hydrostatic wall-normal pressure distribution within a fluid. u_k and ρ_k are the mean fluid velocity and density in field k. The momentum sources are $s_k^{\mathrm{mom}} = \tau_k\sigma_k \pm \tau_\mathrm{i}\sigma_\mathrm{i} - a_k\rho_k g\sin\theta$, where τ is the skin frictions at the walls and interface, θ is the pipe inclination, positive above datum, and g is the gravitational acceleration. Internal mass sources s_k^{mass} are commonly zero.

Both fluid flows are from here assumed incompressible. This allows for the system to be represented on conservative form.[1] Reducing the momentum equations with their respective mass equations, dividing by the respective phase areas and finally eliminating the pressure term by

[1] It is sufficient for one of the fluids to be incompressible and the other the have a negligible level height term for this to be possible.

differencing these equations yields

$$\boldsymbol{v}_t + \boldsymbol{f}_x = \boldsymbol{s} \tag{2.4}$$

where

$$\boldsymbol{v} = \begin{pmatrix} a_\ell \\ q \end{pmatrix}, \quad \boldsymbol{f} = \begin{pmatrix} a_\ell u_\ell \\ [\![\rho u^2/2]\!]_{\mathrm{g}}^{\ell} + w_y h \end{pmatrix}, \quad \boldsymbol{s} = \begin{pmatrix} s_{a_\ell} \\ s_q \end{pmatrix},$$
$$q = [\![\rho u]\!]_{\mathrm{g}}^{\ell}, \quad s_q = -w_x - [\![\tau\sigma/a]\!]_{\mathrm{g}}^{\ell} + \tau_{\mathrm{i}}\sigma_{\mathrm{i}}\left(1/a_\ell + 1/a_{\mathrm{g}}\right).$$

The shorthand

$$[\![\cdot]\!]_{\mathrm{g}}^{\ell} = (\cdot)_\ell - (\cdot)_{\mathrm{g}}$$

is here useful. Specific weight components are $w_x = [\![\rho]\!]_{\mathrm{g}}^{\ell} g \sin\theta$ and $w_y = [\![\rho]\!]_{\mathrm{g}}^{\ell} g \cos\theta$. Although actually derivatives therefrom, these equations are here simply referred to as base mass and momentum equations. The identities

$$a_\ell + a_{\mathrm{g}} = \mathcal{A}, \qquad (au)_\ell + (au)_{\mathrm{g}} = \mathcal{Q}_{\mathrm{m}}, \tag{2.5}$$

where both right hand sides are parametric, finally close the base model (2.4). The second identity originates from summing the gas and liquid mass equations (2.2) and applying the first identity. The mixture flow rate $\mathcal{Q}_{\mathrm{m}}$ is generally expressible as $\mathcal{Q}_{\mathrm{m}} = \mathcal{Q}_{\mathrm{m},0} + \int_{x_0}^{x} (s_{a_{\mathrm{g}}} + s_{a_\ell})\mathrm{d}\xi$. Usually, internal mass sources $s_{a_k} \equiv 0$ such that $\mathcal{Q}_{\mathrm{m}}$ everywhere equals the inlet mixture flow rate, made constant in all examples presented herein.

Primitive variables are recovered through

$$u_\ell = \frac{\rho_{\mathrm{g}}\mathcal{Q}_{\mathrm{m}} + a_{\mathrm{g}} q}{a_{\mathrm{g}}\rho_\ell + a_\ell\rho_{\mathrm{g}}}, \qquad u_{\mathrm{g}} = \frac{\rho_\ell\mathcal{Q}_{\mathrm{m}} - a_\ell q}{a_{\mathrm{g}}\rho_\ell + a_\ell\rho_{\mathrm{g}}}.$$

The friction closures τ_k and τ_{i} in the numerical tests of this article are provided by the Biberg friction model as presented in [3]. Here, classical turbulent boundary layer principles are used to model the gas and liquid velocity profiles in a duct cross section. The interface is modelled as a moving boundary with an initial turbulence level. Figure 2.2 shows an example of such velocity profiles. These profiles are integrated up to yield algebraic expressions that couple wall and interfacial frictions to the average phase velocities and the interface height. Friction correlations for duct flow are correlated to the well-known Colebrook-White formula for single-phase pipe flow, which in turn is used to extend the friction model for two-phase duct flow into formulae for the pipe geometry.

3. A Method of Characteristics

The two-fluid model (2.4) is expressed through a Jacobian $\mathbb{A} = \frac{\partial \boldsymbol{f}}{\partial \boldsymbol{v}}$ as follows:

$$\boldsymbol{v}_t + \mathbb{A}\boldsymbol{v}_x = \boldsymbol{s} \tag{3.1}$$

where

$$\mathbb{A} = \frac{1}{\rho^*}\begin{pmatrix} (\rho u)^* & 1 \\ \kappa^2 & (\rho u)^* \end{pmatrix}.$$

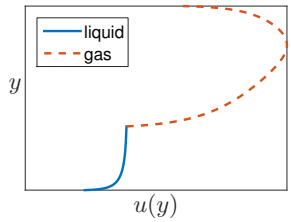

Figure 2.2: Example velocity profile pre-integrated in the Biberg friction model.

An operator

$$\phi^* = \frac{\phi_\ell}{a_\ell} + \frac{\phi_{\mathrm{g}}}{a_{\mathrm{g}}}$$

has here been defined, along with

$$\kappa = \sqrt{\rho^* w_y \mathcal{H}' - \frac{\rho_\ell\rho_{\mathrm{g}}}{a_\ell a_{\mathrm{g}}}\left(u_{\mathrm{g}} - u_\ell\right)^2}. \tag{3.2}$$

The eigenvalues $\lambda^{\pm}$ of $\mathbb{A}$, obtained as the roots of $\det(\mathbb{A} - \lambda\mathbb{I}) = 0$, are

$$\lambda^{\pm} = \frac{(\rho u)^* \pm \kappa}{\rho^*}. \tag{3.3}$$

System (2.4) will be hyperbolic if κ is real. Left eigenvectors $\boldsymbol{\ell}^{\pm}$ (row vectors) are used for the decomposition;

$$\mathbb{A} = \mathbb{L}^{-1}\mathbb{\Lambda}\mathbb{L}, \tag{3.4}$$

where $\mathbb{L} = (\boldsymbol{\ell}^+, \boldsymbol{\ell}^-)^T$, $\boldsymbol{\ell}^{\pm} = (1, \pm 1/\kappa)$ and $\mathbb{\Lambda} = \mathrm{diag}(\lambda^+, \lambda^-)$. Inserting (3.4) into (3.1) and multiplying by $\mathbb{L}$ from the left gives an orthogonal system

$$\boldsymbol{\ell}^{\pm}\frac{\mathrm{d}\boldsymbol{v}}{\mathrm{d}t} = \boldsymbol{\ell}^{\pm}\boldsymbol{s}, \qquad \text{along } \frac{\mathrm{d}x}{\mathrm{d}t} = \lambda^{\pm}. \tag{3.5}$$

The integral form of (3.5) is

$$a_{\ell,j}^{n+1} - a_{\ell,j_\pm}^{n} \pm \int_{q_{j_\pm}^n}^{q_j^{n+1}} \frac{\mathrm{d}q}{\kappa} = \int_{t_{j_\pm}^n}^{t_j^{n+1}} \left(s_{a_\ell} \pm \frac{s_q}{\kappa}\right)\mathrm{d}t, \tag{3.6}$$

where integration has been performed from $(x,t)_{j_\pm}^n$ to $(x,t)_j^{n+1}$ along the path $\frac{\mathrm{d}x}{\mathrm{d}t} = \lambda^{\pm}$. Subscripts $j_\pm$ indicate that state or point reached by following the $\pm$-path backwards in time from $(x,t)_j^{n+1}$. In discrete representations, the integration paths are linearised into line paths

$$\xi_{j,\pm}^n(t) = x_{j_\pm}^n + \lambda_{j_\pm}^{\pm,n+\frac{1}{2}}\left(t - t_{j_\pm}^n\right), \quad t_{j_\pm}^n \le t \le t_j^{n+1}. \tag{3.7}$$

with some intermediate slope $\lambda_{j_\pm}^{\pm,n+\frac{1}{2}}$.

Also linearising equation (3.6) along these respective

paths gives an algebraic system

$$a^{n+1}_{\ell,j} - a^n_{\ell,j_\pm} \pm \frac{q^{n+1}_j - q^n_{j_\pm}}{\kappa^{n+\frac{1}{2}}_{j_\pm}} = \left[\left(s_{a_\ell} \pm \frac{s_q}{\kappa}\right)\Delta t\right]^{n+\frac{1}{2}}_{j_\pm} \quad (3.8)$$

with $\Delta t^n_{j_\pm} = t^{n+1}_j - t^n_{j_\pm}$. The state $\boldsymbol{v}$ is obtainable only at the start and end of the integration, where characteristic paths intersect. Intermediate integrands $\phi^{n+\frac{1}{2}}_{j_\pm}$ are therefore computed as some average of the available intersection states, depending on the method.

Solving (3.8) is straight forward. Suppressing the superscript $n+\frac{1}{2}$, one finds

$$\boldsymbol{v}^{n+1}_j = \frac{\begin{pmatrix}\kappa^{-1}_{j-} & \kappa^{-1}_{j+}\\ 1 & -1\end{pmatrix}\begin{pmatrix}\left(a^n_\ell + s_{a_\ell}\Delta t^n + \frac{q^n + s_q\Delta t^n}{\kappa}\right)_{j+}\\ \left(a^n_\ell + s_{a_\ell}\Delta t^n - \frac{q^n + s_q\Delta t^n}{\kappa}\right)_{j-}\end{pmatrix}}{\kappa^{-1}_{j+} + \kappa^{-1}_{j-}}. \quad (3.9)$$

4. Average Volume Equations for Dynamic Finite Volume Methods

Integration of (2.4) is performed across a grid cell J, first in space from the left cell face at $x_{J-\frac{1}{2}}$ to the right one at $x_{J+\frac{1}{2}}$, and then in time from the present time t^n to the next time level t^{n+1};

$$\int_{t^n}^{t^{n+1}}\int_{x_{J-\frac{1}{2}}}^{x_{J+\frac{1}{2}}} (\partial_t \boldsymbol{v} + \partial_x \boldsymbol{f} - \boldsymbol{s})\,\mathrm{d}x\,\mathrm{d}t = 0. \quad (4.1)$$

Using Leibniz' rule ($x_{j\pm\frac{1}{2}}$ are here generally functions of t,) the first transient term evaluates to

$$\int_{x_{J-\frac{1}{2}}}^{x_{J+\frac{1}{2}}} \partial_t \boldsymbol{v}\,\mathrm{d}x = \partial_t(\Delta x\overline{\boldsymbol{v}}) - (\dot{x}\,\boldsymbol{v})_{J+\frac{1}{2}} + (\dot{x}\,\boldsymbol{v})_{J-\frac{1}{2}}$$

where $\dot{x} = \frac{\mathrm{d}x}{\mathrm{d}t}$ is the control volume border velocity. $\Delta x(t) = x_{J+\frac{1}{2}} - x_{J-\frac{1}{2}}$ is the cell length. The bar indicates the wave cell average and is defined

$$\overline{\phi}_J(t) = \frac{1}{\Delta x}\int_{x_{J-\frac{1}{2}}}^{x_{J+\frac{1}{2}}} \phi\,\mathrm{d}x. \quad (4.2a)$$

Also introducing the temporal average $\langle\cdot\rangle^n$,

$$\langle\phi\rangle^n = \frac{1}{\Delta t^n}\int_{t^n}^{t^{n+1}} \phi\,\mathrm{d}t \quad (4.2b)$$

with $\Delta t^n = t^{n+1} - t^n$, the integral equation (4.1) is cast as

$$(\Delta x\overline{\boldsymbol{v}})^{n+1}_J = (\Delta x\overline{\boldsymbol{v}})^n_J + \Delta t^n\left\langle \Delta x\overline{\boldsymbol{s}}_J - \boldsymbol{f}^{\mathrm{r}}_{J+\frac{1}{2}} + \boldsymbol{f}^{\mathrm{r}}_{J-\frac{1}{2}}\right\rangle^n, \quad (4.3)$$

where the flux terms have been made relative to the shock propagation, i.e.,

$$\boldsymbol{f}^{\mathrm{r}} = \boldsymbol{f} - \dot{x}\boldsymbol{v} = \begin{pmatrix} a_\ell(u_\ell - \dot{x}) \\ \left[\!\left[\rho u\left(\frac{u}{2} - \dot{x}\right)\right]\!\right]^\ell_{\mathrm{g}} + w_y h\end{pmatrix}.$$

It is important to note that Equation (4.3) is still exact.

5. Schemes Based on the Method of Characteristics

Seeking to overcome some of the weaknesses of data scattering and lacking conservation, a number of methods will here be suggested. The first two methods are commonly found in the literature, both usually referred to as 'the method of characteristics.' To differentiate between them, all methods are dubbed some alternation of 'MOC.'

A hat notation $\hat{\phi}$ is from here added to the variables pertaining to the characteristic principle of Section 3 to help distinguish these variables from the finite volume variables of Section 4.

5.1. A Method of Scattered Point Characteristics (MOSPC)

This method is similar to that used by Crowley et. al. [7] and Barnea and Taitel [1] for comparing the results from linear stability theory to simulations without numerical diffusion. They did however simplify the model (2.4) by disregarding the transient terms of the gas phase before constructing a characteristics scheme.

Figure 5.1 shows a schematic of the discrete Method Of Scattered Point Characteristics (MOSPC.)

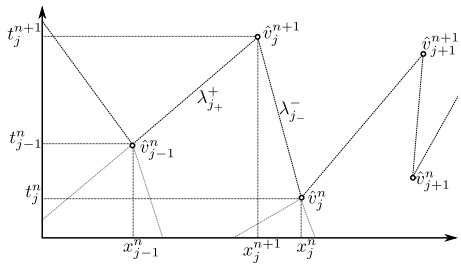

Figure 5.1: Sketch of the MOSPC.

The method consists of solving (3.9) at single-point locations in space and time where characteristic paths intersect. With the presented indexing this means that $\hat{\boldsymbol{v}}^n_{j_\pm} = \hat{\boldsymbol{v}}^n_{j\mp\frac{1}{2}-\frac{1}{2}}$. Intersection points $(\hat{x},\hat{t})^{n+1}_j$ are found through (3.7) by solving $\hat{\xi}^n_{j,\pm}\left(\hat{t}^{n+1}_j\right) = \hat{x}^{n+1}_j$. Intermediate integrands are first chosen $\hat{\phi}^{n+\frac{1}{2}}_{j_\pm} = \phi\left(\hat{\boldsymbol{v}}^n_{j_\pm}\right)$ and are then iterated upon with $\hat{\phi}^{n+\frac{1}{2}}_{j_\pm} = \phi\left(\frac{1}{2}\left(\hat{\boldsymbol{v}}^n_{j_\pm} + \hat{\boldsymbol{v}}^{n+1}_j\right)\right)$. Iteration is not required, but generally improves accuracy and stability some – it will be adopted for numerical tests in all characteristic schemes.

The free scattering of intersection nodes makes data points irregular and unsynchronised, depending on the system being simulated. Scattered point interpolation, described in Figure 5.2, is used to determine end states.

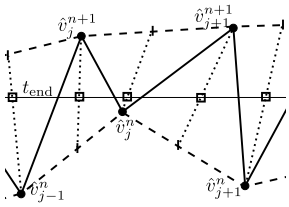

Figure 5.2: Triangular Interpolation. An interpolation point is chosen for each triangle, placed in a centre location along the line $t = t_{\text{end}}$. Barycentric interpolation of the state $\boldsymbol{v}$ is performed on each triangle.

The strength of the MOSPC is that it entails no numerical diffusion or state interpolation other than that used for the end states. It also automatically provides the longest allowable time step for each point individually. Weaknesses are the lack of conservation, that the method does not support fixed mesh arrangements, requires end state interpolation and is poorly suited for handling shock discontinuities.

5.2. A Method of Interpolated Point Characteristics (MOIPC)

This method is similar to the characteristics method used by e.g. Bournaski in [6] for simulating dispersed pipe flow with a virtual mass effect. The method of point interpolated characteristics, abbreviated 'MOIPC', allows for a fixed-mesh uniform time-step formulation of the MOSPC through the use of spatial interpolation. Figure 5.3 gives an illustration. Equal node spacing will here be used. Linear spatial interpolation of $\{\hat{\boldsymbol{v}}_j^n\}$

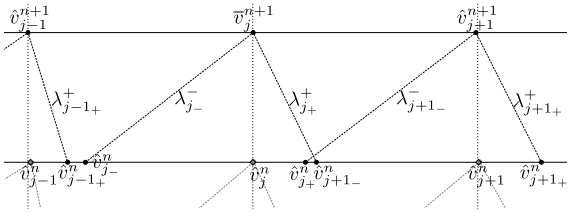

Figure 5.3: Sketch of the MOIPC.

$$\hat{\boldsymbol{v}}_{j_\pm} = \hat{\boldsymbol{v}}_j - (\hat{\boldsymbol{v}}_j - \hat{\boldsymbol{v}}_{j-1})\,\Delta\hat{t}^n\lambda_{j_\pm}^\pm/\Delta x, \qquad \lambda_{j_\pm}^\pm > 0$$
$$\hat{\boldsymbol{v}}_{j_\pm} = \hat{\boldsymbol{v}}_j - (\hat{\boldsymbol{v}}_{j+1} - \hat{\boldsymbol{v}}_j)\,\Delta\hat{t}^n\lambda_{j_\pm}^\pm/\Delta x, \qquad \lambda_{j_\pm}^\pm < 0$$

is applied on each time level to compute point states $\hat{\boldsymbol{v}}_{j_\pm}^n$, which are integrated up to the new time level using (3.9). Higher order interpolation would not necessarily improve the scheme accuracy as this may violate the MOC's domain of dependence [18]. Including interpolated states in an iteration process for the intermediate state does not seem to be a stable procedure. Instead $\hat{\phi}_{j_\pm}^{n+\frac{1}{2}} = \phi\big(\frac{1}{2}(\hat{\boldsymbol{v}}_j^n + \hat{\boldsymbol{v}}_j^{n+1})\big)$ is used for the intermediate integrands. Time steps are chosen $\Delta\hat{t}^n = \mathcal{C}\,\Delta x/\max_{j,\pm}\{\lambda_{j_\pm}^\pm\}$, $\mathcal{C}$ being the Courant number.

Also the MOIPC lacks the conservation property.

5.3. A Method of Interpolated Cell Characteristics (MOICC)

A new hybridisation with a finite volume method is now proposed with the intention of achieving conservation. The MOICC is a combination of the MOIPC with the finite volume method on a fixed grid. Figure 5.4 shows an illustration. Instead of proceeding from the states $\{\hat{\boldsymbol{v}}_j^{n+1}\}$

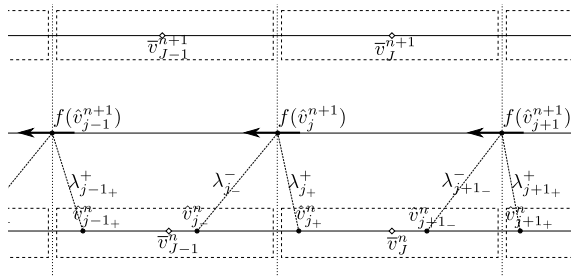

Figure 5.4: Sketch of the MOICC.

computed from the characteristic equation (3.9), these intersection states are used to compute the fluxes of a fixed grid finite volume method. Adopting Eulerian time integration on the source term $\langle\overline{\boldsymbol{s}}\rangle^n \approx \boldsymbol{s}(\overline{\boldsymbol{v}}^n) = \overline{\boldsymbol{s}}^n$ and intermediate fluxes $\langle f\rangle^n \approx f^{n+\frac{1}{2}}$ renders the finite volume equation (4.3)

$$\overline{\boldsymbol{v}}_J^{n+1} = \overline{\boldsymbol{v}}_J^n - \frac{\Delta t^n}{\Delta x_J}\left(\boldsymbol{f}_{J+\frac{1}{2}}^{n+\frac{1}{2}} - \boldsymbol{f}_{J-\frac{1}{2}}^{n+\frac{1}{2}}\right) + \Delta t^n\overline{\boldsymbol{s}}_J^n. \qquad (5.1)$$

Characteristic intersection points are used for the intermediate fluxes

$$f_{J-\frac{1}{2}}^{n+\frac{1}{2}} = f\big(\hat{\boldsymbol{v}}_j^{n+1}\big),$$

where $\hat{\boldsymbol{v}}_j^{n+1}$ is computed from (3.9) in an interpolated fashion similar to that of the MOIPC. Cell averages will in the point interpolation of $\hat{\boldsymbol{v}}_{j_\pm}^n$ be equivalent to centre point values and a uniform grid is used:

$$\hat{\boldsymbol{v}}_{j_\pm}^n = \frac{1}{2}\left(\overline{\boldsymbol{v}}_J^n + \overline{\boldsymbol{v}}_{J-1}^n\right) - \left(\overline{\boldsymbol{v}}_J^n - \overline{\boldsymbol{v}}_{J-1}^n\right)\Delta\hat{t}^n\lambda_{j_\pm}^\pm/\Delta x.$$

A stable choice of intermediate integrands is $\hat{\phi}_{j_\pm}^n = \phi\big(\hat{\boldsymbol{v}}_j^{n+1}\big)$. Time steps of the characteristic intersections are $\Delta\hat{t}^n = \frac{1}{2}\Delta x/\max_{j,\pm}|\lambda_{j_\pm}^\pm|$ and for the finite volume method $\Delta t^n = \mathcal{C}\cdot 2\,\Delta\hat{t}^n$.

The MOICC is conservative at the expense of whatever numerical diffusion is inherent in the finite volume representation. Spatial interpolation errors are still present.

5.4. A Method of Cell Centred Characteristics (MOCCC)

The MOICC presented above can show signs of unexpected numerical instability, most prudently observed in the rarefaction wave of the breaking dam test case in Section 7.1. Errors from the spatial interpolation are likely sources for this type of instability. A new proposition, The Method of Cell Centred Characteristics (MOCCC), removes the need for spatial interpolation by abandoning the spatially fixed grid. Figure 5.5 illustrates the principle. The method is similar to the MOICC, but instead

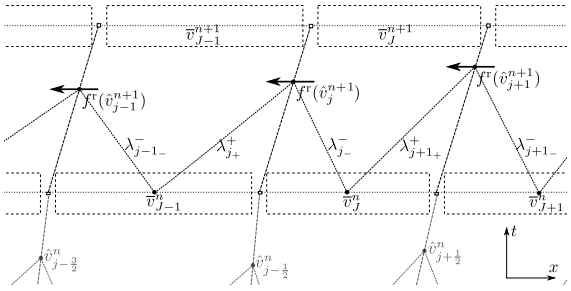

Figure 5.5: Illustration of the MOCCC.

of following the linearised characteristic paths backwards from a pre-determined intersection point $(\hat{x},\hat{t})^{n+1}_{j}$ to some point of interpolation $(\hat{x},\hat{t})^{n}_{j_\pm}$, the characteristic paths are followed forwards in time from cell centre positions $(x,t)^{n}_{J}$ to the new intersection points, as in the MOSPC. Intermediate integrands are computed $\hat{\phi}^{n+\frac{1}{2}}_{j_\pm} = \phi\big(\frac{1}{2}(\hat{\boldsymbol{v}}^{n}_{j_\pm} + \hat{\boldsymbol{v}}^{n+1}_{j})\big)$. The cell centre states are here taken as cell averages, i.e., the characteristic paths are integrated from $\hat{\boldsymbol{v}}^{n}_{j_+} = \overline{\boldsymbol{v}}^{n}_{J-1}$ and $\hat{\boldsymbol{v}}^{n}_{j_-} = \overline{\boldsymbol{v}}^{n}_{J}$.

Cell face translation velocities are then

$$\dot{x}^{n}_{J-\frac{1}{2}} = \frac{\hat{x}^{n+1}_{j} - x^{n}_{J-\frac{1}{2}}}{\hat{t}^{n+1}_{j} - t^{n}} = \frac{\Delta x^{n}_{J}\lambda^{+}_{j_+} + \Delta x^{n}_{J-1}\lambda^{-}_{j_-}}{\Delta x^{n}_{J} + \Delta x^{n}_{J-1}} \tag{5.2}$$

and the next cell face positions are

$$x^{n+1}_{J-\frac{1}{2}} = x^{n}_{J-\frac{1}{2}} + \dot{x}^{n}_{J-\frac{1}{2}}\Delta t^{n}. \tag{5.3}$$

The translation velocity ensures that the cell faces pass through the new characteristic intersection point. Relative flux averages are computed from the characteristic intersection as an intermediate state $\langle \boldsymbol{f}^{r}\rangle^{n}_{J-\frac{1}{2}} = \boldsymbol{f}^{r}\big(\hat{\boldsymbol{v}}^{n+1}_{j}\big)$ and $(\Delta x\overline{\boldsymbol{v}})^{n+1}_{J}$ is given from (4.3). Eulerian time integration $\langle\overline{\boldsymbol{s}}\rangle^{n} \approx \boldsymbol{s}(\overline{\boldsymbol{v}}^{n})$ is again applied for the source term, and the averages states $\overline{\boldsymbol{v}}^{n+1}_{J} = (\Delta x\overline{\boldsymbol{v}})^{n+1}_{J}/\Delta x^{n+1}_{J}$ are computed after translation. Time steps are chosen $\Delta t^{n} = \mathcal{C}\cdot 2\,\min_j \Delta\hat{t}^{n}_{j}$.

Negative cell lengths are very unlikely to occur in a simulation of natural flow. Expressions (5.2) and (5.3), alternatively studying Figure 5.5, reveals that cell length irregularities are intrinsically counteracted by the cell propagation set-up ($\Delta x^{n}_{J} \to 0$ guarantees $\Delta x^{n+1}_{J} > 0$.) Negative cell length can only occur if integrated in time directly from a long cell (as compared to the neighbouring cells) beyond the time step of the characteristic intersection. The characteristics paths would then have to be very irregular in the manner $\lambda^{+}_{j_+} > \lambda^{+}_{j+1_+}$, $\lambda^{-}_{j_-} > \lambda^{-}_{j+1_-}$. A formal guarantee against negative cell lengths can be provided by imposing $\Delta t < \min_J \left\{ \frac{\Delta x_J}{\dot{x}_{J-\frac{1}{2}} - \dot{x}_{J+\frac{1}{2}}} \,\middle|\, J : \dot{x}_{J-\frac{1}{2}} > \dot{x}_{J+\frac{1}{2}} \right\}$. The numerical examples presented here never come close to activating this limit.

6. A Roe Scheme

Roe's approximate Riemann solver [15] is among the most popular finite volume schemes for non-linear hyperbolic problems. Its main principle lies in solving linearised Riemann problems

$$\begin{aligned} &\boldsymbol{v}_t + \hat{\mathbb{A}}(\boldsymbol{v}_{\mathrm{L}},\boldsymbol{v}_{\mathrm{R}})\boldsymbol{v}_x = 0 \\ &\boldsymbol{v}(x,0) = \boldsymbol{v}_{\mathrm{L}}\ (x<0), \quad \boldsymbol{v}(x,0) = \boldsymbol{v}_{\mathrm{R}}\ (x>0) \end{aligned} \tag{6.1}$$

at the cell faces. $\hat{\mathbb{A}}$, $\boldsymbol{v}_{\mathrm{L}}$ and $\boldsymbol{v}_{\mathrm{R}}$ are constants respective to each cell face. Roe schemes are effective at discontinuities, but they require the formulation of so-called Roe-averaged matrices $\hat{\mathbb{A}}(\boldsymbol{v}_{\mathrm{L}},\boldsymbol{v}_{\mathrm{R}})$ at the cell faces with the properties that

i) $\hat{\mathbb{A}}(\boldsymbol{v}_{\mathrm{L}},\boldsymbol{v}_{\mathrm{R}})$ is diagonalizable with real eigenvalues,

ii) $\hat{\mathbb{A}}(\boldsymbol{v}_{\mathrm{L}},\boldsymbol{v}_{\mathrm{R}}) \to \mathbb{A}(\boldsymbol{v})$ smoothly as $\boldsymbol{v}_{\mathrm{L}},\boldsymbol{v}_{\mathrm{R}} \to \boldsymbol{v}$ and

iii) $\hat{\mathbb{A}}(\boldsymbol{v}_{\mathrm{L}},\boldsymbol{v}_{\mathrm{R}})\,[\![\boldsymbol{v}]\!]^{\mathrm{R}}_{\mathrm{L}} = [\![\boldsymbol{f}]\!]^{\mathrm{R}}_{\mathrm{L}}$.

$[\![\cdot]\!]^{\mathrm{R}}_{\mathrm{L}} = (\cdot)_{\mathrm{R}} - (\cdot)_{\mathrm{L}}$. Generally, $\phi_{\mathrm{L}} = \phi(\boldsymbol{v}_{\mathrm{L}})$ and $\phi_{\mathrm{R}} = \phi(\boldsymbol{v}_{\mathrm{R}})$. The first and second properties are required for hyperbolicity and consistency, respectively. The third property ensures, by the Rankine-Hugoniot condition, that single shocks of the linear system (6.1) are shocks of the non-linear system (2.4).

Consider the following splitting of the flux function:

$$\boldsymbol{f} = \boldsymbol{f}_{\mathrm{u}} + \boldsymbol{f}_{\mathrm{h}} \tag{6.2}$$

where

$$\boldsymbol{f}_{\mathrm{u}} = \Big(a_\ell u_\ell, [\![\rho u/2]\!]^{\ell}_{\mathrm{g}}\Big)^{T}, \qquad \boldsymbol{f}_{\mathrm{h}} = (0, w_y h)^{T}.$$

We need a suitable integration path over which $\boldsymbol{f}$ is easily evaluated; $\boldsymbol{f}$ is written in terms of a parameter vector $\boldsymbol{w}$, rendering it a low-order polynomial. Primitive variable are suitable in the case of $\boldsymbol{f}_{\mathrm{u}}$, i.e.

$$\boldsymbol{w} = (a_\ell, a_{\mathrm{g}}, u_\ell, u_{\mathrm{g}})^{T}.$$

Note that $\frac{\partial \boldsymbol{v}}{\partial \boldsymbol{w}}$ is constant and that $\frac{\partial \boldsymbol{f}_{\mathrm{u}}}{\partial \boldsymbol{w}}$ is linear in $\boldsymbol{w}$. A linear path

$$\boldsymbol{w} = \tilde{\boldsymbol{w}}(z) = \boldsymbol{w}_{\mathrm{L}} + [\![\boldsymbol{w}]\!]^{\mathrm{R}}_{\mathrm{L}}\, z$$

is chosen for the integration of $\boldsymbol{f}_\mathrm{u}$. We get

$$\begin{aligned}\llbracket \boldsymbol{f}_\mathrm{u} \rrbracket_\mathrm{L}^\mathrm{R} &= \int_\mathrm{L}^\mathrm{R} \mathrm{d}\boldsymbol{f}_\mathrm{u} = \int_0^1 \frac{\partial \boldsymbol{f}_\mathrm{u}}{\partial \boldsymbol{w}}(\tilde{\boldsymbol{w}}(z)) \frac{\partial \tilde{\boldsymbol{w}}}{\partial s}\,\mathrm{d}z = \frac{\partial \boldsymbol{f}_\mathrm{u}}{\partial \boldsymbol{w}}(\overline{\boldsymbol{w}})\,\llbracket \boldsymbol{w} \rrbracket_\mathrm{L}^\mathrm{R} \\ &= \frac{\partial \boldsymbol{f}_\mathrm{u}}{\partial \boldsymbol{v}}(\overline{\boldsymbol{w}}) \frac{\partial \boldsymbol{v}}{\partial \boldsymbol{w}}\,\llbracket \boldsymbol{w} \rrbracket_\mathrm{L}^\mathrm{R} = \mathbb{A}_\mathrm{u}(\overline{\boldsymbol{w}})\,\llbracket \boldsymbol{v} \rrbracket_\mathrm{L}^\mathrm{R}\,, \end{aligned} \tag{6.3}$$

where the fourth expression is a result of $\frac{\partial \boldsymbol{f}_\mathrm{u}}{\partial \boldsymbol{w}}$ being linear in $\boldsymbol{w}$, and the fifth and sixth from $\frac{\partial \boldsymbol{v}}{\partial \boldsymbol{w}}$ being constant. $\mathbb{A}_\mathrm{u} = \frac{\partial \boldsymbol{f}_\mathrm{u}}{\partial \boldsymbol{v}}$ is the Jacobian of $\boldsymbol{f}_\mathrm{u}$, equalling (3.1) without the $\rho^* w_y \mathcal{H}'$ term.

Consider now $\boldsymbol{f}_\mathrm{h}$. We write

$$\llbracket \boldsymbol{f}_\mathrm{h} \rrbracket_\mathrm{L}^\mathrm{R} = \Big(0, w_y \llbracket h \rrbracket_\mathrm{L}^\mathrm{R}\Big)^T = \mathbb{A}_\mathrm{h}(a_{\ell,\mathrm{L}}, a_{\ell,\mathrm{R}})\,\llbracket \boldsymbol{v} \rrbracket_\mathrm{L}^\mathrm{R}\,, \tag{6.4}$$

where

$$\mathbb{A}_\mathrm{h} = \begin{pmatrix} 0 & 0 \\ w_y \llbracket h \rrbracket_\mathrm{L}^\mathrm{R} / \llbracket a_\ell \rrbracket_\mathrm{L}^\mathrm{R} & 0 \end{pmatrix}.$$

Inserting (6.3) and (6.4) into (6.2),

$$\llbracket \boldsymbol{f} \rrbracket_\mathrm{L}^\mathrm{R} = \llbracket \boldsymbol{f}_\mathrm{u} \rrbracket_\mathrm{L}^\mathrm{R} + \llbracket \boldsymbol{f}_\mathrm{h} \rrbracket_\mathrm{L}^\mathrm{R} = (\mathbb{A}_\mathrm{u}(\overline{\boldsymbol{w}}) + \mathbb{A}_\mathrm{h})\,\llbracket \boldsymbol{v} \rrbracket_\mathrm{L}^\mathrm{R}\,,$$

the Roe average matrix

$$\hat{\mathbb{A}} = \mathbb{A}_\mathrm{u}(\overline{\boldsymbol{w}}) + \mathbb{A}_\mathrm{h}(a_{\ell,\mathrm{L}}, a_{\ell,\mathrm{R}}) \tag{6.5}$$

is seen to be the Jacobian (3.1) constructed from average primitive variables $\overline{a_k}$ and $\overline{u_k}$, with $\llbracket h \rrbracket_\mathrm{L}^\mathrm{R} / \llbracket a_\ell \rrbracket_\mathrm{L}^\mathrm{R}$ replacing $\mathcal{H}'$. We use $\mathcal{H}'(\overline{a_\ell})$ close to $\llbracket a_\ell \rrbracket_\mathrm{L}^\mathrm{R} = 0$ to avoid numerical 0/0-issues.

Once $\hat{\mathbb{A}}$ is formulated

$$\boldsymbol{f}(0,t) = \frac{1}{2}\left(\boldsymbol{f}_\mathrm{R} + \boldsymbol{f}_\mathrm{L}\right) - \frac{1}{2}|\hat{\mathbb{A}}|\,\llbracket \boldsymbol{v} \rrbracket_\mathrm{L}^\mathrm{R} \tag{6.6}$$

provides the solution of the linearised problem (6.1). Here,

$$|\hat{\mathbb{A}}| = \hat{\mathbb{L}}^{-1}|\hat{\mathbb{\Lambda}}|\hat{\mathbb{L}}, \quad |\hat{\mathbb{\Lambda}}| = \mathrm{diag}\left(|\hat{\lambda}^+|, |\hat{\lambda}^-|\right), \tag{6.7}$$

with the 'hat' indicating the Roe intermediate state which in (6.5) is the state of arithmetically averaged primitive variables and $\llbracket h \rrbracket_\mathrm{L}^\mathrm{R} / \llbracket a_\ell \rrbracket_\mathrm{L}^\mathrm{R}$ replacing $\mathcal{H}'$.

The solution (6.6) is applied for each cell flux $\boldsymbol{f}_{J-\frac{1}{2}}$ in (5.1) without spatial reconstruction: $\boldsymbol{v}_\mathrm{R} = \boldsymbol{v}_J$, $\boldsymbol{v}_\mathrm{L} = \boldsymbol{v}_{J-1}$. Each time step is chosen $\Delta t^n = \mathcal{C}\,\Delta x / \max_{J,\pm} |\hat{\lambda}^{\pm,n}_{J-\frac{1}{2}}|$. The numerical tests presented herein are never in danger of promoting entropy violations in the Roe scheme, which may happen if an expansion fan straddles the time axis of problem (6.1). See e.g. [13] for entropy corrections.

A relative Roe scheme

The MOCCC of Section 5.4 holds a distinct advantage over fixed-grid methods in that time steps are restricted by a relative characteristic speed rather than an absolute one. There is no reason why this feature cannot also be extended onto the Roe scheme, provided we are willing to adopt a non-fixed grid. Linearising the Riemann problem (6.1) in a *relative* frame now yields a relative Roe matrix

$$|\hat{\mathbb{A}}^\mathrm{r}| = \hat{\mathbb{L}}^{-1}|\hat{\mathbb{\Lambda}}^\mathrm{r}|\hat{\mathbb{L}}, \quad |\hat{\mathbb{\Lambda}}^\mathrm{r}| = \mathrm{diag}\big(|\hat{\lambda}^+| - \dot{x}, |\hat{\lambda}^-| - \dot{x}\big).$$

The translation velocity should either be made uniform, e.g.,

$$\dot{x}^n = \frac{1}{2}\left(\max_J\left\{\hat{\lambda}^{+,n}_{J-\frac{1}{2}}\right\} + \min_J\left\{\hat{\lambda}^{-,n}_{J-\frac{1}{2}}\right\}\right), \tag{6.8}$$

or computed in a way that ensures non-negative cell lengths, for example computed by (5.2) as in the MOCCC.

7. Numerical experiments

Those schemes not based on the finite volume averages, the MOSPC and the MOIPC, are generally not conservative and will slowly lose or gain mass and momentum depending on numerical errors. The loss of momentum is slow enough for the source term to counteract, but changes in the total liquid amount will become noticeable in long running simulations. These errors are suppressed in the linear stability tests of Section 7.2 and roll-wave tests of Section 7.3 by uniformly distributing the phase fraction error during runtime. This is done in the manner $a^n_{\ell,j} := a^n_{\ell,j} + \overline{a^0_{\ell,j}} - \overline{a^n_{\ell,j}}$, bars here indicating the spatial average over the entire pipe.

Simulation results will also be compared with a more basic method to provide a better perspective. The staggered 'donor-cell' or 'upwind' scheme, here abbreviated 'SUW', is still commonly used for the two fluid model [11, 5, 12]. It is formulated on a staggered grid stencil, collecting information from the direction of convection. For completeness, this scheme is presented in Equation (7.1) assuming convection from left to right.

$$a^{n+1}_{\ell,J} = a^n_{\ell,J} - \frac{\Delta t}{\Delta x}\left(a^n_{\ell,J} u^n_{\ell,j+1} - a^n_{\ell,J-1} u^n_{\ell,j}\right), \tag{7.1a}$$

$$\begin{aligned} q^{n+1}_j = q^n_j &- \frac{\Delta t}{\Delta x}\left[\!\!\left[\rho \frac{{u^n_j}^2 - {u^n_{j-1}}^2}{2}\right]\!\!\right]^\ell_\mathrm{g} \\ &- \frac{\Delta t}{\Delta x} w_y \left(h^{n+1}_J - h^{n+1}_{J-1}\right) + \Delta t\, s_q\big(a^{n+1}_{\ell,J}, q^n_j\big). \end{aligned} \tag{7.1b}$$

New area fraction information is used in the momentum equation after first solving the mass equation. This makes the scheme more implicit and numerically stable, but also more diffusive. Alternatively, measures like selecting smaller time steps, using a non-staggered grid, etc. also stabilise the scheme, though all such options increase stability at the cost of increased numerical diffusivity.

This staggered upwind scheme provides less numerical diffusion than its non-staggered equivalent, which in turn is less diffusive than the Lax-Friedrich scheme, results from which are not shown for the sake of briefness.

7.1. Breaking dam

A breaking dam test case here presented as a first test, the results of which are also relatable to surge wave cases and similar. The test case is a Riemann problem with initial conditions $\boldsymbol{v}(x<0,0)=\boldsymbol{v}_{\mathrm{L}}$, $\boldsymbol{v}(x>0,0)=\boldsymbol{v}_{\mathrm{R}}$. Here, $u_{\mathrm{L}}=u_{\mathrm{R}}=0.5\,\mathrm{m/s}$, $\theta=\rho_{\mathrm{g}}=\tau_{\mathrm{g}}=\tau_{\ell}=0$ and channel flow is imposed by temporarily defining $\mathcal{H}=a_{\ell}/d$. The left and right velocities have been chosen high enough for the flow to be supercritical ($\lambda^{+},\lambda^{-}>0$); the upwind scheme appears to be unstable at the shock if the flow is sub-critical (regardless of time step.) Same applies for the non-staggered upwind scheme and the Lax-Friedrich scheme. All Courant numbers equal one.

Consider first the MOSPC. Shocks will, in the MOSPC, manifest as the clustering of characteristic points in space and time. Nodes downstream a shock will progress quicker in time than those upstream, such that the present characteristic of one node eventually crosses an older node path computed many time steps previous. This results is an inversed fan of ambiguous, overlapping states. Figure 7.1a shows such an inversed fan. A shock conditioning routine is imposed on the MOSPC which enables a correct prediction of the shock in the problem – Figure 7.1b. This routine consists of occasionally excluding progressed from the time integration step and removing node pairs whose paths threaten to cross without intersecting.

Figure 7.2 shows the level height at $t=0.05\,\mathrm{s}$ with $\Delta x=0.008\,d$. Most accurate is the MOSPC which, apart from the effect of end state interpolation, has points that follow the analytical solution precisely. As seen from Figure 7.2 and the MOSPC space-time path plot of Figure 7.1b, nodes bifurcate along the rarefaction wave wedge, splitting the left and right states in space. Linear interpolation within the rarefaction wave divide agrees with the analytical solution. The shock is also obtained without dissipation (the two intermediate shock points seen in the figure are from the end state interpolation.)

The other schemes show minor numerical diffusion on the shocks, with the Roe and the MOIPC schemes having the sharpest fronts. All of these schemes have stronger numerical diffusion on the rarefaction wave, except for the MOICC whose rarefaction wave shows an artificial wave formation. This artificial wave is not very sensitive to the choice of Courant number.

7.2. Linear instability

The viscous Kelvin-Helmholtz (VKH) criterion originates from applying linear stability theory to a uniformly stratified steady state solution – see e.g., [1]. The theory predicts flow *instability*, with growing waves, *if*

$$w_y\mathcal{H}'-\left(\rho\,(U-C_{\mathrm{crit}})^2\right)^{*}<0, \tag{7.2a}$$

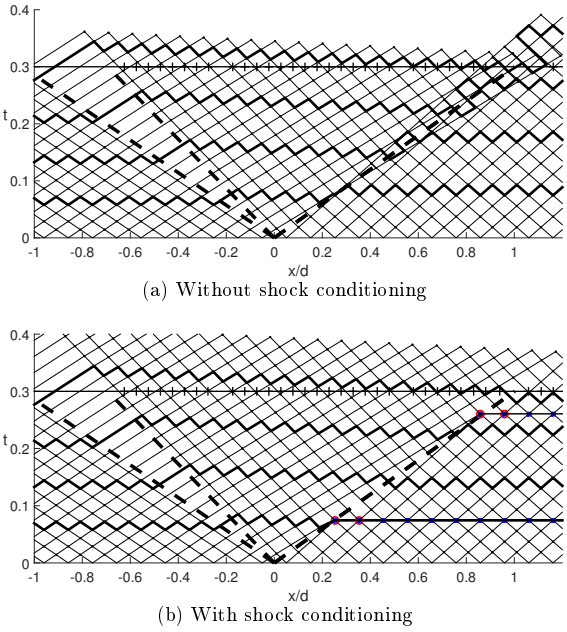

(a) Without shock conditioning

(b) With shock conditioning

Figure 7.1: MOSPC node path in the breaking dam test case. Initial conditions $u_{\mathrm{L}}=u_{\mathrm{R}}=0\,\mathrm{m/s}$ are here used for better visualization, otherwise cf. Figure 7.2.

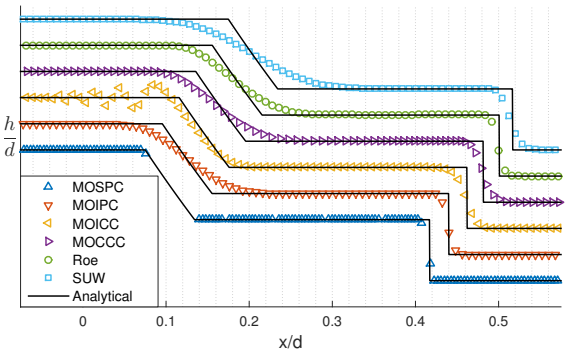

Figure 7.2: The breaking dam test case with initial conditions $u_{\mathrm{L}}=u_{\mathrm{R}}=0.5\,\mathrm{m/s}$, $h_{\mathrm{L}}=.115/d$, $h_{\mathrm{R}}=.085/d$. Level height/phase fraction at $t=0.05\,\mathrm{s}$.

where the critical wave celerity is

$$C_{\text{crit}} = \frac{\frac{\partial S}{\partial a_\ell}}{\frac{\partial S}{\partial (au)_{\text{g}}} - \frac{\partial S}{\partial (au)_\ell}}. \tag{7.2b}$$

Upper-case symbols here indicate a steady state. For a flow state to remain steady it must satisfy the so-called *holdup equation*

$$S(A_k, U_k) = 0. \tag{7.2c}$$

At the limit of marginal stability one can show from (7.2a) and (3.3) that the characteristic velocities are $\lambda^+_{\text{crit}} = C_{\text{crit}}$ and $\lambda^-_{\text{crit}} = 2\left(\frac{(\rho u)^*}{\rho^*} - C_{\text{crit}}\right) < C_{\text{crit}}$, i.e., the viscous Kelvin-Helmholtz criterion corresponds to a state where the flow turns hydraulically critical (all information moves in one direction) relative to the disturbance wave. The supercritical flow will in turn have to develop into a shock relative to the disturbance wave, telling us that the roll-wave regime will ensue if the pipe cross section is not breached first or strong surface tension effects are present. The +-waves distributes the information relative to the disturbance and dominates in the wave evolution.

liquid density	ρ_ℓ	998	kg/m^3
gas density	ρ_{g}	50	kg/m^3
liquid dynamic viscosity	μ_ℓ	1.61E-5	Pa s
gas dynamic viscosity	μ_{g}	1.00E-3	Pa s
internal pipe diameter	d	0.1	m
wall roughness		2E-5	m
Pipe inclination	θ	1°	–
Mean level height	$\overline{h}$	0.02	m

Table 1: Fixed parameters.

Fixed fluid and pipe properties are in the following tests the same as in [10] for upwards-directed flow, presented in Table 1. With these parameters, (7.2) predicts that the stratified flow will turn unstable at $Q_{\text{m,crit}}/A = 3.153\,\text{m/s}$.

Figure 7.3 shows the observed values of the critical superficial velocity $Q_{\text{m,crit}}/A$ at which wave growth is observed in a simulation. These values may be compared to the value from linear stability theory, labeled 'Analytical' in the figure. A disturbance of the order 1E-7 relative to the state variables were imposed on all simulations. The longest wavelength, spanning the entire simulation domain, is most resistant to numerical diffusion; simulations at the critical limit always grew into this wave, regardless of the disturbance. A Courant number $\mathcal{C} = 0.95$, based broadly on the observed stability behaviour, is applied for all finite volume-type schemes. The MOSPC has no Courant number as the time steps are locally chosen exactly according to the information path. A Courant number equalling 0.999 was used in the MOIPC.

The pure characteristic methods, the MOSPC and the MOIPC, show very precise stability predictions for all tested resolutions. The MOICC, MOCCC and Roe schemes also show accurate predictions, whereas the staggered upwind scheme is dominated by numerical diffusion for the low-resolution simulations and fail to become unstable altogether in the 16 grid cell simulation. A central feature of this test is that the error in $Q_{\text{m,crit}}$ is strongly dependent upon the choice of Courant number. Because the unperturbed flow is uniform this means that all information collected from the λ^+-paths reach an older node directly, i.e., $\hat{\boldsymbol{v}}^n_{j+} = \hat{\boldsymbol{v}}^n_{j-1}$. The +-paths dominate in the wave evolution and so the MOIPC performs nearly as perfectly as the MOSPC in this test.

The results of the other schemes seems very dependent upon the Courant number, approaching the analytical solution as $\mathcal{C}$ nears unity. It seems therefore that the property of a method to remain stable at high Courant numbers is strongly desirable in capturing wave instabilities. Finite volume schemes, excluding the staggered upwind scheme, where here all given the same Courant number of 0.95 based on an overall consideration of stability. The main disadvantage of the staggered upwind scheme in this respect is that the time step limit is only estimated based on convective phase speeds rather than the characteristic speeds.

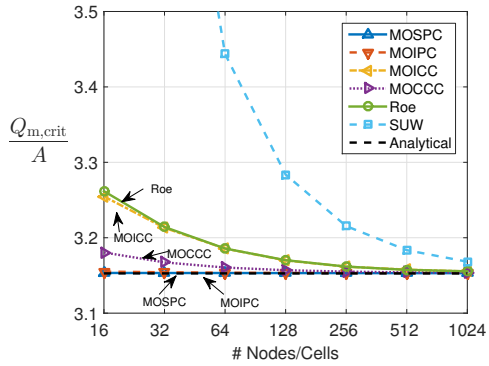

Figure 7.3: Observed critical mixture velocity $\mathcal{Q}_{\text{m,crit}}/\mathcal{A}$ wave growth in discrete model representations. Analytical solution from linear stability theory, Equations (7.2).

7.3. Roll-wave

Steady-state roll-wave predictions are presented in this section. The same flow parameters and Courant numbers are used here as in the linear stability test case of the previous section (Table 1.) A higher mixture flow rate $\mathcal{Q}_{\text{m}}/A = 3.4\,\text{m/s}$ drives the wave regime. A small, single-period sinusoidal wave is used as initial condition and each simulation is run until a steady state is reached. (The term 'steady state' refers here to flows which are time independent in a particular moving frame.) These predicted profiles may be compared to the analytical, numerically

integrated profile solution of Watson [22], labeled 'Analytical' in the plots. The wave celerity c of this solution equals the wave front shock velocity and is obtained from the Rankine-Hugoniot condition that a shock inveriant

$$\left[\!\left[\rho(u-c)^2/2\right]\!\right]_{\mathrm{g}}^{\ell} + w_y h \Big]\!\Big]_{\mathrm{L}}^{\mathrm{R}} = 0 \tag{7.3}$$

should be maintained across the discontinuity.[2] In this case, the value is $c = 1.4408\,\mathrm{m/s}$. Figure 7.4 shows the predicted wave profiles in terms of level height for 128 nodes/grid cells. Wave celerity plots and wave height plots are presented in Figure 7.5 as functions of the node/cell number with a 2-based logarithmic abscissa. Displayed Δh wave height values are the temporal averages $\langle \max_J\{h_J^n\} - \min_J\{h_J^n\}\rangle$ over a number of time steps after the respective waves reached a steady state. Likewise, the wave celerity values are similar time set averages $\left\langle \left(x^{n+1}_{J^{n+1}_{\max}} - x^n_{J^n_{\max}}\right)/\Delta t^n \right\rangle$, $J^n_{\max}$ being the cell index whose liquid fraction is greatest at time level n.

The Roe scheme is seed to predict the wave celerity very well for 64 grid cells and more. This is to be expected as the Roe scheme is a linearised Riemann solver.

The conservative characteristic methods, the MOICC and MOCCC, are also seen to converge to the same celerity solution, though somewhat more slowly. Simulations turn numerically unstable with the MOICC at 32 grid cells; a Courant number of 0.95 does not appear to stabilise the MOICC scheme sufficiently in this case.

The MOIPC does not appear to converge towards the correct wave celerity. This is attributable to the methods' lack of conservation, particularly across the shock, where the shock invariant (7.3) should be maintained. (Continuity is indirectly assumed in the integration step (3.6)-(3.8).)

The MOSPC also lacks the conservation property. In addition, the steady state solutions of the MOSPC seems dependent upon whatever numerical trickery is applied for the shock conditioning. Lacking a well-defined routine yielding consistent roll-wave results, the MOSPC has been excluded from Figure 7.5.

7.4. Time steps

Finally, the method efficiencies in terms of them steps are considered. Table 2 shows average time steps relative to the cell lengths, where the average time step $\langle \Delta t \rangle$ is the arithmetic average of $\{\Delta t^n\}$ and $\langle \Delta x \rangle$ is the domain length divided by the number of cells or nodes. The values of $\langle \Delta t \rangle / \langle \Delta x \rangle$ were largely independent of the number of cells/nodes. Where a slight dependency is present (foremost in the MOCCC) the table shows the 128 cell simulation value. It is seen that the MOCCC has about 4.6 times longer time steps that its fixed-grid counterparts

[2] This can be seen from integrating (2.4) in a relative frame thinly over the shock. All but the relative fluxes disappear.

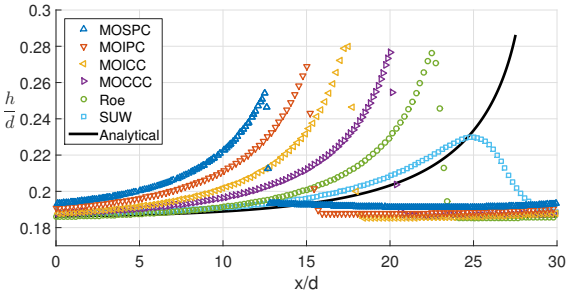

Figure 7.4: Single wave simulations, steady state, 128 nodes/grid cells. $\mathcal{Q}_{\mathrm{m}}/\mathcal{A} = 3.4\,\mathrm{m/s}$ and the parameters in Table 1.

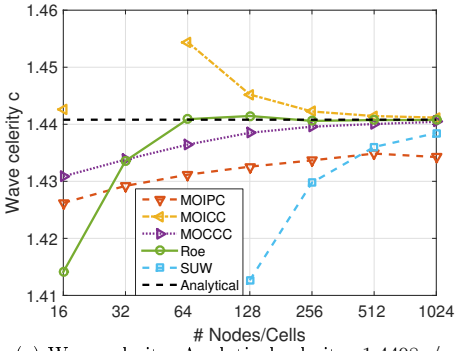

(a) Wave celerity. Analytical celerity: $1.4408\,\mathrm{m/s}$

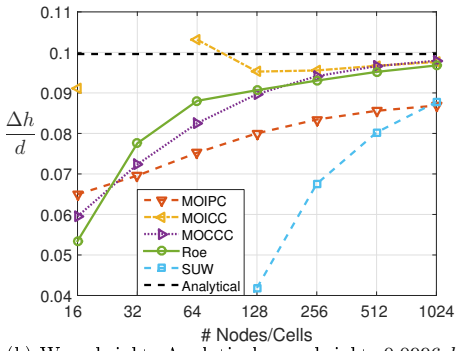

(b) Wave height. Analytical wave height: $0.0996\,d$

Figure 7.5: Single wave simulation. $\mathcal{Q}_{\mathrm{m}}/\mathcal{A} = 3.4\,\mathrm{m/s}$ and the parameters in Table 1.

	VKH	roll-wave
MOSPC	1.85	–
MOIPC	0.80	0.66
MOICC	0.76	0.62
MOCCC	3.46	2.01
Roe	0.76	0.62
SUW	0.53	0.44

Table 2: $\langle \Delta t \rangle / \langle \Delta x \rangle$: Measured mean time step relative to the mean cell length [s/m]. 'VKH' refers to the viscous Kelvin-Helmholtz tests of Section 7.2 and 'roll-wave' to the tests of Section 7.3.

in the plane stratified case and 3.2 times in the roll-wave case. The time step advantage is less in the roll-wave case as the range of characteristic velocities is grater.

Formulating the Roe scheme in a dynamic frame, as described at the end of Section 6, provides the Roe scheme with time steps similar to those presented for the MOCCC in Table 2. Whether cell border velocities were computed from (5.2) or (6.8) did not make a significant difference on the time step length. It was however found that the relative Roe scheme was somewhat less numerically stable in some cases, compared with the fixed-grid version and the MOCCC, requiring a smaller Courant number.

8. Discussion

One of the main arguments for resorting to characteristic methods is to detect the onset of hydrodynamic instability without suffering from artificial flow stabilisation from numerical diffusion. It would however appear that the numerical diffusion from the Roe scheme, with a Courant number close to unity, is small, at least compared with the staggered upwind schemes, whose effect on wave growth predictions is already well documented [12, 14, 11]. The Roe method has the additional advantage of being a Riemann solver, whereas continuity is implicitly assumed in the path integration of the method of characteristics. It is therefore expected that the Roe method provides better wave celerity predictions. Some may also argue that the introduction of a control volume averaging in the hybridisations (the MOICC and the MOCCC) makes these more finite volume method than MOC in nature.

The MOSPC sometimes predict two-wave solutions of the same problem depending on numerical settings, such as the number of nodes and iterations on the intermediate states. A two-wave solution was on occasion also observed with the MOIPC if no interpolation was made on the intermediate integrand ($\hat{\phi}^{n+\frac{1}{2}}_{j\pm} = \hat{\phi}^{n}_{j}$.) It is a fact that there exists a family of steady wave solutions satisfying (2.4) [22, 8]. Which of the possible wave solutions will be realised is thought to be a question of wave stability and the initial state; we cannot make any direct decree about which solution is more correct. Investigations into the stability of similar families of wave solutions have been made by, e.g., Tougou [19]. In this context it is prudent to point out that numerical diffusion prompts wave coalescence and that the shock condition (7.3) is a central component in the stability of roll-wave solutions.

9. Conclusions

Methods from the literature (MOSPC, MOIPC and Roe's method) have been adopted to the incompressible two-fluid model for pipe flows. In addition, hybrids of the characteristic and finite volume methods (MOICC and MOCCC) have been proposed to achieve conservation. The method of scattered point characteristics (MOSPC) is excellent for predicting the onset of viscous linear instability, even when the numerical resolution is poor. However, the method in this unrestricted form is poorly suited for the non-linear wave regime which follows. Better at handling the roll-wave regime are methods where nodes do not scatter and collide (MOIPC) and schemes which are conservative (MOICC, MOCCC and the finite volume methods.) Only the numerically conservative methods were observed to converge towards a correct roll-wave solution. The Roe solver is designed for shock discontinuities and shows both better accuracy and stability in the presence of wave fronts. Though outperformed by characteristic methods, these finite volume methods also predict the onset of viscous linear instability very well, even when poorly resolved, if allowed a CFL-number close to unity.

Method efficiency can be greatly enhanced if one allows for a dynamic grid arrangement, such that grid cells follow the main convective drift in characteristic information. This seems a very natural part of characteristic methods, also enhancing the numerical stability and eliminating the need for interpolation. The feature is however also easily expendable to other finite volume methods.

On the whole, the Roe and the conservative versions of the MOC seem to yield results of similar quality. The characteristic methods show and advantage in the linear wave regime and the Roe scheme shows an advantage in the non-linear one. The Roe scheme also has the advantage that it can adopt, but does not require, a dynamic grid formulation.

Acknowledgements

This work is financed by The Norwegian University of Science and Technology (NTNU) as a contribution the Multiphase Flow Assurance programme (FACE.) The author would like to thank Tore Flatten for his very useful feedback and Kontorbamse for the comforting support.

Nomenclature

Latin symbols

$\mathcal{A}$	Cross-sectional area (parameter)	m^2
a_k	Cross-sectional area occupied by phase k	m^2

$\mathbb{A}$	Jacobian of $\boldsymbol{f}$, Eq. (3.1)	
$\hat{\mathbb{A}}$	Roe-averaged matrix	
c	Wave celerity	$\mathrm{m\,s^{-1}}$
$\mathcal{C}$	Courant number	–
d	Diameter (parameter)	m
$\boldsymbol{f}$	Fluxes	
g	Gravitational acceleration (parameter)	$\mathrm{m\,s^{-1}}$
$h, \mathcal{H}$	Height of the interface in the pipe cross section	m
q	$q = [\![\rho u]\!]_{\mathrm{g}}^{\ell}$	$\mathrm{m^3\,s^{-1}}$
$\mathcal{Q}_{\mathrm{m}}$	Mixture flow rate (parameter)	$\mathrm{m^3\,s^{-1}}$
s	Source	
t	Time	
u	Fluid velocity	$\mathrm{m\,s^{-1}}$
$\boldsymbol{v}$	Conservative variables; $\boldsymbol{v} = (a_\ell, q)^T$	
$\boldsymbol{w}$	Net specific weight: $\boldsymbol{w} = -[\![\rho]\!]_{\mathrm{g}}^{\ell}\,\boldsymbol{g}$ (parameter)	$\mathrm{kg\,m^{-2}\,s^{-2}}$
x	Spatial position	
$\dot{x}$	Control volume border velocity	$\mathrm{m\,s^{-1}}$

Greek Symbols

θ	Pipe inclination, positive above datum (parameter)	–
κ	Eq. (3.2)	$\mathrm{kg\,m^{-4}\,s^{-1}}$
$\lambda^{\pm}$	Eigenvalues	$\mathrm{m\,s^{-1}}$
ρ	Density (parameter)	$\mathrm{kg\,m^{-3}}$
σ	Perimeter length	m
τ	Skin friction	$\mathrm{kg\,m^{-1}\,s^{-2}}$
ϕ	Dummy variable	

Sub- and superscripts

*	$\phi^* = \frac{\phi_\ell}{A_\ell} + \frac{\phi_{\mathrm{g}}}{A_{\mathrm{g}}}$
g	Gas
j/J	Node/cell index
$j_\pm$	Indicating $\pm$-path leading to node j
k	Generic phase: $k \in \{\mathrm{g}, \ell\}$
ℓ	Liquid
L	Left shock limit
(n)	Time iteration
R	Right shock limit

Encasements

$[\![\cdot]\!]_{\mathrm{L}}^{\mathrm{R}}$	$(\cdot)_{\mathrm{R}} - (\cdot)_{\mathrm{L}}$
$[\![\cdot]\!]_{\mathrm{g}}^{\ell}$	$(\cdot)_{\ell} - (\cdot)_{\mathrm{g}}$
$\overline{\phi}$	Spatial average – Eq. (4.2a)
$\langle\phi\rangle$	Temporal average – Eq. (4.2b)
$\hat{\phi}$	Indicating MOC variable

Abbreviations

MOC Method of characteristics
MOCCC Method of cell centred characteristics; Sec. 5.4
MOICC Method of interpolated cell characteristics; Sec. 5.3
MOIPC Method of interpolated point characteristics; Sec. 5.2
MOSIC Method of scattered point characteristics; Sec. 5.1
SUW Staggered upwind method; Sec. 7

[1] D. Barnea and Y. Taitel. Interfacial and structural stability of separated flow. *International Journal of Multiphase Flow*, 20 (supplissue):387 – 414, 1994/08/. ISSN 0301-9322. URL http://dx.doi.org/10.1016/0301-9322(94)90078-7.

[2] Dvora Barnea and Yehuda Taitel. Non-linear interfacial instability of separated flow. *Chemical Engineering Science*, 49(14): 2341 – 2349, 1994. ISSN 00092509. URL http://dx.doi.org/10.1016/0009-2509(94)E0047-T.

[3] D. Biberg. A mathematical model for two-phase stratified turbulent duct flow. *Multiphase Science and Technology*, 19(1):1 – 48, 2007. ISSN 0276-1459. URL http://dx.doi.org/10.1615/MultScienTechn.v19.i1.10.

[4] Dag Biberg. An explicit approximation for the wetted angle in two-phase stratified pipe flow. *Canadian Journal of Chemical Engineering*, 77(6):1221 – 1224, 1999. ISSN 00084034.

[5] M. Bonizzi, P. Andreussi, and S. Banerjee. Flow regime independent, high resolution multi-field modelling of near-horizontal gas-liquid flows in pipelines. *International Journal of Multiphase Flow*, 35(1):34 – 46, 2009. ISSN 03019322. URL http://dx.doi.org/10.1016/j.ijmultiphaseflow.2008.09.001.

[6] E. Bournaski. Numerical simulation of unsteady multiphase pipeline flow with virtual mass effect. *International Journal for Numerical Methods in Engineering*, 34(3):727 – 740, 1992. ISSN 00295981.

[7] C. J. Crowley, G. B. Wallis, and J. J. Barry. Validation of a one-dimensional wave model for the stratified-to-slug flow regime transition, with consequences for wave growth and slug frequency. *International Journal of Multiphase Flow*, 18(2):249 – 271, 1992. ISSN 03019322. URL http://dx.doi.org/10.1016/0301-9322(92)90087-W.

[8] R.F. Dressler. Mathematical solution of the problem of roll-waves in inclined open channels. *Communications on Pure and Applied Mathematics*, 2:149 – 194, 1949/06/. URL http://dx.doi.org/10.1002/cpa.3160020203.

[9] T. Flatten and T.S. Munkejord. The approximate riemann solver of roe applied to a drift-flux two-phase flow model. *Mathematical Modelling and Numerical Analysis*, 40(4):735 – 64, 2006/07/. ISSN 0764-583X. URL http://dx.doi.org/10.1051/m2an:2006032.

[10] H. Holmås. Numerical simulation of transient roll-waves in two-phase pipe flow. *Chemical Engineering Science*, 65(5):1811 – 25, 2010/03/01. ISSN 0009-2509. URL http://dx.doi.org/10.1016/j.ces.2009.11.031.

[11] R.I. Issa and M.H.W. Kempf. Simulation of slug flow in horizontal and nearly horizontal pipes with the two-fluid model. *International Journal of Multiphase Flow*, 29(1):69 – 95, 2003/01/. ISSN 0301-9322. URL http://dx.doi.org/10.1016/S0301-9322(02)00127-1.

[12] T.K. Kjeldby, R.A.W.M. Henkes, and O.J. Nydal. Lagrangian slug flow modeling and sensitivity on hydrodynamic slug initiation methods in a severe slugging case. *International Journal of Multiphase Flow*, 53:29 – 39, 2013. ISSN 0301-9322. doi: http://dx.doi.org/10.1016/j.ijmultiphaseflow.2013.01.002. URL http://www.sciencedirect.com/science/article/pii/S0301932213000165.

[13] Randall J LeVeque. *Finite volume methods for hyperbolic problems*, volume 31. Cambridge university press, 2002.

[14] Jun Liao, Renwei Mei, and James F. Klausner. A study on the numerical stability of the two-fluid model near ill-posedness. *International Journal of Multiphase Flow*, 34(11):1067 – 1087, 2008. ISSN 03019322. URL http://dx.doi.org/10.1016/j.ijmultiphaseflow.2008.02.010.

[15] P. L. Roe. Approximate riemann solvers, parameter vectors, and difference schemes. *Journal of Computational Physics*, 135 (2):250 – 250, 1997. ISSN 00219991. URL http://dx.doi.org/10.1006/jcph.1997.5705.

[16] V.L. Streeter. Waterhammer analysis of pipelines. *ASCE – Proceedings – Journal of the Hydraulics Division*, 90(HY4, Part 1):151 – 172, 1964.

[17] V.L. Streeter. Unsteady flow calculations by numerical methods. *Transactions of the ASME. Series D, Journal of Basic*

Engineering, 94(2):457 – 66, 1972/06/. ISSN 0021-9223. URL http://dx.doi.org/10.1115/1.3425444.

[18] K. Suwan and A. Anderson. Method of lines applied to hyperbolic fluid transient equations. *International Journal for Numerical Methods in Engineering*, 33(7):1501 – 1511, 1992. ISSN 00295981.

[19] H. Tougou. Stability of turbulent roll-waves in an inclined open channel. *Journal of the Physical Society of Japan*, 48(3):1018 – 23, 1980/03/. ISSN 0031-9015. URL http://dx.doi.org/10.1143/JPSJ.48.1018.

[20] I. Toumi. A weak formulation of roe's approximation riemann solver. *Journal of Computational Physics*, 102(2):360 – 73, 1992/10/. ISSN 0021-9991. URL http://dx.doi.org/10.1016/0021-9991(92)90378-C.

[21] I. Toumi and A. Kumbaro. An approximate linearized riemann solver for a two-fluid model. *Journal of Computational Physics*, 124(2):286 – 300, 1996/03/15. ISSN 0021-9991. URL http://dx.doi.org/10.1006/jcph.1996.0060.

[22] M. Watson. Wavy stratified flow and the transition to slug flow. In C.P. Fairhurst, editor, *Multi-phase Flow – Proceedings of the 4th International Conference*, pages 495–512, Cranfield, UK, 1989.

PAPER IV

The Stability of Roll-Waves in Two-Phase Pipe Flow

Andreas H. Akselsen

Under review in
The International Journal of Multiphase Flow

The Stability of Roll-Waves in Two-Phase Pipe Flow

A.H. Akselsen*

Department of Energy and Process Engineering, Norwegian University of Science and Technology, Kolbjørn Hejes v. 1B, 7491 Trondheim, Norway

Abstract

Roll-wave trains constitutes a well-known two-phase flow regime in pipes. There exists a one-parameter family of steady roll-wave train solutions, provided the flow conditions are within the roll-wave range. This means that wave train solutions can be constructed from out of a wide range of wavelengths. That band of wavelengths which will be observed in nature is however fairly narrow. The wavelength distribution is believed to be related to wave train stability and the flow disturbances.

Steady roll-wave train solutions are in this article subjected to a linear stability analysis. Comparisons are made with predictions from direct numerical Roe scheme simulations. Good agreement is observed; after an initial stage of wave coalescence, simulated wavelengths are distributed among the shorter of those wavelengths which are predicted linearly stable. Also the observed disturbance frequency and rate of decay agrees with the analysis predictions. Finally, the stability of pressure driven gas-liquid trains is compared to that of gravity driven free surface trains.

Keywords: roll-waves; stability; two-phase; pipe flow; two-fluid model

1. Introduction

Roll-waves trains consist of a series of exponentially profiled wave structures, often called 'bores', connected by hydraulic jumps. Thomas [14] was amongst the first to publish analytical expressions for the roll-wave profiles of channel flows using a moving belt analogy. He also provided insight into the conditional nature of roll-waves, in particular into the necessity of friction.

Dressler [6] went on to formalise these solutions, also providing continuous wave solutions to the corresponding viscous problem. He found that an entropically valid one-parameter family of roll-wave solutions exists with the specification of channel slope, resistance and wave speed. A solution is unique if also the wavelength is specified. This theory does however not explain why wave trains in nature are observed to consist of a relatively narrow band of wavelengths.

Richard and Gavrilyuk [11] extended Dressler's roll-wave solutions to account for turbulent shear and dissipation. Reynolds' stresses are related to enstrophy in the wave, providing wave-breaking as a model extension. Very good agreement was found with the experimental data of Brock's [4], appropriately breaking off the sharp wave tip of the Dressler solutions.

Tougou and Tamada addressed the issue of roll-wave train stability in channel flow. Both laminar [13] and turbulent [15] flows were considered. Their linear stability analysis indicated that wavelengths observed in nature will be those of greatest linear stability. Balmforth and Mandre [1] also performed a stability analyses for shallow water roll-waves using a somewhat different technique.

Miya et. al. [10] derived at profile solutions similar to those of Dressler for gas-liquid duct flows, also including shape factors for the velocity profiles. Watson [16] in turn formulated such solutions for gas-liquid flow in pipes. This model had a form similar to that for channel flows, but with a geometrical complexity making it unsuited for analytical integration. Algebraically explicit profile solutions are therefore unavailable for pipe flows. The increased complexity of the equations also made solution uniqueness difficult to prove; this was instead assumed.

Comparisons between roll-wave experiments and predictions from finely resolved numerical representations have been made by multiple authors. For instance, in the work of Brook et. al. [5] the solutions of Dressler is compared to roll-wave simulation results of the shallow water equations using a second order Godunov method. Holmås [7] compared a 'pseudospectral' representation (using fast Fourier transformation) of the incompressible two-fluid pipe flow model with Johnson's experiments [8]. The Biberg model [3] for pre-integrated turbulent shear and velocity profiles was here incorporated with an extension to the interfacial turbulence closure to account for the effect of wave-breaking.

A stability analysis similar to those given by Tougou and Tamada will here be applied to Watson's model for roll-waves in two-phase pipe flows. Emphasis is placed on the stability of pressure propelled flows as opposed to

*Corresponding author
Email address: andreas.h.akselsen@ntnu.no (A.H. Akselsen)

gravity driven flows. Stability predictions are compared to finely resolved numerical Roe scheme simulations.

2. The Two-Fluid Model for Pipe Flow

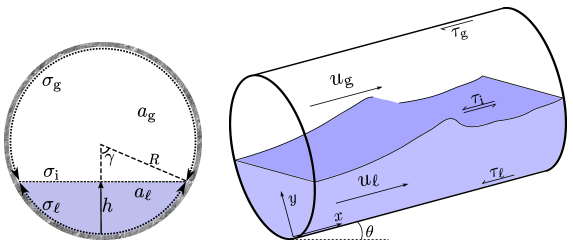

Figure 2.1: Pipe cross-section

Figure 2.1 illustrate the pipe geometry and some of the quantities appearing the two-fluid model. The circular pipe geometry itself enters into the modelling through the relation between the level height h, the specific areas a_k and the peripheral lengths σ_k and σ_i. These are algebraically interchangeable:

$$h = \mathcal{H}(a_\ell). \tag{2.1}$$

The inverse of the geometric function $\mathcal{H}$ can be explicitly expressed as

$$a_\ell = \mathcal{H}^{-1}(h) = R^2\left(\gamma - {}^1\!/_2 \sin 2\gamma\right), \quad \gamma = \arccos\left(1 - \frac{h}{R}\right).$$

R is here the pipe inner radius and γ the interface half-angle. The perimeter lengths are

$$\sigma_\ell = 2R\gamma, \qquad \sigma_g = 2R\left(\pi - \gamma\right), \qquad \sigma_i = 2R\sin\gamma.$$

The compressible, isothermal, four-equation two-fluid model for stratified pipe flow results from an averaging of the conservation equations across the cross sectional area. Field k, occupied by either gas, $k = g$, or liquid, $k = \ell$, is segregated from the other field. The model is commonly written

$$\begin{aligned}
&(\rho_k \tilde{a}_k)_t + (\rho_k \tilde{a}_k \tilde{u}_k)_x = 0,\\
&(\rho_k \tilde{a}_k \tilde{u}_k)_t + \left(\rho_k \tilde{a}_k \tilde{u}_k^2\right)_x + \tilde{a}_k \tilde{p}_{i,x} + \rho_k g \cos\theta\, \tilde{a}_k \tilde{h}_x = \tilde{s}_k.
\end{aligned}$$

Tildes have here been added to distinguish functions of the fixed frame coordinate x. p_i is the pressure at the interface, assumed the same for each phase as surface tension is neglected. h is the height of the interface from the pipe floor, and the term in which it appears originates from approximating a hydrostatic wall-normal pressure distribution within each field. a_k is the cross-section area within field k, and u_k and ρ_k are the mean fluid velocity and density in these fields. The momentum sources are $s_k = \tau_k \sigma_k \pm \tau_i \sigma_i / - a_k \rho_k g \sin\theta$, where τ is the skin frictions at the walls and interface, θ is the pipe inclination, positive above datum, and g is the gravitational acceleration.

Both fluids flows are from here assumed incompressible. This allows for the system to be represented on conservative form.[1] Reducing the momentum equations with their respective mass equations and eliminating the pressure term between them yields

$$\tilde{\boldsymbol{v}}_t + \tilde{\boldsymbol{f}}_x = \tilde{\boldsymbol{s}}, \tag{2.2}$$

with components

$$\boldsymbol{v} = \left(a_\ell, [\rho u]_g^\ell\right)^T, \qquad \boldsymbol{f} = (q_\ell, j)^T, \qquad \boldsymbol{s} = (0, s)^T.$$

Symbols for the flux and source components have here been defined and are

$$\begin{aligned}
q_k &= a_k u_k, \qquad j = \left[\rho u^2/2\right]_g^\ell + w_y h,\\
s &= -w_x - [\tau\sigma/a]_g^\ell + \tau_i \sigma_i \left(1/a_\ell + 1/a_g\right).
\end{aligned}$$

The shorthand

$$[\cdot]_g^\ell = (\cdot)_\ell - (\cdot)_g$$

is useful throughout. Constant weight parameters have been grouped into $w_x = [\rho]_g^\ell\, g \sin\theta$ and $w_y = [\rho]_g^\ell\, g \cos\theta$. Although really derivatives therefrom, these equations are here simply referred to as base mass and momentum equations.

The identities

$$a_\ell + a_g = \mathcal{A}, \qquad q_\ell + q_g = \mathcal{Q}, \tag{2.3}$$

where the latter conditions has been obtained from summing the mass equation over the two phases, finally close the base model. Both $\mathcal{A}$ and $\mathcal{Q}$ are parametric – the former may be made to vary in space according to the geometry and the latter in time according to the mixture rate imposed upon the system.

3. The Steady Roll-Wave Solutions

The profile equation is obtained by searching for system solutions which are steady within a moving reference frame. A chance in spatial coordinates $x \to \xi = x - Ct$ is performed, C being a constant translation velocity equal to the wave celerity. The base model (2.2) with the new relative variables $\psi(\xi, t) = \tilde{\psi}(x, t)$ then reads

$$\boldsymbol{v}_t + \boldsymbol{f}_{r,\xi} = \boldsymbol{s} \tag{3.1}$$

The coordinate transformation brings about a new term which has been absorbed into the convection term. Its net effect is to make convection flux velocities relative to ξ, i.e.

$$u_{k,r} = u_k - C.$$

[1] It is sufficient for one of the fluids to be incompressible and the other to have a negligible level height term for this to be possible.

$\boldsymbol{f}_\mathrm{r} = (q_{\ell,\mathrm{r}}, j_\mathrm{r})^T$ are the fluxes with $u_{\mathrm{k,r}}$ replacing u_k.

Profiles

Denoting the properties of steady profile solutions with upper-case symbols, the profile equation is obtained by substituting $\psi(\xi,t) \to \Psi(\xi)$ in (3.1). As the transient term drops out the mass equation component and (2.3) reviles

$$Q_{k,\mathrm{r}} = A_k U_{k,\mathrm{r}} = \text{const.}. \tag{3.2}$$

Regarding Q_r, J_r and S as functions of A_ℓ subjected to (3.2), the chain rule applied to the momentum equation component of (3.1) yields the profile equation

$$A_{\ell,\xi} = \frac{S(A_\ell)}{J'_\mathrm{r}(A_\ell)}. \tag{3.3}$$

The numerator is

$$J'_\mathrm{r} \equiv \frac{\mathrm{d}J_\mathrm{r}}{\mathrm{d}A_\ell} = w_y \mathcal{H}' - \left(\rho\, U_\mathrm{r}^2\right)^*$$

with $\mathcal{H}' = \frac{\mathrm{d}\mathcal{H}}{\mathrm{d}A_\ell}$. Another useful operator

$$\psi^* = \frac{\psi_\ell}{A_\ell} + \frac{\psi_\mathrm{g}}{A_\mathrm{g}}$$

has here been introduced.

A transition from subcritical flow, ($\mathrm{sign}(\lambda^-) \neq \mathrm{sign}(\lambda^+)$) to supercritical flow ($\mathrm{sign}(\lambda^-) = \mathrm{sign}(\lambda^+)$) is necessary for the formation of periodic hydraulic jumps. In fact, the root of the fast characteristic λ^+ (see (A.9)) coincides with the root of J'_r in what is known as the 'critical point' $A_{\ell,0}$. For a steady state to be possible, and (3.3) to be integrable, C must be such that also S has a root at the critical point $A_{\ell,0}$, that is $C:\ J'_\mathrm{r}(A_{\ell,0};C) = S(A_{\ell,0};C) = 0$. Supercritical flow is found in the range $A_\ell < A_{\ell,0}$ and subcritical in the range $A_\ell > A_{\ell,0}$. Profile solutions are obtained by numerically integrating (3.3) inversed, i.e., $\xi = \int J'_\mathrm{r}/S\,\mathrm{d}A_\ell$.

Shocks

Entropically valid solutions of (3.3) are monotone, but periodic wave trains are possible by piecewise connecting profile solutions through shocks. Integrating the conservation equations (3.1) thinly over a shock front reviles that $q_{\ell,\mathrm{r}}$ and j_r are shock invariants, i.e.

$$[\boldsymbol{f}_\mathrm{r}]_-^+ = \boldsymbol{0}, \tag{3.4}$$

where the '+' and '−' respectively constitutes the right and left limits of a shock front. $\psi_\pm = \psi(\xi_\pm)$ and $[\cdot]_-^+ = (\cdot)_+ - (\cdot)_-$. The first shock condition component is trivially achieved in the steady wave train by virtue of (3.2), while the momentum flux shock condition reads

$$\left[\tfrac{1}{2}\left[\rho\, U_\mathrm{r}^2\right]_\mathrm{g}^\ell + w_y\, H\right]_-^+ = 0. \tag{3.5}$$

Wave profiles are assumed identical along the wave train. The wave profile is therefore repeating such that for any integer n we have $\Psi(\xi + n\lambda) = \Psi(\xi)$, λ being the wavelength (not to be confused with the characteristics $\lambda^\pm$.) The left and right limit states are therefore the states at the tip and tail of the same profile solution. Condition (3.5) links these states. Figure 3.1 shows a schematic.

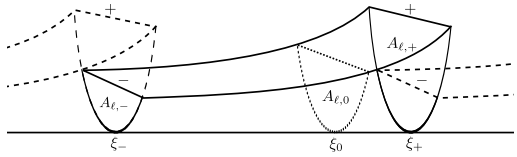

Figure 3.1: Illustration of the steady wave solution.

For a set of fluid and geometry parameters, equations (2.3), (3.3) and (3.4) generate a one-parameter family of wave train solutions.

4. The Linear Stability of Roll-Wave Trains

The procedure adopted for analysing the linear stability of the steady roll-wave trains is inspired by Tougou and Tamada [15, 13], and Balmforth and Mandre [1].

The Disturbace Function

Perturbations are imposed on the steady state:

$$\psi(\xi,t) = \Psi(\xi) + \hat{\psi} e^{\omega t}, \qquad \psi \in \{a_k, u_k, \varepsilon\} \tag{4.1}$$

where the *pulsation* ω is a (complex) constant. A disturbance function $\hat{f}(\xi)$ is then introduced and defined by

$$\hat{a}_\ell = \hat{f}_\xi. \tag{4.2a}$$

Inserting these definitions into the mass equation component of (3.1) and integrating once yields

$$\hat{u}_\ell = -\frac{\omega \hat{f} + \hat{f}_\xi\, U_{\ell,\mathrm{r}}}{A_\ell}. \tag{4.2b}$$

An arbitrary integration constant has here been dropped. Further, due to the identities (2.3), the following holds:

$$\hat{a}_\mathrm{g} = -\hat{f}_\xi, \tag{4.2c}$$

$$\hat{u}_\mathrm{g} = \frac{\omega \hat{f} + \hat{f}_\xi\, U_{\mathrm{g,r}}}{A_\mathrm{g}}. \tag{4.2d}$$

The disturbance function $\hat{f}$ is here that eigenfunction which will provide a constant ω in (4.1) throughout the wave.

The friction closure is kept unspecified. Following the common practice in stability studies of pipe flows [2], S is expressed with the discharges (analogous to superficial

velocities) as separate variables, i.e., $S(A_\ell) = \mathcal{S}(A_\ell, Q_\ell, Q_\mathrm{g})$. Subject to (3.2), the chain rule yields

$$S' = \frac{\mathrm{d}S}{\mathrm{d}A_\ell} = \mathcal{S}_{A_\ell} + C\left(\mathcal{S}_{Q_\ell} - \mathcal{S}_{Q_\mathrm{g}}\right), \tag{4.3}$$

where

$$\mathcal{S}_{A_\ell} = \left(\frac{\partial \mathcal{S}}{\partial A_\ell}\right)_{Q_\ell, Q_\mathrm{g}}, \quad \mathcal{S}_{Q_\ell} = \left(\frac{\partial \mathcal{S}}{\partial Q_\ell}\right)_{A_\ell, Q_\mathrm{g}}, \quad \mathcal{S}_{Q_\mathrm{g}} = \left(\frac{\partial \mathcal{S}}{\partial Q_\mathrm{g}}\right)_{A_\ell, Q_\ell}.$$

Substituting $\hat{\psi}$ from (4.2) into the momentum equation component of (3.1) and linearising results in

$$\mathcal{R}_2 \hat{f}_{\xi\xi} + \mathcal{R}_1 \hat{f}_\xi + \omega \mathcal{R}_0 \hat{f} = 0, \tag{4.4}$$

where

$$\begin{aligned}
\mathcal{R}_2 &= J_\mathrm{r}', \\
\mathcal{R}_1 &= 3\left(\rho U_\mathrm{r}^2 \frac{A_\xi}{A}\right)^* - 2\,\omega\,(\rho U_\mathrm{r})^* - S' \\
\mathcal{R}_0 &= 2\left(\rho U_\mathrm{r} \frac{A_\xi}{A}\right)^* - \omega \rho^* + \mathcal{S}_{Q_\ell} - \mathcal{S}_{Q_\mathrm{g}}.
\end{aligned}$$

J_r', being the denominator of the profile equation (3.3), equals zero at the critical point $A_{\ell,0}$, which is a double root. It then follows from (4.4) that

$$\hat{f}_{\xi,0} = -\omega \hat{f}_0 \left.\frac{\mathcal{R}_0}{\mathcal{R}_1}\right|_0. \tag{4.5}$$

L'Hôpital's rule $A_{\ell,\xi,0} = J_\mathrm{r}''(A_{\ell,0})/S'(A_{\ell,0})$ may here be used for evaluating $\hat{f}_{\xi,0}$.

Integration of (4.4) can be done with either A_ℓ or H as independent variable. Because only the inverse $A_\ell = \mathcal{H}^{-1}(H)$ is an explicit function, H is used in the presented numerical experiments. The chain rule yields

$$\begin{aligned}
\hat{f}_\xi &= \mathcal{H}' A_{\ell,\xi} \frac{\mathrm{d}\hat{f}}{\mathrm{d}H}, \\
\hat{f}_{\xi\xi} &= (\mathcal{H}' A_{\ell,\xi})^2 \frac{\mathrm{d}^2 \hat{f}}{\mathrm{d}H^2} + \left(\mathcal{H}'' A_{\ell,\xi}^2 + \mathcal{H}' A_{\ell,\xi\xi}\right) \frac{\mathrm{d}\hat{f}}{\mathrm{d}H}.
\end{aligned}$$

The double derivative $A_{\ell,\xi\xi}$ has appeared above and is

$$A_{\ell,\xi\xi} = \left(\frac{S'}{S} - \frac{J_\mathrm{r}''}{J_\mathrm{r}'}\right) A_{\ell,\xi}^2$$

with

$$J_\mathrm{r}'' = w_y\,\mathcal{H}'' + 3\left[\rho\,(U_\mathrm{r}/A)^2\right]_\mathrm{g}^\ell$$

and S' from (4.3). Derivatives of the the geometric function $\mathcal{H}$ are

$$\mathcal{H}' = 1/\sigma_\mathrm{i}, \qquad \mathcal{H}'' = 4\,(h - R)\,\mathcal{H}'^4.$$

Shocks

A shock, unperturbed travelling with the celerity C, will be displaced by a length $\varepsilon(t) = \hat{\varepsilon}\, e^{\omega t}$. The perturbed shock speed is then $c = C + \omega\varepsilon$. Shock conditions (3.4) must now be evaluated at the location $\xi_\pm + \varepsilon$ of the perturbed shock, $\xi_\pm$ being an unperturbed shock position. The left and right shock states are expressed through Taylor-expansions, $\Psi(\xi_\pm + \varepsilon) = \Psi(\xi_\pm) + \varepsilon\Psi_\xi(\xi_\pm)$, disregarding all higher-order terms. We get

$$[A_\ell \hat{u}_{\ell,\mathrm{r}} + \hat{a}_\ell U_{\ell,\mathrm{r}}]_-^+ = 0, \tag{4.6a}$$

$$\left[\left[\rho U_\mathrm{r}\,(\hat{\varepsilon}\, U_\xi + \hat{u}_\mathrm{r})\right]_\mathrm{g}^\ell + w_y \mathcal{H}'\,(\hat{\varepsilon} A_{\ell,\xi} + \hat{a}_\ell)\right]_-^+ = 0, \tag{4.6b}$$

with $\hat{u}_{k,\mathrm{r}} = \hat{u}_k - \omega\hat{\varepsilon}$. Inserting the disturbances (4.2) into (4.6) and eliminating $\hat{\varepsilon}$ then yields a perturbed shock condition

$$\left[J_\mathrm{r}' \hat{f}_\xi - \omega\,(\rho U_\mathrm{r})^* \hat{f}\right]_-^+ - \frac{[\hat{f}]_-^+}{[A_\ell]_-^+}\left[S - \omega\,[\rho U_\mathrm{r}]_\mathrm{g}^\ell\right]_-^+ = 0 \tag{4.7}$$

linking the eigenfunction value $\hat{f}_-$ at the right-wave tail to the value $\hat{f}_+$ at the left-wave front.

Stability of Wave Trains

Solutions of the eigenfunction problem (4.4)–(4.5) may be written as the family

$$\hat{f} = b\hat{F}, \qquad \hat{F}(\xi_0) = 1, \tag{4.8}$$

b being an arbitrary constant.

Let n be the sequential count of roll-waves down along a wave train. The origin of n is irrelevant. $\hat{F}$ is also λ-periodic, $\hat{F}(\xi + n\lambda) = \hat{F}(\xi)$, because $\hat{F}$ depends only on the steady wave solution. Indexing individual values of b according to the wave count, one may express the disturbance along the entire wave train as

$$\hat{f}(\xi + n\lambda) = b_n \hat{F}(\xi); \qquad 0 \le \xi \le \lambda, \quad n \in \mathbb{Z}.$$

Consider a shock connecting wave n to wave $n+1$. The left shock state may be written $\hat{f}_+ = b_n \hat{F}(\xi_+)$ and the right $\hat{f}_- = b_{n+1}\hat{F}(\xi_-)$. The amplification across each shock is therefore repeating in both $n > 0$ and $n < 0$ directions along the wave train; for a disturbance to be bounded in a infinite or periodic spatial domain the amplification must have the form $b_{n+1} = b_n e^{i\,2\pi/m}$, m being the number of roll-waves in a disturbance period. A periodic disturbance then has the form

$$\hat{f}(\xi + n\lambda) = b_0 \hat{F}(\xi) e^{i\,2\pi\frac{n}{m}}; \quad 0 \le \xi \le \lambda, \quad n \in \mathbb{Z}, \quad m \in \mathbb{N}.$$

The stability of a wave train is determined by searching for ω-roots of (4.7) for given values of m. Roots in the right half of the complex plane, $\Re(\omega) > 0$, are unstable.

$\hat{F}$ from (4.4), (4.5) and (4.8) has solutions obtainable with a Frobenius method about the critical point. However, the geometric relations and any extensive friction closure entail Taylor expansions which make such formulations impracticable. $\hat{F}$ is instead determined by integrating (4.4) numerically, using a Rounge-Kutta ODE solver. Integration is performed from $\left(H_0 + \delta_H, 1 + \delta_H \frac{\mathrm{d}\hat{F}}{\mathrm{d}H}\big|_0\right)$ to $\left(H_+, \hat{F}_+\right)$ on the subcritical side, and from $\left(H_0 - \delta_H, 1 - \delta_H \frac{\mathrm{d}\hat{F}}{\mathrm{d}H}\big|_0\right)$ to $\left(H_-, \hat{F}_-\right)$ on the supercritical side, δ_H being a tiny height step for the purpose of avoiding numerical 0/0-issues.

Partial derivatives of friction closures of arbitrary complexity may be computed in a discrete manner

$$\mathcal{S}_{A_\ell} = \left(\mathcal{S}(A_\ell + \tfrac{1}{2}\delta_A, q_\ell, q_\mathrm{g}) - \mathcal{S}(A_\ell - \tfrac{1}{2}\delta_A, q_\ell, q_\mathrm{g})\right)/\delta_A, \quad \text{etc..}$$

The stability analysis for open channel roll-waves, such as presented by cited authors, is regained by choosing $\mathcal{H}(a_\ell) = a_\ell/d$, $\mathcal{A} = d^2$, $\rho_\mathrm{g} = \tau_\mathrm{g} = \tau_\mathrm{i} = 0$.

5. The Stability of Uniform Stratified Flow

The well-known 'viscous Kelvin-Helmholtz' (VKH) criterion [2] is often used for predicting whether or not the flow regime is uniformly stratified. This analysis proceeds by inserting a Fourier disturbance mode in the uniform flow solution $S = 0$. In absence of surface tension, the resulting dispersion equation can, despite the complicated expressions usually presented, be written

$$J'_\mathrm{r} + \frac{i}{k} S' = 0, \tag{5.1}$$

$k = 2\pi/\lambda$ being the wavenumber. The celerity C appearing in J'_r and S' is here a complex value, related to the wave growth in the same manner at the pulsation in (4.1) by $\omega = -ikC$.

Notice that the condition for marginally stable flow, i.e., when C is real, will simply read $S = S' = J'_\mathrm{r} = 0$, with $J'_\mathrm{r} < 0$ resulting in wave growth. Note further that this can be inferred directly from (3.3) as a zero-amplitude roll-wave. All points are then critical points ($J'_\mathrm{r} = S = 0$) where the profile slope is at an equilibrium with respect to A_ℓ ($S' = 0$).

6. Numerical Experiments

Stability predictions are in this section compared with direct simulations of the base model (2.2). A Roe scheme, presented in Appendix A, is implemented for the purpose. Simulations are carried out with periodic boundary conditions. This means that the globally average area fractions stay constant in time. $\mathcal{Q}$ is also kept constant. Direct simulations are carried out over domains large large enough to avoid the boundaries influencing the statistics. A small pointwise random disturbance is issued to the uniform steady initial conditions.

The friction closures τ_k and τ_i in the numerical tests are provided by the Biberg friction model as presented in [3]. A quick summary of this model now follows: Classical turbulent boundary layer principles are used to model the gas and liquid velocity profiles in a duct cross section. The interface is modelled as a moving boundary with an initial turbulence level, representing smaller interface waves, etc.. Figure 6.1 shows examples of such velocity profiles for free surface and two-phase flows. These profiles are integrated up to yield algebraic expressions that couple wall and interfacial frictions to the average phase velocities and the interface heights. Friction correlations for duct flow are then correlated to the well-known Colebrook-White formula for single-phase pipe flow, which is in turn used to extend the closure into formulae for the pipe geometry.

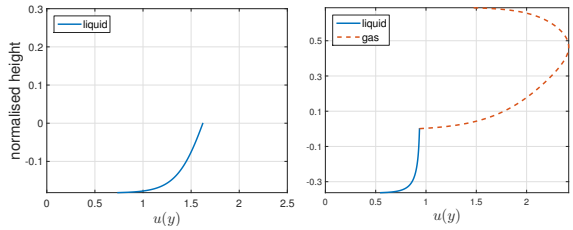

(a) Free surface flow (b) Gas-liquid flow

Figure 6.1: Example velocity profile pre-integrated in the Biberg friction model.

liquid density	ρ_ℓ	998	$\mathrm{kg/m^3}$
gas density	ρ_g	50	$\mathrm{kg/m^3}$
liquid dynamic viscosity	μ_ℓ	1.00E-3	Pa s
gas dynamic viscosity	μ_g	1.61E-5	Pa s
internal pipe diameter	d	0.1	m
wall roughness		2E-5	m

Table 1: Fixed parameters.

Figures 6.2 – 6.4 present wavelength predictions from the stability analyses and direct simulations. Fixed parameters are given in Table 1 and correspond to those used in [7] and [8]. Flow rates are chosen low enough for the waves to grow from a random disturbance without ever breaching the cross section or flow characteristics turning complex.[2] Presented results are normalised by the VKH growth rates of the respective uniform flows as provided by (5.1). Normalised time and pulsation are $T = t \cdot \Re(\omega_\mathrm{VKH})$, $\Omega = \omega/\Re(\omega_\mathrm{VKH})$, respectively.

[2] This range of flow conditions is rather narrow, with a weak growth rate. Holmås, in the cited paper, managed to simulate a much wider flow range within the roll-wave regime by expanding Biberg's friction closure with a wave breaking model. This model does however introduce level height derivative terms into the source model, altering the discontinuous nature of the roll-wave model on which the present stability analysis is based.

The first case, Figure 6.2, is a one degree upwards-inclined pipe with superficial velocities $\overline{q_\ell}/\mathcal{A} = 0.125\,\mathrm{m/s}$ and $\overline{q_\mathrm{g}}/\mathcal{A} = 3.50\,\mathrm{m/s}$ (in the corresponding uniform flow.) Resulting liquid levels are low, with $\overline{a_\ell}/\mathcal{A} = 0.11$. Figure 6.2a show the roots of Ω satisfying (4.7). Roots with a positive real component are unstable. According to this figure, unstable wavelengths are predicted to be those shorter than about $40\,d$. Roots whose disturbance period is one ($m = 1$) or two ($m = 2$) roll-wave lengths are real, located along the abscissa. m is made continuous in the plot, though only positive integer values can be realised. The unstable roots appear to converge towards some singular point, independent of m, at higher wavelengths, the influence of which is unclear.

This predictions of Figure 6.2a seem to agree with the direct simulation of Figure 6.2b, which shows that the wavelengths quickly arrange themselves between 35 an $120\,d$ in a slowly decaying, oscillating fashion.

A horizontal pipe is used for the second case, Figure 6.3. Here, $\overline{q_\ell}/\mathcal{A} = 0.35\,\mathrm{m/s}$ and $\overline{q_\mathrm{g}}/\mathcal{A} = 1.00\,\mathrm{m/s}$, resulting in $\overline{a_\ell}/\mathcal{A} = 0.49$. A typical velocity profile for this case is displayed in Figure 6.1b. Figure 6.3a show that the range of unstable Ω converges towards $\Omega = 0$ (which always exist) with increasing wavelength, and then exists only in the left plane after $\lambda \gtrsim 200\,d$. The direct simulation of Figure 6.2b shows waves ranging from around 180 an $1200\,d$, oscillating strongly in time.

Examining period and decay of the larger oscillations seen in Figure 6.3b, one finds $\Omega \sim -0.0015 + 0.04i$, placing the dominating disturbances close by the ordinate in accordance with the long-wavelength stability predictions seen in Figure 6.3a. Similar observations can be made with Figure 6.2, though the amplitudes and frequencies are harder to make out.

Let us finally attempt to compare gravity-driven free surface flows and pressure-driven gas-liquid flows. The gas phase is removed ($\rho_\mathrm{g} = \tau_\mathrm{g} = \tau_\mathrm{i} = 0$) and a negative pipe inclination θ drives a free surface flow. This free surface flow is uniformly stable if the liquid level and flow rate is identical to that in the previous case, and increasing the flow rate makes the free surface flow *more* stable as opposed to the previous pressure driven flows. The pipe inclination and average liquid fraction are chosen such that the liquid flow rate $\overline{q_\ell}$ and VKH growth rate, $\Re(\omega_\mathrm{VKH})$, are the same as in the previous case. This happens at $\theta = -1.27°$, $\overline{q_\ell}/\mathcal{A} = 0.35\mathrm{m/s}$, where $\overline{a_\ell}/\mathcal{A} = 0.28$. Figure 6.4 shows the stability map and simulated wavelength distribution. Again, oscillation frequency and decay seem to agree with the stability map.

Compared to the pressure driven flow of Figure 6.3, the wavelength distribution of the gravity driven flow develops more steadily, but with some coalescence events occurring at a later stage. Figure 6.5 shows snapshots of the level heights during the initial developing stages of to two simulations. The free surface simulation is seen to have wavelengths and wave heights distributed within more narrow bands. Surviving wavelengths in the free surface flow are of the same order of magnitude as those from the pressure driven flow, and the same can be said for the frequency and decay of the disturbance oscillations. The difference in wavelength bands is however not readily evident from comparing the two stability maps of Figure 6.3a and 6.4a. The difference can possibly be attributed to the unstable small-wavelength roots, which in the pressure driven flow are seen to be more oscillatory and would thus promote a more irregular wavelength distribution after the initial coalescence stage.

(a) Ω stability map. Contour lines show Ω values forming roots in (4.7) at specified wavelengths. Normalised wavelengths λ/d are numerically indicated within the respective contour lines.

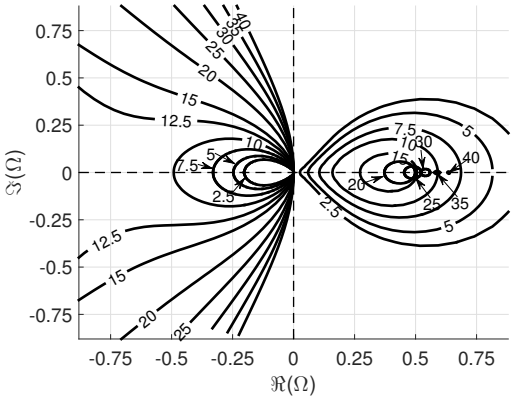

(b) Direct simulation. 10 000 grid cells in a $2\,000\,d$ long simulation domain.

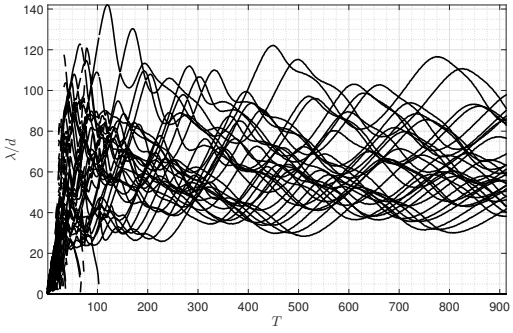

Figure 6.2: $\theta = 1°$, $\overline{q_\ell}/\mathcal{A} = 0.125\,\mathrm{m/s}$, $\overline{q_\mathrm{g}}/\mathcal{A} = 3.50\,\mathrm{m/s}$

7. Conclusions

A stability analysis has been presented which provides predictions in agreement with numerical simulations. The analysis seems to give a lower wavelength limit, below which wave trains are unstable. Simulations indicate that

(a) Ω stability map, cf. caption of Figure 6.2a

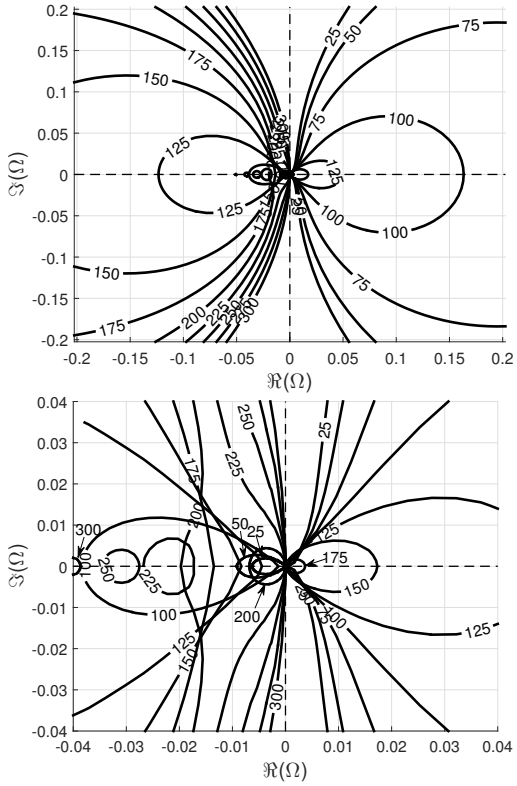

(b) Direct simulation. 10 000 grid cells in a 10 000 d long simulation domain.

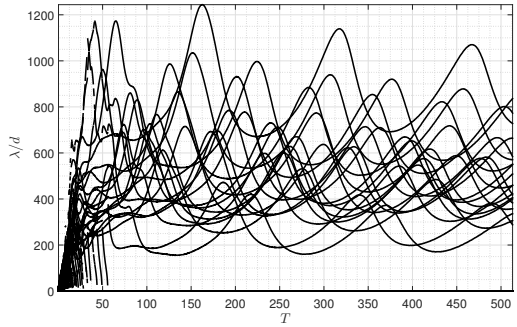

Figure 6.3: $\theta = 0°$, $\overline{q_\ell}/\mathcal{A} = 0.35\,\mathrm{m/s}$, $\overline{q_\mathrm{g}}/\mathcal{A} = 1.00\,\mathrm{m/s}$

(a) Ω stability map, cf. caption of Figure 6.2a

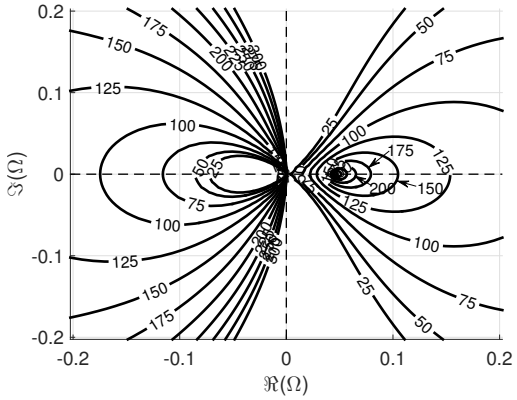

(b) Direct simulation. 10 000 grid cells in a 10 000 d long simulation domain.

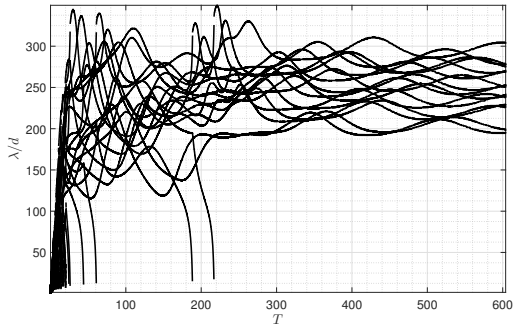

Figure 6.4: Free surface flow; $\theta = -1.27°$, $\overline{q_\ell}/\mathcal{A} = 0.35\mathrm{m/s}$. VKH growth rate $\Re(\omega_\mathrm{VKH})$ is the same as in Figure 6.3.

(a) Snapshots cf. Figure 6.3b

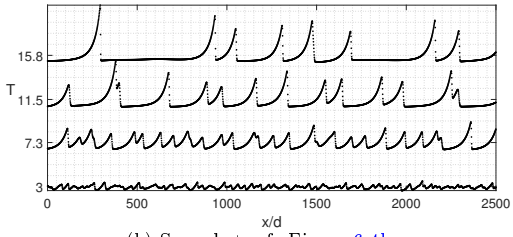

(b) Snapshots cf. Figure 6.4b

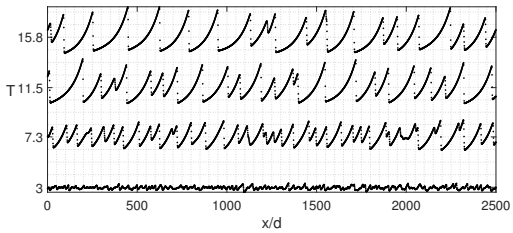

Figure 6.5: Snapshots of level heights h at specific times early in the simulations. Only a portion of the simulation domains are shown.

the wavelength distribution will range close above this lower wavelength limit.

Acknowledgements

This work is financed by The Norwegian University of Science and Technology (NTNU) as a contribution the Multiphase Flow Assurance programme (FACE.)

Appendix A. A Roe Scheme

The base model (2.2) may be written in terms of a Jacobian $\mathbb{A} = \frac{\partial \boldsymbol{f}}{\partial \boldsymbol{v}}$ as follows:

$$\tilde{\boldsymbol{v}}_t + \mathbb{A}\tilde{\boldsymbol{v}}_x = \tilde{\boldsymbol{s}}, \tag{A.1}$$

with the Jacobian

$$\mathbb{A} = \frac{1}{\rho^*}\begin{pmatrix} (\rho u)^* & 1 \\ \kappa^2 & (\rho u)^* \end{pmatrix}, \tag{A.2}$$

and

$$\kappa = \sqrt{\rho^* w_y \mathcal{H}' - \frac{\rho_\ell \rho_\mathrm{g}}{a_\ell a_\mathrm{g}}\left(u_\mathrm{g} - u_\ell\right)^2}.$$

Roe's approximate Riemann solver [12] is among the most popular finite volume schemes for non-linear hyperbolic problems. Its main principle lies in linearising (A.1) and solving the Riemann problems

$$\begin{gathered} \tilde{\boldsymbol{v}}_t + \hat{\mathbb{A}}(\boldsymbol{v}_\mathrm{R}, \boldsymbol{v}_\mathrm{L})\tilde{\boldsymbol{v}}_x = 0 \\ \tilde{\boldsymbol{v}}(x,0) = \boldsymbol{v}_\mathrm{L},\ (x<0); \quad \tilde{\boldsymbol{v}}(x,0) = \boldsymbol{v}_\mathrm{R},\ (x>0) \end{gathered} \tag{A.3}$$

at the cell faces. $\hat{\mathbb{A}}(\boldsymbol{v}_\mathrm{R}, \boldsymbol{v}_\mathrm{L})$ is the so-called Roe-averaged matrix of $\mathbb{A}$. $\hat{\mathbb{A}}$, $\boldsymbol{v}_\mathrm{L}$ and $\boldsymbol{v}_\mathrm{R}$ are constants respective to each cell face. Roe schemes are effective at discontinuities, but they require the formulation of $\hat{\mathbb{A}}(\boldsymbol{v}_\mathrm{L}, \boldsymbol{v}_\mathrm{R})$ at the cell faces with the properties that

i) $\hat{\mathbb{A}}(\boldsymbol{v}_\mathrm{L}, \boldsymbol{v}_\mathrm{R})$ is diagonalizable with real eigenvalues,

ii) $\hat{\mathbb{A}}(\boldsymbol{v}_\mathrm{L}, \boldsymbol{v}_\mathrm{R}) \to \mathbb{A}(\boldsymbol{v})$ smoothly as $\boldsymbol{v}_\mathrm{L}, \boldsymbol{v}_\mathrm{R} \to \boldsymbol{v}$, and

iii) $\hat{\mathbb{A}}(\boldsymbol{v}_\mathrm{L}, \boldsymbol{v}_\mathrm{R})\,[\boldsymbol{v}]_\mathrm{L}^\mathrm{R} = [\boldsymbol{f}]_\mathrm{L}^\mathrm{R}$.

Generally, $\psi_\mathrm{L} = \psi(\boldsymbol{v}_\mathrm{L})$ and $\psi_\mathrm{R} = \psi(\boldsymbol{v}_\mathrm{R})$. The first and second properties are required for hyperbolicity and consistency, respectively. The third property ensures, by the Rankine-Hugoniot condition, that single shocks of the linear system (A.3) are shocks of the non-linear system (2.2).

Consider condition iii) and the following splitting of the flux function:

$$\boldsymbol{f} = \boldsymbol{f}_\mathrm{u} + \boldsymbol{f}_\mathrm{h} \tag{A.4}$$

where

$$\boldsymbol{f}_\mathrm{u} = \left(a_\ell u_\ell, [\rho u/2]_\mathrm{g}^\ell\right)^T, \qquad \boldsymbol{f}_\mathrm{h} = (0, w_y h)^T.$$

We need a suitable integration path over which $\boldsymbol{f}$ is easily evaluated; $\boldsymbol{f}$ is written in terms of a parameter vector $\boldsymbol{w}$, rendering it a low-order polynomial. Primitive variable are suitable in the case of $\boldsymbol{f}_\mathrm{u}$, i.e.,

$$\boldsymbol{w} = (a_\ell, a_\mathrm{g}, u_\ell, u_\mathrm{g})^T.$$

Note that $\frac{\partial \boldsymbol{v}}{\partial \boldsymbol{w}}$ is constant and that $\frac{\partial \boldsymbol{f}_\mathrm{u}}{\partial \boldsymbol{w}}$ is linear in $\boldsymbol{w}$. A linear path

$$\boldsymbol{w} = \widetilde{\boldsymbol{w}}(z) = \boldsymbol{w}_\mathrm{L} + [\boldsymbol{w}]_\mathrm{L}^\mathrm{R}\, z$$

is chosen for the integration of $\boldsymbol{f}_\mathrm{u}$. We get

$$\begin{aligned} [\boldsymbol{f}_\mathrm{u}]_\mathrm{L}^\mathrm{R} &= \int_\mathrm{L}^\mathrm{R} \mathrm{d}\boldsymbol{f}_\mathrm{u} = \int_0^1 \frac{\partial \boldsymbol{f}_\mathrm{u}}{\partial \boldsymbol{w}}(\widetilde{\boldsymbol{w}}(z))\frac{\partial \widetilde{\boldsymbol{w}}}{\partial z}\,\mathrm{d}z = \frac{\partial \boldsymbol{f}_\mathrm{u}}{\partial \boldsymbol{w}}(\overline{\boldsymbol{w}})\,[\boldsymbol{w}]_\mathrm{L}^\mathrm{R} \\ &= \frac{\partial \boldsymbol{f}_\mathrm{u}}{\partial \boldsymbol{v}}(\overline{\boldsymbol{w}})\frac{\partial \boldsymbol{v}}{\partial \boldsymbol{w}}\,[\boldsymbol{w}]_\mathrm{L}^\mathrm{R} = \mathbb{A}_\mathrm{u}(\overline{\boldsymbol{w}})\,[\boldsymbol{v}]_\mathrm{L}^\mathrm{R}, \end{aligned} \tag{A.5}$$

where $\overline{\boldsymbol{w}} = \frac{1}{2}(\boldsymbol{w}_\mathrm{L} + \boldsymbol{w}_\mathrm{R})$. The fourth expression is a result of $\frac{\partial \boldsymbol{f}_\mathrm{u}}{\partial \boldsymbol{w}}$ being linear in $\boldsymbol{w}$, and the fifth and sixth from $\frac{\partial \boldsymbol{v}}{\partial \boldsymbol{w}}$ being constant. $\mathbb{A}_\mathrm{u} = \frac{\partial \boldsymbol{f}_\mathrm{u}}{\partial \boldsymbol{v}}$ is the Jacobian of $\boldsymbol{f}_\mathrm{u}$, equalling (A.2) without the $\rho^* w_y \mathcal{H}'$ term.

Now consider $\boldsymbol{f}_\mathrm{h}$. We write

$$[\boldsymbol{f}_\mathrm{h}]_\mathrm{L}^\mathrm{R} = \left(0, w_y\,[h]_\mathrm{L}^\mathrm{R}\right)^T = \mathbb{A}_\mathrm{h}(a_{\ell,\mathrm{L}}, a_{\ell,\mathrm{R}})\,[\boldsymbol{v}]_\mathrm{L}^\mathrm{R}, \tag{A.6}$$

where

$$\mathbb{A}_\mathrm{h} = \begin{pmatrix} 0 & 0 \\ w_y[h]_\mathrm{L}^\mathrm{R}/[a_\ell]_\mathrm{L}^\mathrm{R} & 0 \end{pmatrix}.$$

Inserting (A.5) and (A.6) into (A.4),

$$[\boldsymbol{f}]_\mathrm{L}^\mathrm{R} = [\boldsymbol{f}_\mathrm{u}]_\mathrm{L}^\mathrm{R} + [\boldsymbol{f}_\mathrm{h}]_\mathrm{L}^\mathrm{R} = \left(\mathbb{A}_\mathrm{u}(\overline{\boldsymbol{w}}) + \mathbb{A}_\mathrm{h}\right)[\boldsymbol{v}]_\mathrm{L}^\mathrm{R},$$

the Roe average matrix

$$\hat{\mathbb{A}} = \mathbb{A}_{\mathrm{u}}(\overline{\boldsymbol{w}}) + \mathbb{A}_{\mathrm{h}}(a_{\ell,\mathrm{L}}, a_{\ell,\mathrm{R}}) \tag{A.7}$$

is seen to be the Jacobian (A.2) constructed from average primitive variables $\overline{a_k}$ and $\overline{u_k}$, with $[h]_{\mathrm{L}}^{\mathrm{R}}/[a_\ell]_{\mathrm{L}}^{\mathrm{R}}$ replacing $\mathcal{H}'$. We use $\mathcal{H}'(\overline{a_\ell})$ close to $[a_\ell]_{\mathrm{L}}^{\mathrm{R}} = 0$ to avoid numerical 0/0-issues.

Once $\hat{\mathbb{A}}$ is formulated,

$$\boldsymbol{f}(0,t) = \frac{1}{2}\left(\boldsymbol{f}_{\mathrm{R}} + \boldsymbol{f}_{\mathrm{L}}\right) - \frac{1}{2}\left|\hat{\mathbb{A}}\right|[\boldsymbol{v}]_{\mathrm{L}}^{\mathrm{R}} \tag{A.8}$$

provides the solution of the linearised problem (A.3). Here,

$$\left|\hat{\mathbb{A}}\right| = \hat{\mathbb{L}}^{-1}\left|\hat{\mathbb{\Lambda}}\right|\hat{\mathbb{L}}$$

the 'hat' indicating the Roe intermediate state which in (A.7) is the state of arithmetically averaged primitive variables and $[h]_{\mathrm{L}}^{\mathrm{R}}/[a_\ell]_{\mathrm{L}}^{\mathrm{R}}$ replacing $\mathcal{H}'$. Absolute eigenvalue and eigenvector matrices are

$$\left|\mathbb{\Lambda}\right| = \begin{pmatrix} \left|\lambda^+\right| & 0 \\ 0 & \left|\lambda^-\right| \end{pmatrix} \qquad \text{and} \qquad \mathbb{L} = \begin{pmatrix} 1 & 1/\kappa \\ 1 & -1/\kappa \end{pmatrix}$$

respectively,

$$\lambda^{\pm} = \frac{(\rho u)^* \pm \kappa}{\rho^*} \tag{A.9}$$

being the eigenvalues of $\mathbb{A}$.

Integrating (2.2) in space and time over a control volume cell j yields the common finite volume expression

$$\boldsymbol{v}_j^{\mathrm{new}} = \boldsymbol{v}_j - \frac{\Delta t}{\Delta x}\left\langle \boldsymbol{f}_{j+\frac{1}{2}} - \boldsymbol{f}_{j-\frac{1}{2}} \right\rangle + \Delta t \left\langle \boldsymbol{s}_j \right\rangle \tag{A.10}$$

where 'new' refers to the state at the next time level, the j-index to the spatial average of cell j and the angle brackets to the temporal average over the time step. The solution (A.8) is here applied directly to each average cell flux $\left\langle \boldsymbol{f}_{j-\frac{1}{2}} \right\rangle$ in (A.10) without spatial reconstruction: $\boldsymbol{v}_{\mathrm{R}} = \boldsymbol{v}_j$, $\boldsymbol{v}_{\mathrm{L}} = \boldsymbol{v}_{j-1}$. Each time step is chosen $\Delta t = \Delta x / \max_{j,\pm}\left|\hat{\lambda}^{\pm}_{j-\frac{1}{2}}\right|$. The numerical tests presented herein are never in danger of promoting entropy violations in the Roe scheme, which may happen if an expansion fan straddles the time axis of problem (A.3). See e.g. [9] for entropy corrections.

[1] N.J. Balmforth and S. Mandre. Dynamics of roll waves. *Journal of Fluid Mechanics*, 514:1 – 33, 2004. ISSN 00221120. URL http://dx.doi.org/10.1017/S0022112004009930.

[2] D. Barnea and Y. Taitel. Structural and interfacial stability of multiple solutions for stratified flow. *International Journal of Multiphase Flow*, 18(6):821 – 30, 1992/11/. ISSN 0301-9322. URL http://dx.doi.org/10.1016/0301-9322(92)90061-K. Kelvin-Helmholtz stability;multiple solutions;liquid level;stratified two-phase upwards flow;hysteresis;structural stability analysis;interfacial stability analysis;.

[3] D. Biberg. A mathematical model for two-phase stratified turbulent duct flow. *Multiphase Science and Technology*, 19(1):1 – 48, 2007. ISSN 0276-1459. URL http://dx.doi.org/10.1615/MultScienTechn.v19.i1.10.

[4] R.R. Brock. Development of roll-wave trains in open channels. *American Society of Civil Engineers, Journal of the Hydraulics Division*, 95(HY4):1401 – 1427, 1969.

[5] B.S. Brook, S.A.E.G. Falle, and T.J. Pedley. Numerical solutions for unsteady gravity-driven flows in collapsible tubes: evolution and roll-wave instability of a steady state. *Journal of Fluid Mechanics*, 396:223 – 56, 1999/10/10. ISSN 0022-1120. URL http://dx.doi.org/10.1017/S0022112099006084.

[6] R.F. Dressler. Mathematical solution of the problem of roll-waves in inclined open channels. *Communications on Pure and Applied Mathematics*, 2:149 – 194, 1949/06/. URL http://dx.doi.org/10.1002/cpa.3160020203.

[7] H. Holmås. Numerical simulation of transient roll-waves in two-phase pipe flow. *Chemical Engineering Science*, 65(5):1811 – 25, 2010/03/01. ISSN 0009-2509. URL http://dx.doi.org/10.1016/j.ces.2009.11.031.

[8] G.W. Johnson. *A Stuy of Stratified Gas-Liquid Pipe Flow*. PhD thesis, Univ. Oslo, 2005. dr. scient.

[9] Randall J LeVeque. *Finite volume methods for hyperbolic problems*, volume 31. Cambridge university press, 2002.

[10] M. Miya, D.E. Woodmansee, and T.J. Hanratty. A model for roll waves in gas-liquid flow. *Chemical Engineering Science*, 26(11):1915 – 31, 1971/11/. ISSN 0009-2509. URL http://dx.doi.org/10.1016/0009-2509(71)86034-7. liquid film;high speed gas flow;flow surges;roll waves;height;wall shear stress;gas pressure;mathematical model;.

[11] G.L. Richard and S.L. Gavrilyuk. A new model of roll waves: Comparison with brock's experiments. *Journal of Fluid Mechanics*, 698:374 – 405, 2012. ISSN 00221120. URL http://dx.doi.org/10.1017/jfm.2012.96.

[12] P. L. Roe. Approximate riemann solvers, parameter vectors, and difference schemes. *Journal of Computational Physics*, 135 (2):250 – 250, 1997. ISSN 00219991. URL http://dx.doi.org/10.1006/jcph.1997.5705.

[13] K. Tamada and H. Tougou. Stability of roll-waves on thin laminar flow down an inclined plane wall. *Journal of the Physical Society of Japan*, 47(6):1992 – 8, 1979/12/. ISSN 0031-9015. URL http://dx.doi.org/10.1143/JPSJ.47.1992.

[14] H. A. Thomas. The propagation of waves in steep prismatic conduits. In *Hydraulics Conf.*, pages 214–229, Carnegie Institute of Technology, Pittsburgh, 1939.

[15] H. Tougou. Stability of turbulent roll-waves in an inclined open channel. *Journal of the Physical Society of Japan*, 48(3):1018 – 23, 1980/03/. ISSN 0031-9015. URL http://dx.doi.org/10.1143/JPSJ.48.1018.

[16] M. Watson. Wavy stratified flow and the transition to slug flow. In C.P. Fairhurst, editor, *Multi-phase Flow – Proceedings of the 4th International Conference*, pages 495–512, Cranfield, UK, 1989.

PAPER V

The Kelvin-Helmholtz/von Neumann Stability of Discrete Representations of the Two-Fluid Model for Stratified Two-Phase Flow

Andreas H. Akselsen

Under review in
The International Journal of Multiphase Flow

The Kelvin-Helmholtz/von Neumann Stability of Discrete Representations of the Two-Fluid Model for Stratified Two-Phase Flow

A.H. Akselsen[a,*]

[a] *Department of Energy and Process Engineering, Norwegian University of Science and Technology*

Abstract

Many dynamic pipe flow simulator tools are capable of predicting the onset of hydrodynamic flow instability through detailed simulation. These instabilities provide a natural mechanism for flow regime transition. The quality and reliability of flow predictions are however strongly dependent upon the numerics within these simulator tools, the scheme type and resolution in particular.

A Kelvin-Helmholtz stability analysis for the differential two-fluid model is in the present work presented and extended to discrete representations of said model. This analysis provides algebraic expressions which give instantaneous, quantitative information into i) when a studied scheme will predict linear wave growth, ii) the rate of growth and the expected growing wavelength, and iii) the wave speeds. These stability expressions adhere to a wider family of finite volume methods, directly applicable to any specific formulation within this group. Both the spatial and temporal discretization are found to play decisive roles in a method's predictive capability. Fundamental aspects of how numerical errors from the temporal integration affects the predicted stability are explored. Numerical errors are observed to manifest in increased, as well as reduced, wave growth. Low-frequency growth from numerical errors is not always easily distinguished from physical wave growth. The linear analysis is demonstrated to be useful in understanding the predictions made by simulator tools, and in choosing the appropriate numerical method and simulation parameters for optimizing the simulation efficiency and reliability.

Keywords: discrete stability; Kelvin-Helmholtz; von Neumann; two-phase; pipe flow; two-fluid model

1. Introduction

Stability analyses of the two-fluid model have been performed by numerous authors. For example, Taitel and Dukler [17] used linear theory with a simplified, inviscid two-fluid model to predict flow regime transition to slug flow. Barnea and Taitel [4] presented a derivation of the Kelvin-Helmholtz stability criterion for viscous flows (henceforth abbreviated the VKH criterion) and examined the non-linear flow development through simulation [5]. Barnea also performed a stability analysis on a discrete upwind type scheme of a simplified version of the two-fluid model for annular flow [3]. Here it was shown again how an intrinsically unstable, ill-posed differential model may display stable behaviour if provided with sufficient numerical diffusion. (The annular interface is inherently unstable locally though it may be stable in a statistical sense.) Barnea argued that the discrete model can be regarded as a legitimate model for the average flow, even though the differential model is ill-posed.

Issa and Kempf [12] have been credited with first demonstrating that the predicted wave growth from transient simulations of the full two-fluid model coincides with the wave growth from Kelvin-Helmholtz theory, and suggested that such simulated wave growth gives a natural transition into a wavy or slugging flow regime.

In [16], Stewart presented a von Neumann analysis on two variants of the two-fluid model, one with a term exchanging momentum between the phases and one without. The two-fluid model is known for obtaining complex eigenvalues if the momentum exchange is insufficient, which means that the model can no longer be deemed part of a well-posed hyperbolic initial value problem [10]. Stewart showed that *well-behaved* discrete solutions, *i.e.*, steady flow solutions, were obtainable on discretizations of non-hyperbolic systems, provided the mesh resolution was restricted.

Liao et al. [14] performed a linear stability study on a discrete two-fluid model with a staggered grid arrangement, comparing various interpolations for the convection term. This analysis was limited to implicit time integration, considering the convection terms only. Numerical errors arising from the dislocation of staggered information, as well as form the conservative formulation, appears to have been neglected. The paper concluded that the central difference discretization was superior to the first and higher order non-centred interpolations. Liao et al. also examined the evolution of the wavelength distributions from

*Corresponding author

Email address: andreas.h.akselsen@ntnu.no (A.H. Akselsen)

a random initial disturbance, and the behaviour as the model turns ill-posed.

The light water reactor safety analysis codes RELAP5 and CATHARE have also been studied with von Neumann analysis by Pokharna et al.. [15], looking into how numerical diffusion and terms added to achieve model hyperbolicity affect stability predictions. They found the numerical regularization to be dominant in the cases studied. Fullmer et al. [9] preformed similar analyses on an upwind discretization of the two-fluid model, demonstrating the mesh size dependency of the predicted stability in both the linear and nonlinear range. A Reynolds stress modelling was shown provide grid independent regularization.

The present article focuses on providing general theory for a wider family of discrete two-fluid model representations. This will be done by relating the predicted growth and decay of the discrete representations directly to the growth results of the Kelvin-Helmholtz analysis of the differential two-fluid model. Linear theory of the type here presented is demonstrated to be powerful tool when it comes to assessing the predictive capability of any chosen discrete representation, providing support with decisions related to the parametric setup prior to simulation and interpreting the simulation results. *Predictive capability* here refers to the reliability and accuracy with which a discrete representation predicts wave growth or decay under limited computational resolution. It will be shown that the growth and dispersion response of discrete representations is perfectly analogous to that of the differential model. What's more, the differential Kelvin-Helmholtz expression directly provides that growth and dispersion which will be predicted by the discrete methods in the linear range, provided these representations uses the same discrete differentiations all over.

2. The Two-Fluid Model

The compressible, adiabatic, equal pressure four-equation two-fluid model for stratified pipe flow results from an averaging of the conservation equations across the cross-section area. The model is commonly written

$$\partial_t(\rho a)_\kappa + \partial_x(\rho a u)_\kappa = 0, \tag{2.1a}$$

$$\partial_t(\rho a u)_\kappa + \partial_x\left(\rho a u^2\right)_\kappa + a_\kappa \partial_x p_\mathrm{i} + \rho_\kappa a_\kappa g\cos\theta\,\partial_x h = s_\kappa, \tag{2.1b}$$

$$a_\ell + a_\mathrm{g} = \mathcal{A}, \tag{2.1c}$$

$$p_\mathrm{i} = \mathcal{P}_\mathrm{g}(\rho_\mathrm{g}) = \mathcal{P}_\ell(\rho_\ell). \tag{2.1d}$$

Field κ, occupied by either gas, $\kappa = \mathrm{g}$, or liquid, $\kappa = \ell$, is segregated from the other field. Subscript i indicates the fluid interface; see Figure 2.1. p_i is here the pressure at the interface, assumed the same for each phase and given by some equation of state $\mathcal{P}$. h is the height of the interface from the pipe floor, and the term in which it appears originates from approximating a hydrostatic wall-normal pressure distribution. u_κ and ρ_κ are the mean fluid velocity and density in field κ. The momentum sources are $s_\kappa = -\tau_\kappa\sigma_\kappa \pm \tau_\mathrm{i}\sigma_\mathrm{i} - a_\kappa\rho_\kappa g\sin\theta$, where τ is the skin frictions at the walls and interface. θ is the pipe inclination, positive above datum, and g is the gravitational acceleration.

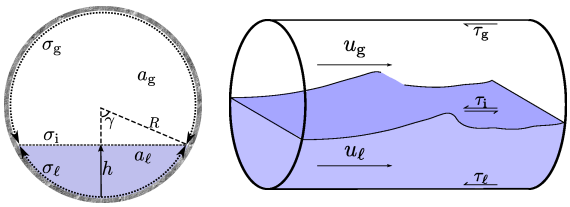

Figure 2.1: Pipe cross-section

The circular pipe geometry itself enters into the modelling through the relation between the level height h, the specific areas a_κ and the peripheral lengths σ_κ and σ_i. These are algebraically interchangeable through a geometric function

$$h = \mathcal{H}(a_\ell) \tag{2.2}$$

whose derivative is $\mathcal{H}' = 1/\sigma_\mathrm{i}$. See *e.g.*[1] for expressions of the geometric relationships.

Fluid compressibility is commonly ignored when considering the surface wave stability of (2.1). This enables us to base the stability analysis on the incompressible two-fluid model, which has lower rank and a conservative form.

Assuming incompressible phases, the two-equation model is obtained by reducing the momentum equations with their respective mass equations and eliminating the pressure term between them, resulting in

$$\partial_t \boldsymbol{v} + \partial_x \boldsymbol{f} = \nu\partial_{xx}\boldsymbol{v} + \boldsymbol{s} \tag{2.3}$$

with conserved variables and fluxes

$$\boldsymbol{v} = \left(a_\ell, \rho_\ell u_\ell - \rho_\mathrm{g} u_\mathrm{g}\right)^T, \quad \boldsymbol{f} = (q_\ell, j)^T, \quad \boldsymbol{s} = (0, s)^T.$$

Symbols for the flux and source components have here been defined and are

$$q_\kappa = a_\kappa u_\kappa, \qquad j = \tfrac{1}{2}\left(\rho_\ell u_\ell^2 - \rho_\mathrm{g} u_\mathrm{g}^2\right) + m_y h,$$
$$s = -m_x - \frac{\tau_\ell\sigma_\ell}{a_\ell} + \frac{\tau_\mathrm{g}\sigma_\mathrm{g}}{a_\mathrm{g}} + \tau_\mathrm{i}\sigma_\mathrm{i}\left(\frac{1}{a_\ell} + \frac{1}{a_\mathrm{g}}\right),$$
$$\nu = 0.$$

A dummy viscous term has been added to the system, the purpose of which lies in evaluating the artificial numerical viscosity present in some discrete representations. Specific weight coefficients have been grouped into $m_x = (\rho_\ell -$

$\rho_g)g\sin\theta$ and $m_y = (\rho_\ell - \rho_g)g\cos\theta$. The identities

$$a_\ell + a_g = \mathcal{A}(x), \qquad q_\ell + q_g = \mathcal{Q}(t), \tag{2.4}$$

where the latter has been obtained from summing the two mass equations, close the model. Both $\mathcal{A}$ and $\mathcal{Q}$ are parametric.

Finally, the eigenstructure of (2.3) is useful to know. The Jacobian of $\boldsymbol{f}$ is

$$\frac{\partial \boldsymbol{f}}{\partial \boldsymbol{v}} = \frac{1}{\rho^*}\begin{pmatrix} (\rho u)^* & 1 \\ \varkappa^2 & (\rho u)^* \end{pmatrix}, \tag{2.5}$$

whose eigenvalues are

$$\lambda^\pm = \frac{(\rho u)^* \pm \varkappa}{\rho^*}. \tag{2.6}$$

A new variable

$$\varkappa = \sqrt{\rho^* m_y \mathcal{H}' - \frac{\rho_\ell \rho_g}{a_\ell a_g}(u_g - u_\ell)^2}. \tag{2.7}$$

has here been introduced along with the operator

$$\psi^* = \frac{\psi_\ell}{a_\ell} + \frac{\psi_g}{a_g}. \tag{2.8}$$

3. Kelvin-Helmholtz Stability

The viscous Kelvin-Helmholtz (VKH) stability analysis is here presented in some detail, which will later be related directly to the stability of discrete representations.

Variable of the steady state $\boldsymbol{v} = \boldsymbol{V}$ will in the following be assigned upper-case symbols.[1] The steady state solution $\boldsymbol{V}$ satisfies the so-called *holdup equation*

$$s(\boldsymbol{V}) = S = 0. \tag{3.1}$$

linearizeing (2.3) about the steady state,

$$\boldsymbol{v} = \boldsymbol{V} + \tilde{\boldsymbol{v}},$$

yields

$$\left(\mathbb{I}(\partial_t - \nu\partial_{xx}) + \frac{\partial \boldsymbol{F}}{\partial \boldsymbol{V}}\partial_x - \frac{\partial \boldsymbol{S}}{\partial \boldsymbol{V}}\right)\tilde{\boldsymbol{v}} = \boldsymbol{0}. \tag{3.2}$$

Let's briefly look at the general solution of (3.2). It may be written

$$\tilde{\boldsymbol{v}}(x,t) = \sum_k \mathbb{P}^{-1}\mathrm{e}^{\mathrm{i}k(x-\mathbb{C}_k t)}\mathbb{P}\,\hat{\boldsymbol{v}}_k^0 \tag{3.3}$$

[1] The state $\boldsymbol{V}$ could also be non-uniform provided the perturbation wavelengths are much smaller than the length scales of the flow state [15].

where $\mathrm{e}^{-\mathrm{i}k\mathbb{C}_k t} = \mathrm{diag}_p(\mathrm{e}^{-\mathrm{i}kc_{k,p}t})$, $c_{k,p}$ being the p-th eigenvalues of $\mathbb{H}_k = \frac{\partial \boldsymbol{F}}{\partial \boldsymbol{V}} - \mathrm{i}k\nu\mathbb{I} + \frac{\mathrm{i}}{k}\frac{\partial \boldsymbol{S}}{\partial \boldsymbol{V}}$ and $\mathbb{P}$ containing their corresponding eigenvectors. $\hat{\boldsymbol{v}}_k^0$ are the Fourier modes of the initial conditions.

Proof. Solution (3.3) satisfies the initial conditions by virtue of $\hat{\boldsymbol{v}}_k^0$ being the Fourier modes of these and $\mathrm{e}^{-\mathrm{i}k\mathbb{C}\cdot 0} = \mathbb{I}$. Further we have

$$\begin{aligned}\partial_t \mathbb{P}^{-1}\mathrm{e}^{-\mathrm{i}k\mathbb{C}t}\mathbb{P} &= \mathbb{P}^{-1}\mathrm{diag}_p(-\mathrm{i}kc_p\mathrm{e}^{-\mathrm{i}kc_p t})\mathbb{P} \\ &= \mathbb{P}^{-1}(-\mathrm{i}k\mathbb{C})\mathrm{e}^{-\mathrm{i}k\mathbb{C}t}\mathbb{P} = -\mathrm{i}k\mathbb{H}\mathbb{P}^{-1}\mathrm{e}^{-\mathrm{i}k\mathbb{C}t}\mathbb{P}.\end{aligned}$$

Directly inserting (3.3) into (3.2) then yields

$$\sum_k \left(-\mathrm{i}k\mathbb{H}_k + k^2\nu\mathbb{I} + \frac{\partial \boldsymbol{F}}{\partial \boldsymbol{V}}\mathrm{i}k - \frac{\partial \boldsymbol{S}}{\partial \boldsymbol{V}}\right)\mathbb{P}^{-1}\mathrm{e}^{\mathrm{i}k(x-\mathbb{C}_k t)}\mathbb{P}\,\hat{\boldsymbol{v}}_k = \boldsymbol{0}.$$

The bracket term cancels at each wavenumber due to the definition of $\mathbb{H}_k$. □

So, the linear response of the system will be through the growth and dispersion of a number of linear waves. We will not bother too much with this general solution, but are interested in the stability behaviour of (3.2) – stable flow occurs if the real component of all eigenvalues is negative or zero. The solution (3.3) is just a linear combination of waves; we re-write it to the form

$$\tilde{\boldsymbol{v}}(x,t) = \sum_k \sum_{p=1,2} \hat{\boldsymbol{v}}_{k,p}\mathrm{e}^{\mathrm{i}k(x-c_{k,p}t)}. \tag{3.4}$$

Inserting (3.4) into (3.2) yields the algebraic system

$$\sum_k \sum_{p=1,2} \frac{\partial \boldsymbol{E}_{k,p}}{\partial \boldsymbol{V}}\hat{\boldsymbol{v}}_{k,p}\mathrm{e}^{\mathrm{i}k(x-c_{k,p}t)} = \boldsymbol{0}, \tag{3.5}$$

with

$$\boldsymbol{E}_{k,p} = \boldsymbol{V}(\delta_t^{k,p} - \nu\delta_{xx}^k) + \boldsymbol{F}\delta_x^k - \boldsymbol{S}. \tag{3.6}$$

Each p-term must solve (3.5) individually if the sum is to be a solution at all times. Suppressing both sum indices we simply write

$$\frac{\partial \boldsymbol{E}}{\partial \boldsymbol{V}}\hat{\boldsymbol{v}} = \boldsymbol{0}. \tag{3.7}$$

The δ-operators appearing in (3.6), accounting for the effect of the partial derivatives, are defined

$$\delta \equiv \frac{\partial \exp \mathrm{i}k(x-ct)}{\exp \mathrm{i}k(x-ct)}. \tag{3.8}$$

Note that these are simple scalars effectively flipping the various terms straight angles in the complex plane:

$$\delta_t = -\mathrm{i}kc, \qquad \delta_x = \mathrm{i}k, \qquad \delta_{xx} = -k^2.$$

Using δ operators will allow solutions to be extended directly to discrete representations.

Because (3.7) is linear we may express it uniquely in terms of one of the disturbance properties, say $\hat{a}_\ell$: $\frac{\partial \boldsymbol{V}}{\partial A_\ell}\hat{a}_\ell =$

$\hat{\boldsymbol{v}}$, yielding

$$\boldsymbol{E}' = \boldsymbol{0}, \tag{3.9}$$

where $\Psi' \equiv \frac{\mathrm{d}\Psi}{\mathrm{d}A_\ell}$. We further define a viscous phase celerity

$$c_\nu \equiv -\frac{\delta_t - \nu\delta_{xx}}{\delta_x}, \tag{3.10}$$

which evaluates to $c_\nu = c + \mathrm{i}k\nu$. Inserting (3.6) and (3.10) into (3.9) now yields

$$\boldsymbol{F}'_{\mathrm{r}}\delta_x - \boldsymbol{S}' = \boldsymbol{0}. \tag{3.11}$$

The components of $\boldsymbol{F}_{\mathrm{r}}$ are the fluxes in a relative frame, moving with (complex) velocity c_ν. $\boldsymbol{F}_{\mathrm{r}}$ equals $\boldsymbol{F}$ with the relative velocities

$$U_{\kappa,\mathrm{r}} = U_\kappa - c_\nu$$

replacing U_κ. Since the mass equation contains no source term, the first component of (3.11), combined with (2.4), yields directly

$$Q_{\kappa,\mathrm{r}} = A_\kappa U_{\kappa,\mathrm{r}} = \text{const.}, \tag{3.12}$$

which relates both velocity components to A_ℓ. The second component of (3.11) yields the *dispersion equation*

$$J'_{\mathrm{r}}\,\delta_x - S' = 0, \tag{3.13}$$

where $\delta_x = \mathrm{i}k$. Using (3.12) one finds

$$J'_{\mathrm{r}} \equiv \frac{\mathrm{d}J_{\mathrm{r}}}{\mathrm{d}A_\ell} = m_y\mathcal{H}' - \left(\rho U_{\mathrm{r}}^2\right)^* \tag{3.14}$$

(see (2.8)) and

$$S' \equiv \frac{\mathrm{d}S}{\mathrm{d}A_\ell} = \mathcal{S}_{A_\ell} + c_\nu\left(\mathcal{S}_{Q_\ell} - \mathcal{S}_{Q_{\mathrm{g}}}\right). \tag{3.15}$$

The source has here been parameterised as function of A_ℓ and Q_κ with

$$\mathcal{S}_{A_\ell} = \left(\frac{\partial\mathcal{S}}{\partial A_\ell}\right)_{Q_\ell,Q_{\mathrm{g}}}, \quad \mathcal{S}_{Q_\ell} = \left(\frac{\partial\mathcal{S}}{\partial Q_\ell}\right)_{A_\ell,Q_{\mathrm{g}}}, \quad \mathcal{S}_{Q_{\mathrm{g}}} = \left(\frac{\partial\mathcal{S}}{\partial Q_{\mathrm{g}}}\right)_{A_\ell,Q_\ell},$$

easily computed for any source $\mathcal{S}$ from discrete state differentials.

Some alternative forms of presenting J'_{r} should also be pointed out, namely

$$J'_{\mathrm{r}} = \frac{\varkappa^2 - \left((\rho U_{\mathrm{r}})^*\right)^2}{\rho^*} = -\rho^*\det\left(\frac{\partial\boldsymbol{F}_{\mathrm{r}}}{\partial\boldsymbol{V}}\right) = -\rho^*\lambda^+_{\mathrm{r}}\lambda^-_{\mathrm{r}}. \tag{3.16}$$

Extracting any particular growth rate or wave celerity from (3.13) is perfectly straight forward and yields

$$c_\nu = b_1 \pm \sqrt{b_1^2 - b_0} \tag{3.17}$$

with

$$b_1 = \frac{1}{\rho^*}\left((\rho U)^* - \frac{1}{2}\frac{\mathcal{S}_{Q_\ell} - \mathcal{S}_{Q_{\mathrm{g}}}}{\delta_x}\right), \quad b_0 = \frac{1}{\rho^*}\left(\frac{\mathcal{S}_{A_\ell}}{\delta_x} - J'\right),$$

and the definitions (3.10), (3.8) and (3.4). The wave resulting from plus in (3.17) will in the following be termed the 'fast wave'. Conversely, the minus wave will be termed the 'slow wave'.

In the case where $\nu = 0$, the marginal stability condition $c_k \in \mathbb{R}$, often called the VKH criterion, has a particularly simple solution. Both J'_{r} and S' are real in this case, so that (3.13) boils down to

$$S' = 0, \qquad J'_{\mathrm{r}} = 0, \tag{3.18}$$

with $S = 0$ from the holdup equation (3.1). We may therefore regard the VKH criterion as the equilibrium state with respect to changes in phase fraction in the frame of a moving wave perturbation. $S' = 0$ then gives the critical wave celerity c_{crit} and wave growth will occur if $J'_{\mathrm{r}}(c_{\mathrm{crit}}) < 0$.

Note that the rate of growth will in (3.13) depend upon the wavenumber k (present in δ_x,) but that the condition for marginal stability, (3.18), will not.

These results are identical to those provided in *e.g.*, [4, 11, 14], though a different approach has been chosen which provides a physical interpretation.

IKH

Let us conclude this section by remarking on some features of the so-called *inviscid Kelvin-Helmholtz* stability criterion (IKH.) This is the stability of the two-fluid model (2.3) without the source term; $s \equiv 0$. From (3.16) we do however see that celerity c must turn complex if the eigenvalues do. The IKH criterion is thus really a test on hyperbolicity. Inspecting the eigenvalues (2.6), the '*inviscid* Kelvin-Helmholtz' (IKH) criterion can thus be written

$$\text{IKH neutral stability:} \qquad \varkappa = 0.$$

From (3.16) we then find the 'inviscid' critical celerity

$$c_{\mathrm{iv,crit}} = \lambda^+_{\mathrm{iv,crit}} = \lambda^-_{\mathrm{iv,crit}} = (\rho u)^*/\rho^*.$$

Notice that the condition for IKH marginal stability, $\varkappa = 0$, does *not* coincide with the VKH criterion (3.18) in the inviscid limit $S \to 0$. This feature is illustrated in Figure 3.1, showing c in the complex plane with the parameters and closures described later in Section 5.2. For clarity, only the superficial gas velocity $Q_{\mathrm{g}}/\mathcal{A}$ is altered and the source S is reduced sequentially towards zero by multiplying it by constant weights. This does not change the critical state, as long as $S \not\equiv 0$, but the rate of growth near the point of marginal VKH stability converges towards zero. Figure 3.1 also shows the limit where the two-fluid model turns elliptical and ill-posed (assumed well-posed otherwise.) There is a region of positive wave growth within

which the viscous model remains hyperbolic. No such region exists in the inviscid model.

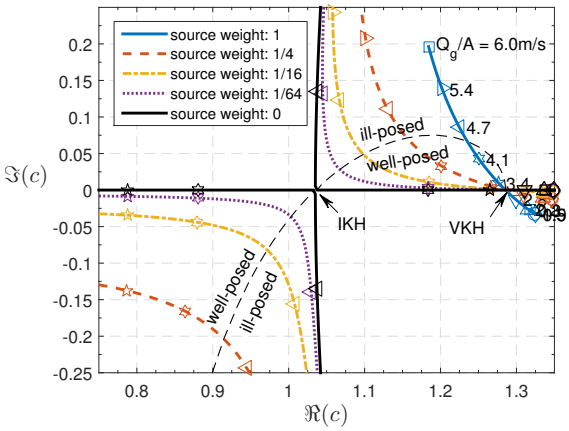

Figure 3.1: Complex celerity c with altering superficial gas velocity $Q_g/\mathcal{A}$. Q_ℓ, A_ℓ and the source differentials are kept constant about the critical VKH state. The source differentials are reduced in steps with a constant 'source weight' between plots. Parameter values are presented in Section 5.2

4. Stability of Discrete Representations

We start the discrete analysis by examining the stability of representations of the two-equation model (2.3). The remarks that then follow relates these results to representations of the four-equation model (2.1). Let $(\delta\psi)_j^n$ symbolize the discrete differentiation operations used in the discretization to represent the partial differentials. System (2.3) may be written

$$(\delta_t \boldsymbol{v})_j^n + (\delta_x \boldsymbol{f})_j = \nu(\delta_{xx}\boldsymbol{v})_j + \boldsymbol{s}_j \tag{4.1}$$

after discretization. ν is here whatever artificial numerical viscosity one chooses to impose on the discretization. For example, $\nu = \Delta x^2/2\Delta t$ and central differences for the spatial derivatives constitutes a Lax-Friedrich scheme.

First, let us regard the stability of (4.1) in the context of a common von Neumann analysis [18]. Introduce $\tilde{\boldsymbol{v}}_j^n = \boldsymbol{v}_j^n - \boldsymbol{V}$ and express $\{\tilde{\boldsymbol{v}}_j^n\}$ and $\{\tilde{\boldsymbol{v}}_j^{n+1}\}$ with spatial Fourier transforms

$$\tilde{\boldsymbol{v}}_j^n = \sum_k \hat{\boldsymbol{v}}_k^n \mathrm{e}^{\mathrm{i}kx_j}, \qquad \tilde{\boldsymbol{v}}_j^{n+1} = \sum_k \hat{\boldsymbol{v}}_k^{n+1}\mathrm{e}^{\mathrm{i}kx_j}. \tag{4.2}$$

Insertion into (4.1) and dropping higher order terms yields a system on the form

$$\sum_k \left(\hat{\boldsymbol{v}}_k^{n+1} - \mathbb{G}_k\hat{\boldsymbol{v}}_k^n\right)\mathrm{e}^{\mathrm{i}kx_j} = \boldsymbol{0},$$

$\mathbb{G}$ being the amplification matrix. We have

$$\hat{\boldsymbol{v}}_k^{n+1} = \mathbb{G}_k\hat{\boldsymbol{v}}_k^n = \mathbb{G}_k\mathbb{G}_k\hat{\boldsymbol{v}}_k^{n-1} = (\mathbb{G}_k)^{n+1}\hat{\boldsymbol{v}}_k^0, \tag{4.3}$$

which provides the result of a common von Neumann analysis, namely that the spectral radius of $\mathbb{G}_k$ must be less or equal to one as a necessary condition for system stability.

Rather than examining $\mathbb{G}_k$, we will use the continuous stability analysis from the previous section for which the solution is already calculated. Notice that the equation (4.2), once (4.3) is inserted, can be written on exactly the form (3.3), provided $\mathbb{G}_k$ is diagonalisable. In this case, $\mathbb{P}$ contains the eigenvectors of $\mathbb{G}_k$ and $c_{k,p}^{\mathrm{d}} = \frac{\mathrm{i}}{k}\frac{\ln\lambda_{\mathrm{G}_k,p}}{\Delta t}$, $\lambda_{\mathrm{G}_k,p}$ being the p-th eigenvalue of $\mathbb{G}_k$. In fact, this is a solution at any point in our discrete system for as long as non-linear effects remain negligible. Again, these are just linear combinations of modes; we may express the discrete point solution analogous to (4.4) by

$$\tilde{\boldsymbol{v}}_j^n = \sum_k \sum_{p=1,2} \hat{\boldsymbol{v}}_{k,p}\mathrm{e}^{\mathrm{i}k(x_j - c_{k,p}^{\mathrm{d}}t_n)}. \tag{4.4}$$

Inserting (4.4) into the discrete model (4.1) and linearizing yields a system analogous to (3.5),

$$\sum_k \sum_{p=1,2} \frac{\partial \boldsymbol{E}_{k,p}^{\mathrm{d}}}{\partial \boldsymbol{V}}\hat{\boldsymbol{v}}_{k,p}\mathrm{e}^{\mathrm{i}k(x_j - c_{k,p}^{\mathrm{d}}t_n)} = \boldsymbol{0}, \tag{4.5}$$

$\boldsymbol{E}^{\mathrm{d}}$ being the discrete equivalent of $\boldsymbol{E}$ from (3.6), differing only in that discrete differential operators

$$\delta^{\mathrm{d}} \equiv \frac{\left(\delta \exp \mathrm{i}k(x - c^{\mathrm{d}}\,t)\right)_j^n}{\exp \mathrm{i}k(x_j - c^{\mathrm{d}}\,t_n)} \tag{4.6}$$

replace δ. These δ^{d} terms, approximating δ, hold all numerical error in its entirety and are simple algebraic expressions. Again, $\boldsymbol{E}^{\mathrm{d}}$ is independent of n and j so that each k,p-term must equal zero individually. The problem is now equivalent to (3.7) and its solution is obtained directly from (3.13)-(3.15), with two celerities for each wavenumber k. Also the discrete viscous celerity c_ν^{d} follow the definition (3.10) using the *discrete* δ^{d} operators. δ^{d} gives the value of δ_t^{d}, which in turn gives the wave growth and dispersion from the chosen time discretization method. For example, the explicit or *forward Euler* time integration has the operator $\delta_t^{\mathrm{d}} = \frac{1}{\Delta t}\left(\mathrm{e}^{-\mathrm{i}kc^{\mathrm{d}}} - 1\right)$. Solving for c^{d} yields $c^{\mathrm{d}} = \frac{1}{k\Delta t}\ln\left(1 + \delta_t^{\mathrm{d}}\Delta t\right)$ with $\delta_t^{\mathrm{d}} = \nu\delta_{xx}^{\mathrm{d}} - c_\nu^{\mathrm{d}}\delta_x^{\mathrm{d}}$ from (3.10).[2]

[2] We may generalize the discrete time differential operators listed in Table 1 by introducing the 'degree of implicitness' r as a linear combination of the forwards and backwards Euler integrations, $\frac{1}{\Delta t}\left(\psi^{n+1} - \psi^n\right) + r(\cdots)^{n+1} + (1-r)(\cdots)^n$. The discrete differential operator for this integration is $\delta_t^{\mathrm{d}} = \frac{1}{\Delta t}\frac{\exp\left(-\mathrm{i}kc^{\mathrm{d}}\right)-1}{r\left(\exp\left(-\mathrm{i}kc^{\mathrm{d}}\right)-1\right)+1}$, giving $c = \frac{1}{k\Delta t}\ln\left(\frac{1+(1-r)\delta_t^{\mathrm{d}}\Delta t}{1-r\delta_t^{\mathrm{d}}\Delta t}\right)$.

			$(\delta\psi)_j^n$	δ^{d}
δ_t	$-\mathrm{i}kc$	explicit	$\frac{1}{\Delta t}\left(\psi_j^{n+1}-\psi_j^n\right)+(\cdots)^n$	$\frac{1}{\Delta t}\left(\mathrm{e}^{-\mathrm{i}\phi_t}-1\right)$
δ_t	$-\mathrm{i}kc$	implicit	$\frac{1}{\Delta t}\left(\psi_j^{n+1}-\psi_j^n\right)+(\cdots)^{n+1}$	$\frac{1}{\Delta t}\left(1-\mathrm{e}^{\mathrm{i}\phi_t}\right)$
δ_t	$-\mathrm{i}kc$	Crank-Nicolson	$\frac{1}{\Delta t}\left(\psi_j^{n+1}-\psi_j^n\right)+\frac{1}{2}(\cdots)^{n+1}+\frac{1}{2}(\cdots)^n$	$\frac{2i}{\Delta t}\tan\frac{\phi_t}{2}$
δ_x	$\mathrm{i}k$	upwind	$\frac{1}{\Delta x}(\psi_j-\psi_{j-1})$	$\frac{2i}{\Delta x}\sin\frac{\phi_x}{2}\,\mathrm{e}^{-\mathrm{i}\frac{\phi_x}{2}}$
δ_x	$\mathrm{i}k$	central difference	$\frac{1}{2\Delta x}(\psi_{j+1}-\psi_{j-1})$	$\frac{\mathrm{i}}{\Delta x}\sin\phi_x$
δ_x	$\mathrm{i}k$	staggered	$\frac{1}{\Delta x}\left(\psi_{j+\frac{1}{2}}-\psi_{j-\frac{1}{2}}\right)$	$\frac{2i}{\Delta x}\sin\frac{\phi_x}{2}$
δ_{xx}	$-k^2$	central difference	$\frac{1}{\Delta x^2}(\psi_{j+1}-2\psi_j+\psi_{j-1})$	$\frac{2}{\Delta x^2}(\cos\phi_x-1)$
$\overline{\psi_j}$	Ψ	mean	$\frac{1}{2}\left(\psi_{j+\frac{1}{2}}+\psi_{j-\frac{1}{2}}\right)$	$\cos\frac{\phi_x}{2}$

Table 1: Some discrete differentiation operators and their corresponding wave operator. $\phi_x = k\Delta x$ and $\phi_t = kc\Delta t$.

δ^{d}-functions for some of the most common discrete differentiations are presented in Table 1. Tabulated operators are presented with phase angles $\phi_x = k\Delta x$ and $\phi_t = kc^{\mathrm{d}}\Delta t$, which represent the phase rotation within a grid cell length or time step, respectively. Constructing similar operators for more complicated interpolations is usually straight forward. For instance, δ_x^{d} in the QUICK scheme is $\frac{1}{8\Delta x}\left(3e^{\mathrm{i}\phi_x}+3-7e^{-\mathrm{i}\phi_x}+\mathrm{e}^{-i2\phi_x}\right)$. Notice that all operators listed in Table 1 are consistent, *i.e.*, they satisfy $\delta^{\mathrm{d}} \to \delta$ as Δx and Δt approach zero.

Remark 1. *The stability behaviour of a discrete representation will converge towards that of the continuous model if*

$$c_\nu^{\mathrm{d}} \equiv -\frac{\delta_t^{\mathrm{d}} - \nu\delta_{xx}^{\mathrm{d}}}{\delta_x^{\mathrm{d}}} \to c + \mathrm{i}k\nu.$$

For this to happen, all δ^{d} operators must be consistent ($\delta^{\mathrm{d}} \to \delta$) and Δx and Δt must approach zero together, smoothly.

Remark 2. *The predicted linear stability is independent of which variable the discrete system is solved for, provided the discrete differentiations δ^{d} are independent of this choice.*

Remark 3. *The predicted linear stability is independent of the form of the discrete system, be it conservative, primitive, four-equation, two-equation, etc., provided the discrete differentiations δ^{d} are independent of these choices.*

Remark 2 and 3 are results of the linearisation. This is briefly illustrated by Taylor expanding any chosen variable $\boldsymbol{v}(\boldsymbol{w})$ about $\boldsymbol{W}$ which yields

$$\tilde{\boldsymbol{v}} = \boldsymbol{V} + \frac{\partial \boldsymbol{V}}{\partial \boldsymbol{W}}\tilde{\boldsymbol{w}} + \mathcal{O}(|\tilde{\boldsymbol{w}}|^2),$$

where $\boldsymbol{V} = \boldsymbol{v}(\boldsymbol{W})$. We may thus define

$$\tilde{\boldsymbol{w}} \equiv \frac{\partial \boldsymbol{W}}{\partial \boldsymbol{V}}\tilde{\boldsymbol{v}}$$

and freely impose variable transformations which does not affect the *linear* stability of the system, provided those transformation matrices exist.

Further, in linearizing an arbitrary discretized variable $\boldsymbol{w}$, and remembering that $(\delta \boldsymbol{W})_j^n = 0$, one finds

$$(\delta \boldsymbol{w})_j^n \to \delta^{\mathrm{d}}\tilde{\boldsymbol{w}} = \frac{\partial \boldsymbol{W}}{\partial \boldsymbol{V}}\delta^{\mathrm{d}}\tilde{\boldsymbol{v}}.$$

The linear system of one variable will thus only be a factorization of the same system in another variable, as alluded to in Remark 2. Also noted in the remark, δ^{d} must be unchanged in the variable transformation of the last equality.

Finally, any type term representation based on the chain rule will, after the linearization, be equivalent. For example

$$\left(\frac{\partial f}{\partial w}\right)_j^n (\delta \boldsymbol{w})_j^n \to \left(\frac{\partial \boldsymbol{F}}{\partial \boldsymbol{W}} + \mathcal{O}(\tilde{\boldsymbol{w}})\right)\delta^{\mathrm{d}}\tilde{\boldsymbol{w}} = \delta^{\mathrm{d}}\tilde{\boldsymbol{f}}.$$

Any discrete representation of system 2.1 will thus be equivalent, provided the discrete differential operators δ_t^{d}, δ_x^{d} and δ_{xx}^{d} are respectively the same.

A consequence of Remark 3 is that four equation formulations of the compressible system (2.1) is equivalent to (4.1) provided we do not mix different discrete differentiations. Examples of commonly used mixed discrete differentiations are convection flux terms of the form

$$(\psi u)_{j+\frac{1}{2}} = \begin{cases} \psi_j \overline{u_{j+\frac{1}{2}}} & \text{if } \overline{u_{j+\frac{1}{2}}} \geq 0, \\ \psi_{j+1}\overline{u_{j+\frac{1}{2}}} & \text{otherwise,} \end{cases}$$

(which linearizes to a central difference in $\tilde{u}$ and an upwind difference in $\tilde{\psi}$.) Staggered grid formulations, in which the differentiation depends on the proximity of the data points, is another example.

Incompressible fluids are assumed in the stability analysis itself in the present work, even though the representation is of the compressible model. This is common practise and provides us with simple, explicit stability expressions, though denies us information about the sonic stability. Including density variations is straightforward, but necessitates solving a higher order dispersion equation numerically.

Example 1 (The stability of a Lax-Friedrich and a local

Lax-Friedrich scheme). *The Lax-Friedrich scheme is commonly written*

$$\frac{\boldsymbol{v}^{n+1}-\boldsymbol{v}^n}{\Delta t}+\frac{\boldsymbol{f}_{j+\frac{1}{2}}-\boldsymbol{f}_{j-\frac{1}{2}}}{\Delta x}=\boldsymbol{s}_j$$

with

$$\boldsymbol{f}_{j+\frac{1}{2}}=\tfrac{1}{2}(\boldsymbol{f}_{j+1}+\boldsymbol{f}_j)-\frac{\nu}{\Delta x}(\boldsymbol{v}_{j+1}-\boldsymbol{v}_j).$$

Numerical viscosities in the Lax-Friedrich scheme and the local Lax-Friedrich scheme are then

$$\nu^{\mathrm{LF}}=\frac{\Delta x^2}{2\Delta t}\qquad\text{and}\qquad\nu^{\mathrm{LLF}}=\frac{\Delta x}{2}\max|\lambda^{\pm}|,$$

respectively. Thus, the local Lax-Friedrich scheme determines the artificial numerical diffusion according to spectral radius of $\frac{\partial \boldsymbol{f}}{\partial \boldsymbol{v}}$. *Eigenvalues, presented in* (2.6), *are computed at the steady state* $\boldsymbol{v}=\boldsymbol{V}$.

These schemes use simple central differences; from Table 1 we find $\delta_x^{\mathrm{d}}=\frac{\mathrm{i}}{\Delta x}\sin\phi_x$ *and* $\delta_{xx}^{\mathrm{d}}=\frac{2}{\Delta x^2}(\cos\phi_x-1)$. *Extracting the stability equations of either scheme is strikingly easy; equation* (3.17) *gives* c_ν^{d}, δ_t^{d} *is obtained from the definition* (3.10) *and the complex wave celerity from the expression of the chosen time discretization.*

Example 2 (The stability of a scheme for the compressible model on a staggered grid). *Say we wish to simulate the compressible model* (2.1) *with a staggered grid discretizations. Staggered grids are quite common with this model as the staggered grid offers a tight stencil for most of the data points and denies so-called checkerboard solutions of the pressure field (see e.g. [8].)*

Upper-case indices J *are used for the mass control volume centre points, and lower-case indices* j *for the momentum ones. The staggered grid is constructed with the momentum control volumes shifted spatially half a cell length behind the mass control volumes, i.e.,* $x_j=x_J-\frac{1}{2}\Delta x$, *as illustrated in Figure 4.1.*

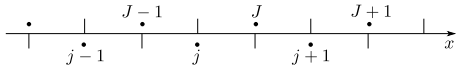

Figure 4.1: The staggered grid; cells and indices.

As opposed to on a co-located grid (non-staggered,) the orientation of the data points is likely to affect the way in which individual terms are discretized, and therefore also the stability behaviour. A particular choice has therefore been made for the variables of this example, namely physically conserved variables of specific mass $\rho a_\kappa=\rho_\kappa a_\kappa$ *and specific momentum* $\rho q_\kappa=\rho_\kappa q_\kappa$. *A sensible discretization can be written*

$$\begin{aligned}(\delta_t\rho a_\kappa)_J^n+(\delta_x\rho q_\kappa)_J^n&=\nu(\delta_{xx}\rho a_\kappa)_J^n\\(\delta_t\rho q_\kappa)_j^n+(\delta_x(\rho qu)_\kappa)_j^n+\overline{a_{\kappa,j}}(\delta_x p)_j^n+g_y\overline{\rho a_{\kappa,j}}(\delta_x h)_j^n&\\=\nu(\delta_{xx}\rho q_\kappa)_j^n+s_{\kappa,j},&\end{aligned}$$

$$a_{\ell,J}+a_{\mathrm{g},J}=\mathcal{A},\quad a_{\kappa,J}=\frac{\rho a_{\kappa,J}}{\rho_{\kappa,J}},$$

with

$$\begin{aligned}p_J&=\mathcal{P}(\rho a_{\ell,J},\rho a_{\mathrm{g},J}),\\h_J&=\mathcal{H}(a_{\ell,J}),\\s_{\kappa,j}&=\mathcal{S}_\kappa\Big(\overline{a_{\kappa,j}},\tfrac{\rho q_{\ell,j}^n}{\overline{\rho_{\ell,j}}},\tfrac{\rho q_{\mathrm{g},j}^n}{\overline{\rho_{\mathrm{g},j}}}\Big),\end{aligned}$$

and arithmetic averaging

$$\overline{w_j}=\tfrac{1}{2}(w_J+w_{J-1})$$

being used in between data points. The momentum convection term $(\delta_x(\rho qu)_\kappa)_j^n$ *is for now kept purely symbolic. Compressibility effects are dismissed in the linear analysis and densities again made constant, as in all VKH analyses. The discrete pressure differential* $(\delta_x p)_j^n$ *can again be eliminated between the momentum equations after dividing eace by* $\overline{a_{\kappa,j}}$. *Thus, a Fourier solution on the form* (4.4) *once more yields a linearized system similar to* (4.5), *but with the variables* $\tilde{\boldsymbol{w}}=(\tilde a_\ell,\tilde a_{\mathrm{g}},\tilde q_\ell,\tilde q_{\mathrm{g}})^T$. *The system reads*

$$\frac{\partial \boldsymbol{E}^{\mathrm{d}}}{\partial \boldsymbol{W}}\hat{\boldsymbol{w}}=\begin{pmatrix}-c_\nu^{\mathrm{d}}\,\hat a_\ell+\delta_x\hat q_\ell\\-c_\nu^{\mathrm{d}}\,\hat a_{\mathrm{g}}+\delta_x\hat q_{\mathrm{g}}\\\left[\left[\frac{\rho}{A}\left(-c_\nu^{\mathrm{d}}\,\hat q+\widehat{\delta_x^{\mathrm{d}}qu}\right)\right]_{\mathrm{g}}^{\ell}+m_y\mathcal{H}'\delta_x^{\mathrm{d}}\hat a_\ell\right.\\\left.-\hat a_\ell\cos\tfrac{\phi_x}{2}\,\mathcal{S}_{A_\ell}-\hat q_\ell\mathcal{S}_{Q_\ell}-\hat q_{\mathrm{g}}\mathcal{S}_{Q_{\mathrm{g}}}\right]\\\hat a_\ell+\hat a_{\mathrm{g}}\end{pmatrix}$$

with $[\cdot]_{\mathrm{g}}^{\ell}=(\cdot)_\ell-(\cdot)_{\mathrm{g}}$. *The tight stencil reduces the error in the* δ_x^{d} *operator to* $\delta_x^{\mathrm{d}}=\frac{2i}{\Delta x}\sin\frac{\phi_x}{2}$ *for those data points located favourably on the staggered grid. In this case only the momentum convection term requires an alternative form of spacial differencing. We split it into* $\hat a_\kappa$ *and* $\hat q_\kappa$ *components and define* $\delta_{a,x}^{\mathrm{d}}$ *and* $\delta_{q,x}^{\mathrm{d}}$ *by*

$$\widehat{\delta_x^{\mathrm{d}}(qu)}_\kappa=2U_\kappa\delta_{q,x}^{\mathrm{d}}\hat q_\kappa-U_\kappa^2\delta_{a,x}^{\mathrm{d}}\hat a_\kappa$$

so that the term become analogues to the previous examples.

The simplest approach is to take the determinant of $\frac{\partial \boldsymbol{E}_p^{\mathrm{d}}}{\partial \boldsymbol{W}}$, *requiring it to be zero for every wavenumber. A discrete version of* (3.13) *then emerges with*

$$\begin{aligned}J'_{\mathrm{r,d}}&=m_y\mathcal{H}'-\left(\rho\left(U^2\tfrac{\delta_{a,x}^{\mathrm{d}}}{\delta_x^{\mathrm{d}}}-2Uc_\nu^{\mathrm{d}}\tfrac{\delta_{q,x}^{\mathrm{d}}}{\delta_x^{\mathrm{d}}}+{c_\nu^{\mathrm{d}}}^2\right)\right)^*,\\S'_{\mathrm{d}}&=\cos\tfrac{\phi_x}{2}\,\mathcal{S}_{A_\ell}+c_\nu^{\mathrm{d}}(\mathcal{S}_{Q_\ell}-\mathcal{S}_{Q_{\mathrm{g}}}).\end{aligned}$$

$J'_{\mathrm{r,d}}$ *is of course identical in form to* (3.14) *if* $\delta_{a,x}^{\mathrm{d}}=\delta_{q,x}^{\mathrm{d}}=$

δ_x^{d}, *and* S'_{d} *to* (3.15) *if not for the arithmetic average, as pointed out in Remark 3.*

An upwind-type interpolation may be chosen for the momentum convection term to complete the example. If we choose, say,

$$(\delta_x(\rho q u)_\kappa)_j^n = \tfrac{1}{\Delta x}\big(\rho a_{\kappa,J}\overline{u_{\kappa,j}}^2 - \rho a_{\kappa,J-1}\overline{u_{\kappa,j-1}}^2\big),$$

with $\overline{u_{\kappa,j}} = \rho q_{\kappa,j}/\overline{a_{\kappa,j}}$, *we get*

$$\delta_{a,x}^{\mathrm{d}} = \tfrac{2i}{\Delta x}\Big(\mathrm{e}^{-\mathrm{i}\frac{\phi_x}{2}}\sin\phi_x - \sin\tfrac{\phi_x}{2}\Big),$$
$$\delta_{q,x}^{\mathrm{d}} = \tfrac{2i}{\Delta x}\mathrm{e}^{-\mathrm{i}\frac{\phi_x}{2}}\sin\tfrac{\phi_x}{2}.$$

This is a rather diffusive choice, made to stabilize the scheme as the staggered conservative variable formulation turns out to provide very little diffusion otherwise. Solving for other variables, such as phase fractions and velocities, is also quite common and would entail other differentiations and result in a different dispersion equation. One may for example look to the example in [14], although this example appear to neglect that some of the information in the momentum equation is dislocated.

Example 3 (The Stability of a Roe Scheme)**.** *The Roe scheme is presented in Appendix A. A viscous matrix, the Roe matrix, is used in this scheme in place of a scalar viscosity. Let's split it into a diagonal part and an off-diagonal part:*

$$\tfrac{\Delta x}{2}\,\mathbb{L}^{-1}|\Lambda|\mathbb{L} = \nu\mathbb{I} + \nu_{\mathrm{T}}\begin{pmatrix}0 & 1/\varkappa\\ \varkappa & 0\end{pmatrix}$$

where

$$\nu = \tfrac{\Delta x}{2}\tfrac{1}{2}\big(|\lambda^+| + |\lambda^-|\big), \qquad \nu_{\mathrm{T}} = \tfrac{\Delta x}{2}\tfrac{1}{2}\big(|\lambda^+| - |\lambda^-|\big)$$

Following the previous procedure, we regain the form (3.13)*, but with*

$$J'_{\mathrm{r,d}} = \frac{(\gamma\varkappa)^2 - \big((\rho U_{\mathrm{r}})^*\big)^2}{\rho^*} = m_y\mathcal{H}' - \big(\rho U_{\mathrm{r}}^2\big)^* - \frac{1-\gamma^2}{\rho^*}\varkappa^2,$$
$$S'_{\mathrm{d}} = \gamma\mathcal{S}_{A_\ell} + c^{\mathrm{d}}_{\nu,\nu_{\mathrm{T}}}\big(\mathcal{S}_{Q_\ell} - \mathcal{S}_{Q_{\mathrm{g}}}\big),$$

where

$$\gamma = 1 - \nu_{\mathrm{T}}\frac{\rho^*}{\varkappa}\frac{\delta^{\mathrm{d}}_{xx}}{\delta^{\mathrm{d}}_x} \quad \text{and} \quad c^{\mathrm{d}}_{\nu,\nu_{\mathrm{T}}} = c^{\mathrm{d}}_{\nu} - \nu_{\mathrm{T}}\frac{(\rho U)^*}{\varkappa}\frac{\delta^{\mathrm{d}}_{xx}}{\delta^{\mathrm{d}}_x}.$$

Central difference operators $\delta_x^{\mathrm{d}} = \frac{\mathrm{i}}{\Delta x}\sin\phi_x$, $\delta^{\mathrm{d}}_{xx} = \frac{2}{\Delta x^2}(\cos\phi_x - 1)$ *are again implied. The viscous terms will disappear form* $c^{\mathrm{d}}_{\nu,\nu_{\mathrm{T}}}$ *if both characteristics are of the same sign; the predicted wave celerity will be very precise as the flow turns unstable.*

In fact, because $\mathbb{L}^{-1}|\Lambda|\mathbb{L}$ *equals the Roe matrix* $\left(\frac{\partial \boldsymbol{F}}{\partial \boldsymbol{V}}\right)^{\mathrm{Roe}}$ *from* (A.1) *if both eigenvalues are positive, and* $-\left(\frac{\partial \boldsymbol{F}}{\partial \boldsymbol{V}}\right)^{\mathrm{Roe}}$ *if both eigenvalues are negative, and because the Roe matrix is designed to obey*

$$\left(\frac{\partial \boldsymbol{F}}{\partial \boldsymbol{V}}\right)^{\mathrm{Roe}}_{j+\frac{1}{2}}(\boldsymbol{v}_{j+1} - \boldsymbol{v}_j) = \boldsymbol{f}_{j+1} - \boldsymbol{f}_j,$$

the stability of the Roe scheme (A.2) *is identical to that of the simple upwind scheme*

$$\boldsymbol{f}_{j+\frac{1}{2}} = \begin{cases}\boldsymbol{f}_j, & \lambda^+ > 0,\ \lambda^- > 0\\ \boldsymbol{f}_{j+1}, & \lambda^+ < 0,\ \lambda^- < 0\end{cases} \tag{4.7}$$

in the case of supercritical flow. Then, the growth and celerity equations once more reduce to (3.17) *with the upwind differentiation* $\delta_x^{\mathrm{d}} = \frac{1}{\Delta x}\big(1 - \mathrm{e}^{-\mathrm{i}\phi_x}\big) = \frac{2i}{\Delta x}\sin\frac{\phi_x}{2}\,\mathrm{e}^{-\mathrm{i}\frac{\phi_x}{2}}$ *and no net artificial viscosity;* $\nu = 0$.

Equation (3.16) *reveals that the VKH criterion* (3.18)*, where wave growth is at an equilibrium with* $c = c_{\mathrm{crit}} \in \mathbb{R}$*, coincides with hydraulically critical flow relative to the perturbation wave. That is, one of the relative eigenvalues* $\lambda_{\mathrm{r}}^{\pm} = \lambda^{\pm} - c$ *equals zero at neutral stability. This means that the Roe scheme is equivalent to* (4.7) *whenever the VKH wave growth is positive.*

5. Numerical Tests and Results

Predictions from a number of schemes will here be presented, namely the explicit and implicit variants of the Lax-Friedrich scheme (Example 1), abbreviated LF, the staggered upwind scheme solved for conservative variables (Example 2), abbreviated UWS, and the Roe scheme (Example 3.) The aim of these comparisons is not to establish a favourite amongst the chosen representations, but to demonstrate how the linear theory provides a powerful simulation support tool. Indeed, multiple considerations are important when choosing a scheme. Many choices can be made both stable and accurate if the simulation parameters are collected with the aid of the hitherto presented linear theory.

5.1. Initial Conditions

Disregarding compressibility, the flow development that springs out from the initial conditions will generally consist of two waves per wavenumber, as given in the solution (3.4) or (4.4). These solutions show that $\hat{\boldsymbol{v}}_k^0 = \sum_p \hat{\boldsymbol{v}}_{k,p}$, each $\hat{\boldsymbol{v}}_{k,p}$ superimposing one of the two $c_{k,p}$ waves. In order for a simulation to provide only a single wave c_{k_1,p_1} the initial conditions must be $\hat{\boldsymbol{v}}^0_{k_1} = \hat{\boldsymbol{v}}_{k_1,p_1}$, $\hat{\boldsymbol{v}}^0_{k\neq k_1} = 0$, where $\hat{\boldsymbol{v}}_{k_1,p_1}$ satisfies (3.7). This was implicitly carried through in the VKH derivation of Section 3 by the transformation $\frac{\partial \boldsymbol{V}}{\partial A_\ell}\hat{a}_\ell = \hat{\boldsymbol{v}}$, which revealed (3.12). (3.12) implies the transformation $\frac{\partial \boldsymbol{V}}{\partial A_\ell} = \big(1, -(\rho U_{\mathrm{r}})^*\big)^T$. Thus, after choosing a volumetric disturbance $\hat{a}_{\ell,k_1}$, a pure c_{k_1,p_1} disturbance wave is obtained by choosing

$$\hat{v}^0_{2,k_1} = [\rho\hat{u}]^\ell_{\mathrm{g}} = -\big(\rho\big(U - c^{\mathrm{d}}_{\nu,k_1,p_1}\big)\big)^*\,\hat{a}^0_{\ell,k_1}. \tag{5.1}$$

Corresponding primitive variables $\hat{u}_\kappa$ are found from the transformation matrix (B.1b).

Figure 5.1 shows a single wavelength $\hat{a}^0_{\ell,k_1}$, simulated twice with an explicit, non-staggered Lax-Friedrich scheme. First, the initial perturbation is applied only to the phase fraction, *i.e.*, $\hat{u}^0_{\kappa,k} \equiv 0$. Expression (5.1) is used for the phase velocities in the second simulation. After a short transition period where both waves interact, the fast wave is seen to dominate the growth of the first simulation. No transition period is observed in the second simulation. Indeed, Liao et al. [14] demonstrated that the wave growth of a simulation with fairly random initial conditions quickly turns independent of these and develops according the the dominant wavelength. A figure similar to 5.1 is also presented in [7] for gravity driven flows in collapsible tubes.

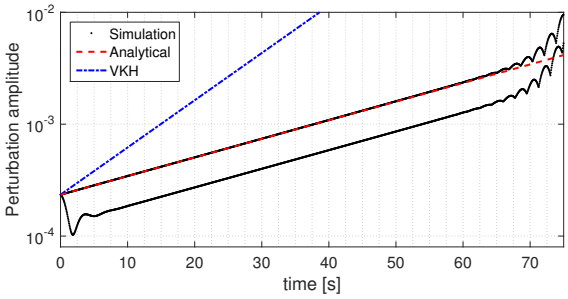

Figure 5.1: Perturbation wave amplitude $\max_j\{\tilde{a}^n_{\ell,j}\}/\mathcal{A}$ vs. time.
Comparing single wave simulation with initial conditions $\hat{\boldsymbol{v}}^0_{k_1} = (\hat{a}^0_{\ell,k_1}, 0)^T$ (plot with initial disturbance) to simulation with initial conditions from (5.1) (plot without initial disturbance); explicit Lax-Friedrich simulation.

5.2. Test Case

The setup for the computational examples will now be presented. This setup is chosen fairly arbitrarily and corresponds to the experimental and numerical setup used in [11, 13, 1, 2]. The friction closures τ_κ and τ_{i} are from the Biberg friction model as presented in [6], also described in the other citations just mentioned. Fixed parameters are presented in Table 2 unless otherwise stated and constitutes a high-pressure, positively inclined flow. The flow state is chosen such that the flow is weakly unstable according the differential VKH criterion. Truly fixed flow parameters in the incompressible flow simulations are the steady state level height $\overline{h} = 0.2d$ and mixture velocity $\mathcal{Q}/\mathcal{A} = 3.4\,\mathrm{m/s}$. The equivalent mean liquid area fraction is $A_\ell/\mathcal{A} = 0.142$ and the chosen friction closures will yield the steady state superficial velocities $Q_\ell/\mathcal{A} \approx 0.154\,\mathrm{m/s}$ and $Q_{\mathrm{g}}/\mathcal{A} \approx 3.245\,\mathrm{m/s}$. The overall properties of the friction closure does not affect the linear stability analysis; only their resulting steady state $S = 0$ and its state derivatives enter into it. In this particular case we have $\mathcal{S}_{A_\ell} = 1.39\mathrm{E}6\,\mathrm{kg/m^6s^2}$, $\mathcal{S}_{Q_\ell} = -9.07\mathrm{E}5\,\mathrm{kg/ms}$ and $\mathcal{S}_{Q_{\mathrm{g}}} = 7.63\mathrm{E}4\,\mathrm{kg/ms}$.

Only numerical parameters are varied in the tests provided in this section. The wavelength is therefore fixed at 30 diameters and the cell lengths are varied. Of course, doing it the other way around would also be insightful, showing which wavelengths one can expect to see on any given grid arrangement.

liquid density	ρ_ℓ	998	$\mathrm{kg/m^3}$
gas density	ρ_{g}	50	$\mathrm{kg/m^3}$
liquid dynamic viscosity	μ_ℓ	1.00E-3	Pa s
gas dynamic viscosity	μ_{g}	1.61E-5	Pa s
internal pipe diameter	d	0.1	m
wall roughness		2E-5	m
pipe inclination	θ	1°	–
mean level height	$\overline{h}$	0.02	m
mixture velocity	$\mathcal{Q}/\mathcal{A}$	3.4	m/s
wavelength	λ	3	m

Table 2: Fixed parameters.

The time steps are regulated using a CFL number, which makes the time step length proportional to the grid cell length (see Remark 1.) The spectral radius will typically be used for selecting the time step length in schemes where the characteristic information is computed, and the CFL number chosen close to unity; $\Delta t = \mathrm{CFL}\,\Delta x/\max_{j,\pm}|\lambda^\pm_j|$ with $\mathrm{CFL} = 0.95$ has been adopted in the presented Roe and local Lax-Friedrich schemes. One of the phase velocities is commonly used in schemes not based on the model eigenstructure. Following [14], the liquid velocity is chosen to limit the time step for the staggered upwind and Lax-Friedrich schemes, $\Delta t = \mathrm{CFL}\,\Delta x/\max_j|u_{\ell,j}|$, with $\mathrm{CFL} = 0.5$. Implicit scheme simulations are performed by iterating on the new state with a 0.5 relaxation factor.

5.3. Predictions

First, Figure 5.2 validates that the theory corresponds precisely to the linear growth of the discrete representations and shows the further development into the nonlinear range. The simulation domain here consists of 128 cells containing a single wave of the prescribed 30 diameter wavelength. Subfigure ((a)) show the wave growth by logarithmically plotting the largest liquid fraction amplitudes. The spatial locations of the wave crest peeks are plotted in Subfigure ((b)), providing the wave speed. Initial conditions are set to accommodate the most unstable wave, which is in these cases the fast wave.

The presented schemes provide a range of different behaviours. We note immediately from Figure 5.2a that all implicit schemes are significantly more diffusive than their explicit counterparts, with numerical diffusion dominating the weak wave growth present in the differential solution. Explicit versions of both the Lax-Friedrich scheme and the staggered upwind scheme eventually reach a final unstable state in which waves grow until the model is no

longer hyperbolic and simulations crash. They do so, however, in quite different manners. Where the Lax-Friedrich scheme first appears diffusive for then to be dominated by a high-wavenumber instability, the upwind scheme simply overpredicts the growth rate of the principle wave. This is further illustrated in Figure 5.3, showing growth rates and snapshots of simulations in which the differential model is stable due to a lower mixture velocity. The former instability will usually be regarded as a 'numerical instability,' commonly identified by the sudden unphysical high-wavenumber growth. Determining, from visual inspection, whether the latter instability is 'physical or not' is however not as straight forward as there are essentially no differences between the natural wave growth and the growth here attributed to numerical errors.

Lastly, the explicit Roe scheme is in Figure 5.2a seen to accurately match the continuous growth rate of the differential model. It also developers into a steady roll-wave solution, which is a valid solution for the differential problem (see [1];) Roe schemes are designed to be well adopted for strongly non-linear flows.

The dispersion error of a 128 cell wave is very small, as seen in Figure 5.2b; wave crest positions are overlapping for as long as the waves remain in the linear range.

(a) Wave growth: Perturbation wave amplitude $\max_j\{\tilde{a}^n_{\ell,j}\}/\mathcal{A}$ vs. time.

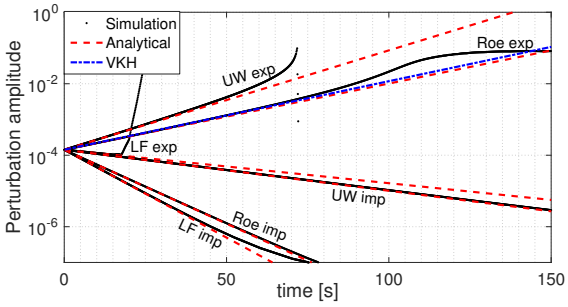

(b) Wave celerity: Perturbation peak location vs. time.

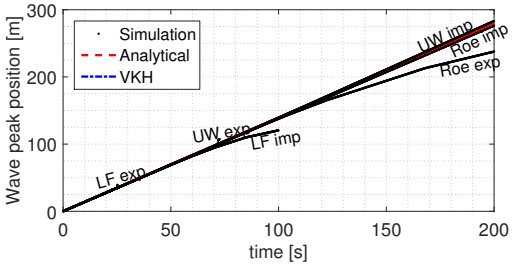

Figure 5.2: Numerical simulations vs. linear theory. Wavelength 30 d. 128 cells; $\phi_x = \pi/64$.

Next we examine the response of the 30 diameter wave

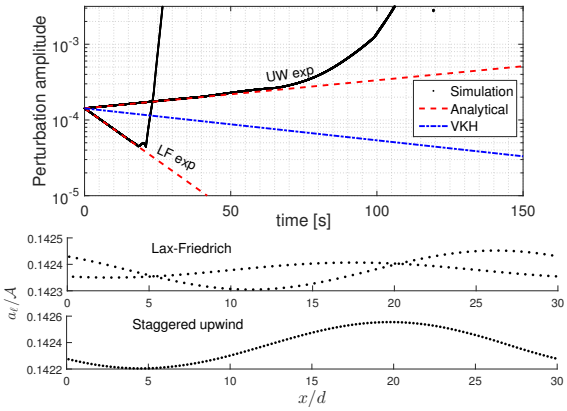

Figure 5.3: Wave growth and accompanying snapshots from unstable Lax-Friedrich and staggered upwind simulations. The mixture velocity $\mathcal{Q}/\mathcal{A}$ equals here 3.1 m/s, at which the differential model is stable.

to changes in the spatial resolution. Figure 5.4 shows the wave growth, or *pulsation*, $k\,\Im(c^{\mathrm{d}})$ [1/s] and the wave celerity $\Re(c^{\mathrm{d}})$ [m/s]. Both the fast and the slow waves are shown, a bold line used for the wave with the higher growth rate. Subfigure ((a)) shows that the Roe scheme gives very accurate growth results for $\phi \leq \pi/32$ (using 64 cells or more) and predicts wave growth for all ϕ. An accurate celerity for the fast wave is observed in Subfigure ((b)) for all ϕ. The explicit Lax-Friedrich and implicit staggered upwind schemes start predicting wave growth around $\phi = \pi/100$, and the implicit Roe and implicit Lax-Friedrich schemes start doing so around $\phi = \pi/210$. The explicit upwind scheme overpredicts the wave growth everywhere above $\phi = \pi/3$. Finally, we see that the explicit Lax-Friedrich scheme becomes unstable around $\phi \gtrsim \frac{2}{3}\pi$, and that it is then the slow wave that has taken over the growth. In fact, from Subfigure ((b)) we see that the 'slow' wave moves faster here. This very particular finding is tested and confirmed in Figure 5.5, where three-celled waves ($\phi_x = \frac{2}{3}\pi$) are applied as the initial condition. Two simulations are shown wherein the initial velocity condition (5.1) is made to accommodate the fast wave in one and the slow wave in the other. The simulations follow the predicted growth behaviour precisely, with the slow wave growing and the fast wave diminishing. After a while though, also the fast wave simulation becomes unstable as the slow wave grows from out of numerical inaccuracies. The plotted points are the maximum amplitudes of the spatial node sets; there is some scattering of these points as the simulated waves are represented by a regularly alternating three-point pattern.

Next we look at how the discrete representations respond to changes in the time step. We have already observed that there is a significant difference in the stability and diffusivity of explicit and implicit time step integra-

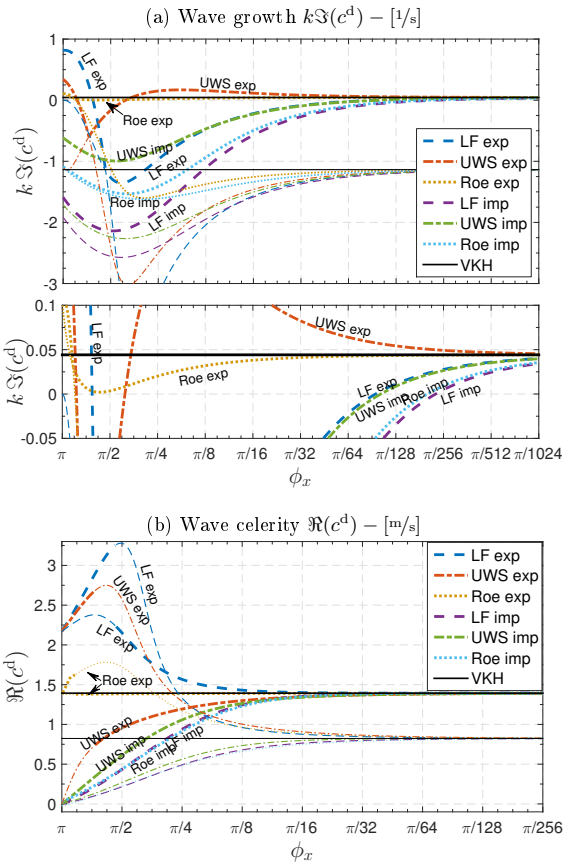

Figure 5.4: Linear theory with varying cell lengths Δx. 30 d wavelength. $\phi_x = k\,\Delta x = 2\pi/(\#$ cells in a wave)

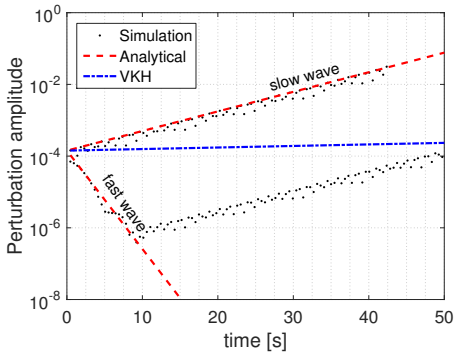

Figure 5.5: Explicit Lax-Friedrich scheme. Three cells per wave; $\phi_x = \frac{2}{3}\pi$.

tion. A strong time step dependence was also noted in [1] for both linear and non-linear wave simulations. Figure 5.6 shows the wave growth and wave celerity as functions of the CFL number. Time steps Δt are selected on the basis of these as per the individual method descriptions, *i.e.*, based on the spectral radius $\max|\lambda^{\pm}|$ in the Roe schemes and on the liquid velocity u_ℓ in the Lax-Friedrich and upwind schemes.

We first note that the explicit and implicit versions of all schemes converge towards the same growth and celerity as the CFL number approaches zero, except for the Lax-Friedrich scheme whose numerical diffusion is inversely proportional to the time step length and thus approaches infinity with reducing CFL number. Growth increases 'with increasing explicitness' for the Roe and upwind scheme. As noted in [1], growth predictions seems to be accurate in explicit schemes based on characteristic information, in this case the Roe scheme, as the CFL number nears unity. An interpretation of why this is is shown in Figure 5.7; information from the upwind mean state would spread nicely over the cell face during the time step limited by CFL ≈ 1. This is particularly so if the cell face fluxes are dominated by information travelling along the path of the quickest characteristic, which seem to be case for supercritical flows.

The celerity graphs shown in Figure 5.6b show that the wave celerity of the Roe scheme becomes increasingly accurate as the time step is reduced. Indeed, the Roe scheme is designed to provide the accurate shock speeds for non-linear problems. Both centred schemes (Roe and Lax-Friedrich) provide better estimates of the wave celerity than the upwind scheme, whose dispersion error is mostly caused by the $\mathrm{e}^{-\mathrm{i}\phi_x/2}$ term generated by the spatially asymmetric upwind formulation.

An alternative way of presenting the schemes' ability to predict wave growth is through a flow map such as that presented in Figure 5.8. This map is of the same 30 diameter wave with 128 cells ($\phi_x = \pi/64$,) and the flow rates are now varying. The CFL-numbers are specified as before and a root searcher is employed to identify the critical point. Numerically searching for the critical state makes this form of visualization more computationally costly than the other plots presented in this section, which were all explicitly computed. Note that Equation (3.18) is not valid in the discrete representations because c_ν^{d} does not equal c^{d}. A consequence is that the marginal stability of a discrete representation is wavelength dependent, while the marginal stability of the differential model is not.

The local Lax-Friedrich scheme, not included amongst the presented results, gave growth results nearly identical to that of the Roe scheme all over. This indicates that it is the characteristic information in the viscous term and time step, rather than the off-diagonal contribution, that accounts for the favourable growth results of the Roe scheme. The local Lax-Friedrich scheme does however not converge

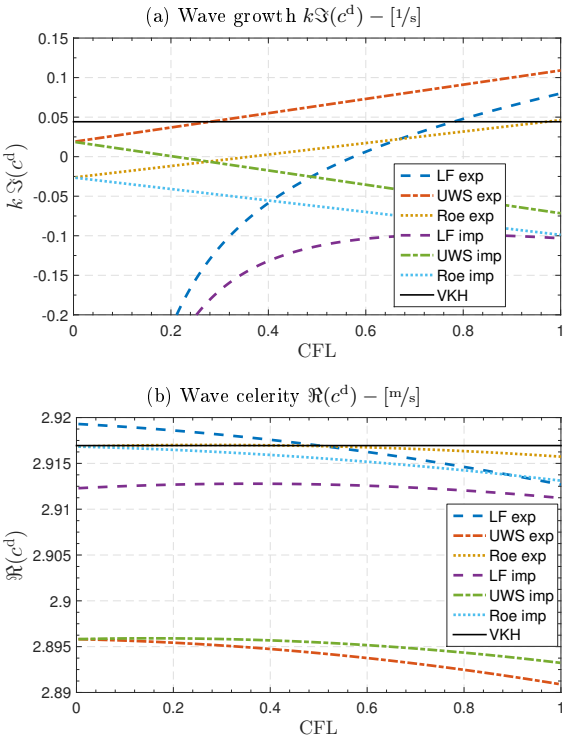

Figure 5.6: Linear theory with varying CFL number, showing the fast wave. 128 celled wave; $\phi_x = \pi/64$

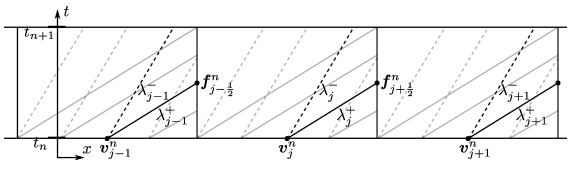

Figure 5.7: Sketch of the characteristic paths at CFL = 1

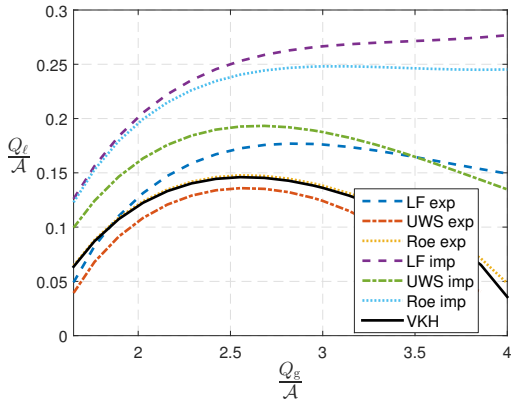

Figure 5.8: Flow map predicted by various schemes. $\phi_x = \pi/64$.

as precisely with respect to the wave celerity $\Re(c^{\mathrm{d}})$ as the Roe scheme, slightly underpredicting the fast celerity in plots similar to those of Figure 5.4b and 5.6b. This scheme was also seen to the have the same type of slow wave instability near $\phi = \pi$ as the simple Lax-Friedrich scheme.

So how does the time integration affect the stability and diffusivity of our solution? Let us examine the influence of the time discretization on a centred, non-staggered scheme without artificially added viscosity (using $\nu = 0$ in the Lax-Friedrich scheme.) Such a scheme, though on a staggered grid, was in [14] deemed the most accurate amongst those tested. Figure 5.9 shows the growth rates and wave celerities of this centred scheme with an explicit and implicit time integration, the liquid velocity based CFL number equalling 0.5. The curves for when the time step approaches zero are also shown. Note first that the high-wavenumber slow-wave instability of the explicit Lax-Friedrich scheme is not present here, attributing that phenomenon to the artificial viscosity ν. The growth rates of the fast wave in Subfigure ((a)) are near mirror images of each other, the numerical error being predominantly attributed to the time step integration. This is important to be aware of; numerical diffusion errors are often thought of as a symptom of the *spatial* discretisation alone.

If the wave growth in this example is dominated by the time integration then we would expect accurate growth results for small time steps Δt. In fact, since $\delta^{\mathrm{d}}_x = \frac{\mathrm{i}}{\Delta x}\sin\phi_x$ is purely imaginary, examining the dispersion equation (3.13)-(3.15) reveals that c^{d}_ν equals the critical VKH celerity exactly at the state of marginal VKH stability. The discrete growth rates at marginal stability will then be the exact VKH growth if also δ^{d}_t is purely imaginary, which is the case if $\Delta t \to 0$. Wave growth shown in Subfigure 5.9a for vanishing time steps is thus very close to the differential growth as the considered state is close to the marginally stable state. Spatial discretisation errors are

manifested foremost in the real components of c, *i.e.*, the wave speeds, which are often deemed to be of secondary importance.

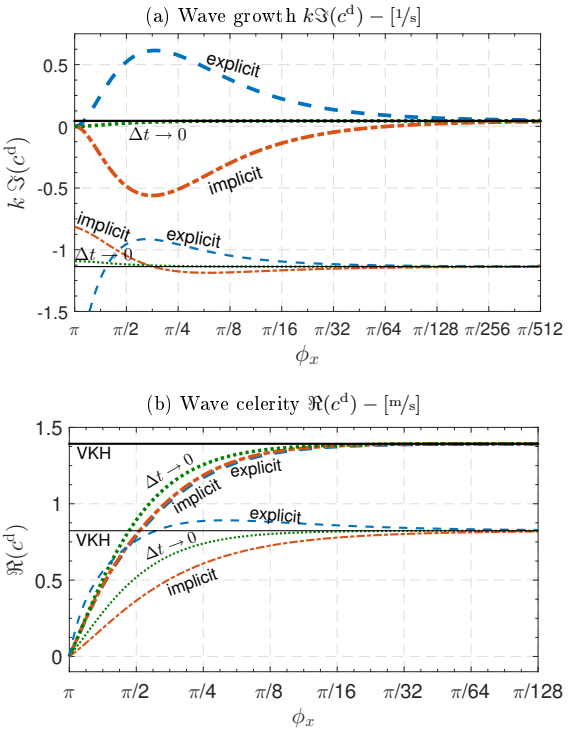

Figure 5.9: Non-staggered centred difference scheme with $\nu = 0$.

Figure 5.10 shows plots similar to the celerity plots shown back in Section 3, Figure 3.1, where viscous and inviscid Kelvin-Helmholtz celerities were compared under varying gas rates. The plots in Figure 5.10 show the errors form the time integration only, *i.e.*, $\delta_t^{\mathrm{d}} = \delta_t = -ikc$, equivalent to the error as Δx approaches zero. A somewhat shorter wave, one diameter in length, has here been chosen to highlight the time integration effect, and the time step is $\Delta t = 0.0025\,\mathrm{s}$.

The general trend of the time integration error is most easily observed from the thinner lines in Figure 5.10, showing the celerities in the inviscid case $S \equiv 0$. These lines would follow the abscissa if not for the error, as in Figure 3.1. The effect of the time integration error is to curve the celerity lines about the origin, convexly if the integration is foremost directed forwards in time (explicit,) and concavely if it is foremost directed backwards in time (implicit.) Errors are thus seen to increase with $\Re(c^{\mathrm{d}})$, which for the fast wave is means that it increases with decreasing $Q_{\mathrm{g}}/\mathcal{A}$. Crank-Nicolson integration, abbreviated 'C-N' in the figure, is seen to be quite accurate in this case.

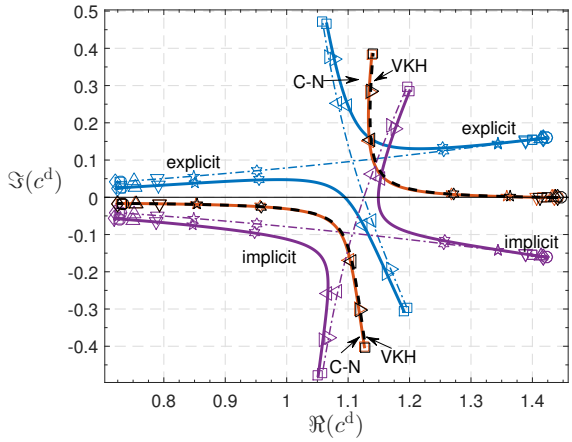

Figure 5.10: Complex celerity c under varying superficial gas velocity $Q_{\mathrm{g}}/\mathcal{A}$, plotted with time integration error only ($\delta_t^{\mathrm{d}} = \delta_t$.) Explicit, implicit and Crank-Nicolson time integrations are shown, cf. Table 1, along with the differential VKH celerity. Thinner lines (dot-dashed) show the corresponding explicit and implicit IKH celerities (where $S \equiv 0$.) The considered wave is one diameter long and $\Delta t = 0.0025\,\mathrm{s}$. State parameters and markers for the superficial gas velocities are the same as in Figure 3.1

6. Concluding Remarks

Practically no computational effort is associated with the linear stability expressions. The examples presented in the previous section demonstrate some of the information instantaneously available through use of linear theory. This theory was shown to give quantitative discretization requirements for obtaining physical wave growth for any given wavelength. Conversely, it tells us what wavelength we can expect to see grow on any given grid, and how these waves move and grow in the discrete representation compared to in the differential model. Numerical errors were shown to manifest in both suppressed and excited growth, the latter being related to what is usually referred to as *numerical instabilities*. Some such instabilities were also observed in the low-wavenumber range where there is very little distinction between numerical and physical instabilities. Discrete stability theory was further able to demonstrate the way in which the time discretization affects predicted stability and to indicate appropriate values for the CFL number.

This information can aid in choosing reliable simulation parameters prior to simulation, and may give insight into whether or not simulation results can be considered physical.

[1] A. H. Akselsen. Characteristic methods and Roe's method for the incompressible two-fluid model for stratified pipe flow. Under review in the International Journal of Multiphase Flow, April 2016.

[2] A. H. Akselsen. The stability of roll-waves in two-phase pipe flow. Submitted to the International Journal of Multiphase Flow, Match 2016.

[3] D. Barnea. Stability analysis of annular flow structure, using a discrete form of the 'two-fluid model'. *International Journal of Multiphase Flow*, 17(6):705 – 16, 1991/11/. ISSN 0301-9322. URL http://dx.doi.org/10.1016/0301-9322(91)90052-5.

[4] D. Barnea and Y. Taitel. Kelvin-Helmholtz stability criteria for stratified flow viscous versus non-viscous (inviscid) approaches. *International Journal of Multiphase Flow*, 19(4):639 – 649, 1993. ISSN 03019322. URL http://dx.doi.org/10.1016/0301-9322(93)90092-9.

[5] Dvora Barnea and Yehuda Taitel. Non-linear interfacial instability of separated flow. *Chemical Engineering Science*, 49(14): 2341 – 2349, 1994. ISSN 00092509. URL http://dx.doi.org/10.1016/0009-2509(94)E0047-T.

[6] D. Biberg. A mathematical model for two-phase stratified turbulent duct flow. *Multiphase Science and Technology*, 19(1):1 – 48, 2007. ISSN 0276-1459. URL http://dx.doi.org/10.1615/MultScienTechn.v19.i1.10.

[7] B.S. Brook, S.A.E.G. Falle, and T.J. Pedley. Numerical solutions for unsteady gravity-driven flows in collapsible tubes: evolution and roll-wave instability of a steady state. *Journal of Fluid Mechanics*, 396:223 – 56, 1999/10/10. ISSN 0022-1120. URL http://dx.doi.org/10.1017/S0022112099006084.

[8] J. H. Ferziger and M. Peric. *Computational Methods for Fluid Dynamics*. Springer, Berlin, 1999.

[9] William D. Fullmer, Victor H. Ransom, and Martin A. Lopez De Bertodano. Linear and nonlinear analysis of an unstable, but well-posed, one-dimensional two-fluid model for two-phase flow based on the inviscid Kelvin-Helmholtz instability. *Nuclear Engineering and Design*, 268:173 – 184, 2014. ISSN 00295493. URL http://dx.doi.org/10.1016/j.nucengdes.2013.04.043.

[10] D. Gidaspow. Multiphase flow and fluidization. *Journal of Fluid Mechanics*, 287:405 – 405, 1995. ISSN 00221120.

[11] H. Holmås. Numerical simulation of transient roll-waves in two-phase pipe flow. *Chemical Engineering Science*, 65(5):1811 – 25, 2010/03/01. ISSN 0009-2509. URL http://dx.doi.org/10.1016/j.ces.2009.11.031.

[12] R.I. Issa and M.H.W. Kempf. Simulation of slug flow in horizontal and nearly horizontal pipes with the two-fluid model. *International Journal of Multiphase Flow*, 29(1):69 – 95, 2003/01/. ISSN 0301-9322. URL http://dx.doi.org/10.1016/S0301-9322(02)00127-1.

[13] G.W. Johnson. *A Study of Stratified Gas-Liquid Pipe Flow*. PhD thesis, Univ. Oslo, 2005. dr. scient.

[14] Jun Liao, Renwei Mei, and James F. Klausner. A study on the numerical stability of the two-fluid model near ill-posedness. *International Journal of Multiphase Flow*, 34(11):1067 – 1087, 2008. ISSN 03019322. URL http://dx.doi.org/10.1016/j.ijmultiphaseflow.2008.02.010.

[15] Himanshu Pokharna, Michitsugu Mori, and Victor H. Ransom. Regularization of two-phase flow models. *J. Comput. Phys.*, 134(2):282–295, July 1997. ISSN 0021-9991. doi: 10.1006/jcph.1997.5695. URL http://dx.doi.org/10.1006/jcph.1997.5695.

[16] H.B. Stewart. Stability of two-phase flow calculation using two-fluid models. *Journal of Computational Physics*, 33(2):259 – 70, 1979/11/. ISSN 0021-9991. URL http://dx.doi.org/10.1016/0021-9991(79)90020-2.

[17] Y. Taitel and A.E. Dukler. A model for predicting flow regime transitions in horizontal and near horizontal gas-liquid flow. *AIChE Journal*, 22(1):47 – 55, 1976/01/. ISSN 0001-1541. URL http://dx.doi.org/10.1002/aic.690220105.

[18] J. VonNeumann and R. D. Richtmyer. A method for the numerical calculation of hydrodynamic shocks. *Journal of Applied Physics*, 21(3):232–237, 1950. doi: http://dx.doi.org/10.1063/1.1699639. URL http://scitation.aip.org/content/aip/journal/jap/21/3/10.1063/1.1699639.

Appendix A. A Roe Scheme

The Roe scheme is commonly written

$$\frac{\boldsymbol{v}_j^{n+1}-\boldsymbol{v}_j^n}{\Delta t}+\frac{\boldsymbol{f}_{j+\frac{1}{2}}-\boldsymbol{f}_{j-\frac{1}{2}}}{\Delta x}=\boldsymbol{s}_j$$

where $\boldsymbol{f}_{j\pm\frac{1}{2}}$ are the fluxes in the solution of the linearized Riemann problem

$$\begin{gathered}\boldsymbol{v}_t+\left(\frac{\partial \boldsymbol{F}}{\partial \boldsymbol{V}}\right)^{\text{Roe}}_{j+\frac{1}{2}}\boldsymbol{v}_x=0\\ \boldsymbol{v}(x,0)=\boldsymbol{v}_j,\ (x<0);\quad \boldsymbol{v}(x,0)=\boldsymbol{v}_{j+1},\ (x>0)\end{gathered}\tag{A.1}$$

at each cell face $x_{j+\frac{1}{2}}$. $\frac{\partial \boldsymbol{F}}{\partial \boldsymbol{V}}^{\text{Roe}}_{j+\frac{1}{2}}$ is the Roe-average of the Jacobian (2.5), constant in each Riemann problem. Using arithmetic mean notation $\overline{w}=\frac{1}{2}(w_j+w_{j+1})$, the Roe matrix of model (2.3) is

$$\frac{\partial \boldsymbol{F}}{\partial \boldsymbol{V}}^{\text{Roe}}_{j+\frac{1}{2}}=\left.\frac{\partial \boldsymbol{f}}{\partial \boldsymbol{v}}\right|_{\overline{\boldsymbol{w}},\widetilde{\mathcal{H}}'};$$

the Jacobian evaluated with the mean primitive variables

$$\overline{\boldsymbol{w}}=(\overline{a}_\ell,\overline{a}_{\text{g}},\overline{u}_\ell,\overline{u}_{\text{g}})^T$$

and

$$\widetilde{\mathcal{H}}'=\begin{cases}\frac{h_{j+1}-h_j}{a_{\ell,j+1}-a_{\ell,j}}, & a_{\ell,j+1}\neq a_{\ell,j}\\ \mathcal{H}'(\overline{a}_\ell), & \text{otherwise}\end{cases}$$

replacing $\mathcal{H}'$.

The flux solution of (A.1) may be written

$$\boldsymbol{f}_{j+\frac{1}{2}}=\overline{\boldsymbol{f}}-\tfrac{1}{2}\mathbb{L}^{-1}|\Lambda|\mathbb{L}(\boldsymbol{v}_{j+1}-\boldsymbol{v}_j)\tag{A.2}$$

where

$$|\Lambda|=\begin{pmatrix}|\lambda^+| & 0\\ 0 & |\lambda^-|\end{pmatrix},\qquad\text{and}\qquad \mathbb{L}=\begin{pmatrix}1 & 1/\varkappa\\ 1 & -1/\varkappa\end{pmatrix}$$

are the absolute eigenvalue and eigenvector matrices of $\left(\frac{\partial \boldsymbol{F}}{\partial \boldsymbol{V}}\right)^{\text{Roe}}_{j+\frac{1}{2}}$, respectively. These are evaluated from (2.6) and (2.7) at the mean state $\overline{\boldsymbol{w}}$ with $\widetilde{\mathcal{H}}'$ replacing $\mathcal{H}'$.

Appendix B. Transformation Matrices

Conversion between primitive variables $\boldsymbol{w}=(a_\ell,a_{\text{g}},u_\ell,u_{\text{g}})^T$ and conservative variables $\boldsymbol{v}=\left(a_\ell,[\rho u]^\ell_{\text{g}}\right)^T$ of the *incompressible* system (obeying (2.4)) is often useful. Transfor-

mation matrices for these are

$$\frac{\partial \boldsymbol{V}}{\partial \boldsymbol{W}} = \begin{pmatrix} 1 & 0 & 0 & 0 \\ 0 & 0 & \rho_\ell & -\rho_\mathrm{g} \end{pmatrix}, \tag{B.1a}$$

$$\frac{\partial \boldsymbol{W}}{\partial \boldsymbol{V}} = \frac{1}{A_\ell A_\mathrm{g} \rho^*} \begin{pmatrix} A_\ell A_\mathrm{g} \rho^* & 0 \\ -A_\ell A_\mathrm{g} \rho^* & 0 \\ \rho_\mathrm{g}(U_\mathrm{g} - U_\ell) & A_\mathrm{g} \\ \rho_\ell(U_\mathrm{g} - U_\ell) & -A_\ell \end{pmatrix}. \tag{B.1b}$$

PAPER VI

A Dual Grid Method for the Compressible Two-Fluid Model which Combines Robust Flux Splitting Methodology with High-Resolution Capturing of Incompressible Dynamics

Andreas H. Akselsen

Under review in
The International Journal of Multiphase Flow

A Dual Grid Method for the Compressible Two-Fluid Model which Combines Robust Flux Splitting Methodology with High-Resolution Capturing of Incompressible Dynamics

A.H. Akselsen*

Department of Energy and Process Engineering, Norwegian University of Science and Technology, Kolbjørn Hejes v. 1B, 7491 Trondheim, Norway

Abstract

The speed of sound in two-phase pipe flow systems is often several orders of magnitude greater than the travelling speed of hydraulic information (volume fractions.) Dynamically simulating such flows requires resolving sonic and hydraulic waves existing at vastly different spatial and temporal scales. If simulated on the same gird, the need for accuracy in hydraulic waves will necessitate an exaggerated resolution of sonic waves. Likewise, time steps restricted by the speed of sound are small compared to the time scales active in hydraulic waves. This constitutes a waist of computational potential. The method proposed herein tackles the problem of computation efficiency by numerically decoupling the sonic and hydraulic spatial scales.

The proposed dual grid method solves a four-equation compressible two-fluid model in a principal grid which robustly accounts for the pressure evolution and conserves mass and momentum. An incompressible two-equation model is at the same time solved on a finer grid, resolving the details of the hydraulic evolution. Information from both model formulations is coupled through the terms of the governing transport equations, providing consistency between the grids. Accurate and finely resolved schemes can then be employed for the incompressible two-fluid model without suffering from the time and stability restrictions otherwise placed by sonic waves. At the same time, the Hybrid Central-Upwind flux splitting scheme of Evje and Flåtten [15] allows for a numerically robust treatment of the sonic waves without losing hydraulic accuracy.

The dual grid method is tested against three dissimilar problems: A shock tube problem, a surge wave – counter current pressure wave problem and a roll-wave case. In all problems, the proposed scheme provided significant increases in computational efficiency and accuracy as compared with a single grid arrangement.

Keywords: dual grid method, hybrid central-upwind scheme, two-phase flow, pipe flow, two-fluid model, Roe scheme

1. Introduction

Dynamic flow simulators have become a vital tools in places like the nuclear industry [18, 8] and the petroleum industry [9, 23]. Predictions of the flow topology, fluid transport and pressure loss, as well as the simulation of potentially damaging or dangerous scenarios, are among the key features of these simulation tools. Many, if not most, such simulators are based on the so-called two-fluid model, which is derived from averaging of the basic conservation equations over district flow fields – for example a gas and a liquid field. Particularly relevant is that the two-fluid model is known for containing the physical mechanism accounting for the hydrodynamic growth of long-wavelength instabilities [7]. Capturing this mechanism has in recent years become a popular method for predicting the flow field topology and flow regime transitions in dynamic simulators [19]. The methodology has even found its way into commercial software for large scale pipeline systems [22, 18].

The characteristic speeds active in gas-liquid flows can differ by several orders of magnitude. Sonic waves are artefacts of fluid compressibility and propagate much quicker than hydraulic waves pertaining to changes in the volume fraction. Yet it is the hydraulic waves which are deemed responsible for the hydrodynamic growth of long-amplitude surface waves, often of primary interest. Sonic waves work on a time scale too small to affect long-amplitude waves significantly, giving the pressure an idle role regarding surface waves. All the same, sonic waves must be computed carefully enough for the simulation procedure to remain numerically stable, placing a strict time step restriction on explicit systems.

An efficient way of allowing for numerical scales suited for the slower hydraulic evolution is to ignore compressibility altogether. The four-equation two-fluid model may

*Corresponding author
Email address: andreas.h.akselsen@ntnu.no (A.H. Akselsen)

then be reduced to a two-equation form as two pressure waves are removed from the system. Keyfitz et al. have analysed the incompressible two-fluid model in a commonly cited work [21]. Wangensteen [30] proposed a flux splitting technique using this incompressible two-fluid model for intermittent single phase – two phase flows (slug flow.) He also constructed a Roe scheme based on Keyfitz' formulation. The incompressible two-fluid model was also used by Holmås [17] to effectively simulate high-pressure flow in the roll-wave regime. These simulations compared favourably to the experimental campaign of Johnson [20]. Holmås' formulation of the incompressible model was based on the formulation used by Watson [31] in deriving analytical solitary roll-wave profile solutions. This formulation is somewhat cleaner than the one investigated by Keyfitz et al.. The present author has used this incompressible model formulation to construct a Roe scheme and schemes based on the principle of characteristics [1], proving very efficient. Numerical requirements for accurately predicting the onset of Kelvin-Helmholtz instabilities have in [2] been examined using linear theory.

The present article revisits the dual grid methodology for resolving hydraulic and sonic waves on separate grids. The principal method was investigated back in [4] using a primitive decoupling based on discriminating between gas and liquid phases. The gas phase was attributed to sonic waves, receiving a coarse grid, while the liquid phase was resolved in greater detail. That method validated the principle, but suffered from grid dependent disturbances due to the projection of large scale hydraulic information down onto a smaller scale. The method presented in the present article bases instead the scale separation on the compressibility itself, projecting only information regarding compressibility down onto the smaller scales. An improved two-way coupling between the two computational grids is achieved using the flux splitting approach due to Evje and Flåtten [15], which also ensures a robust treatment of the pressure. At the same time, the presented dual grid scheme exploits the benefits of the incompressible two-fluid model, in particular its neatness and simple eigenstructure. The resulting method is one which successfully neutralizes the difference in sonic and hydraulic travelling speeds. It allows for simple, explicit and affordable simulation of a family of cases which on a single grid arrangement would require a semi-implicit formulation or a lot of computer power.

This article is structured as follows: The four-equation two-fluid model for stratified pipe flow is briefly presented in Section 2. Section 3 goes through the elements of the dual grid scheme. This includes a summary of the Hybrid Central-Upwind (HCU) flux splitting scheme (Subsection 3.1,) the incompressible two-fluid model and the Roe applied (Subsection 3.3,) and the means of coupling the compressible HCU and incompressible Roe schemes (Subsections 3.4.1 and 3.4.2.) Section 4 is dedicated to demonstrating that the two-grid arrangement does not alter the properties of the HCU scheme presented in [15]. Three numerical tests are given in Section 5: One of the shock tube tests in the original HCU publication is repeated with extra subgrid resolution in Subsection 5.1. Sonic-hydraulic wave interactions are examined in the test case of Subsection 5.2, where a surge-wave meets an oncoming pressure wave. Finally, a roll-wave flow situation is reproduced in Subsection 5.3. This test examines the accuracy and time-step dependency of the Roe scheme, also viewed in light of the two-fluid model's potential and limitations as a predictive tool. A summary is given in Section 6.

2. The Two-Fluid Model for Stratified Pipe Flows

The compressible, equal pressure four-equation two-fluid model for stratified pipe flow results from an averaging of the conservation equations within a flow field over the cross-section area. The model is commonly written

$$\partial_t m_k + \partial_x i_k = 0, \tag{2.1a}$$
$$\partial_t i_k + \partial_x u_k i_k + a_k \partial_x p + g_y m_k \partial_x h = s_k, \tag{2.1b}$$
$$a_\ell + a_\mathrm{g} = \mathcal{A}, \tag{2.1c}$$
$$\rho_k = \rho_k(p). \tag{2.1d}$$

Linear equations of state

$$\rho_k(p) = \rho_{k,0} + \frac{\partial \rho_k}{\partial p}\Big|_0 (p - p_0) \tag{2.2}$$

are used in this work. Excluding energy equations and any temperature dependency in the equations of state makes this model isentropic. Specific mass $m_k = \rho_k a_k$ and momentum $i_k = \rho_k a_k u_k$ are conserved properties. Field k, occupied by either gas, $k = \mathrm{g}$, or liquid, $k = \ell$, is segregated from the other field. p is here the pressure at the interface, assumed the same for each phase. Surface tension has been neglected. h is the height of the interface from the pipe floor, and the term in which it appears originates from approximating a hydrostatic wall-normal pressure distribution. u_k and ρ_k are the mean fluid velocity and density in field k. The momentum sources are $s_k = -\tau_k \sigma_k \pm \tau_\mathrm{i} \sigma_\mathrm{i} - m_k g_x$, where τ_k and σ_k is the skin friction and perimeter of the pipe wall in field k, respectively. τ_i and σ_i refer to the interphase; see Figure 2.1. $g_x = g \sin\theta$ and $g_y = g \cos\theta$ are the horizontal and vertical components of the gravitational acceleration, respectively. θ is here the pipe inclination, positive above datum

The circular pipe geometry governs the relationship between the level height h, the specific areas a_k and the perimeter lengths σ_k and σ_i. These are algebraically interchangeable through a geometric function

$$h = \mathcal{H}(a_\ell) \tag{2.3}$$

whose derivative is $\mathcal{H}' = 1/\sigma_\mathrm{i}$. See e.g. [1] for expressions

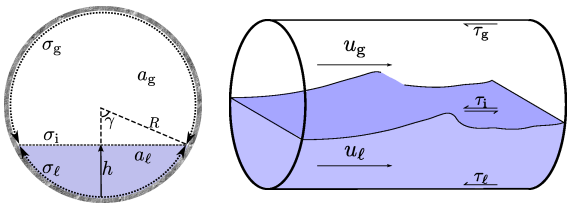

Figure 2.1: Pipe cross-section

of the geometric relationships.

Finally, a *pressure evolution equation* may be obtained from the model (2.1) by summing both mass equations and applying the chain rule to the time differential. Using (2.1c) and (2.1d), we obtain

$$\partial_t p + (\rho_g \partial_x i_\ell + \rho_\ell \partial_x i_g)\kappa = 0, \tag{2.4}$$

where

$$\kappa = \frac{1}{\rho_g a_\ell \frac{\partial \rho_\ell}{\partial p} + \rho_\ell a_g \frac{\partial \rho_g}{\partial p}}. \tag{2.5}$$

The mixture speed of sound may be approximated as $\sqrt{(\rho_\ell a_g + \rho_g a_\ell)\kappa}$ [13].

3. The Dual Grid Scheme

The dual grid scheme uses a two-grid formulation of the same set of transport equations, the purpose of which is to allow for numerical treatment of sonic waves (waves in pressure) and hydraulic waves (waves in volume fraction) at different spatial scales. The grid on which the compressible two-fluid model is solved will be term the *principle grid*. Alongside this, an incompressible two-fluid model is solved on a finer grid which we shall term the *subgrid*. The purpose of the subgrid computations is to capture the hydraulic surface flow details. The purpose of the principle grid computations is to account for compressibility, pressure waves and to maintain a numerically conservative formulation. Information contained in the two grids needs to be coupled for the evolution of the principle and subgrid models to remain consistent.

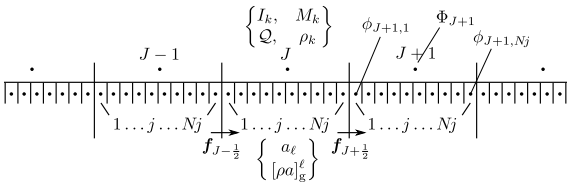

Figure 3.1: Grid arrangement of the dual scale scheme

Figure 3.1 shows a schematic of the two grids in the dual grid scheme. Upper-case symbols will in the following be reserved for discrete variables associated with the principal grid, lower-case symbols being used for subgrid variables. Likewise, upper-case indexation J generally refer to cells of the principal grid, while lover-case indices j pertain to the subgrid cells. Double indexation $\phi_{J,j}$ will be used whenever we wish to specify the position of a subgrid cell in relation to the principal grid, but not consistently. The subgird domain is divided with an integer number of subgrid cells Nj per principal grid cell. For simplicity, we make both grids uniform with Nj constant. The total number of principal grid cells is denoted NJ, and the total number of subgird cells is then $NJ \cdot Nj$.

In the following, the numerical schemes of the principal grid and the subgrid are presented, followed by a description of the method used to couple information from the two.

3.1. Principle Grid – The Hybrid Central-Upwind Scheme

A finite volume differentiation of (2.1) is written in terms of conserved variables

$$\frac{M^{n+1}_{k,J} - M^n_{k,J}}{\Delta t} + \frac{I^n_{k,J+\frac{1}{2}} - I^n_{k,J-\frac{1}{2}}}{\Delta X} = 0, \tag{3.1a}$$

$$\begin{aligned}\frac{I^{n+1}_{k,J} - I^n_{k,J}}{\Delta t} &+ \frac{(UI)^n_{k,J+\frac{1}{2}} - (UI)^n_{k,J-\frac{1}{2}}}{\Delta X} \\ &+ A_{k,J}\frac{P^{n+1}_{J+\frac{1}{2}} - P^{n+1}_{J+\frac{1}{2}}}{\Delta X} \\ &+ g_y M^n_{k,J}\frac{H^n_{J+\frac{1}{2}} - H^n_{J-\frac{1}{2}}}{\Delta X} = S^n_{k,J}.\end{aligned} \tag{3.1b}$$

The Hybrid Central-Upwind (HCU) scheme is used for the terms in (3.1), now briefly presented. See [15] for more details.

Pressure Differentiation

Sonic terms are treated with Lax-Friedrich discretization, which is centred and viscous. Thus formulating the pressure evolution equation (2.4) in a control volume placed over the cell face $J + \frac{1}{2}$ yields

$$\begin{aligned}P^{n+1}_{J+\frac{1}{2}} =& \frac{1}{2}\left(P^n_{J+1} + P^n_J\right) - \frac{\Delta t}{\Delta x}\kappa^n_{J+\frac{1}{2}} \\ &\times \left[\rho^n_{g,J+\frac{1}{2}}\left(I^n_{\ell,J+1} - I^n_{\ell,J}\right) + \rho^n_{\ell,J+\frac{1}{2}}\left(I^n_{g,J+1} - I^n_{g,J}\right)\right].\end{aligned} \tag{3.2}$$

Flux Splitting

The flux splitting in the HCU scheme is based on the way in which the phase fraction is a function of the local pressure and specific mass. Precisely, differentiating $m_k = a_k \rho_k$ gives

$$\mathrm{d}m_k = a_k \frac{\partial \rho_k}{\partial p}\mathrm{d}p + \rho_k \mathrm{d}a_k. \tag{3.3}$$

Inspired by (3.3), convective fluxes $I_k = \rho_k A_k U_k$ are split into a sonic flux F_P, related to pressure changes, and a hydraulic flux F_{A_ℓ}, related to changes in volume fraction,

as follows:

$$I_\ell = A_\ell \frac{\partial \rho_\ell}{\partial p} F_P + \rho_\ell F_{A_\ell}, \tag{3.4a}$$

$$I_\mathrm{g} = A_\mathrm{g} \frac{\partial \rho_\mathrm{g}}{\partial p} F_P - \rho_\mathrm{g} F_{A_\ell}. \tag{3.4b}$$

We wish to differentiate the convective fluxes I_k in such a way that F_P receives sufficient numerical diffusion for robustness while retaining a high accuracy in F_{A_ℓ}. Rearranging (3.4) in terms of F_P and F_{A_ℓ}, we write

$$F_P = \left(\rho_\mathrm{g} I^\mathrm{C}_\ell + \rho_\ell I^\mathrm{C}_\mathrm{g}\right)\kappa, \tag{3.5a}$$

$$F_{A_\ell} = \left(\frac{\partial \rho_\mathrm{g}}{\partial p} A_\mathrm{g} I^\mathrm{U}_\ell + \frac{\partial \rho_\ell}{\partial p} A_\ell I^\mathrm{U}_\mathrm{g}\right)\kappa. \tag{3.5b}$$

The 'C' appended to the phase fluxes in (3.5a) indicates that these are to be computed in a centred manner, with numerical viscosity sufficient to ensure stability in the sonic features of the mass transport. Likewise, the 'U' added to the phase fluxes in (3.5b) indicates that an upwind discretization is to be applied, providing higher accuracy in the flux component attributed to slower hydraulic waves. Later, we will see how this flux splitting can be utilized further in the dual grid scheme by associating the sonic fluxes with a spatial scale which is long in comparison to the spatial scale of the hydraulic fluxes.

Inserting (3.5) back into (3.4) now yields

$$I_\ell = \left(\rho_\mathrm{g} A_\ell \frac{\partial \rho_\ell}{\partial p} I^\mathrm{C}_\ell + \rho_\ell A_\mathrm{g} \frac{\partial \rho_\mathrm{g}}{\partial p} I^\mathrm{U}_\ell + \rho_\ell A_\ell \frac{\partial \rho_\ell}{\partial p}\left(I^\mathrm{C}_\mathrm{g} - I^\mathrm{U}_\mathrm{g}\right)\right)\kappa, \tag{3.6a}$$

$$I_\mathrm{g} = \left(\rho_\ell A_\mathrm{g} \frac{\partial \rho_\mathrm{g}}{\partial p} I^\mathrm{C}_\mathrm{g} + \rho_\mathrm{g} A_\ell \frac{\partial \rho_\ell}{\partial p} I^\mathrm{U}_\mathrm{g} + \rho_\mathrm{g} A_\mathrm{g} \frac{\partial \rho_\mathrm{g}}{\partial p}\left(I^\mathrm{C}_\ell - I^\mathrm{U}_\ell\right)\right)\kappa. \tag{3.6b}$$

Cell face subscripts $J+\frac{1}{2}$ are here implied as (3.6) is formulated at the cell faces of the principal grid. Note that (3.6) is consistent, i.e., it reduces to simple equalities as $I^\mathrm{C}_k, I^\mathrm{U}_k \to I_k$.

Central difference convective fluxes I^C_k have been related to the pressure evolution and should therefore be differentiated in a consistent way. The pressure evolution equation (3.2) is expressed with Lax-Friedrich differentiation, in a control volume covering the cell face $J+\frac{1}{2}$. Convective fluxes of the pressure control volume are thus located at cell centres. Expressing cell face fluxes $I^\mathrm{C}_{k,J+\frac{1}{2}}$ as the arithmetic mean of these, the modified Lax-Friedrich fluxes

$$I^\mathrm{C}_{k,J+\frac{1}{2}} = \frac{1}{2}(I_{k,J+1} + I_{k,J}) - \frac{1}{4}\frac{\Delta x}{\Delta t}(M_{k,J+1} - M_{k,J}) \tag{3.7}$$

are obtained. Upwind fluxes were in [15] chosen

$$I^\mathrm{U}_{k,J+\frac{1}{2}} = \begin{cases} M_{k,J}\overline{U_{k,J+\frac{1}{2}}} & \text{if} \quad \overline{U_{k,J+\frac{1}{2}}} > 0, \\ M_{k,J+1}\overline{U_{k,J+\frac{1}{2}}} & \text{otherwise} \end{cases} \tag{3.8}$$

with $\overline{U_{k,J+\frac{1}{2}}} = \frac{1}{2}(U_{k,J+1} + U_{k,J})$. Momentum convection is in the HCU scheme the natural extension of (3.8), namely

$$(UI)_{k,J+\frac{1}{2}} = \begin{cases} I_{k,J}\overline{U_{k,J+\frac{1}{2}}} & \text{if} \quad \overline{U_{k,J+\frac{1}{2}}} > 0, \\ I_{k,J+1}\overline{U_{k,J+\frac{1}{2}}} & \text{otherwise.} \end{cases} \tag{3.9}$$

3.2. The Incompressible Two-Fluid Model

We will use an incompressible two-equation formulation of the two-fluid model (2.1) as the hydraulic model for the subgrid. The incompressibility of this model eliminates sonic waves such that finer grids can be used without needing reduced time steps.

Reducing the momentum equations of (2.1) with their respective mass equations and eliminating the pressure term between them results in

$$\partial_t \boldsymbol{v} + \partial_x \boldsymbol{f} = \boldsymbol{s} + \boldsymbol{e}, \tag{3.10}$$

with variables, fluxes and sources

$$\boldsymbol{v} = \begin{pmatrix} a_\ell \\ [\rho u]^\ell_\mathrm{g} \end{pmatrix}, \quad \boldsymbol{f} = \begin{pmatrix} a_\ell u_\ell \\ \frac{1}{2}\left[\rho u^2_\ell\right]^\ell_\mathrm{g} + g_y\,[\rho]^\ell_\mathrm{g}\,h \end{pmatrix},$$

$$\boldsymbol{s} = \begin{pmatrix} 0 \\ -g_x\,[\rho]^\ell_\mathrm{g} - \left[\frac{\tau\sigma}{a}\right]^\ell_\mathrm{g} + \tau_\mathrm{i}\sigma_\mathrm{i}\left(\frac{1}{a_\ell} + \frac{1}{a_\mathrm{g}}\right) \end{pmatrix}.$$

The compressibility terms read

$$\boldsymbol{e} = \begin{pmatrix} \frac{a_\ell}{\rho_\ell}(\partial_t + u_\ell \partial_x)\rho_\ell \\ \left[u\,\partial_t \rho + \left(u^2/2 + g_y\,[\rho]^\ell_\mathrm{g}\,h\right)\partial_x \rho\right]^\ell_\mathrm{g} \end{pmatrix}. \tag{3.11}$$

The short-hand

$$[\cdot]^\ell_\mathrm{g} = (\cdot)_\ell - (\cdot)_\mathrm{g}$$

has here been introduced. Assuming incompressible phases, $\boldsymbol{e} \equiv \boldsymbol{0}$, the identities

$$a_\ell + a_\mathrm{g} = \mathcal{A}(x), \qquad a_\ell u_\ell + a_\mathrm{g} u_\mathrm{g} = \mathcal{Q}(t), \tag{3.12}$$

close the model (3.10). The latter identity in (3.12) has been obtained from summing the gas and liquid mass equations and applying the former identity. Both $\mathcal{A}$ and $\mathcal{Q}$ are parametric.

3.3. Subgrid – A Roe Scheme

The Roe scheme presented in [1] will be applied to the incompressible model (3.10) in the subgrid. Model (3.10) is only a second order system and has a conservative form. In

contrast to the compressible two-fluid model (2.1), the incompressible model has an explicit and simple eigenstructure. The conservative form also means that a linearized Riemann solvers does not have to address the issue of an integration path the non-conservative terms appearing in the compressible model, such as Toumi and Kumbaro did in [29].[1]

Quickly summarized, the explicit Roe scheme for (3.10) computes

$$\boldsymbol{v}_j^{n+1} = \boldsymbol{v}_j^n - \frac{\Delta t}{\Delta x}\left(\boldsymbol{f}_{j+\frac{1}{2}}^n - \boldsymbol{f}_{j-\frac{1}{2}}^n\right) + \Delta t\, \boldsymbol{s}_j^n \tag{3.13}$$

with the fluxes

$$\boldsymbol{f}_{j+\frac{1}{2}} = \tfrac{1}{2}(\boldsymbol{f}_{j+1} + \boldsymbol{f}_j) - \tfrac{1}{2}|\hat{\mathbb{A}}|_{j+\frac{1}{2}}(\boldsymbol{v}_{j+1} - \boldsymbol{v}_j). \tag{3.14}$$

$\hat{\mathbb{A}}_{j+\frac{1}{2}}$ is here the Roe average matrix of the Jacobian $\frac{\partial \boldsymbol{f}}{\partial \boldsymbol{v}}$ at the cell face and

$$|\hat{\mathbb{A}}| = \begin{pmatrix} |\lambda^+| + |\lambda^-| & (|\lambda^+| - |\lambda^-|)/\varkappa \\ (|\lambda^+| - |\lambda^-|)\varkappa & |\lambda^+| + |\lambda^-| \end{pmatrix}. \tag{3.15}$$

Eigenvalues of (3.10) are

$$\lambda^\pm = \frac{\frac{\rho_\ell u_\ell}{a_\ell} + \frac{\rho_g u_g}{a_g} \pm \varkappa}{\frac{\rho_\ell}{a_\ell} + \frac{\rho_g}{a_g}}, \tag{3.16}$$

with

$$\varkappa = \sqrt{g_y\,[\rho]_g^\ell \left(\frac{\rho_\ell}{a_\ell} + \frac{\rho_g}{a_g}\right)\mathcal{H}' - \frac{\rho_\ell \rho_g}{a_\ell a_g}(u_g - u_\ell)^2}. \tag{3.17}$$

(3.15) is computed with the following average state properties

$$a_{k,j+\frac{1}{2}} = \tfrac{1}{2}(a_{k,j+1} + a_{k,j}), \tag{3.18a}$$

$$u_{k,j+\frac{1}{2}} = \tfrac{1}{2}(u_{k,j+1} + u_{k,j}), \tag{3.18b}$$

$$\mathcal{H}'_{j+\frac{1}{2}} = \begin{cases} \frac{h_{j+1} - h_j}{a_{\ell,j+1} - a_{\ell,j}} & \text{if } a_{\ell,j+1} \neq a_{\ell,j}, \\ \mathcal{H}'\left(a_{\ell,j+\frac{1}{2}}\right) & \text{otherwise.} \end{cases} \tag{3.18c}$$

Particularly, this Roe scheme reduces to the very simple upwind scheme

$$\boldsymbol{f}_{j+\frac{1}{2}} = \begin{cases} \boldsymbol{f}_j & \text{if} \quad \lambda^+, \lambda^- > 0, \\ \boldsymbol{f}_{j+1} & \text{if} \quad \lambda^+, \lambda^- < 0, \end{cases}$$

if both characteristic velocities are of the same sign. See [1] for more details on this Roe scheme. Time steps are dynamically computed according the characteristics:

$$\Delta t = \mathrm{CFL}\frac{\Delta x}{\max\{|\lambda_j^\pm|\}}. \tag{3.19}$$

[1] One should however note that the weak shock solutions of the Riemann problem will depend on the variables for which the model (3.10) is formulated, in this case $\boldsymbol{v} = (a_\ell, [\rho u]_g^\ell)^T$, so that shocks are not strictly momentum conserving [21].

As we shall see later, the accuracy of the explicit Roe scheme increases significantly as the CFL number approaches one. This can be explained by the way in which the information from the upwind mean state would spread nicely over the cell face during the time integration if CFL ≈ 1, particularly if the cell face fluxes are dominated by information travelling along the path of the quickest characteristic. Figure 3.2 illustrates this. Accuracy dependence

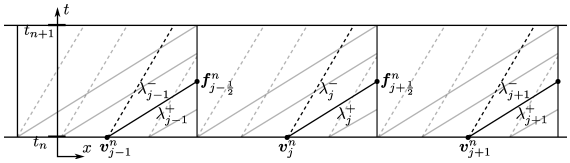

Figure 3.2: Sketch of the characteristic paths at CFL $= 1$.

on the CFL number is likely to be reduced if a higher order state reconstruction is used in the Roe scheme, which would place the approximated state close to the cell face.

As an alternative to the Roe scheme, a simpler form of upwind discretization

$$\begin{aligned} f_{1,j+\frac{1}{2}} &= a_{\ell,j}\max(u_{\ell,j}, 0) + a_{\ell,j+1}\min(u_{\ell,j+1}, 0), \\ f_{2,j+\frac{1}{2}} &= [a_j u_j \max(u_j, 0) + a_{j+1}u_{j+1}\min(u_{j+1}, 0)]_g^\ell \\ &\quad + g_y\,[\rho]_g^\ell\, \tfrac{1}{2}(h_{j+1} + h_j). \end{aligned} \tag{3.20}$$

is also proposed. The max/min formulation has been suggested in order for the flux function to remain continuous.

3.4. Coupling the grids

The compressibility error (3.11) of the subgrid model (3.10), along with its primitive variable formulation, means that average properties of the principal grid and the subgrid may diverge with time, if not treated carefully. However, directly adjusting state variables in the subgird violates the information flow of the system and usually results in numerical disturbance waves transcending from the principal grid down onto the subgrid [4]. Rather than trying to force exact consistency between the grids, we settle for term-by-term couplings in the scheme equation system which ensures either consistency or close proximity. The term-by-term couplings mean that the subgrid methodology can be regarded by way of a scheme extension, which does not necessitate significant alterations to a single grid implementation.

The following measures are suggested:

1. The model (2.1) is restricted to compressibility in the gas phase only.
2. Upwind mass fluxes I_k^{U} of the principal grid is made to correspond precisely to the volumetric flux $f_1 = a_\ell u_\ell$ of the subgrid where the cell faces of the two grids overlap.

3. Subgrid information is applied to the hydraulic terms of the compressible model.

Measure 1 ensures that the phase fraction error in (3.11) vanished in the subgrid model. It further reduces the HCU liquid convection (3.6a) to $I_{\ell,J+\frac{1}{2}} = I^{\mathrm{U}}_{\ell,J+\frac{1}{2}}$. Measure 2 will in turn ensure that that the volumetric flow entering and leaving a cell of the principal grid exactly equals the net flux through the overlapping subgrid cells. Analogous to the divergence theorem, we then achieve $A^n_{\ell,J} = \frac{1}{Nj}\sum_{j=1}^{Nj} a^n_{\ell,J,j}$; that the mean volume fractions remains equal in both grids within the domain of a principal gird cell.

Momentum consistency between grids is not directly imposed. Close proximity of the momentum in the two grids is however maintained, in part through the 3rd measure. Measures 2 and 3 will be described in more detail in Subsection 3.4.2.

Measure 1, of modelling the liquid phase as being incompressible, can be a restrictive assumption. It also means that we sacrifice some of the phaseal symmetry inherent in the HCU and Roe schemes. Volume fraction inconsistencies are however believed to be small for most cases if also the liquid phase is made weakly compressible.

3.4.1. Coupling the Principal Model to the Subgrid Model

After solving the subgrid equations (3.13) for $\boldsymbol{v} = (a_\ell, [\rho u]^\ell_{\mathrm{g}})^T$ new primitive variables are recovered through

$$\begin{aligned} a_\ell &= v_1, \\ a_{\mathrm{g}} &= \mathcal{A} - a_\ell, \end{aligned} \qquad u_\ell = \frac{\rho_{\mathrm{g}}\mathcal{Q} + a_{\mathrm{g}}v_2}{a_{\mathrm{g}}\rho_\ell + a_\ell\rho_{\mathrm{g}}}, \quad u_{\mathrm{g}} = \frac{\rho_\ell\mathcal{Q} - a_\ell v_2}{a_{\mathrm{g}}\rho_\ell + a_\ell\rho_{\mathrm{g}}}. \tag{3.21}$$

We have here 'assumed' incompressibility locally and used (3.12). Densities and the mixture flow rate, which are constant in an incompressible flow situation, are interpolated from the principal grid variables; if $\tilde{\rho}^n_k(x)$ are interpolations of $\{\rho^n_{k,J}\}$ and $\tilde{\mathcal{Q}}^n(x)$ is an interpolation of $\left\{\frac{I^n_{\ell,J}}{\rho^n_{\ell,J}} + \frac{I^n_{\mathrm{g},J}}{\rho^n_{\mathrm{g},J}}\right\}$, then

$$\rho^n_{k,j} = \tilde{\rho}^n_k(x_j), \qquad \mathcal{Q}^n_j = \tilde{\mathcal{Q}}^n(x_j). \tag{3.22}$$

We thus solve the 'locally incompressible' subgrid model (3.13), but impose a compressible evolution indirectly by using spatially varying densities and mixture flow rate in (3.21). The interpolation applied to the tests presented herein are simple quadratic functions with mean value nodes placed in the cell centres. Conservative interpolation is possible, but not deemed worthwhile.

Generally, the use of interpolation from a larger scale down onto a differential model on a smaller scale causes numerical problems around discontinuities. All the same, we allow for interpolation on those variables which are constant in the incompressible model. Unless a discontinuity is imposed as an initial condition, alterations in these discrete variables should occur fairly smoothly through the principal grid due to the diffusiveness of the Lax-Friedrich scheme. Therefore, we do not expect to see formations in density and mixture flow rate which appear discontinuous from the subgrid.

3.4.2. Coupling the Subgrid Model to the Principal Model

We now seek to obtain a two-way coupled grid arrangement, proposing term-by-term couplings to the compressible model (3.1).

The subgrid liquid flow rates $f_1 = a_\ell u_\ell$ from (3.14) can be used for computing upwind mass convection I^{U}_k in (3.6), provided sonic waves do not dominate flow convection. Instead of (3.8), the fluxes

$$\begin{aligned} I^{\mathrm{U}}_{\ell,J+\frac{1}{2}} &= \rho_{\ell,J}\max(f_{1,J+\frac{1}{2}}, 0) \\ &\quad + \rho_{\ell,J+1}\min(f_{1,J+\frac{1}{2}}, 0), \end{aligned} \tag{3.23a}$$

$$\begin{aligned} I^{\mathrm{U}}_{\mathrm{g},J+\frac{1}{2}} &= \rho_{\mathrm{g},J}\max(\mathcal{Q}_J - f_{1,J+\frac{1}{2}}, 0) \\ &\quad + \rho_{\mathrm{g},J+1}\min(\mathcal{Q}_{J+1} - f_{1,J+\frac{1}{2}}, 0) \end{aligned} \tag{3.23b}$$

are proposed. Here, $f_{1,J+\frac{1}{2}} = f_{1,J,Nj+\frac{1}{2}} = f_{1,J+1,\frac{1}{2}}$ according to the index notation of Figure 3.1. The flux splitting of the HCU scheme is perfect for this purpose as the phase fraction component of the mass fluxes are now compounded from the appropriate scales, using a reliable Roe upwind scheme based on the volume fraction characteristics. The pressure component of the mass fluxes is in turn confined to a longer spatial scale and is supplied with sufficient stabilization. As noted earlier, expression (3.24a) provides perfect volume fraction consistency between the principal grid and the subgrid if ρ_ℓ is constant.

Analogous to the HCU scheme, a natural extension of (3.23),

$$\begin{aligned} (UI)_{\ell,J+\frac{1}{2}} &= \rho_{\ell,J}u_{\ell,J,Nj}\max(f_{1,J+\frac{1}{2}}, 0) \\ &\quad + \rho_{\ell,J+1}u_{\ell,J+1,1}\min(f_{1,J+\frac{1}{2}}, 0), \end{aligned} \tag{3.24a}$$

$$\begin{aligned} (UI)_{\mathrm{g},J+\frac{1}{2}} &= \rho_{\mathrm{g},J}u_{\mathrm{g},J,Nj}\max(\mathcal{Q}_J - f_{1,J+\frac{1}{2}}, 0) \\ &\quad + \rho_{\mathrm{g},J+1}u_{\mathrm{g},J+1,1}\min(\mathcal{Q}_{J+1} - f_{1,J+\frac{1}{2}}, 0), \end{aligned} \tag{3.24b}$$

is used for the momentum convection terms in place of (3.9). We have suggested using principal grid density and mixture rate values in (3.23) and (3.24). This is to reduce the influence of interpolation errors from (3.22) should there be a jump in density in the principal grid due to the initial conditions. We may reduce such errors even further by recomputing the convection velocities appearing in (3.24) from (3.21) with the upwind $\{\boldsymbol{v}_{J,j}\}$ from the subgrid and the upwind $\{\rho_{k,J}\}$ and $\{\mathcal{Q}_J\}$ from the principal variables.

Also the non-conservative terms and the source terms of the compressible model (3.1) can be computed using subgrid information. Using skin frictions already com-

puted in the subgrid and taking the average

$$S_k^n = \frac{1}{Nj}\sum_{j=1}^{Nj}\left(-\tau_{k,j}^n\sigma_{k,j}^n \pm \tau_{\mathrm{i},j}^n\sigma_{\mathrm{i},j}^n - m_{k,j}^n g_{x,j}\right) \tag{3.25}$$

is suggested for the compressible model. In as far as the non-conservative level height term is necessary in the integral momentum equations,[2] this may be computed

$$(g_y M_k \partial_x H)_J = \frac{1}{Nj}\sum_{j=1}^{Nj} g_{y,j}(\rho a)_{k,j}\frac{h_{j+1}-h_{j-1}}{2\Delta x}. \tag{3.26}$$

Subgrid information could potentially also help with the non-conservative form of the pressure term in (3.1). The author has experimented with using the two-fluid model to back-compute an incompressible pressure gradient $(\partial_x p)_j$ in each subgrid cell and then adding the averaging difference $\langle a_k\partial_x p\rangle - \langle a_\ell\rangle\langle\partial_x p\rangle$ to the HCU pressure term as a measure of integration path error. However, no real improvement could be observed in the presented numerical tests and the original HCU pressure term is kept unaltered herein.

Figure 3.3 shows an illustration of the dual grid scheme simulation procedure with the couplings presented in this section.

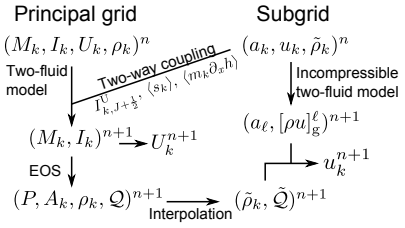

Figure 3.3: Computational procedure of the dual grid scheme.

4. The Contact Discontinuity

The aim of this section is to show that the dual-grid HCU/Roe scheme maintains the nice properties of the single grid HCU scheme concerning contact discontinuities. Disinterested readers may proceed directly to the next section.

Consider the following contact discontinuity, analogous to (32) in [15]:

$$\left\{\begin{array}{c} u_{\ell,\mathrm{L}} = u_{\mathrm{g},\mathrm{L}} = u_{\ell,\mathrm{R}} = u_{\mathrm{g},\mathrm{R}} = u \\ a_{\ell,\mathrm{L}} \neq a_{\ell,\mathrm{R}} \\ p_{\mathrm{L}} = p_{\mathrm{R}} \\ g \to 0 \\ s \equiv 0 \end{array}\right\} \tag{4.1}$$

The two-fluid model (2.1) reduces to

$$\partial_t a_\ell + u\,\partial_x a_\ell = 0$$

under these conditions, and the problem solution is simply a uniform advection of the initial state, i.e., $a_\ell(x,t) = a_\ell(x-ut,0)$. Fluxes corresponding to this solution are

$$i_{k,J+\frac{1}{2}} = \begin{cases}\rho_k a_{k,\mathrm{L}} u & \text{if} \quad u \geq 0,\\ \rho_k a_{k,\mathrm{R}} u & \text{if} \quad u < 0,\end{cases} \tag{4.2a}$$

$$(ui)_{k,J+\frac{1}{2}} = u i_{k,J+\frac{1}{2}} \tag{4.2b}$$

Proposition 1. *Both the Roe scheme (3.14) and the simple upwind scheme (3.20) will with the two-way couplings presented in Subsection 3.4 reduce to the correct upwind fluxes (4.2) in the contact discontinuity (4.1).*

Proof. Note first that $\varkappa$ and the eigenvalues $\lambda^\pm$ in the Roe scheme (3.14), (3.15) will in the contact discontinuity (4.1) reduce to

$$\varkappa \to 0, \qquad \lambda^+, \lambda^- \to u,$$

and so the Roe matrix (3.15) reduces to

$$\tfrac{1}{2}|\hat{\mathbb{A}}|_{j+\frac{1}{2}} \to |u|\mathbb{I}.$$

The weightless limit $g \to 0$, rather then $g = 0$, was chosen in (4.1) to sort out the $0/0$ alien otherwise appearing as the upper right matrix component of $|\hat{\mathbb{A}}|$. The Roe scheme fluxes (3.14) then reduce to

$$\boldsymbol{f}_{j+\frac{1}{2}} \to \begin{pmatrix}\frac{1}{2}(a_{\ell,\mathrm{R}} + a_{\ell,\mathrm{L}})u - \frac{1}{2}(a_{\ell,\mathrm{R}} - a_{\ell,\mathrm{L}})|u| \\ \frac{1}{2}(\rho_\ell - \rho_{\mathrm{g}})u^2\end{pmatrix}.$$

From examination, one finds that also the simple upwind scheme (3.20) will reduce to this same expression.

The sub-to-principal grid couplings (3.23) and (3.24) then reduce to

$$I^{\mathrm{U}}_{\ell,J+\frac{1}{2}} \to \begin{cases}\rho_\ell a_{\ell,\mathrm{L}} u & \text{if} \quad u \geq 0,\\ \rho_\ell a_{\ell,\mathrm{R}} u & \text{if} \quad u < 0,\end{cases}$$

$$I^{\mathrm{U}}_{\mathrm{g},J+\frac{1}{2}} \to \begin{cases}\rho_{\mathrm{g}}(\mathcal{A}\,u - a_{\ell,\mathrm{L}}u) = \rho_{\mathrm{g}} a_{\mathrm{g},\mathrm{L}} u & \text{if} \quad u \geq 0,\\ \rho_{\mathrm{g}}(\mathcal{A}\,u - a_{\ell,\mathrm{R}}u) = \rho_{\mathrm{g}} a_{\mathrm{g},\mathrm{R}} & \text{if} \quad u < 0,\end{cases}$$

and

$$(UI)_{k,J+\frac{1}{2}} \to u I^{\mathrm{U}}_{k,J+\frac{1}{2}}.$$

[2] The two-fluid model (2.1) is unconditionally ill-posed without it, though the discrete equations may be regarded as some well-behaved model of the average state provided sufficient momentum exchange between phases and a sufficiently coarse grid [28, 6, 16].

We have used that $\mathcal{Q}_J = \frac{I_{\ell,J}}{\rho_{\ell,J}} + \frac{I_{g,J}}{\rho_{g,J}}$ reduces to the constant $\mathcal{A}\,u$ in the contact (4.1). These upwind fluxes are identical to (4.2). □

Remark 1. *The centred mass fluxes $I^{\mathrm{C}}_{k,J+\frac{1}{2}}$ are constructed from the original HCU variable of the principal grid only. From Proposition 1 in [15] (proof included,) we have that the $I^{\mathrm{C}}_{k,J+\frac{1}{2}}$ fluxes are 'pressure preserving' as per Definition 1 in said reference, i.e., they will not cause disturbances to the pressure.*

Proposition 2. *Abgrall's principle, that*

> *A flow, uniform in pressure and velocity must remain uniform in the same variables during its time evolution,*

is maintained in the contact discontinuity (4.1) with the two-way coupled model described in Section 3, both with the Roe scheme (3.14) and with the simple upwind scheme (3.20) in the subgrid. Particularly, this means that pressure and velocities will remain uniform and undisturbed.

Proof. Except for the upwind fluxes I^{U}_k, all variables in (3.6) pertain to the principal grid, collected as in the original HCU scheme. Further, by Proposition 1, upwind fluxes I^{U}_k have the property of being consistent with the contact discontinuity solution (4.2). Likewise, centred fluxes I^{C}_k have by Remark 1 the property of being pressure conserving. The other subgrid couplings, (3.25) and (3.26), reduce to zero in the contact (4.1). Lemma 1 and the discussion of Section 6.2 in [15] then applies without further alterations to the proofs presented therein. □

The conclusions just reached also holds for the non-stratified model adjustment (5.1) in the numerical test section as this term also reduces to zero in the contact (4.1).

5. Numerical Tests

5.1. A Shock Tube Problem

Figures 5.1 and 5.2 show the modified large relative velocity (LRV) shock tube problem studied in [15, 13]. Left and right initial states in this problem are

$$\begin{bmatrix} p \\ a_\ell/\mathcal{A} \\ u_{\mathrm{g}} \\ u_\ell \end{bmatrix}_{\mathrm{L}} = \begin{bmatrix} 265\,000\,\mathrm{Pa} \\ 0.7 \\ 65\,\mathrm{m/s} \\ 10\,\mathrm{m/s} \end{bmatrix}, \quad \begin{bmatrix} p \\ a_\ell/\mathcal{A} \\ u_{\mathrm{g}} \\ u_\ell \end{bmatrix}_{\mathrm{R}} = \begin{bmatrix} 265\,000\,\mathrm{Pa} \\ 0.1 \\ 50\,\mathrm{m/s} \\ 15\,\mathrm{m/s} \end{bmatrix}.$$

The two-fluid model simulated in this problem is not the stratified one, but one in which the term replacement

$$m_k(\partial_x h)\, g\cos\theta \to \Delta p\, \partial_x a_k, \tag{5.1}$$
$$\Delta p = \frac{\sigma}{\mathcal{A}} \frac{a_\ell a_{\mathrm{g}} \rho_\ell \rho_{\mathrm{g}}}{\rho_{\mathrm{g}} a_\ell + \rho_\ell a_{\mathrm{g}}} (u_{\mathrm{g}} - u_\ell)^2\, \partial_x a_k$$

is made in the momentum equation (2.1b). This term has a physical interpretation only for bubbly flows, but ensures model hyperbolicity if $\sigma > 1$ (see (3.17).) $\sigma = 1.2$ is used in these simulations. Fluid properties in the equations of state (2.2) are

$$\rho_{\ell,0} = 1000\,\mathrm{kg/m^3}, \qquad \rho_{\mathrm{g},0} = 0\,\mathrm{kg/m^3}, \qquad p_0 = 10^5\,\mathrm{Pa},$$
$$\left.\frac{\partial \rho_\ell}{\partial p}\right|_0 = 10^{-6}\,\mathrm{m^2/s^2}, \quad \left.\frac{\partial \rho_{\mathrm{g}}}{\partial p}\right|_0 = 10^{-5}\,\mathrm{m^2/s^2}.$$

No sources terms are present.

As in [15], $NJ = 100$ principal cells are used with a time step $\Delta t = 0.001\,\mathrm{s}$. $Nj = 50$ subgrid cells are added pre principal cell. The Roe scheme (3.14) is only applicable to the stratified two-fluid model; the simple upwind scheme (3.20) is instead employed for the subgrid model (3.10) with the alteration (5.1). The reference is computed with the single grid HCU scheme using 10 000 grid cells.

Figure 5.1 shows a one-way coupled simulation where only the couplings in Subsection 3.4.1 are applied. Because the HCU scheme is itself unaltered, principal grid and reference results are here identical to those presented in [15], Figure 4. Flow details attributed to hydraulic waves are seen to be accurately recovered in the subgrid. Volume fractions of the two grids are however not within proximity near the location of the initial discontinuity due to the inconsistent mass fluxes in the one-way coupling; the volume fraction suffers from more numerical diffusion in the principal grid than in the subgrid.

The full two-way coupling is adopted in Figure 5.2, showing the same simulation case. Mass proximity is here ensured through the flux (3.24a), errors from liquid compressibility being insignificantly small. Subgrid fluxes (3.23) and (3.24) also provide high accuracy and close proximity in the fluid velocities. Pressure is not computed in the subgird, but the pressure predictions are improved via the other equation terms. Term-by-term testing indicates that the computation of (5.1) from the subgrid data contributed the most to the improved pressure prediction. It is here done analogous to (3.26), namely

$$(\Delta P\, \partial_x A_\ell)_J = \frac{1}{Nj} \sum_{j=1}^{Nj} (\Delta p)_j \frac{a_{\ell,j+1} - a_{\ell,j-1}}{2\Delta x}.$$

Numerical disturbances from the interpolation of ρ_k and $\mathcal{Q}$ across the initial discontinuity, as mentioned in Subsection 3.4.2, are present. These are confined around the location of the initial discontinuity and are quite small.

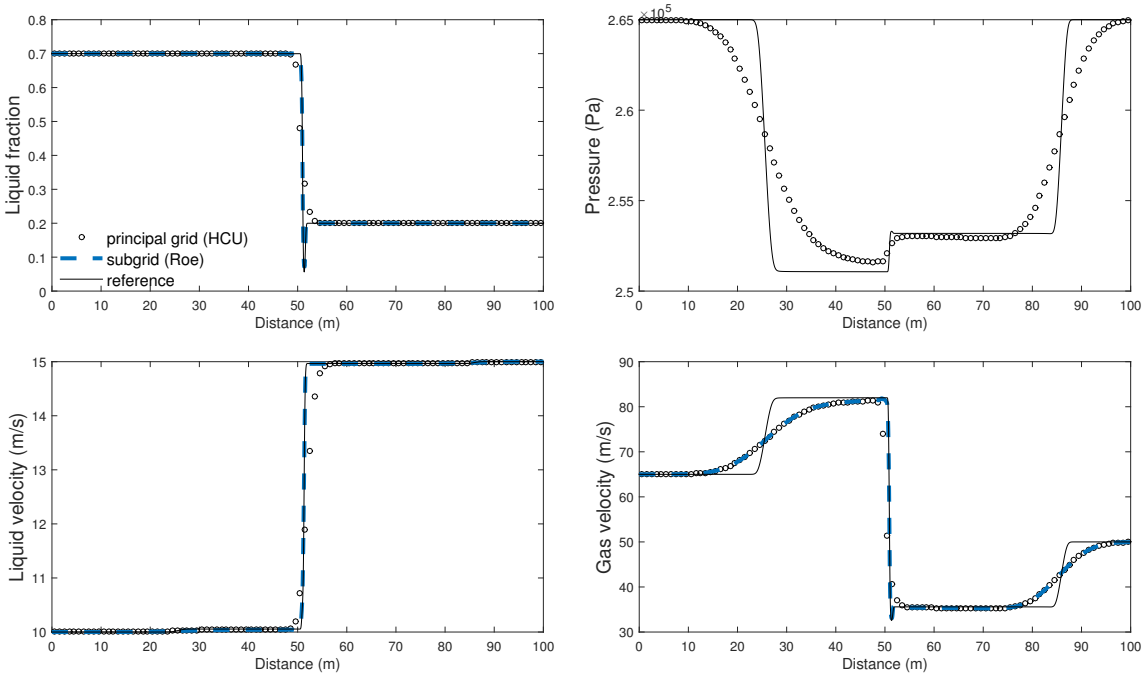

Figure 5.1: Modified LRV shock tube problem, cf. Figure 4 in [15]. $t = 0.1\,\mathrm{s}$, $\Delta t = 0.001\,\mathrm{s}$. One-way coupling (suggestions in Subsection 3.4.2 not applied, i.e., the original HCU scheme is shown.)

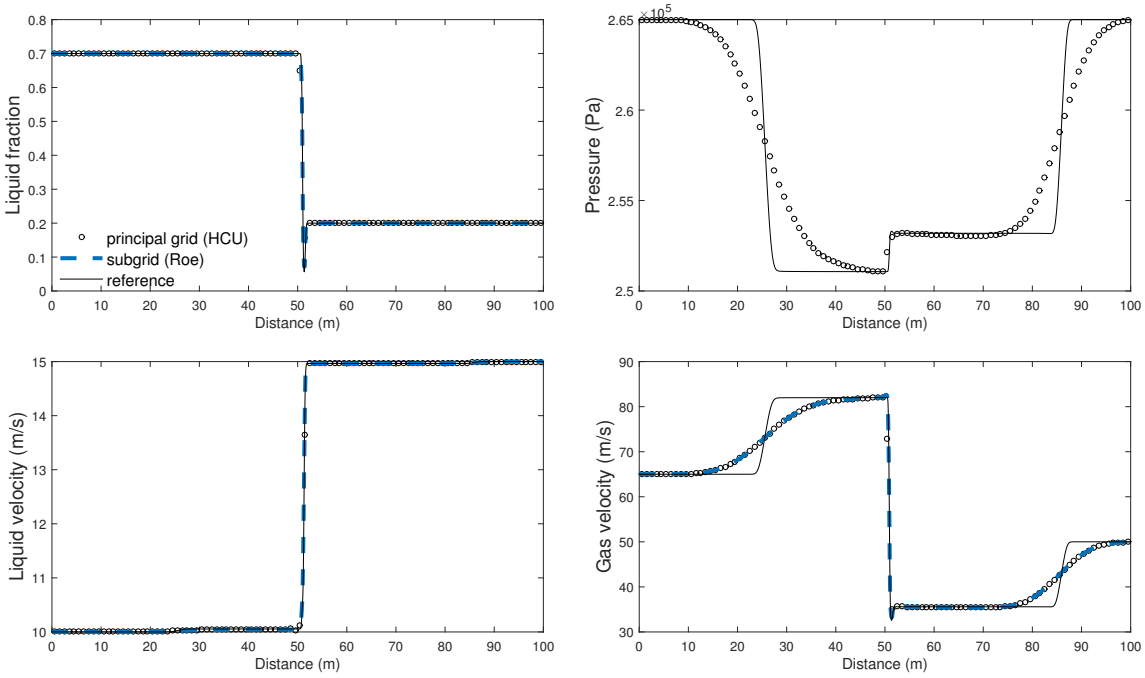

Figure 5.2: Modified LRV shock tube problem, cf. Figure 4 in [15]. $t = 0.1\,\mathrm{s}$, $\Delta t = 0.001\,\mathrm{s}$. Two-way coupling (suggestions in Subsection 3.4.2 applied.)

5.2. Surge Wave

For the final two cases we will use

$$\rho_{\ell,0} = 1000\,\mathrm{kg/m^3}, \quad \rho_{g,0} = 50\,\mathrm{kg/m^3}, \quad p_0 = 8\cdot 10^5\,\mathrm{Pa},$$
$$\left.\frac{\partial \rho_\ell}{\partial p}\right|_0 = 0\,\mathrm{m^2/s^2}, \qquad \left.\frac{\partial \rho_g}{\partial p}\right|_0 = 7.77\cdot 10^{-5}\,\mathrm{m^2/s^2},$$

for the equations of state (2.2), and the fluid and pipe properties

liquid viscosity	μ_ℓ	$1.00\cdot 10^{-3}$	Pa s
gas viscosity	μ_g	$1.61\cdot 10^{-5}$	Pa s
internal pipe diameter	d	0.1	m
wall roughness		$2\cdot 10^{-5}$	m
pipe inclination	θ	0°	–

These properties corresponds to the experimental and numerical setup used in [17, 20, 1, 2, 3]. The friction closures τ_k and τ_i are from the Biberg friction model as presented in [10], also described in the other references just mentioned.

We simulate a 100 m long horizontal pipeline with an initial outlet pressure at 8 bara. A constant liquid mass flux of 1.5 kg/s and a constant gas mass flux of 1.0 kg/s are supplied at the inlet. Liquid fraction through the inlet is 0.19, giving a fairly smooth transition into the test section. The initial state in the pipeline corresponds to the superficial velocities $a_\ell u_\ell/\mathcal{A} \approx 0.1$ m/s, $a_g u_g/\mathcal{A} \approx 3.1$ m/s, which does *not* match the inlet conditions. A surge wave starting from the inlet at $t = 0$ results. Further, at $t = 30$ s, we instantaneously reduce the outlet pressure to 7.5 bara, creating a counter current pressure wave which interacts with the surge wave front and the inlet.[3]

Figure 5.3a shows snapshots of two such surge wave simulations, one with the single grid HCU scheme and one with the dual grid HCU/Roe scheme. 2 000 grid cells are used in the single grid HCU scheme in order for the surge and pressure waves to maintain fairly sharp fronts. A time step $\Delta t = 0.00025$ s, which is close to the numerical stability limit, is used. The dual grid HCU/Roe scheme is on the other hand run with $NJ = 50$ principal cells and $Nj = 25$ subgrid cells per principal cell. The time step is limited to $\Delta t = 0.01$ s by the sonic speeds.

The time of each snapshot increases (unevenly) through the panels, showing the pressure wave as it passes over the surge wave front and bounces back off of the inlet. This pressure wave bounces back and forth across the pipeline a couple of times before dying out. The comparatively slow surge wave front does not react noticeably to the change in flow conditions until the pressure wave makes its second return passing, but hydraulic waves are created at the inlet in tune with the pressure wave oscillations. A similar wave is also created just behind the front of the surge wave itself, though this wave is smaller and is quickly suppressed by the front so that it cannot be seen in the plots.

Compared to the single grid simulation, the dual grid simulation shows a more diffusive pressure wave but nearly no differences in the surge wave. Subgrid phase velocities remain within close proximity of the velocities in the principal gird, the single point subgrid data points forming lines through their respective stair plot of principal grid data. Because of the volume flux consistency, liquid fractions in both grids are always perfectly synchronized without the orientation of one grid disturbing the other.

In terms of efficiency, the single grid HCU scheme requires 8 000 000 cell computations per simulated second. In comparison, the dual grid HCU/Roe scheme simulation requires 5 000 HCU computations and 125 000 Roe cell computations per simulated second. Each HCU computation also includes an equation of state computation.

Resolution in the dual grid scheme was here chosen to give a phase fraction solution similar to the single grid scheme. A reasonable resolution of the sonic wave was also acquired. Indeed, because it is the sonic speeds which limit the time steps we may increase the number of subgird cells even further at only linearly increasing computational cost. A single panel snapshot where the subgrid resolution is $Nj = 100$ is shown in Figure 5.3b. Accuracy is further improved by the fact that the Roe scheme becomes more accurate as the CFL number (3.19) approaches unity [1, 2].

Let's go even further. We use only $NJ = 10$ principal cells and sufficient subgrid cells for the time step to be limited by the hydraulic CFL = 1 limit (3.19), rather than the sonic time restrictions. This warrants the choice of $Nj = 125$ subgrid cells per integral cell, yielding a CFL = 1 time step of $\Delta t \approx 0.058$ s.

Figure 5.4 shows the resulting simulations compared with the same single grid reference. The pressure wave is now more or less lost to numerical diffusion, but the switch from one steady pressure condition to another is accurate. Details of the volume fractions are captured and highly resolved. With the Roe CFL number at unity, a very sharp surge wave front is observed some time after the pressure jump. The inlet wave is also generated appropriately. Its wavelength resembles the wavelength of the reference, suggesting that errors in the sonic velocities are not severe, despite the diffusiveness of the pressure wave. Because of the high CFL number, these inlet waves do not die away from numerical diffusion.

Some discrepancies are seen with the liquid fraction late in the simulation. Most notably, the surge wave front lags slightly behind the single grid front in the later panels, after the pressure jump. Liquid fraction in between the inlet wave and surge wave front is consequently higher. The liquid fraction after the inlet wave is again accurate, suggesting that this discrepancy is caused by the numerical dissipation of the pressure wave. Inlet conditions may also have influenced the discrepancy.

[3] At some locations the eigenvalues (3.16) turn complex at the moment when the pressure wave washes in through the pipeline. This is a not a shortcoming of the subgrid model but of the two-fluid model itself. Simple upwind fluxes (3.20) are used with a reduced time step at the moments when this happens.

Again we consider the increase in computational efficiency. The dual grid HCU/Roe scheme simulation now required about 175 HCU cell computations and 22 000 Roe cell computations per simulated second. Assuming the cost of a Roe and a HCU cell computation are comparable, the single grid HCU simulation is more than 350 times as computationally expensive as the latter dual grid simulation.

5.3. Roll-Waves

Let us finally consider flow in the roll-wave regime. This type of flow is on the whole unaffected by compressibility. Yet, to support expansion, slug formation, changing flow conditions, etc., it is one which we would like to be able to simulate efficiently also with a compressible model. Johnson's high-pressure experimental campaign [20] is chosen for the simulation setup.

We limit ourselves to a single high gas rate case from Johnson's campaign. Superficial velocities are $a_g u_g/\mathcal{A} \approx 3.50\,\mathrm{m/s}$ and $a_\ell u_\ell/\mathcal{A} \approx 0.25\,\mathrm{m/s}$, and the test section is horizontal. These superficial velocities are acquired by a $1.970\,\mathrm{kg/s}$ liquid injection rate and a $1.385\,\mathrm{kg/s}$ gas injection rate at the inlet. This is a low-amplitude wave case in which the two-fluid model is fairly well behaved.[4] A pointwise random disturbance within $\pm 5\%$ of the injection rates is imposed at the inlet at each time step. $NJ = 20$ principal grid cells are used with $Nj = 100$ subgrid cells per principal cell. The high number of subgrid cells is again chosen not for the purpose of spatial resolution, which would be fine also with fewer subgrid cells, but to allow for a hydraulic CFL number near unity without violating the sonic time step restrictions.

Figure 5.5 shows simulations at four different CFL numbers; CFL = 0.5, 0.75, 0.95 and 1.0. High wavenumber growth is severely reduced for the lower CFL numbers, as can be seen from the profile plots of Figure 5.5a. Growth of all but the shortest wavelengths takes place in all simulations, but the rate of growth compared to the travelling time means that the time traces observed in Figure 5.5b differ in each case. Growth of smaller wavelengths is hampered the most, which in turn affects the observed wave frequency. The wavelength distribution will remain inlet dependent if the growth and travelling time is insufficient for the waves to develop well into the non-linear wave range. A time trace of the relevant experiment from Johnson's campaign [20] is also shown in Figure 5.5b, although experimental evaluation is not our primary interest in this test.

[4] Hydraulic eigenvalues can occasionally turn complex locally at a wave peak at some time or another during the simulation. Again, this is a feature of the two-fluid model (2.1). We will here simply bypass the issue by limiting the liquid fraction locally according to $\varkappa^2 > 0$.

Let us for a moment consider the linear growth of the two-fluid model. By linear growth we mean the growth of perturbations before they turn large enough for non-linear effects to hamper of enforce the growth. Figure 5.6 presents graphs computed from the linear theory presented in [1]. Growth rate ω expresses the exponential/geometric perturbation growth of the differential/discrete two-fluid model. Such graphs are drawn at virtually no computational expense and provide great insight into the accuracy of our discrete representations. The figure shows the linear growth of the differential two-fluid model (3.10), together with the linear growth of the Roe scheme using $NJ \cdot Nj = 2\,000$ grid cells at varying CFL numbers. Linear growth in the differential two-fluid model is strongest in the shortest wavelengths, with no finite wavelength of dominant growth (surface tension neglected.) As a consequence, the wavelength distribution that emerges from out of the initial linear growth range will not be predisposed to any particular finite wavelength attributed to the model itself. Discrete representations, on the other hand, will suffer from numerical dissipation around the higher wavenumbers and will therefore emerge with a dominant wavelength.

Now we consider the simulation efficiency. Time steps for the CFL = 0.95 simulation are around $\Delta t = 6 \cdot 10^{-3}\,\mathrm{s}$. The equivalent time step for a single grid HCU simulation with $NJ = 2\,000$ grid cells is $\Delta t = 7.5 \cdot 10^{-5}\,\mathrm{s}$. We might be tempted do say that the increase in computational efficiency is approximately $6 \cdot 10^{-3}\,\mathrm{s}/7.5 \cdot 10^{-5}\,\mathrm{s} = 80$, yet this does not take into account the accuracy-time step dependency shown earlier. Indeed, considering the tiny time step imposed by the sonic restrictions, linear growth with 2 000 HCU cells will be comparable to the graph marked 'CFL $\to$ 0' in Figure 5.6. A snapshot of this simulation is in fact shown in the second panel of Figure 5.5a. For the wave growth to be similar to the 'CFL = 0.75' graph in Figure 5.6, and thus be comparable to the CFL = 0.75 plots of Figure 5.5, something like $NJ = 10\,000$ grid cells are needed. The time step then will be around $\Delta t = 1.5 \cdot 10^{-5}\,\mathrm{s}$, needing approximately $6.7 \cdot 10^{8}$ computations per simulated second. Computational expense is then 2 000 times that of the dual grid simulations.

Naturally, the accuracy of higher order schemes may be less dependent on the CFL number, as mentioned back in Subsection 3.3. Likewise, implicit time integration allows for time steps which are unrestricted by the sonic speeds. However, the resolution will be comparable to the graph marked 'CFL = 1.0, implicit' in Figure 5.6 if the scheme is first order accurate with a plain backwards Euler time integration. Weakly implicit schemes [14], which elevates the sonic CFL restriction while retaining explicitness in the hydraulic terms, is perhaps a better alternative. Large time-step schemes [25, 24] can also be used to bypass the stringent acoustic CFL-restrictions.

We'll conclude this section by making a few remarks

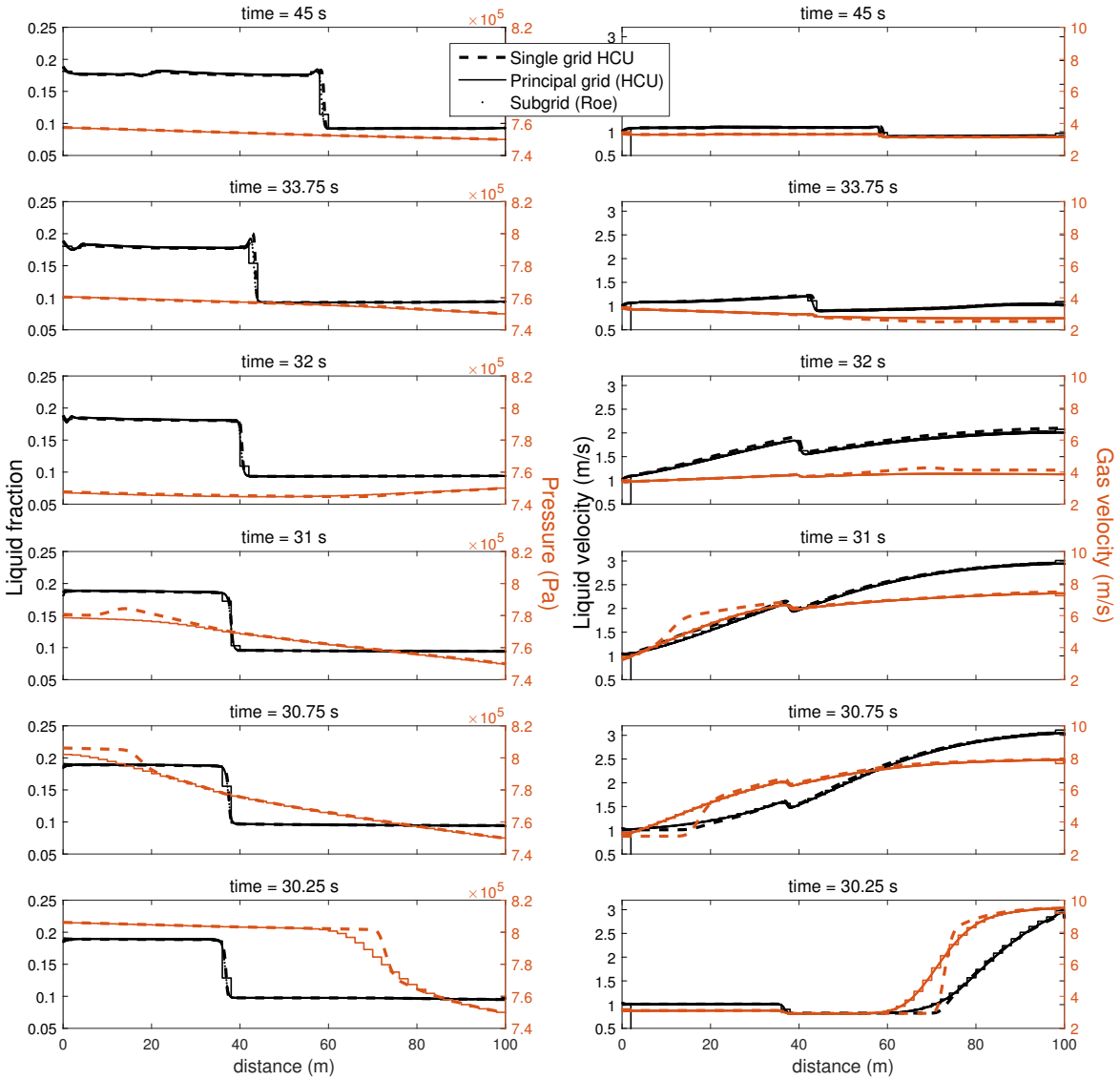

(a) $\{NJ = 50,\ Nj = 25,\ \Delta t = 0.01\,\mathrm{s}\}$

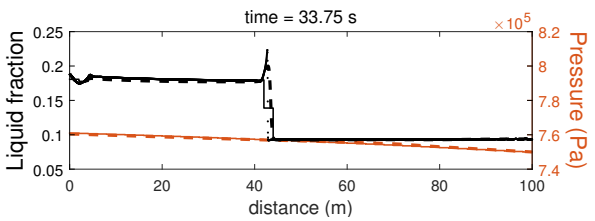

(b) $\{NJ = 50,\ Nj = 100,\ \Delta t = 0.01\,\mathrm{s}\}$

Figure 5.3: Surge wave – counter current pressure wave. Dual grid HCU/Roe scheme vs. single grid HCU scheme with $\{NJ = 2000,\ \Delta t = 0.00025\,\mathrm{s}\}$.

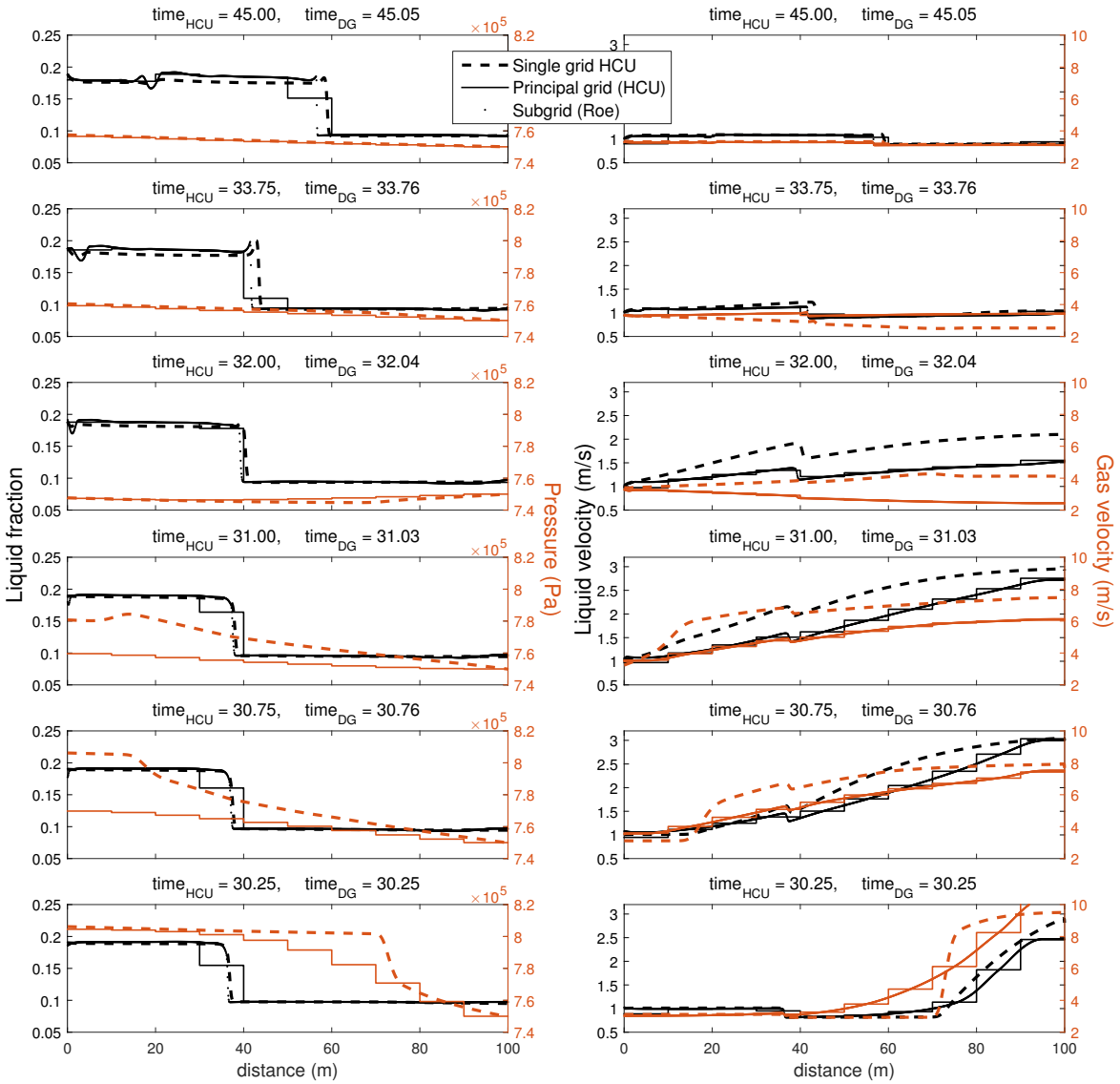

Figure 5.4: Surge wave – counter current pressure wave. Dual grid HCU/Roe scheme with $\{NJ = 10,\ Nj = 125,\ \Delta t \approx 0.058\,\mathrm{s}\ (\mathrm{CFL} = 1)\}$ vs. single grid HCU scheme with $\{NJ = 2000,\ \Delta t = 0.00025\,\mathrm{s}\}$.

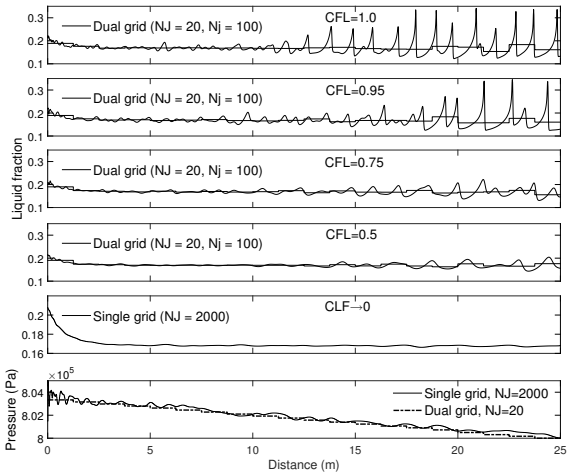

(a) Simulation snapshots.

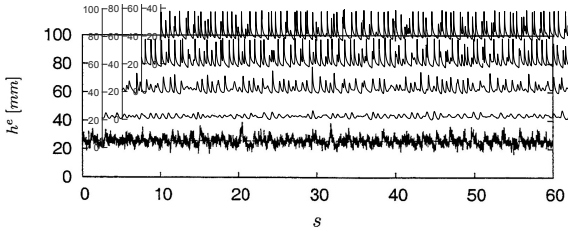

(b) Time trace of level height h. Bottom: Experimental, Johnson [20]. Second from bottom and up: Dual grid simulations of increasing CFL-numbers 0.5, 0.75, 0.95 and 1.0, respectively. $NJ = 20$, $Nj = 100$. Sampling at $x = 24\,\mathrm{m}$.

Figure 5.5: $a_g u_g/\mathcal{A} \approx 3.50\,\mathrm{m/s}$, $a_\ell u_\ell/\mathcal{A} \approx 0.25\,\mathrm{m/s}$, $\theta = 0^\circ$.

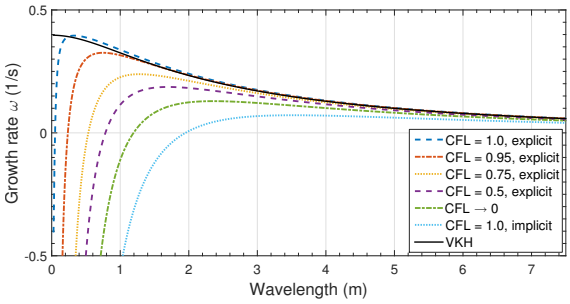

Figure 5.6: Linear wave growth of the two-fluid model (3.10) and of Roe scheme representations of said model. Flow state is as per the case description of Subsection 5.3, with $NJ \cdot Nj = 2\,000$ grid cells.

about using the two-fluid model for simulating detailed surface wave phenomena. Simulated wave frequencies are *overstimated* compared to the experimental time trace shown in Figure 5.5b. Holmås [17] simulated Johnson's experimental campaign using the incompressible model (3.10) and the same Biberg friction closure as applied here. Though showing good statistical agreement with Johnson's measurements, wave frequencies were *underestimated* in Holmås' simulations. The main differences between those simulations and the ones presented here are that Holmås used periodic boundary conditions and extended the Biberg friction model with a wave-breaking correlation.[5] He also used a pseudospectral scheme with a viscous filter which removes higher wavenumbers from the solution. Indeed, the derivation of two-fluid model (2.1) is rooted in a long wavelength assumption. This assumption justifies ignoring motion in the normal direction when averaging the original Euler equations. The long wavelength assumption is effectively violated at steep wave fronts [32]. Holmås used this to justify removing higher wavenumbers with the viscous filter. This, in combination with his wave-breaking model extension, allowed for simulations at flow rates far higher than those that causes ill-posedness and uncontrolled growth in the unadjusted two-fluid model.

Accounting for the dynamic pressure [5, 26] and the turbulent dissipation within waves seems to be important in mending the long wavelength violation of roll-wave simulations, limiting the predicted wave height and growth. Most progress on this has perhaps been made with free surface roll-waves. Worth mentioning is Richard and Gavrilyuk [27] who extended the well-known solitary roll-wave profile solutions of the shallow water equations to include dissipation through turbulent vorticity. These new profiles matched the experimental profile measurements of Brock [11] quite well. Cao et. al. [12] used similar turbulence modelling to generate dynamic simulation results where wave frequency and height statistics agreed well with Brock's experiments.

A final remark: It seems unlikely that the simulated roll-wave length distribution of the example case presented here has grown fully independent of the wavelengths emerging from the linear growth range. The travelling time needed for a wave regime to evolve will depend on the strength of the initial disturbance and the simulated growth rate. Tests using a wave spectrum disturbance at the inlet, instead of the pointwise random disturbance, showed a weak spectrum dependency. Similar sentiments were voiced by Holmås in [17].

6. Summary

A dual grid arrangement has been proposed which combines the HCU scheme [15] due to Evje and Flåtten with

[5] This wave-breaking extension entails a liquid fraction gradient term which effectively alters the eigenstructure of the two-fluid model (3.10) on which the Roe scheme (3.14) is based.

the incompressible two-fluid model. The resulting method retains the robustness of the original HCU scheme with regard to the sonic evolution. In addition, it allows for significant improvements in the accuracy and resolution of hydraulic waves at only moderate computational expense. The increased efficiency is achieved chiefly by allowing the numerical time scales of sonic and hydraulic information to match.

Principal and subgrid models are in the presented scheme coupled loosely through the terms in the governing transport equations. The incompressible subgrid methodology can therefore be regarded by way of a scheme extension, which does not necessitate significant alterations to a single grid scheme.

Three fundamentally different test cases have been presented. The pressure waves is important in the shock tube case of Subsection 5.1. Applying an incompressible subgird model here allowed for the recapturing of hydraulic shock details otherwise lost to diffusion. A surge wave – counter current pressure wave case was presented in Subsection 5.2. Here, the pressure-surge interactions were maintained when reducing the sonic resolution, improving computational efficiency by 1-2 orders of magnitude. Accurate hydraulic development and the essentials of the pressure-surge interactions were retained even when coarsening the principal grid enough to eliminate the sonic wave front altogether. Computational efficiency was then increased by 2-3 orders of magnitude. Finally, it was demonstrated that computational efficiency was improved by more than 3 orders of magnitude in an example roll-wave case. Steady roll-wave flow is one of many situations where pressure dynamics play an idle role, acting as a steady background state. We are usually not interested in the sonic propagation in such cases, but would still like for the simulated model to support compressible behaviour. Transitions to slug formations or sudden external alterations to the flow state are examples requiring a compressible model.

Acknowledgements

This work is financed by The Norwegian University of Science and Technology (NTNU) as a contribution the Multiphase Flow Assurance programme (FACE.) A personal thanks to Kontorbamse.

References

[1] A. H. Akselsen. Characteristic methods and Roe's method for the incompressible two-fluid model for stratified pipe flow. Under review in the International Journal of Multiphase Flow, April 2016.

[2] A. H. Akselsen. The Kelvin-Helmholtz/von Neumann stability of discrete representations of the two-fluid model for stratified two-phase flow. Under review in the International Journal of Multiphase Flow, April 2016.

[3] A. H. Akselsen. The stability of roll-waves in two-phase pipe flow. Submitted to the International Journal of Multiphase Flow, Match 2016.

[4] A. H. Akselsen and O. J. Nydal. Applying multiple grids to a multi-field model – the resolution requirements of individual fields in the two-fluid model for 1d pipe flow. *Journal of Dispersion Science and Technology*, 36(10):1378–1387, 2015.

[5] S. Banerjee. Separated flow models. ii. higher order dispersion effects in the averaged formulation. *International Journal of Multiphase Flow*, 6(3):241 – 8, 1980/06/.

[6] D. Barnea. Stability analysis of annular flow structure, using a discrete form of the 'two-fluid model'. *International Journal of Multiphase Flow*, 17(6):705 – 16, 1991/11/.

[7] D. Barnea and Y. Taitel. Kelvin-Helmholtz stability criteria for stratified flow viscous versus non-viscous (inviscid) approaches. *International Journal of Multiphase Flow*, 19(4):639 – 649, 1993.

[8] F. Barre and M. Bernard. The CATHARE code strategy and assessment. *Nuclear Engineering and Design*, 124(3):257 – 84, 1990/12/.

[9] K. H. Bendlksen, D. Malnes, R. Moe, and S. Nuland. Dynamic two-fluid model olga. theory and application. *SPE Production Engineering*, 6(2):171 – 180, 1991.

[10] D. Biberg. A mathematical model for two-phase stratified turbulent duct flow. *Multiphase Science and Technology*, 19(1):1 – 48, 2007.

[11] R. Brock. Development of roll-wave trains in open channels. *American Society of Civil Engineers, Journal of the Hydraulics Division*, 95(HY4):1401 – 1427, 1969.

[12] Z. Cao, P. Hu, K. Hu, G. Pender, and Q. Liu. Modelling roll waves with shallow water equations and turbulent closure. *Journal of Hydraulic Research*, 0(0):1–17, 0.

[13] S. Evje and T. Flåtten. Hybrid flux-splitting schemes for a common two-fluid model. *Journal of Computational Physics*, 192(1):175 – 210, 2003/11/20.

[14] S. Evje and T. Flåtten. Weakly implicit numerical schemes for a two-fluid model. *SIAM Journal on Scientific Computing*, 26(5):1449 – 1484, 2005.

[15] S. Evje and T. Flåtten. Hybrid central-upwind schemes for numerical resolution of two-phase flows. *Mathematical Modelling and Numerical Analysis*, 39(2):253 – 73, 2005/03/.

[16] W. D. Fullmer, V. H. Ransom, and M. A. Lopez De Bertodano. Linear and nonlinear analysis of an unstable, but well-posed, one-dimensional two-fluid model for two-phase flow based on the inviscid Kelvin-Helmholtz instability. *Nuclear Engineering and Design*, 268:173 – 184, 2014.

[17] H. Holmås. Numerical simulation of transient roll-waves in two-phase pipe flow. *Chemical Engineering Science*, 65(5):1811 – 25, 2010/03/01.

[18] Information Systems Laboratories, Inc., Rockville, Maryland, Idaho. *RELAP5/MOD3.3 code manual volume I: code structure, system models and solution methods*, December 2001.

[19] R. Issa and M. Kempf. Simulation of slug flow in horizontal and nearly horizontal pipes with the two-fluid model. *International Journal of Multiphase Flow*, 29(1):69 – 95, 2003/01/.

[20] G. Johnson. *A Study of Stratified Gas-Liquid Pipe Flow*. PhD thesis, Univ. Oslo, 2005. dr. scient.

[21] B. Keyfitz. Lack of hyperbolicity in the two-fluid model for two-phase incompressible flow. *Discrete and Continuous Dynamical Systems – Series B*, 3(4):541–563, Nov. 2003.

[22] J. Kjolaas, A. De Leebeeck, and S. Johansen. Simulation of hydrodynamic slug flow using the LedaFlow slug capturing model. pages 365 – 383, Cannes, France, 2013.

[23] M. Larsen, E. Hustvedt, P. Hedne, and T. Straume. Petra: A novel computer code for simulation of slug flow. *Proceedings - SPE Annual Technical Conference and Exhibition*, Pi:965 – 976, 1997.

[24] R. J. Leveque. Large time step shock-capturing techniques for scalar conservation laws. *SIAM Journal on Numerical Analysis*, 19(6):1091–1109, 1982.

[25] S. Lindqvist and H. Lund. A large time step roe scheme ap-

plied to two-phase flow. In *European Congress on Computational Methods in Applied Sciences and Engineering (ECCOMAS)*, Crete, Greece, June 2016. https://www.eccomas2016.org/proceedings/.

[26] F. Renault and O. J. Nydal. Influence of dynamic pressure terms on stratified two-phase flow stability : Presented at the 5th international conference on multiphase flow, yokohama, japan, may 30-june 4, 2004. 2004.

[27] G. L. Richard and S. L. Gavrilyuk. A new model of roll waves: Comparison with brock's experiments. *Journal of Fluid Mechanics*, 698:374 – 405, 2012.

[28] H. Stewart. Stability of two-phase flow calculation using two-fluid models. *Journal of Computational Physics*, 33(2):259 – 70, 1979/11/.

[29] I. Toumi and A. Kumbaro. An approximate linearized riemann solver for a two-fluid model. *Journal of Computational Physics*, 124(2):286 – 300, 1996/03/15.

[30] T. Wangensteen. *Mixture-Slip Flux Splitting for the numerical computation of 1D two phase flow*. PhD thesis, NTNU, September 2010.

[31] M. Watson. Wavy stratified flow and the transition to slug flow. In C. Fairhurst, editor, *Multi-phase Flow – Proceedings of the 4th International Conference*, pages 495–512, Cranfield, UK, 1989.

[32] G. Whitham. *Linear and Nonlinear Waves*. Wiley, 1974.

Appendix B

Additional Texts

A Linear Stability Analyses of Discrete Representations of the Two-Fluid Model for Stratified Two-Phase Flow

Andreas H. Akselsen
Department of Energy and Process Engineering, Norwegian University of Science and Technology
Kolbjørn Hejes v. 1B, 7491 Trondheim, Norway
andreas.h.akselsen@ntnu.no

Abstract

Hydrodynamic flow instabilities provide natural mechanism for flow regime transition, the prediction of which is achievable through detailed simulation. The quality and reliability of such predictions are however strongly dependent upon the applied numerical method and resolution. A Kelvin-Helmholtz stability analysis for the differential two-fluid model is in the present work presented and extended to discrete representations of said model. This analysis provides algebraic expressions which give instantaneous, quantitative information into i) when a studied scheme will predict linear wave growth, ii) the rate of growth and the expected growing wavelength, and iii) the wave speeds. These stability expressions adhere to a wider family of finite volume methods. Both the spatial and temporal discretization are found to play decisive roles in a method's predictive capability. Numerical errors are observed to manifest in increased, as well as reduced, wave growth. Low-frequency growth from numerical errors is not always easily distinguished from physical wave growth. The linear analysis is demonstrated to be useful in understanding the predictions made by simulator tools, and in choosing the appropriate numerical method and simulation parameters for optimizing the simulation efficiency and reliability.

Keywords: Discrete stability; Kelvin-Helmholtz; two-phase; pipe flow; two-fluid model

1. Introduction

Stability analyses of the two-fluid model have been performed by numerous authors. For example, Barnea and Taitel [1] presented a derivation of the Kelvin-Helmholtz stability criterion for viscous flows (henceforth abbreviated the VKH criterion) and examined the non-linear flow development through simulation [2]. Barnea also performed a stability analysis on a discrete upwind type scheme of a simplified version of the two-fluid model for annular flow [4]. Here it was shown again how an intrinsically unstable, ill-posed differential model may display stable behaviour if provided with sufficient numerical diffusion. (The annular interface is inherently unstable locally though it may be stable in a statistical sense.) Barnea argued that the discrete model can be regarded as a legitimate model for the average flow, even though the differential model is ill-posed. Issa and Kempf [3] have been credited with first demonstrating that the predicted wave growth from transient simulations of the full two-fluid model coincides with the wave growth from Kelvin-Helmholtz theory, and suggested that such simulated wave growth gives a natural transition into a wavy or slugging flow regime. Liao et al. [5] performed a linear stability study on a discrete two-fluid model with a staggered grid arrangement, comparing various interpolations for the convection term. This analysis was limited to implicit time integration, considering the convection terms only. Numerical errors arising from the dislocation of staggered information, as well as form the conservative formulation, appears to have been neglected. The paper concluded that the central difference discretization was superior to the first and higher order non-centred interpolations. Liao et al. also examined the evolution of the wavelength distributions from a random initial disturbance, and the behaviour as the model turns ill-posed.

The present article focuses on providing general theory for a wider family of discrete two-fluid model representations. This will be done by relating the predicted growth and decay of the discrete representations directly to the growth results of the Kelvin-Helmholtz analysis of the differential two-fluid model. Linear theory of the type here presented is demonstrated to be powerful tool when it comes to assessing the predictive capability of any chosen discrete representation, providing support with decisions related to the parametric setup prior to simulation and interpreting the simulation results. *Predictive capability* here refers to the reliability and accuracy with which a discrete representation predicts wave growth or decay under limited computational resolution. It will be shown that the growth and dispersion response of discrete representations is perfectly analogous to that of the differential model. What's more, the differential Kelvin-Helmholtz expression directly provides that growth and dispersion which will be predicted by the discrete methods in the linear range, provided these representations uses the same discrete differentiations all over.

2. The Two-Fluid Model

The compressible, adiabatic, equal pressure four-equation two-fluid model for stratified pipe flow results from an averaging of the conservation equations across the cross-section area. The model is commonly written

$$\partial_t(\rho a)_\kappa + \partial_x(\rho a u)_\kappa = 0, \tag{2.1a}$$

$$\partial_t(\rho a u)_\kappa + \partial_x\left(\rho a u^2\right)_\kappa + a_\kappa \partial_x p_\mathrm{i} + \rho_\kappa a_\kappa g \cos\theta\, \partial_x h = s_\kappa, \tag{2.1b}$$

$$a_\ell + a_\mathrm{g} = \mathcal{A}, \tag{2.1c}$$

$$p_\mathrm{i} = \mathcal{P}_\mathrm{g}(\rho_\mathrm{g}) = \mathcal{P}_\ell(\rho_\ell). \tag{2.1d}$$

Field κ, occupied by either gas, $\kappa = \mathrm{g}$, or liquid, $\kappa = \ell$, is segregated from the other field. Subscript i indicates the fluid interface; see Fig. 2.1. p_i is here the pressure at the interface, assumed the same for each phase and given by some equation of state $\mathcal{P}$. h is the height of the interface from the pipe floor,

and the term in which it appears originates from approximating a hydrostatic wall-normal pressure distribution. u_κ and ρ_κ are the mean fluid velocity and density in field κ. The momentum sources are $s_\kappa = -\tau_\kappa\sigma_\kappa \pm \tau_\mathrm{i}\sigma_\mathrm{i} - a_\kappa\rho_\kappa g\sin\theta$, where τ is the skin frictions at the walls and interface. θ is the pipe inclination, positive above datum, and g is the gravitational acceleration.

The circular pipe geometry itself enters into the modelling through the relation between the level height h, the specific areas a_κ and the peripheral lengths σ_κ and σ_i. These are algebraically interchangeable through a geometric function

$$h = \mathcal{H}(a_\ell) \tag{2.2}$$

whose derivative is $\mathcal{H}' = 1/\sigma_\mathrm{i}$.

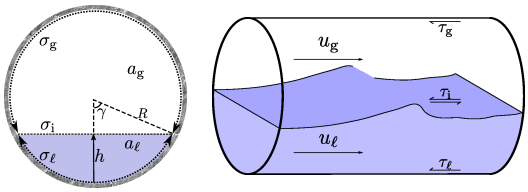

Figure 2.1: Pipe cross-section

Fluid compressibility is commonly ignored when considering the surface wave stability of (2.1). This enables us to base the stability analysis on the incompressible two-fluid model, which has lower rank and a conservative form.

Assuming incompressible phases, the two-equation model is obtained by reducing the momentum equations with their respective mass equations and eliminating the pressure term between them, resulting in

$$\partial_t\boldsymbol{v} + \partial_x\boldsymbol{f} = \nu\partial_{xx}\boldsymbol{v} + \boldsymbol{s} \tag{2.3}$$

with conserved variables and fluxes

$$\boldsymbol{v} = \big(a_\ell,\, \rho_\ell u_\ell - \rho_\mathrm{g} u_\mathrm{g}\big)^T, \qquad \boldsymbol{f} = (q_\ell,\, j)^T, \qquad \boldsymbol{s} = (0,\, s)^T.$$

Symbols for the flux and source components have here been defined and are

$$q_\kappa = a_\kappa u_\kappa, \qquad j = \tfrac{1}{2}\big(\rho_\ell u_\ell^2 - \rho_\mathrm{g} u_\mathrm{g}^2\big) + m_y h,$$
$$s = -m_x - \frac{\tau_\ell\sigma_\ell}{a_\ell} + \frac{\tau_\mathrm{g}\sigma_\mathrm{g}}{a_\mathrm{g}} + \tau_\mathrm{i}\sigma_\mathrm{i}\left(\frac{1}{a_\ell} + \frac{1}{a_\mathrm{g}}\right),$$
$$\nu = 0.$$

A dummy viscous term has been added to the system, the purpose of which lies in evaluating the artificial numerical viscosity present in some discrete representations. Specific weight coefficients have been grouped into $m_x = (\rho_\ell - \rho_\mathrm{g})g\sin\theta$ and $m_y = (\rho_\ell - \rho_\mathrm{g})g\cos\theta$. The identities

$$a_\ell + a_\mathrm{g} = \mathcal{A}(x), \qquad q_\ell + q_\mathrm{g} = \mathcal{Q}(t), \tag{2.4}$$

where the latter has been obtained from summing the two mass equations, close the model. Both $\mathcal{A}$ and $\mathcal{Q}$ are parametric.

3. Kelvin-Helmholtz Stability

The viscous Kelvin-Helmholtz (VKH) stability analysis is here presented in some detail, which will later be related directly to the stability of discrete representations.

Variable of the steady state $\boldsymbol{v} = \boldsymbol{V}$ will in the following be assigned upper-case symbols. The steady state solution $\boldsymbol{V}$ satisfies the so-called *holdup equation*

$$s(\boldsymbol{V}) = S = 0. \tag{3.1}$$

Linearizeing (2.3) about the steady state,

$$\boldsymbol{v} = \boldsymbol{V} + \tilde{\boldsymbol{v}},$$

yields

$$\left(\mathbb{I}(\partial_t - \nu\partial_{xx}) + \frac{\partial\boldsymbol{F}}{\partial\boldsymbol{V}}\partial_x - \frac{\partial\boldsymbol{S}}{\partial\boldsymbol{V}}\right)\tilde{\boldsymbol{v}} = 0. \tag{3.2}$$

The linear response of the system to any perturbation of the steady state will be through the growth and dispersion of a number of linear waves. For any set of initial condition, the solution of (3.2) is just a linear combination of waves; we write it in the form

$$\tilde{\boldsymbol{v}}(x,t) = \sum_k \sum_{p=1,2} \hat{\boldsymbol{v}}_{k,p}\mathrm{e}^{\mathrm{i}k(x-c_{k,p}t)}, \tag{3.3}$$

where $\hat{\boldsymbol{v}}_k^0 = \sum_{p=1,2}\hat{\boldsymbol{v}}_{k,p}$ are Fourier modes of the initial conditions. The proof that (3.3) is a solution has been omitted for briefness. Stable flow occurs if the real components of all eigenvalues are negative or zero. Inserting (3.3) into (3.2) yields the algebraic system

$$\sum_k \sum_{p=1,2} \frac{\partial\boldsymbol{E}_{k,p}}{\partial\boldsymbol{V}}\hat{\boldsymbol{v}}_{k,p}\mathrm{e}^{\mathrm{i}k(x-c_{k,p}t)} = 0, \tag{3.4}$$

with

$$\boldsymbol{E}_{k,p} = \boldsymbol{V}(\delta_t^{k,p} - \nu\delta_{xx}^k) + \boldsymbol{F}\delta_x^k - \boldsymbol{S}. \tag{3.5}$$

Each p-term must solve (3.4) individually if the sum is to be a solution at all times. Suppressing both sum indices we simply write

$$\frac{\partial\boldsymbol{E}}{\partial\boldsymbol{V}}\hat{\boldsymbol{v}} = 0. \tag{3.6}$$

The δ-operators appearing in (3.5), accounting for the effect of the partial derivatives, are defined

$$\delta \equiv \frac{\partial\exp\mathrm{i}k(x-ct)}{\exp\mathrm{i}k(x-ct)}. \tag{3.7}$$

Note that these are simple scalars effectively flipping the various terms straight angles in the complex plane:

$$\delta_t = -\mathrm{i}kc, \qquad \delta_x = \mathrm{i}k, \qquad \delta_{xx} = -k^2.$$

Using δ operators will allow solutions to be extended directly to discrete representations.

Because (3.6) is linear we may express it uniquely in terms of one of the disturbance properties, say $\hat{a}_\ell : \frac{\partial\boldsymbol{V}}{\partial A_\ell}\hat{a}_\ell = \hat{\boldsymbol{v}}$, yielding

$$\boldsymbol{E}' = 0, \tag{3.8}$$

where $\Psi' \equiv \frac{\mathrm{d}\Psi}{\mathrm{d}A_\ell}$. We further define a viscous phase celerity

$$c_\nu \equiv -\frac{\delta_t - \nu\delta_{xx}}{\delta_x}, \tag{3.9}$$

which evaluates to $c_\nu = c + \mathrm{i}k\nu$. Inserting (3.5) and (3.9) into (3.8) now yields

$$\boldsymbol{F}_\mathrm{r}'\delta_x - \boldsymbol{S}' = 0. \tag{3.10}$$

The components of $\boldsymbol{F}_\mathrm{r}$ are the fluxes in a relative frame, moving with (complex) velocity c_ν. $\boldsymbol{F}_\mathrm{r}$ equals $\boldsymbol{F}$ with the relative velocities $U_{\kappa,\mathrm{r}} = U_\kappa - c_\nu$ replacing U_κ. Since the mass equation contains no source term, the first component of (3.10), combined with (2.4), yields directly

$$Q_{\kappa,\mathrm{r}} = A_\kappa U_{\kappa,\mathrm{r}} = \mathrm{const.}, \tag{3.11}$$

which relates both velocity components to A_ℓ. The second component of (3.10) yields the *dispersion equation*

$$J'_{\mathrm{r}}\,\delta_x - S' = 0, \tag{3.12}$$

where $\delta_x = \mathrm{i}k$. Using (3.11) one finds

$$J'_{\mathrm{r}} \equiv \frac{\mathrm{d}J_{\mathrm{r}}}{\mathrm{d}A_\ell} = m_y\mathcal{H}' - \frac{\rho_\ell U^2_{\ell,\mathrm{r}}}{A_\ell} - \frac{\rho_{\mathrm{g}} U^2_{\mathrm{g,r}}}{A_{\mathrm{g}}} \tag{3.13}$$

and

$$S' \equiv \frac{\mathrm{d}S}{\mathrm{d}A_\ell} = \mathcal{S}_{A_\ell} + c_\nu\big(\mathcal{S}_{Q_\ell} - \mathcal{S}_{Q_{\mathrm{g}}}\big). \tag{3.14}$$

The source has here been parameterised as function of A_ℓ and Q_κ with

$$\mathcal{S}_{A_\ell} = \left(\frac{\partial\mathcal{S}}{\partial A_\ell}\right)_{Q_\ell,Q_{\mathrm{g}}}, \quad \mathcal{S}_{Q_\ell} = \left(\frac{\partial\mathcal{S}}{\partial Q_\ell}\right)_{A_\ell,Q_{\mathrm{g}}}, \quad \mathcal{S}_{Q_{\mathrm{g}}} = \left(\frac{\partial\mathcal{S}}{\partial Q_{\mathrm{g}}}\right)_{A_\ell,Q_\ell},$$

easily computed for any source $\mathcal{S}$ from discrete state differentials.

Extracting any particular growth rate or wave celerity from (3.12) is perfectly straight forward and yields

$$c_\nu = b_1 \pm \sqrt{b_1^2 - b_0} \tag{3.15}$$

with

$$\rho^* = \frac{\rho_\ell}{A_\ell} + \frac{\rho_{\mathrm{g}}}{A_{\mathrm{g}}},$$

$$b_1 = \frac{1}{\rho^*}\left(\frac{\rho_\ell U_\ell}{A_\ell} + \frac{\rho_{\mathrm{g}} U_{\mathrm{g}}}{A_{\mathrm{g}}} - \frac{1}{2}\frac{\mathcal{S}_{Q_\ell} - \mathcal{S}_{Q_{\mathrm{g}}}}{\delta_x}\right),$$

$$b_0 = \frac{1}{\rho^*}\left(\frac{\rho_\ell U_\ell^2}{A_\ell} + \frac{\rho_{\mathrm{g}} U_{\mathrm{g}}^2}{A_{\mathrm{g}}} - m_y\mathcal{H}' + \frac{\mathcal{S}_{A_\ell}}{\delta_x}\right)$$

and the definitions (3.9), (3.7) and (3.3). The wave resulting from plus in (3.15) will in the following be termed the 'fast wave'. Conversely, the minus wave will be termed the 'slow wave'.

The condition for marginal stability (the limit state at which growth turns positive) is often called the VKH criterion. Noting that both J'_{r} and S' are real if c is real and $\nu = 0$, the VKH criterion may simply be written

$$S' = 0, \qquad J'_{\mathrm{r}} = 0, \tag{3.16}$$

with $S = 0$ from the holdup equation (3.1). We may therefore regard the VKH criterion as the equilibrium state with respect to changes in phase fraction in the frame of a moving wave perturbation.

Note that the rate of growth will in (3.12) depend upon the wavenumber k (present in δ_x,) but that the condition for marginal stability, (3.16), will not.

These results are identical to those provided in *e.g.*, [1, 6, 5], though a different approach has been chosen which provides a physical interpretation.

Let us conclude this section by remarking on some features of the so-called *inviscid Kelvin-Helmholtz* stability criterion (IKH.) This is the stability of the two-fluid model without the source term; $s \equiv 0$. Solving (3.16), or inspecting (2.3), we then find that the 'inviscid' celerity equals the eigenvalues of $\frac{\partial \boldsymbol{f}}{\partial \boldsymbol{v}}$, whose introduction has been omitted. Wave growth then entails complex eigenvalues. Thus, the IKH criterion is really a test on hyperbolicity.

The IKH criterion does *not* coincide with the VKH criterion (3.16) in the inviscid limit $S \to 0$, a feature which is illustrated in Fig. 3.1, showing c in the complex plane with the parameters and closures described later in Section 5.1. Only the superficial gas velocity $Q_{\mathrm{g}}/\mathcal{A}$ is altered and the source S is reduced towards zero in steps. This does not change the critical state, as long as $S \not\equiv 0$, but the rate of growth near the critical state converges towards zero. Fig. 3.1 also shows the limit where the two-fluid model turns elliptical and ill-posed (assumed well-posed otherwise.) There is a region of positive wave growth within which the viscous model remains hyperbolic. No such region exists in the inviscid model.

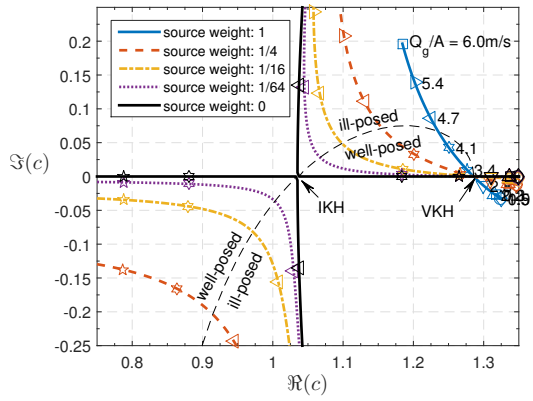

Figure 3.1: Complex celerity c with altering superficial gas velocity $Q_{\mathrm{g}}/\mathcal{A}$. The source differentials are reduced in steps between plots.

4. Stability of Discrete Representations

We start the discrete analysis by examining the stability of representations of the two-equation model (2.3). The remarks that then follow relates these results to representations of the four-equation model (2.1). Let $(\delta\psi)^n_j$ symbolize the discrete differentiation operations used in the discretization to represent the partial differentials. System (2.3) may be written

$$(\delta_t \boldsymbol{v})^n_j + (\delta_x \boldsymbol{f})_j = \nu(\delta_{xx}\boldsymbol{v})_j + \boldsymbol{s}_j \tag{4.1}$$

after discretization.

Table 1: Some discrete differentiation operators and their corresponding wave operator. $\phi_x = k\Delta x$ and $\phi_t = kc\Delta t$.

	$(\delta\psi)^n_j$	δ^{d}
δ_t	$\frac{1}{\Delta t}\left(\psi_j^{n+1} - \psi_j^n\right) + (\cdots)^n$	$\frac{1}{\Delta t}\left(\mathrm{e}^{-\mathrm{i}\phi_t} - 1\right)$
δ_t	$\frac{1}{\Delta t}\left(\psi_j^{n+1} - \psi_j^n\right) + (\cdots)^{n+1}$	$\frac{1}{\Delta t}\left(1 - \mathrm{e}^{\mathrm{i}\phi_t}\right)$
δ_t	Crank-Nicolson	$\frac{2i}{\Delta t}\tan\frac{\phi_t}{2}$
δ_x	$\frac{1}{\Delta x}\left(\psi_j - \psi_{j-1}\right)$	$\frac{2i}{\Delta x}\mathrm{e}^{-\mathrm{i}\frac{\phi_x}{2}}\sin\frac{\phi_x}{2}$
δ_x	$\frac{1}{2\Delta x}\left(\psi_{j+1} - \psi_{j-1}\right)$	$\frac{\mathrm{i}}{\Delta x}\sin\phi_x$
δ_x	$\frac{1}{\Delta x}\left(\psi_{j+\frac{1}{2}} - \psi_{j-\frac{1}{2}}\right)$	$\frac{2i}{\Delta x}\sin\frac{\phi_x}{2}$
δ_{xx}	$\frac{1}{\Delta x^2}\left(\psi_{j+1} - 2\psi_j + \psi_{j-1}\right)$	$\frac{2}{\Delta x^2}\left(\cos\phi_x - 1\right)$
$\overline{\psi_j}$	$\frac{1}{2}\left(\psi_{j+\frac{1}{2}} + \psi_{j-\frac{1}{2}}\right)$	$\cos\frac{\phi_x}{2}$

After linearization, the solution of (4.1) may again be written as a linear combination of waves; analogous to (4.2), the discrete point solution is

$$\tilde{\boldsymbol{v}}^n_j = \sum_k \sum_{p=1,2} \hat{\boldsymbol{v}}_{k,p}\mathrm{e}^{\mathrm{i}k(x_j - c^{\mathrm{d}}_{k,p}t_n)}, \tag{4.2}$$

where $\tilde{\boldsymbol{v}}^n_j = \boldsymbol{v}^n_j - \boldsymbol{V}$. The proof that this is a solution has been omitted for the sake of briefness. Inserting (4.2) into the discrete

model (4.1) and linearizing yields a system analogous to (3.4),

$$\sum_k \sum_{p=1,2} \frac{\partial \boldsymbol{E}^{\mathrm{d}}_{k,p}}{\partial \boldsymbol{V}} \hat{\boldsymbol{v}}_{k,p} \mathrm{e}^{\mathrm{i}k(x_j - c^{\mathrm{d}}_{k,p} t_n)} = 0, \tag{4.3}$$

$\boldsymbol{E}^{\mathrm{d}}$ being the discrete equivalent of $\boldsymbol{E}$ from (3.5), differing only in that discrete differential operators

$$\delta^{\mathrm{d}} \equiv \frac{\left(\delta \exp \mathrm{i}k(x - c^{\mathrm{d}}\, t)\right)^n_j}{\exp \mathrm{i}k(x_j - c^{\mathrm{d}}\, t_n)} \tag{4.4}$$

replace δ. These δ^{d} terms, approximating δ, hold all numerical error in its entirety and are simple algebraic expressions. Again, $\boldsymbol{E}^{\mathrm{d}}$ is independent of n and j so that each k, p-term must equal zero individually. The problem is now equivalent to (3.6) and its solution is obtained directly from (3.12)-(3.14), with two celerities for each wavenumber k. Also the discrete viscous celerity c^{d}_ν follow the definition (3.9) using the *discrete* δ^{d} operators. δ^{d} gives the value of δ^{d}_t, which in turn gives the wave growth and dispersion from the chosen time discretization method. δ^{d}-functions for some of the most common discrete differentiations are presented in Table 1. Constructing similar operators for more complicated interpolations is usually straight forward. Notice that all operators listed in Table 1 are consistent, *i.e.*, they satisfy $\delta^{\mathrm{d}} \to \delta$ as Δx and Δt approach zero.

Remark 1. *The stability behaviour of a discrete representation will converge towards that of the continuous model if*

$$c^{\mathrm{d}}_\nu \equiv -\frac{\delta^{\mathrm{d}}_t - \nu \delta^{\mathrm{d}}_{xx}}{\delta^{\mathrm{d}}_x} \to c + \mathrm{i}k\nu.$$

For this to happen, all δ^{d} operators must be consistent ($\delta^{\mathrm{d}} \to \delta$) and Δx and Δt must approach zero together, smoothly.

Remark 2. *The predicted linear stability is independent of which variable the discrete system is solved for, provided the discrete differentiations δ^{d} are independent of this choice.*

Remark 3. *The predicted linear stability is independent of the form of the discrete system, be it conservative, primitive, four-equation, two-equation, etc., provided the discrete differentiations δ^{d} are independent of these choices.*

A consequence of Remark 3 is that four equation formulations of the compressible system (2.1) is equivalent to (4.1) provided we do not mix different discrete differentiations. However, incompressible fluids are assumed in the stability analysis itself, even though the representation is of the compressible model. This is common practise, but denies us information about the sonic stability.

Example 1 (The stability of an explicit Lax-Friedrich scheme)**.** *The Lax-Friedrich scheme is commonly written*

$$\frac{\boldsymbol{v}^{n+1} - \boldsymbol{v}^n}{\Delta t} + \frac{\boldsymbol{f}_{j+\frac{1}{2}} - \boldsymbol{f}_{j-\frac{1}{2}}}{\Delta x} = \boldsymbol{s}_j$$

with

$$\boldsymbol{f}_{j+\frac{1}{2}} = \tfrac{1}{2}(\boldsymbol{f}_{j+1} + \mathrm{j}) - \tfrac{1}{2}\tfrac{\Delta x}{\Delta t}(\boldsymbol{v}_{j+1} - \boldsymbol{v}_j).$$

Numerical viscosities in the Lax-Friedrich is then

$$\nu^{\mathrm{LF}} = \frac{\Delta x^2}{2\Delta t}.$$

This schemes uses simple central differences; from Table 1 we find $\delta^{\mathrm{d}}_t = \frac{1}{\Delta t}\left(\mathrm{e}^{-\mathrm{i}\phi_t} - 1\right)$, $\delta^{\mathrm{d}}_x = \frac{\mathrm{i}}{\Delta x}\sin\phi_x$ and $\delta^{\mathrm{d}}_{xx} = \frac{2}{\Delta x^2}(\cos\phi_x - 1)$. Extracting the stability equations is strikingly easy; equation (3.15) *gives c^{d}_ν and δ^{d}_t is obtained from the definition* (3.9)*. The complex wave celerity can then be calculated from the expression for the explicit time discretization, in this case $c = \frac{\mathrm{i}}{k}\ln(\delta^{\mathrm{d}}_t \Delta t + 1)$.*

5. Numerical Tests and Results

Predictions from a number of schemes will here be presented, namely the explicit and implicit variants of the Lax-Friedrich scheme, (Example 1), abbreviated LF, the staggered upwind scheme solved for conservative variables, abbreviated UWS, and the Roe scheme for the two-equation model. Descriptions of the two latter schemes have been omitted. The aim of these comparisons is not to establish a favourite amongst the chosen representations, but to demonstrate how the linear theory provides a powerful simulation support tool. Indeed, multiple considerations are important when choosing a scheme. Many choices can be made both stable and accurate if the simulation parameters are collected with the aid of the hitherto presented linear theory.

5.1. Test Case

This setup for the computational examples is chosen fairly arbitrarily and corresponds to the experimental and numerical setup used in [6, 7]. The friction closures τ_κ and τ_i are from the Biberg friction model as presented in [8]. Fixed parameters are presented in Table 2 unless otherwise stated and constitutes a high-pressure, positively inclined flow. The flow state is chosen such that the flow is weakly unstable according the differential VKH criterion. The equivalent mean liquid area fraction is $A_\ell/\mathcal{A} = 0.142$ and the chosen friction closures will yield the steady state superficial velocities $Q_\ell/\mathcal{A} \approx 0.154\,\mathrm{m/s}$ and $Q_\mathrm{g}/\mathcal{A} \approx 3.245\,\mathrm{m/s}$. The overall properties of the friction closure does not affect the linear stability analysis; only their resulting steady state $S = 0$ and its state derivatives enter into it. In this particular case we have $\mathcal{S}_{A_\ell} = 1.39\mathrm{E}6\,\mathrm{kg/m^6 s^2}$, $\mathcal{S}_{Q_\ell} = -9.07\mathrm{E}5\,\mathrm{kg/ms}$ and $\mathcal{S}_{Q_\mathrm{g}} = 7.63\mathrm{E}4\,\mathrm{kg/ms}$.

Only numerical parameters are varied in the tests provided in this section. The wavelength is therefore fixed at 30 diameters and the cell lengths are varied.

Table 2: Fixed parameters.

liquid density	ρ_ℓ	998	$\mathrm{kg/m^3}$
gas density	ρ_g	50	$\mathrm{kg/m^3}$
liquid dynamic viscosity	μ_ℓ	1.00E-3	Pa s
gas dynamic viscosity	μ_g	1.61E-5	Pa s
internal pipe diameter	d	0.1	m
wall roughness		2E-5	m
pipe inclination	θ	1°	–
mean level height	$\overline{h}$	0.02	m
mixture velocity	$\mathcal{Q}/\mathcal{A}$	3.4	m/s
wavelength	λ	3	m

The time steps are regulated using a CFL number, which makes the time step length proportional to the grid cell length (see Remark 1.) Time steps are limited by the model characteristic with the larger magnitude in the presented Roe scheme, with $\mathrm{CFL} = 0.95$. Following [5], the liquid velocity is used the staggered upwind and Lax-Friedrich schemes, with $\mathrm{CFL} = 0.5$. Implicit scheme simulations are performed by iterating on the new state with a 0.5 relaxation factor.

5.2. Predictions

First, Fig. 5.1 validates that the theory corresponds precisely to the linear growth of the discrete representations and shows the further development into the non-linear range. The simulation domain consists of 128 cells containing a single wave of the prescribed 30 diameter wavelength.

The presented schemes provide a range of different behaviours. We note immediately from Fig. 5.1 that all implicit

schemes are significantly more diffusive than their explicit counterparts, with numerical diffusion dominating the weak wave growth present in the differential solution. Explicit versions of both the Lax-Friedrich scheme and the staggered upwind scheme eventually reach a final unstable state in which waves grow until the model is no longer hyperbolic and the simulations crash. They do so, however, in quite different manners. Where the Lax-Friedrich scheme first appears diffusive for then to be dominated by a high-wavenumber instability, the upwind scheme simply overpredicts the growth rate of the principle wave. This is further illustrated in Fig. 5.2, showing growth rates and snapshots of simulations in which the differential model is stable due to a lower mixture velocity. The former instability will usually be regarded as a 'numerical instability,' commonly identified by the sudden unphysical high-wavenumber growth. Determining, from visual inspection, whether the latter instability is 'physical or not' is however not as straight forward as there are essentially no differences between the natural wave growth and the growth here attributed to numerical errors.

Lastly, the explicit Roe scheme is in Fig. 5.1 seen to accurately match the continuous growth rate of the differential model. It also developers into a steady roll-wave solution, which is a valid solution for the differential problem. Roe schemes are designed to be well adopted for strongly non-linear flows.

The dispersion error of a 128 cell wave is very small and wave crest positions are overlapping for as long as the waves remain in the linear range. This plot is omitted.

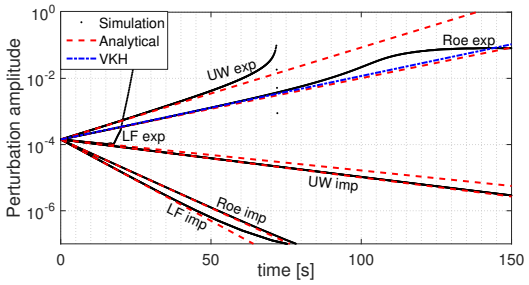

Figure 5.1: Wave growth. Numerical simulations vs. linear theory. Wavelength 30 d. 128 cells; $\phi_x = \pi/64$.

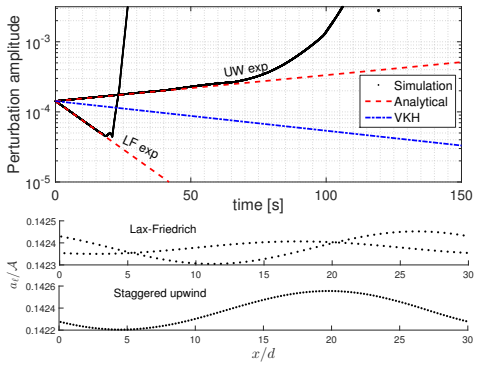

Figure 5.2: Wave growth and accompanying snapshots from unstable Lax-Friedrich and staggered upwind simulations. The mixture velocity $\mathcal{Q}/\mathcal{A}$ equals here $3.1\,^{\mathrm{m}}/_{\mathrm{s}}$, at which the differential model is stable.

Next we examine the response of the 30 diameter wave to changes in the spatial resolution. Fig. 5.3 shows the wave growth, or *pulsation*, $k\,\Im(c^{\mathrm{d}})\,[^{1}/_{\mathrm{s}}]$ and the wave celerity $\Re(c^{\mathrm{d}})\,[^{\mathrm{m}}/_{\mathrm{s}}]$. Both the fast and the slow waves are shown, a bold line used for the wave with the higher growth rate. Subfigure (a) shows that the Roe scheme gives very accurate growth results for $\phi \leq \pi/32$ (using 64 cells or more) and predicts wave growth for all ϕ. An accurate celerity for the fast wave is observed in Subfigure (b) for all ϕ. The explicit Lax-Friedrich and implicit staggered upwind schemes start predicting wave growth around $\phi = \pi/100$, and the implicit Roe and implicit Lax-Friedrich schemes start doing so around $\phi = \pi/210$. The explicit upwind scheme overpredicts the wave growth everywhere above $\phi = \pi/3$. Finally, we see that the explicit Lax-Friedrich scheme becomes unstable around $\phi \gtrsim \frac{2}{3}\pi$, and that it is then the slow wave that has taken over the growth. In fact, from Subfigure (b) we see that the 'slow' wave moves faster here. This very particular finding is tested and confirmed in Fig. 5.4, where three-celled waves ($\phi_x = \frac{2}{3}\pi$) are applied as the initial condition. Two simulations are shown wherein the initial velocity conditions are made to accommodate the fast wave in one and the slow wave in the other. The simulations follow the predicted growth behaviour precisely, with the slow wave growing and the fast wave diminishing. After a while though, also the fast wave simulation becomes unstable as the slow wave grows from out of numerical inaccuracies. The plotted points are the maximum amplitudes of the spatial node sets; there is some scattering of these points as the simulated waves are represented by a regularly alternating three-point pattern.

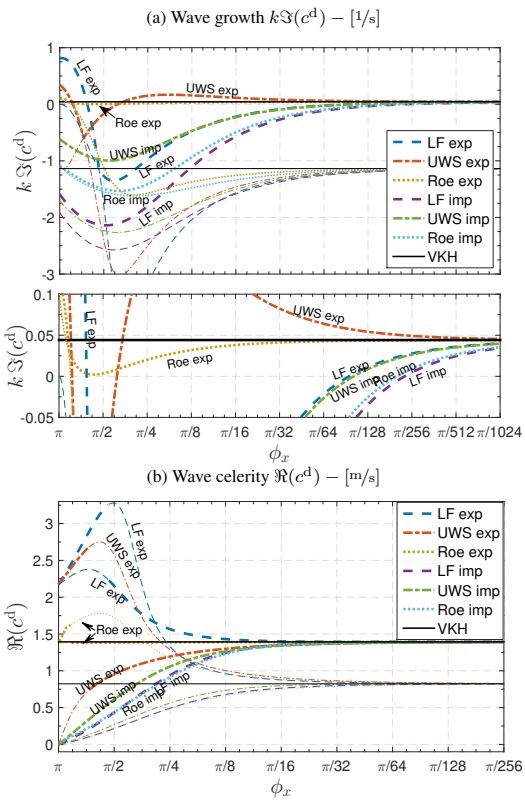

Figure 5.3: Linear theory with varying cell lengths Δx. 30 d wavelength. $\phi_x = k\,\Delta x = 2\pi/(\#\text{ cells in a wave})$

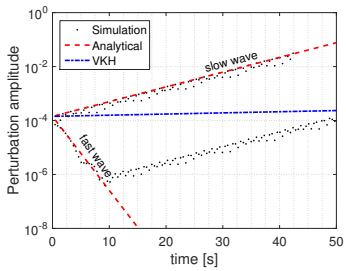

Figure 5.4: Explicit Lax-Friedrich scheme. Three cells per wave; $\phi_x = \frac{2}{3}\pi$.

Finally we look at how the discrete representations respond to changes in the time step. We have already observed that there is a significant difference in the stability and diffusivity of explicit and implicit time step integration. Fig. 5.5 shows the wave growth and wave celerity as functions of the CFL number. Time steps Δt are selected on the basis of these as per the individual method descriptions.

We first note that the explicit and implicit versions of all schemes converge towards the same growth and celerity as the CFL number approaches zero, except for the Lax-Friedrich scheme whose numerical diffusion is inversely proportional to the time step length and thus approaches infinity with reducing CFL number. Growth increases 'with increasing explicitness' for the Roe and upwind scheme. Growth predictions seems to be accurate in explicit schemes based on characteristic information, in this case the Roe scheme, as the CFL number nears unity.

The celerity graphs shown in Figure 5.5b show that the wave celerity of the Roe scheme becomes increasingly accurate as the time step is reduced. Indeed, the Roe scheme is designed to provide the accurate shock speeds for non-linear problems. Both centred schemes (Roe and Lax-Friedrich) provide better estimates of the wave celerity than the upwind scheme, whose dispersion error is mostly caused by the $\mathrm{e}^{-\mathrm{i}\phi_x/2}$ term generated by the spatially asymmetric upwind formulation.

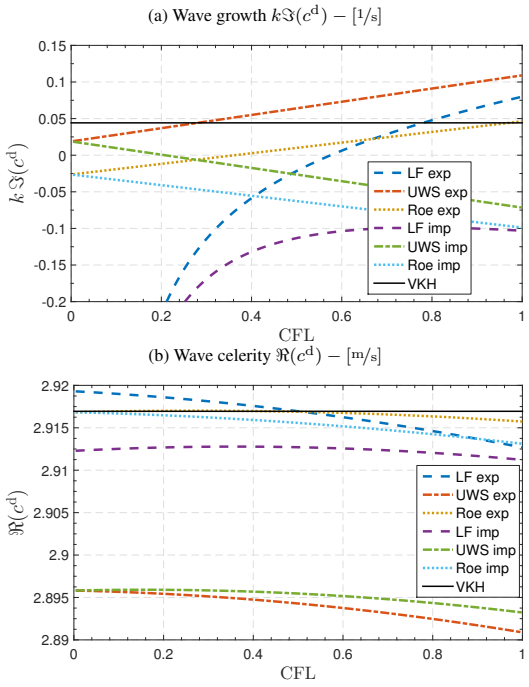

Figure 5.5: Linear theory with varying CFL number, showing the fast wave. 128 celled wave; $\phi_x = \pi/64$

6. Concluding Remarks

Practically no computational effort is associated with the linear stability expressions. The examples presented in the previous section demonstrate some of the information instantaneously available through use of linear theory. This information can aid in choosing reliable simulation parameters prior to simulation, and may give insight into whether or not simulation results can be considered physical.

Acknowledgements

This work is financed by The Norwegian University of Science and Technology (NTNU) as a contribution the Multiphase Flow Assurance programme (FACE.) The author thanks Kontorbamse for his technical support.

References

[1] D. Barnea and Y. Taitel, "Kelvin-helmholtz stability criteria for stratified flow viscous versus non-viscous (inviscid) approaches," *International Journal of Multiphase Flow*, vol. 19, no. 4, pp. 639 – 649, 1993.

[2] D. Barnea and Y. Taitel, "Non-linear interfacial instability of separated flow," *Chemical Engineering Science*, vol. 49, no. 14, pp. 2341 – 2349, 1994.

[3] R. Issa and M. Kempf, "Simulation of slug flow in horizontal and nearly horizontal pipes with the two-fluid model," *International Journal of Multiphase Flow*, vol. 29, no. 1, pp. 69 – 95, 2003/01/.

[4] D. Barnea, "Stability analysis of annular flow structure, using a discrete form of the 'two-fluid model'," *International Journal of Multiphase Flow*, vol. 17, no. 6, pp. 705 – 16, 1991/11/.

[5] J. Liao, R. Mei, and J. F. Klausner, "A study on the numerical stability of the two-fluid model near ill-posedness," *International Journal of Multiphase Flow*, vol. 34, no. 11, pp. 1067 – 1087, 2008.

[6] H. Holmås, "Numerical simulation of transient roll-waves in two-phase pipe flow," *Chemical Engineering Science*, vol. 65, no. 5, pp. 1811 – 25, 2010/03/01.

[7] G. Johnson, *A Stuy of Stratified Gas-Liquid Pipe Flow*. PhD thesis, Univ. Oslo, 2005. dr. scient.

[8] D. Biberg, "A mathematical model for two-phase stratified turbulent duct flow," *Multiphase Science and Technology*, vol. 19, no. 1, pp. 1 – 48, 2007.

An Introductory Summery of The Biberg Friction Model for Pipe Flow

A.H. Akselsen

Department of Energy and Process Engineering, Norwegian University of Science and Technology, Kolbjørn Hejes v. 1B, 7491 Trondheim, Norway

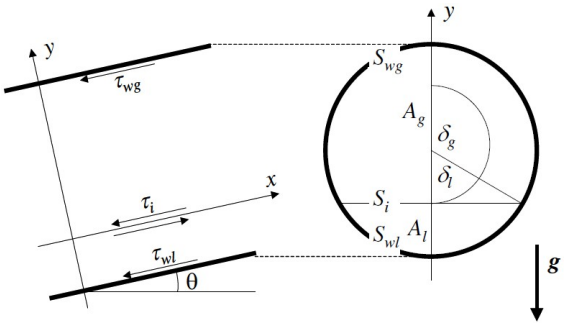

Figure 2.1: Reference system and variables; cross section of channel and pipe. Figure copied from [1].

1. Introduction

This summery is based, in its entirety, on the article [1] which, despite the title, presents a friction model for both pipe and channel flow; a full velocity profile model is given for channel flows and analogous friction correlations are extracted from this onto pipe flows. The full model is extensive, touching upon numerous modelling concerns. This summery is intended to ease the encounter with the Biberg model, highlighting the essentials while keeping the number of variable and expressions small.

2. Momentum Balance

Regarding a single fluid phase, the x-momentum equation for the average velocity reads

$$\frac{\mathrm{D}\rho u}{\mathrm{D}t} = -\frac{\partial p}{\partial x} - \rho g \cos\theta + \frac{\partial \tau_{xy}}{\partial y}. \tag{2.1}$$

All terms but the last are considered constant in y. Integrating yields $\tau_{xy} \propto y$. τ_{xy} contains the full turbulent shear after the Reynolds averaging, i.e.

$$\tau_{xy} = \mu \frac{\partial u}{\partial y} - \rho \overline{u'v'}. \tag{2.2}$$

In what follows, it is best to regard wall and interface shears τ_w and τ_i as known. Also the full shear τ_{xy} is then known since $\tau_{xy} \propto y$ by (2.1). The actual shears are recovered from searching for velocity profiles generating the appropriate mean velocities.

3. The Algebraic Eddy Viscosity Model for Channel Flows

This model is based on some well-known concepts from early turbulence theory. These involve the Boussinesq assumption $-\rho\overline{u'v'} = \mu^\mathrm{t}\frac{\partial u}{\partial y}$ and disregarding the molecular viscosity; $\mu \approx 0$. Prandtl's mixing length hypothesis, together with his assumption for the turbulent velocity scale, yields

$$\sqrt{\frac{|\tau_{xy}|}{\rho}} = \ell \left|\frac{\partial u}{\partial y}\right|. \tag{3.1}$$

This constitutes a coupling between an (assumed known) shear and a velocity gradient through a mixing length function ℓ. The mixing length hypothesis of Prandtl and von Kármán is a historical cornerstone turbulent theory. Sidestepping all of that, simply regard (3.1) as the definition of ℓ and let it be modelled based on the law of the wall[1]. The law of the wall is in a generic from written

$$u(y_\mathrm{w}) = \frac{\sqrt{\tau_\mathrm{w}/\rho}}{\kappa} \ln y_\mathrm{w} + C_\mathrm{w}, \tag{3.2}$$

subscripts indicating a coordinate system relative to the 'wall' to which the law is applied. The empirical von Kármán constant κ equals 0.4. The constant C_w has two different forms, depending on whether the 'wall' is smooth or fully rough – more on this in Section 4. Equation (3.2) thus provides modelling information for the mixing length ℓ.

Applying the law of the wall (3.2) to both channel wall and the interface and then differentiating yields, after applying (3.1),

$$\ell = \kappa\,(h-y)\sqrt{\left|\frac{\tau_{xy}}{\tau_\mathrm{w}}\right|} \qquad \text{near the wall,} \tag{3.3a}$$

$$\ell = \kappa y \sqrt{\left|\frac{\tau_{xy}}{\tau_\mathrm{i}}\right|} \qquad \text{near the interface.} \tag{3.3b}$$

[1] The law of the wall has a strong empirical foundation, validated beyond where the original mixing length hypothesis can be said to be valid. Therefore, the mixing length is here considered a derivative of the law of the wall, rather than the other way around

In accommodating the features of (3.3), Biberg split the mixing length function in the following manner:

$$\ell = \mathcal{L}\mathcal{F}, \tag{3.4}$$

where $\mathcal{L}$ is a function accomplishing

- linearly approaching zero along $\kappa(h-y)$ near the wall, and
- linearly approaching a fixed value ℓ_i along κy near the interface.

ℓ_i is the mixing length at the interface – a closure relation. This value reflects waves and turbulent disturbances here. By assigning a specific interface mixing length value, the velocity profile starts some distance within the log law profile at the interface. $\mathcal{L}$ is made a quadratic function satisfying the two conditions just mentioned.

$\mathcal{F}$ in (3.4) should be made to

- approach $\sqrt{\left|\frac{\tau_{xy}}{\tau_\mathrm{w}}\right|}$ near the wall, and
- approach $\sqrt{\left|\frac{\tau_{xy}}{\tau_\mathrm{i}}\right|}$ near the interface. Of course,
- $\mathcal{F}(y=0) = \mathcal{F}(y=h) = 1$.

$\mathcal{F}$ is generated from interpolation the group $\mathcal{F}\sqrt{\tau_{xy}/\rho}$ such that is satisfies the required values, slopes and curvatures *at* the wall and the interface.

4. Friction Model for Channel Flow

The velocity profile is obtained from the 'definition' (3.1)

$$u = \int \frac{\sqrt{|\tau_{xy}|/\rho}}{\ell}\,\mathrm{d}y, \tag{4.1}$$

and the average velocity from

$$U = \frac{1}{h}\int_0^h u\,\mathrm{d}y. \tag{4.2}$$

Expression (4.1) is here presented somewhat imprecisely as positive velocities are assumes – see [1] for the general expressions. Equation (4.2) now constitutes the friction model; wall and interfacial shears $\{\tau_\mathrm{w}, \tau_\mathrm{i}\}$ generating the prescribed U at channel height h are the target values. Equations (4.1) and (4.2) are analytically pre-integrated so that the solution search is algebraic.

The integration constant of (4.1) is made to coincide with the law of the wall (3.2) at the wall itself and to satisfies the no-slip condition $u_\ell = u_\mathrm{g}$ at the interface. Integration constant C_w from (3.2) is known for smooth and 'fully rough' surfaces, but not directly for anything in between. Biberg solved this issue by turning to the Colebrook-White formula

$$\frac{1}{\sqrt{\lambda}} = -2\log_{10}\left(\frac{2.51}{\mathrm{Re}_D\sqrt{\lambda}} + \frac{k_s}{3.7D}\right), \quad \tau_\mathrm{w} = \frac{\lambda}{4}\frac{\rho U|U|}{2} \tag{4.3}$$

for *single-phase* friction in a *pipe* of 'intermediate' roughness k_s. He found that the Colebrook-White formula (4.3) could be related to the wall friction of (4.2) for both smooth and fully rough channels by substituting D with an effective diameter $D_\mathrm{e}^\mathrm{chan}$. The effective diameter then contained the relevant velocity profile information relating *channel* flow with a turbulent interface to friction in single-phase *pipe* flow;

$$D_\mathrm{e}^\mathrm{chan} = h\,C_\mathrm{e}, \tag{4.4}$$

$C_\mathrm{e} = C_\mathrm{e}\left(\frac{\tau_\mathrm{i}}{\tau_\mathrm{w}}, \frac{\ell_\mathrm{i}}{h}\right)$ being a function of the shear ratio and interfacial turbulence closure only. Generalising, wall friction for an intermediate wall roughness is obtained from the Colebrook-White formula (4.3) applying $D_\mathrm{e}^\mathrm{chan}$ and the appropriate roughness k_s.

5. Friction Model for Pile Flow

Wall friction for *pipe* flow is approximated by coupling the effective diameter $D_\mathrm{e}^\mathrm{chan}$ to hydraulic diameters

$$D_\mathrm{F}^\mathrm{pipe} = \frac{A_k}{S_k}, \qquad D_\mathrm{P}^\mathrm{pipe} = \frac{A_k}{S_k + S_\mathrm{i}} \tag{5.1}$$

for free surface and Poiseuille type flows, respectively. This is done by first expressing the effective channel diameter in terms of the effective channel diameters for free surface and Poiseuille flows, as follows:

$$D_\mathrm{e}^\mathrm{chan} = D_\mathrm{F}^\mathrm{chan}\left(\frac{D_\mathrm{P}^\mathrm{chan}}{D_\mathrm{F}^\mathrm{chan}}\right)^{F^\mathrm{chan}}, \tag{5.2}$$

with the exponent

$$F^\mathrm{chan} \equiv \frac{\ln\left(D_\mathrm{e}^\mathrm{chan}/D_\mathrm{F}^\mathrm{chan}\right)}{\ln\left(D_\mathrm{P}^\mathrm{chan}/D_\mathrm{F}^\mathrm{chan}\right)}.$$

Equation (5.2) simply reads $D_\mathrm{e}^\mathrm{chan} = D_\mathrm{e}^\mathrm{chan}$. F is used to model effective diameters in the presence of a second phase in pipe flows, which would range in between the free surface hydraulic diameter $D_\mathrm{F}^\mathrm{pipe}$ and the Poisuille diameter $D_\mathrm{P}^\mathrm{pipe}$. It is a function of the dimensionless profile variables $\frac{\tau_\mathrm{i}}{\tau_\mathrm{w}}$ and $\frac{\ell_\mathrm{i}}{h}$ only, i.e.,

$$F^\mathrm{pipe} = F^\mathrm{pipe}\left(\tfrac{\tau_\mathrm{i}}{\tau_\mathrm{w}}, \tfrac{\ell_\mathrm{i}}{h}\right)$$

contains the velocity profile information. Replacing hydraylic diameters for free surface and Poisuille channel flow with the respective hydraulic diameters for pipe flow (5.1) in (5.2), the effective pipe flow diameter is

$$D_\mathrm{e}^\mathrm{pipe} = D_\mathrm{F}^\mathrm{pipe}\left(\frac{D_\mathrm{P}^\mathrm{pipe}}{D_\mathrm{F}^\mathrm{pipe}}\right)^{F^\mathrm{pipe}}. \tag{5.3}$$

$\frac{\ell_i}{h}$ being provided by a model closure[2], F^{pipe} is determined form the pipe wall frictions, providing the velocity profile coupling. Pipe wall frictions are now obtainable through the Colebrook-White equation (4.3), replacing D with D_e^{pipe}. Interfacial shear is taken as that found in the channel flow from (4.2) and the no-slip condition $u_\ell = u_g$ at the interface.

The channel flow velocity profile solution now only has an indirect coupling to the pipe wall friction through F. Seeking to understand the connection to the velocity profile model (4.1), one may regard the obtained pipe wall frictions as those frictions which would result from regarding a channel flow with a fictitious height $h^{\text{pipe}} \sim D_e^{\text{pipe}}/C_e$, C_e being the relation (4.4) relating channel flow friction to the Darcy friction factor λ for single-phase pipe flows.

Biberg provides closure correlations for the interfacial turbulence based on experiments form Espedal (1998).

Figure 5.1 shows two velocity profile examples for stratified pipe flow in the 'equivalent channel height' D_e^{pipe}/C_e. The interfacial turbulence closure provided in [1] has been included in Figure a, while in Figure b only the minimum (next to zero) mixing length is enforced at the interface. It is clear how the interfacial mixing length moves the turbulence level further into the log law at the interface. With its value near zero, the interface acts as a solid, moving wall. Larger values of the interfacial mixing lengths contribute to move the peaks of the gas and liquid velocity profiles away from the interface.

Figure 5.2a shows an example of wall and interfacial shears as function of phase height and liquid velocity. U_g is in the figure is computed for U_ℓ and h assuming incompressible flow. In order of descending maxima, the graphed surfaces depict $\tau_{w,\ell}$, τ_i and $\tau_{w,g}$. Figure 5.2b shows the interfacial friction factor λ_i (graph with largest maximum) compared to the friction factor generated simply by multiplying $\lambda_{w,g}$ by an 'interfacial friction multiplier' (near horizontal graph.) It is evident that this latter does not capture any significant dependency of λ_i on U_ℓ and h. The $\lambda_{w,g}$ with which the latter λ_i is determined is computed from the Håland friction formula using mean velocities, as in [2] (no significant difference is made in using $\lambda_{w,g}$ form the Biberg method.)

6. Algorithmic Summery in Computing Wall and Interfacial Shear in Pipes

An algorithm for computing wall and interfacial frictions within a dynamic pipe flow simulator is here presented. Variables and equations listed herein refer to the equations as they appear in [1]. A similar algorithm for computing the steady-state holdup and pressure drop in a pipe is given in appendix D of the same reference.

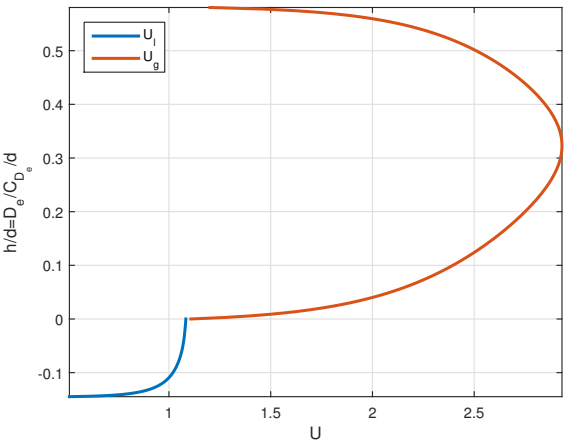

(a) High interfacial turbulence (rough interface): $\frac{\ell_i}{\kappa h_k} = K_k$ from (99) and (114) in [1].

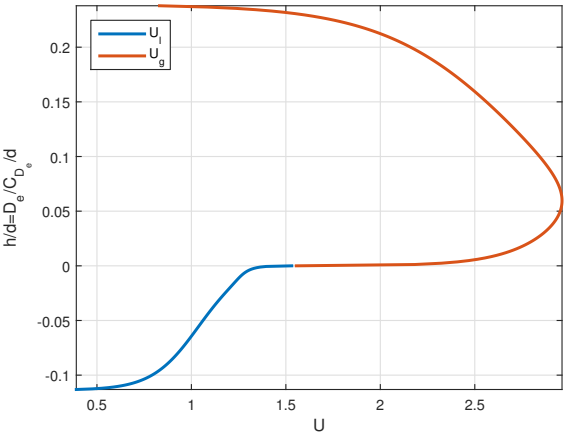

(b) No interfacial turbulence (smooth interface): $\frac{\ell_i}{\kappa h_k} = K_{k,\min}$ from (79) in [1].

Figure 5.1: Gas-liquid velocity profile for stratified pipe flow. Smooth walls. $U_\ell = 1\,\text{m/s}$, $U_g = 2.5\,\text{m/s}$.

[2] grouped as the 'interfacial turbulence parameter' $K = \frac{\ell_i}{\kappa h}$

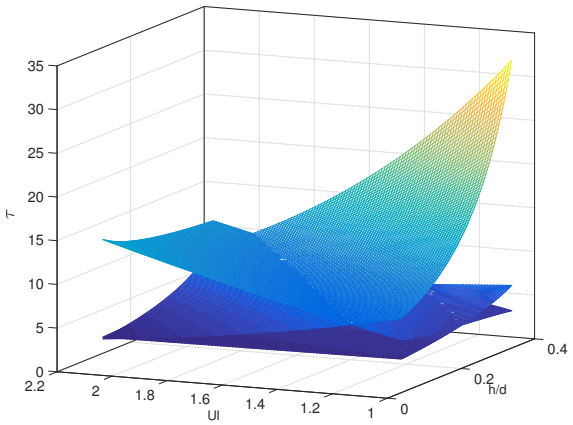

(a) Wall and interfacial shears. Graph with largest maximum: $\tau_{w,\ell}$, with middle maximum: τ_i, with smallest maximum: $\tau_{w,g}$.

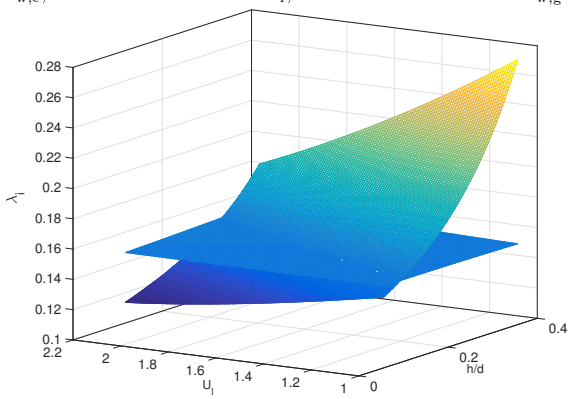

(b) Darcy friction coefficients λ_i for interfacial friction. Graph with largest maximum: λ_i as computed from the Biberg model. Graph with smallest maximum: λ_i as computed from $6 \cdot \lambda_g$ where λ_g is computed directly from Håland's friction formula with the mean velocities, as in [2].

Figure 5.2: Friction properties as function of phase height and liquid velocity. (Incompressible, at constant mixture velocity. $U_m = 3.8\,\mathrm{m/s}$, $\rho_\ell = 1000\,\mathrm{kg/m^3}$, $\rho_g = 50\,\mathrm{kg/m^3}$, $\nu_\ell =$ 1.0e-6 $\mathrm{m^2/s}$, $\nu_g =$ 1.6e-5 $\mathrm{m^2/s}$.)

Algorithm 1 Calculate $\tau_{w,k}$ and $\tau_{i,\ell}$

1: Compute Λ_k^P,Λ_k^F, K_k^F and K_k from (61), (62), (35), (99) and (114).
2: Make initial guesses on R_k, e.g.
   - by applying the hydraulic diameters and mean velocities U_k to the Blasinus, Håland or Colebrook-White formula, or
   - by using R_k values from an earlier computation.
3: **repeat**
4: Compute $K_k^{\min}$ from (79). Use this dynamically as a lower limit on K_k.
5: Compute Ψ_k, Λ_k and $\Delta_{i,k} = \Delta_k(Y = 0)$ from (51), (59) and (48), respectively.
6: Compute D_e^{pipe} from (94) and (95).
7: Compute λ_k, either iteratively from the Colebrook-White formula (71) or using the explicit approximation (132), (133).
8: Compute $\tau_{w,k}$ from (70).
9: Compute $\tau_{i,\ell}$ from (83).
10: Re-compute R_k form their definitions $R_g = \tau_i/\tau_{w,g}$, $R_\ell = -\tau_i/\tau_{w,\ell}$.
11: **until** R_g and R_ℓ has converged.
12: Export $\tau_{w,k}$ and $\tau_{i,\ell}$.

Note that this algorithm uses the definition $R_\ell = -\tau_i/\tau_{w,\ell}$ rather than steady-state relation (105) originating from the holdup equation. Thus, the transient term $\frac{D\rho u}{Dt}$ needs not be zero, only constant in y.

In dynamic simulations it is usually most efficient to store a mesh of state points and dynamically interpolate on this, rather than computing every point again at every time step. This is particularly the case with incompressible model simulations, where the state is determined by two independent variables rather than four.

[1] D. Biberg. A mathematical model for two-phase stratified turbulent duct flow. *Multiphase Science and Technology*, 19(1):1 – 48, 2007. ISSN 0276-1459. URL `http://dx.doi.org/10.1615/MultScienTechn.v19.i1.10`.

[2] Y. Taitel and A.E. Dukler. A model for predicting flow regime transitions in horizontal and near horizontal gas-liquid flow. *AIChE Journal*, 22(1):47 – 55, 1976/01/. ISSN 0001-1541. URL `http://dx.doi.org/10.1002/aic.690220105`.

A Flexible Joint Structural Model

A.H. Akselsen[a,*]

[a]*Department of Energy and Process Engineering, Norwegian University of Science and Technology*

1. Introduction

The structural model presented here is a rigid pipe model with flexible joints. Force and moment balances are solved implicitly in a connected pipeline system. Only simple fluid states are required for communication with an arbitrary multiphase pipe flow model. The coupling back to the fluid model may be of a hydrostatic 'zeroth order' nature, updating pipe inclinations only, or of a higher order, communicating also structural accelerations.

The model is designed to produce a method where the pipeline length is constant and pipe positions are consistent (connectedness). The model is non-stiff and integration in time is robust, without the possibility of unphysical spring oscillations originating form numerical destiffening/relaxation.

2. Model

In this section we present the structural model from the dynamic perspective. We assume that all internal, external and structural forces have been compounded into a single external force and an external moment, though we retain the joint pushing and pulling forces separate as these need to be solved implicitly to achieve pipeline connectedness.

Force models are suggested in Appendix Appendix B. These may be used to compute the external forces and torques from the flow simulation. It is recommended to examine this appendix first if the nature of the external forces is unclear.

2.1. Pipe Equations

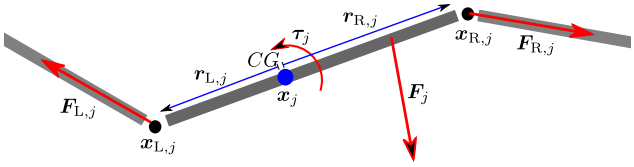

Figure 2.1: Forces acting on a pipe segment

According to Newton's second law, the acceleration of the centre of gravity CG of a pipe j is

$$\frac{\mathrm{d}}{\mathrm{d}t} M_j \dot{\boldsymbol{x}}_j = M_j \ddot{\boldsymbol{x}}_j + \dot{M}_j \dot{\boldsymbol{x}}_j = \sum_k \boldsymbol{F}_{k,j} = \boldsymbol{F}_{\mathrm{L},j} + \boldsymbol{F}_{\mathrm{R},j} + \boldsymbol{F}_j, \tag{2.1}$$

*Corresponding author
Email address: andreas.h.akselsen@ntnu.no (A.H. Akselsen)

where M_j is the total pipe mass and $\boldsymbol{x}_j$ is the location of the CG of pipe j.

Angular acceleration is given from an equivalent balance on the moments:

$$\frac{\mathrm{d}}{\mathrm{d}t} J_j \dot{\boldsymbol{\theta}}_j = J_j \ddot{\boldsymbol{\theta}}_j + \dot{J}_j \dot{\boldsymbol{\theta}}_j = \sum_k \left(\boldsymbol{r}_{k,j} \times \boldsymbol{F}_{k,j} + \boldsymbol{\tau}_{k,j} \right) = \boldsymbol{r}_{\mathrm{L},j} \times \boldsymbol{F}_{\mathrm{L},j} + \boldsymbol{r}_{\mathrm{R},j} \times \boldsymbol{F}_{\mathrm{R},j} + \boldsymbol{r}_j \times \boldsymbol{F}_j + \boldsymbol{\tau}_j,$$

where the vectors $\boldsymbol{r}$ point form the CG to the location of attack of the respective forces. Since the model is purely two-dimensional, angular acceleration takes a purely scalar form in the z direction:

$$J_j \ddot{\theta}_j = \boldsymbol{r}'_{\mathrm{L},j} \cdot \boldsymbol{F}_{\mathrm{L},j} + \boldsymbol{r}'_{\mathrm{R},j} \cdot \boldsymbol{F}_{\mathrm{R},j} + \boldsymbol{r}'_j \cdot \boldsymbol{F}_j + \tau_j - \dot{J}_j \dot{\theta}_j. \tag{2.2}$$

For compactness we have dropped the subscript 'z' in θ_j, which is the z-component of $\boldsymbol{\theta}_j$. Since $r_{\mathrm{z}} = F_{\mathrm{z}} = 0$ we have also introduced

$$\boldsymbol{r}' = \langle -r_y, r_x, 0 \rangle$$

for easy evaluation of the cross products.

Equations (2.1) and (2.2) dictates the change in orientation of pipe segment j. The forces from the joints provide the structural coupling between pipes. These must ensure the connectedness of the pipeline. A third group of equations is needed to procure the joint forces. Here, we compute the joint forces by imposing connectedness – that is, we impose that the position of connected pipe ends coincide:

$$\left\{ \begin{array}{l} \boldsymbol{x}_{\mathrm{L},j} = \boldsymbol{x}_{\mathrm{R},j-1} \Leftrightarrow \boldsymbol{x}_j + \boldsymbol{r}_{\mathrm{L},j} = \boldsymbol{x}_{j-1} + \boldsymbol{r}_{\mathrm{R},j-1} \\ \boldsymbol{x}_{\mathrm{R},j} = \boldsymbol{x}_{\mathrm{L},j+1} \Leftrightarrow \boldsymbol{x}_j + \boldsymbol{r}_{\mathrm{R},j} = \boldsymbol{x}_{j+1} + \boldsymbol{r}_{\mathrm{L},j+1} \end{array} \right\}.$$

The equations of the pipe tip acceleration read

$$\ddot{\boldsymbol{x}}_{\mathrm{L},j} = \ddot{\boldsymbol{x}}_j + \ddot{\boldsymbol{\theta}}_j \times \boldsymbol{r}_{\mathrm{L},j} - \left| \dot{\boldsymbol{\theta}}_j \right|^2 \boldsymbol{r}_{\mathrm{L},j},$$
$$\ddot{\boldsymbol{x}}_{\mathrm{R},j-1} = \ddot{\boldsymbol{x}}_{j-1} + \ddot{\boldsymbol{\theta}}_{j-1} \times \boldsymbol{r}_{\mathrm{R},j-1} - \left| \dot{\boldsymbol{\theta}}_{j-1} \right|^2 \boldsymbol{r}_{\mathrm{R},j-1},$$

where centripetal acceleration plays and important role. An equation for *preservation of* the connectedness[1] is then obtained simpely by imposing $\ddot{\boldsymbol{x}}_{\mathrm{L},j} = \ddot{\boldsymbol{x}}_{\mathrm{R},j-1}$, yielding

$$\ddot{\boldsymbol{x}}_{j-1} - \ddot{\boldsymbol{x}}_j + \ddot{\theta}_{j-1} \boldsymbol{r}'_{\mathrm{R},j-1} - \ddot{\theta}_j \boldsymbol{r}'_{\mathrm{L},j} = \dot{\theta}^2_{j-1} \boldsymbol{r}_{\mathrm{R},j-1} - \dot{\theta}^2_j \boldsymbol{r}_{\mathrm{L},j}. \tag{2.3}$$

The final equation to close the system is applying Newton's 3rd law to the joint forces experienced by two pipes, namely

$$\boldsymbol{F}_{\mathrm{R},j-1} = -\boldsymbol{F}_{\mathrm{L},j}. \tag{2.4}$$

2.2. Correction for Displacement Error

Equation (2.3) is formulated as an acceleration. The joint position seen form two neighbouring pipe segments $\boldsymbol{x}_{\mathrm{L},j}$ and $\boldsymbol{x}_{\mathrm{R},j-1}$ will gradually diverge due to time integration error. The centripetal acceleration terms $\dot{\theta}^2 \boldsymbol{r}$ contribute greatly to reduce the displacement error, particularly if treated semi-implicitly (Section 2.3.) However, over time, using coarse time steps and with violent pipeline movements, it will inevitably succumb to positional divergence.

Displacement corrections cannot be applied to the joint forces as these are obtained from a positional condition. Rather, the pipe acceleration equation (2.3) is supplemented with a spring correction. We assuming the position of contact $\boldsymbol{x}_{j-\frac{1}{2}}$ between pipe $j-1$ and j to be midway between the pipe tip positions

[1] assuming consistent initial conditions: $\boldsymbol{x}_{\mathrm{L},j} = \boldsymbol{x}_{\mathrm{R},j-1}$, $\dot{\boldsymbol{x}}_{\mathrm{L},j} = \dot{\boldsymbol{x}}_{\mathrm{R},j-1}$ for all j at $t = 0$.

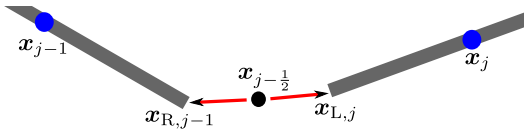

Figure 2.2

$\boldsymbol{x}_{\mathrm{R},j-1}$ and $\boldsymbol{x}_{\mathrm{L},j}$. Rather than imposing equality between the two tip accelerations, we instead impose that the midpoint $\boldsymbol{x}_{j-\frac{1}{2}}$ accelerate towards each pipe tip simultaneously from a correction spring:

$$\ddot{\boldsymbol{x}}_{j-\frac{1}{2}} = \ddot{\boldsymbol{x}}_{\mathrm{R},j-1} + k^{\mathrm{corr}}(\boldsymbol{x}_{j-\frac{1}{2}} - \boldsymbol{x}_{\mathrm{R},j-1})$$
$$\ddot{\boldsymbol{x}}_{j-\frac{1}{2}} = \ddot{\boldsymbol{x}}_{\mathrm{L},j} + k^{\mathrm{corr}}(\boldsymbol{x}_{j-\frac{1}{2}} - \boldsymbol{x}_{\mathrm{L},j}).$$

Equation (2.3) now gets a correction term

$$\ddot{\boldsymbol{x}}_{j-1} - \ddot{\boldsymbol{x}}_{j} + \ddot{\theta}_{j-1}\boldsymbol{r}'_{\mathrm{R},j-1} - \ddot{\theta}_{j}\boldsymbol{r}'_{\mathrm{L},j} = \dot{\theta}^2_{j-1}\boldsymbol{r}_{\mathrm{R},j-1} - \dot{\theta}^2_{j}\boldsymbol{r}_{\mathrm{L},j} + k^{\mathrm{corr}}(\boldsymbol{x}_{\mathrm{L},j} - \boldsymbol{x}_{R,j-1}). \tag{2.5}$$

The correction spring coefficient k^{corr} can be given a very moderate value when the time steps and structural movement are moderate and a semi-implicit centripetal acceleration is used. It may be a good idea to make k^{corr} proportional to some power of the time step.

2.3. Semi-Implicit Centripetal Acceleration

The equations (2.1),(2.2), (2.4) and (2.5) are linear except for the centripetal acceleration terms $\dot{\theta}^2\boldsymbol{r}$. Instead of evaluating the term at the old time, better accuracy is achieved by extrapolating $\dot{\theta}^2$ to the first order in time $\dot{\theta}^2(t+\frac{\Delta t}{2}) = \dot{\theta}^2(t) + \Delta t 2\dot{\theta}(t+\varepsilon\frac{\Delta t}{2})\ddot{\theta}(t+\varepsilon\frac{\Delta t}{2}),\ 0 \le \varepsilon \le 1$.To make is semi-implicit we use

$$\dot{\theta}^2 \to \left(\dot{\theta}^n\right)^2 + \Delta t\, \dot{\theta}^n\ddot{\theta}^{n+1}. \tag{2.6}$$

2.4. Composing a Pipeline System

The translational and rotational momentum equations (2.1) and (2.2) pertain to the pipes and are given integer subscripts j, $j+1$, etc.. We introduce the following coefficient matrices:

$$\boldsymbol{a}^{\mathrm{w}}_j = \begin{pmatrix} \boldsymbol{I}_{2,2} \\ \left[\boldsymbol{r}'^{n+1}_{\mathrm{L},j}\right]^T \end{pmatrix} \qquad \boldsymbol{a}^{\mathrm{p}}_j = \begin{pmatrix} M^{n+1}_j\boldsymbol{I}_{2,2} & \boldsymbol{0}_{2,1} \\ \boldsymbol{0}_{1,2} & J^{n+1}_j \end{pmatrix} \qquad \boldsymbol{a}^{\mathrm{e}}_j = \begin{pmatrix} -\boldsymbol{I}_{2,2} \\ -\left[\boldsymbol{r}'^{n+1}_{\mathrm{R},j}\right]^T \end{pmatrix}. \tag{2.7a}$$

$\boldsymbol{0}$ is here the zero matrix and $\boldsymbol{I}$ the identity matrix. The corresponding right hand side coefficients are

$$\boldsymbol{d}_j = \begin{pmatrix} \boldsymbol{F}^{n+1}_j - \frac{M^{n+1}_j - M^n_j}{\Delta t}\dot{\boldsymbol{x}}^n_j \\ (\boldsymbol{r}'\cdot\boldsymbol{F})^{n+1}_j + \tau^n_j - \frac{J^{n+1}_j - J^n_j}{\Delta t}\dot{\theta n}_j \end{pmatrix}, \tag{2.7b}$$

and the j variable vector is

$$\boldsymbol{w}_j = \begin{pmatrix} \ddot{\boldsymbol{x}}^{n+1}_j \\ \ddot{\theta}^{n+1}_j \end{pmatrix}. \tag{2.7c}$$

It has here been assumed that internal/external flow computations are carried out before the structural computation and hence the $n+1$ indexation on $\boldsymbol{F}_j$ and $\boldsymbol{r}'$.

The equations imposing connectedness through joint forces (2.5) pertain to the intersection between two pipes and are given non-integer subscripts $j-\frac{1}{2}$, $j+\frac{1}{2}$, etc.. The following coefficients are introduced:

$$\boldsymbol{a}^{\mathrm{w}}_{j+\frac{1}{2}} = \begin{pmatrix} \boldsymbol{I}_{2,2} & \left[\boldsymbol{r}'^{n+1}_{j,R} - \Delta t \dot{\theta}^n_j \boldsymbol{r}^{n+1}_{j,R}\right] \end{pmatrix} \qquad \boldsymbol{a}^{\mathrm{e}}_{j+\frac{1}{2}} = \begin{pmatrix} -\boldsymbol{I}_{2,2} & \left[-\boldsymbol{r}'^{n+1}_{j+1,L} + \Delta t \dot{\theta}^n_{j+1} \boldsymbol{r}^{n+1}_{j+1,L}\right] \end{pmatrix}. \tag{2.8a}$$

The $j+\frac{1}{2}$ right hand coefficients are

$$\boldsymbol{d}_{j+\frac{1}{2}} = \left(\dot{\theta}^n_j\right)^2 \boldsymbol{r}^{n+1}_{\mathrm{R},j} - \left(\dot{\theta}^n_{j+1}\right)^2 \boldsymbol{r}^{n+1}_{\mathrm{L},j+1} + k^{\mathrm{corr}}\left(\boldsymbol{x}^n_{\mathrm{L},j+1} - \boldsymbol{x}^n_{\mathrm{L},j}\right) \tag{2.8b}$$

and the $j+\frac{1}{2}$ variable

$$\boldsymbol{w}_{j+\frac{1}{2}} = \boldsymbol{F}^{n+1}_{\mathrm{R},j}. \tag{2.8c}$$

A pipeline system of N_{J} pipe segments may now be written on the form $\boldsymbol{A}\boldsymbol{w} = \boldsymbol{d}$ as

$$\begin{pmatrix}
\boldsymbol{0}_{2,2} & \boldsymbol{a}^{\mathrm{e}}_{\frac{1}{2}} & & & & & & \dots & \boldsymbol{0} \\
\boldsymbol{a}^{\mathrm{w}}_1 & \boldsymbol{a}^{\mathrm{p}}_1 & \boldsymbol{a}^{\mathrm{e}}_1 & & & & & & \vdots \\
 & \boldsymbol{a}^{\mathrm{w}}_{1+\frac{1}{2}} & \boldsymbol{0}_{2,2} & \boldsymbol{a}^{\mathrm{e}}_{1+\frac{1}{2}} & & & & & \\
 & & \ddots & \ddots & \ddots & & & & \\
 & & & \boldsymbol{a}^{\mathrm{w}}_j & \boldsymbol{a}^{\mathrm{p}}_j & \boldsymbol{a}^{\mathrm{e}}_j & & & \\
 & & & & \boldsymbol{a}^{\mathrm{w}}_{j+\frac{1}{2}} & \boldsymbol{0}_{2,2} & \boldsymbol{a}^{\mathrm{e}}_{j+\frac{1}{2}} & & \\
 & & & & & \ddots & \ddots & \ddots & \\
\vdots & & & & & & \boldsymbol{a}^{\mathrm{w}}_{N_{\mathrm{J}}} & \boldsymbol{a}^{\mathrm{p}}_{N_{\mathrm{J}}} & \boldsymbol{a}^{\mathrm{e}}_{N_{\mathrm{J}}} \\
\boldsymbol{0} & \dots & & & & & & \boldsymbol{a}^{\mathrm{w}}_{N_{\mathrm{J}}+\frac{1}{2}} & \boldsymbol{0}_{2,2}
\end{pmatrix}
\begin{pmatrix} \boldsymbol{w}_{\frac{1}{2}} \\ \boldsymbol{w}_1 \\ \boldsymbol{w}_{1+\frac{1}{2}} \\ \vdots \\ \boldsymbol{w}_j \\ \boldsymbol{w}_{j+\frac{1}{2}} \\ \vdots \\ \boldsymbol{w}_{N_{\mathrm{J}}} \\ \boldsymbol{w}_{N_{\mathrm{J}}+\frac{1}{2}} \end{pmatrix} =
\begin{pmatrix} \boldsymbol{d}_{\frac{1}{2}} \\ \boldsymbol{d}_1 \\ \boldsymbol{d}_{1+\frac{1}{2}} \\ \vdots \\ \boldsymbol{d}_j \\ \boldsymbol{d}_{j+\frac{1}{2}} \\ \vdots \\ \boldsymbol{d}_{N_{\mathrm{J}}} \\ \boldsymbol{d}_{N_{\mathrm{J}}+\frac{1}{2}} \end{pmatrix} \tag{2.9}$$

and solved using a sparse diagonal solver. The system matrix has a bandwidth of 9 elements and the size of the system is $(5N_{\mathrm{J}} \pm 2) \times (5N_{\mathrm{J}} \pm 2)$ where the ± 2 depends on the boundary conditions.[2]

Time integration is preformed using simple forward Euler, that is

$$\boldsymbol{w} \to \{\ddot{\boldsymbol{x}}^{n+1}_j, \ddot{\theta}^{n+1}_j\};$$
$$\dot{\boldsymbol{x}}^{n+1}_j = \dot{\boldsymbol{x}}^n_j + \Delta t\, \ddot{\boldsymbol{x}}^{n+1}_j, \quad \boldsymbol{x}^{n+1}_j = \boldsymbol{x}^n_j + \Delta t\, \dot{\boldsymbol{x}}^{n+1}_j, \quad \dot{\theta}^{n+1}_j = \dot{\theta}^n_j + \Delta t\, \ddot{\theta}^{n+1}_j, \quad \theta^{n+1}_j = \theta^n_j + \Delta t\, \dot{\theta}^{n+1}_j.$$

The joint forces $\boldsymbol{F}_{\mathrm{L},j}$ and $\boldsymbol{F}_{\mathrm{R},j}$ are not required for integration or storage. The system (2.9) can be reduced by eliminating these joint forces and the $j+\frac{1}{2}$ rows directly, producing instead a $3N_{\mathrm{J}} \times 3N_{\mathrm{J}}$ system.

2.5. Boundary Conditions

Two types of boundaries are supported; the fixed and the free boundary.

Fixed Boundary

A fixed boundary means that the pipe tip in touch with the boundary is locked in position. Given a fixed left boundary at $\boldsymbol{x}^{\mathrm{fixed}}_{0,\mathrm{L}}$, we have the coefficient

$$\boldsymbol{d}_{\frac{1}{2}} = k^{\mathrm{corr}}\left(\boldsymbol{x}^{\mathrm{fixed}}_{0,\mathrm{L}} - \boldsymbol{x}_{\mathrm{L},j}\right).$$

[2] $+2$ if both boundaries are fixed, 0 if one is fixed and -2 if none are fixed.

Likewise, a right boundary fixed at $\boldsymbol{x}_{0,\mathrm{R}}^{\mathrm{fixed}}$ yields the coefficient

$$\boldsymbol{d}_{N_J+\frac{1}{2}} = k^{\mathrm{corr}}\big(\boldsymbol{x}_{R,N_J} - \boldsymbol{x}_{0,\mathrm{R}}^{\mathrm{fixed}}\big).$$

The rest of the coefficients remain unchanged.

Free Boundary

Free boundaries are not connected to anything and will flop about governed to the forces acting on the system. A pipeline with two free boundaries is equivalent to a loose thread and its position unbounded.

A free left boundary is obtained by removing the leftmost column in $\boldsymbol{A}$ and the top row in $\boldsymbol{A}$, $\boldsymbol{u}$ and $\boldsymbol{d}$ of equation (2.9). A free right boundary is obtained by removing the rightmost column in $\boldsymbol{A}$ and the bottom row in $\boldsymbol{A}$, $\boldsymbol{u}$ and $\boldsymbol{d}$.

3. Examples

Two simulations are preformed on the same arbitrarily constructed pipeline, the properties of which are presented in Table 1. w_{CG} indicates the position of the pipe centre of gravity, $w_{\mathrm{CG}} = 0$ placing it on the left tip, $w_{\mathrm{CG}} = 0.5$ placing it in the pipe centre and $w_{\mathrm{CG}} = 1$ placing it on the right tip. In the first simulation both ends of the pipeline are fixed, while the right end is free in the second simulation. In both simulations we use $\Delta t = 0.1\,\mathrm{s}$, $k^{\mathrm{corr}} = 0.1\,{}^{1}\!/_{\mathrm{s}^2}$.

Pipe no. (j)	$M[\mathrm{kg}]$	$J[\mathrm{kg}\cdot\mathrm{m}^2]$	length [m]	$w_{\mathrm{CG}}[\cdot]$
1	2.7	3.5	3.0	0.4
2	3.0	3.0	4.0	0.4
3	5.0	6.0	4.0	0.6
4	4.0	2.0	3.0	0.2
5	4.0	2.0	3.0	0.2

Table 1: Pipe properties

Both boundaries are fixed

Figure 3.1 show snapshots form a simulation where both boundaries are fixed. During $t \in (1, 10)\,\mathrm{s}$ an external force $\boldsymbol{F}_3 = \langle 1, 2\rangle\,\mathrm{N}$ acts on the third pipe three quarters of its length towards the right (the arrow in Figure 3.1). The pipeline rises and then bounces back at $t > 7.5\,\mathrm{s}$ due to the stretch for the boundaries.

Only the left boundary is fixed

Figure 3.2 show snapshots form a simulation where only the left boundaries is fixed (the boundary position marked with a black ring is stationary, though the snapshots are positioned differently for visibility.) As before, an external force, now $\boldsymbol{F}_3 = \langle -1, 2\rangle\,\mathrm{N}$, acts for nine seconds, three quarters pipe length from the left on the third pipe (the arrow discernible at time $t \in \{2.5, 5, 7.3\}\mathrm{s}$ in Figure 3.1.)
The initial force causes the pipeline to spin about the left boundary joint while the rightmost pipes of the pipeline spin about loosely.

Appendix A. Computing Moments of Inertia

Appendix A.1. Centre of Gravity $\mathbf{x}_j$

The centre of gravity CG for a pipe segment j may be computed through

$$\boldsymbol{x}_j = \frac{1}{M_j}\int_{\boldsymbol{x}_{j-\frac{1}{2}}}^{\boldsymbol{x}_{j+\frac{1}{2}}} \boldsymbol{x}\,\mathrm{d}m = \frac{1}{M_j}\sum_i \boldsymbol{x}_{i,j} m_{i,j}, \tag{A.1}$$

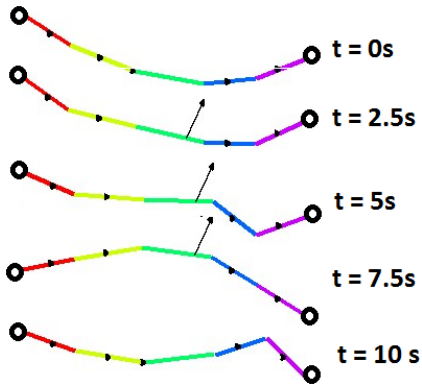

Figure 3.1: Simulation of pipeline from Table 1. Both boundaries are fixed. A single external force $\boldsymbol{F}_3 = \langle 1, 2 \rangle$ N attacks pipe 3 $\frac{3}{4}$ length from the left end during $t \in (1, 10)$ s. $\Delta t = 0.1$ s, $k^{\text{corn}} = 0.1\,1/\text{s}^2$

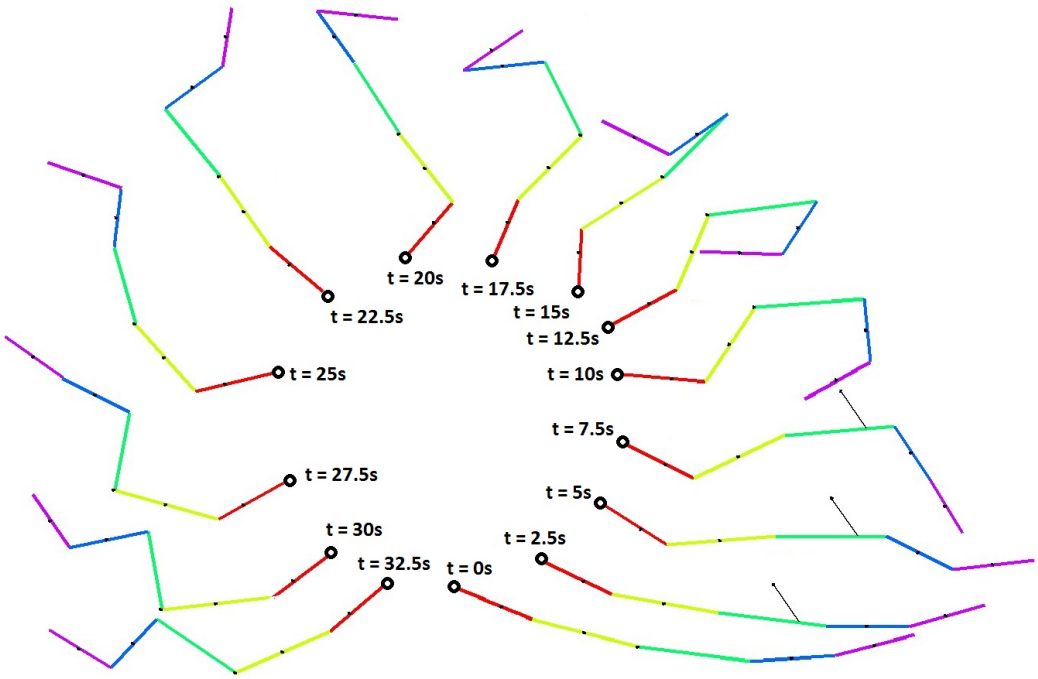

Figure 3.2: Simulation of pipeline from Table 1. Left boundary fixed, right boundary free. A single external force $\boldsymbol{F}_3 = \langle -1, 2 \rangle$ N attacks pipe 3 $\frac{3}{4}$ length from the left end during $t \in (1, 10)$ s. $\Delta t = 0.1$ s, $k^{\text{corn}} = 0.1\,1/\text{s}^2$

where $M_j = \sum_i m_{i,j}$ and the index i is iterated over all sections and phases in the pipe segment. (The integral in (A.1) and those similar to it is to be understood as the integral over a path including all mass between the limit points.)

Appendix A.2. Moment of Inertia J_j

The total moment of inertia about $\boldsymbol{x}_i$ on pipe j is

$$J_i = \int_{\boldsymbol{x}_{j-1/2}}^{\boldsymbol{x}_{j+1/2}} |\boldsymbol{x} - \boldsymbol{x}_i|^2 \, \mathrm{d}m.$$

Expressing inertia about $\boldsymbol{x}_i$ relative to $\boldsymbol{x}_j$ yields (the parallel axis theorem)

$$J_i = J_j + |\boldsymbol{x}_i - \boldsymbol{x}_j|^2 M_j. \tag{A.2}$$

We may use superpositioning over all section masses in pipe j to compute J_j. Let $J_i^{(k)}$ be the moment of inertia from the mass m_k in a single section k about the point $\boldsymbol{x}_i$. Imagine a set of pipes, each containing one section mass m_i in $\boldsymbol{x}_i$ only. Swapping the indices of the parallel axis theorem (A.2), we find that the moment of inertia J_j about the centre of gravity of pipe j is

$$J_j = \sum_i J_j^{(i)} = \sum_i \left[J_i^{(i)} + |\boldsymbol{x}_j - \boldsymbol{x}_i|^2 m_i \right]. \tag{A.3}$$

Assuming the mass m_i within a section i to be uniformly distributed we have

$$J_i^{(i)} = \frac{m_i \Delta x_i^2}{12}.$$

Please note that (A.3) is only valid if the CG is located *between* section (at the cell faces), that is $\boldsymbol{x}_{CG} \in \{\boldsymbol{x}_i \pm \frac{\boldsymbol{\Delta x}}{2}\}$. This is solved simply by splitting the section containing the CG into a left and right part.

Appendix B. Suggested Structural Forces

Forces on a pipe segment can be placed within three groups

(i) External forces

(ii) Internal forces

(iii) Structurally induced forces.

External forces are generated by the surroundings around the extremities of the pipe, excluding the external forces on the fluid within the pipe. Examples are stresses from sea currents, gravitational forces on the pipe structure itself, ect.. External forces are not included in the scope of this text.

Internal forces are the forces which are exerted on the pipe structure from the fluid within the pipe. These forces range form gravitational, frictional and convective forces.

Structurally induced forces are the coupling forces between pipe segments in a pipeline. These forces and torques will pass through the joints which connect the pipe segments.

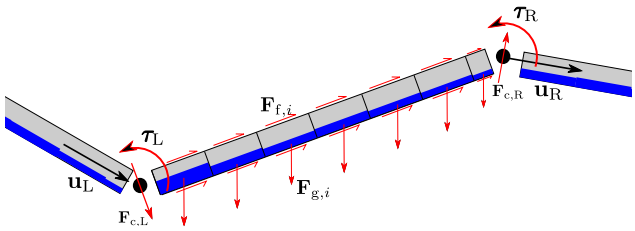

Figure B.1: Schematic of forces acting on a pipe segment.

Appendix B.1. Internal Forces

Gravity

The net gravitational force form all fluid sections i in a pipe j may be expressed as

$$\boldsymbol{F}_{\mathrm{g},j} = \boldsymbol{g} \sum_i m_{i,j} = -g \sum_i m_{i,j} \boldsymbol{e}_y.$$

Of course, the gravitational force passes through the CG. Consequently, no gravitational torque is exerted about the CG[3].

Convection at Pipe Ends

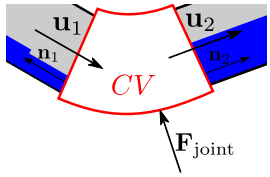

A momentum balance over some joint $j - \frac{1}{2}$ including all fluid phases k may be written

$$\sum_k \left\{ \cancel{\int_{CV} \rho_k \boldsymbol{u}_k \,\mathrm{d}\mathcal{V}} + \oint_{CS} \rho_k \boldsymbol{u}_k (\boldsymbol{u}_k \cdot \boldsymbol{n}) \,\mathrm{d}\mathcal{A} \right\} = \sum_k \sum_{i=1,2} \rho_k A_{k,i} u_{k,i}^2 \boldsymbol{n}_i$$
$$= \sum_k \left\{ \rho_k A_{k,2} u_{k,2}^2 \begin{pmatrix} \cos\phi_2 \\ \sin\phi_2 \end{pmatrix} - \rho_k A_{k,1} u_{k,1}^2 \begin{pmatrix} \cos\phi_1 \\ \sin\phi_1 \end{pmatrix} \right\} = \boldsymbol{F}_\mathrm{joint}.$$

The convective forces form the fluid on the pipe joint $j - \frac{1}{2}$ is then

$$\boldsymbol{F}_{\mathrm{c},j-\frac{1}{2}} = -\boldsymbol{F}_\mathrm{joint}$$

Fluid Friction

The skin friction forces are given by Newton's third law as a simple sum of the reactive wall friction forces from each fluid section i for all phases k:

$$\boldsymbol{F}_\mathrm{f} = \sum_{k,i} \frac{1}{8} \rho_k s_{k,i} \lambda_{k,i} \Delta x_i u_{k,i} \boldsymbol{u}_{k,i}.$$

[3] $$\boldsymbol{\tau}_{\mathrm{g},j} = \sum_i m_{i,j} (\boldsymbol{x}_i - \boldsymbol{x}_\mathrm{CG})_j \times \boldsymbol{g} = -g \cos\phi_j \sum_i m_{i,j} (x_i - x_\mathrm{CG})_j \boldsymbol{e}_z \overset{\text{eq. (A.1)}}{\equiv} \boldsymbol{0}$$

All skin friction forces passes through the CG (assuming a negligible arm due to a small diameter relative to the pipe segment lengths,) and therefore does not contribute with a torque on the system.

Appendix B.2. Structurally induced forces

Joint Forces

The joint forces are the pulling and pushing forces between two pipe segments at the connection joint. These must be found implicitly throughout the system to ensure a connected solution – see Section 2.

Joint Stiffness

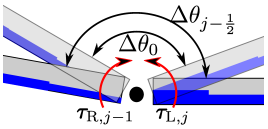

A simple joint stiffness module k_θ may be applied to each joint $j-\frac{1}{2}$:

$$\boldsymbol{\tau}_{\mathrm{L},j} = \left[k_{\theta,j-\frac{1}{2}}(\Delta\theta - \Delta\theta_0)_{j-\frac{1}{2}} - c_{\theta,j-\frac{1}{2}}\Delta\dot{\theta}_{j-\frac{1}{2}}\right]\boldsymbol{e}_z, \qquad \boldsymbol{\tau}_{\mathrm{R},j-1} = -\boldsymbol{\tau}_{\mathrm{L},j}, \tag{B.1}$$

where $\Delta\theta_{j-\frac{1}{2}} = (\theta_{j-1}+\pi) - \theta_j$ and $\Delta\theta_{0,j-\frac{1}{2}}$ is the relaxation angle of joint $j-\frac{1}{2}$. A damping coefficient $c_{\theta,j-\frac{1}{2}}$ is also included in equation (B.1).
The joint torques $\boldsymbol{\tau}_{\mathrm{L},j}$ and $\boldsymbol{\tau}_{\mathrm{R},j}$ about pipe j are centred in each end $\boldsymbol{x}_{\mathrm{L},j}$ and $\boldsymbol{x}_{\mathrm{R},j}$ of the pipe segment.

Computing torques and moments of inertia. We wish to relate all external torques to moments about the centre of gravity $\boldsymbol{x}_j$ of pipe j. Let $\boldsymbol{\tau}_i^{(i)}$ be a torque acting about $\boldsymbol{x}_i$. The angular momentum equation reads

$$\boldsymbol{\tau}_i^{(i)} = \left(J\ddot{\boldsymbol{\theta}}\right)_i^{(i)},$$

$\ddot{\boldsymbol{\theta}}_i^{(i)}$ being angular acceleration generated from the torque $\boldsymbol{\tau}^{(i)}$, acting about $\boldsymbol{x}_i$. The angular acceleration about $\boldsymbol{x}_j$ (the CG of pipe j) is the same as the angular acceleration about $\boldsymbol{x}_i$, i.e., $\ddot{\boldsymbol{\theta}}_i^{(i)} = \ddot{\boldsymbol{\theta}}_j^{(i)}$. Due to the linearity of the angular momentum equation, we may then write

$$\boldsymbol{\tau}_j = \sum_i \boldsymbol{\tau}_i^{(i)} \frac{J_j}{J_i}.$$

Again, the parallel axis theorem (A.2) is used to compute J_i.

The moment generated about the CG from the left and right joint stiffness may then be described by

$$\boldsymbol{\tau}_j = \frac{\boldsymbol{\tau}_{\mathrm{L},j}}{1+\frac{r_{\mathrm{L},j}^2 M_j}{J_j}} + \frac{\boldsymbol{\tau}_{\mathrm{R},j}}{1+\frac{r_{\mathrm{R},j}^2 M_j}{J_j}}, \tag{B.2}$$

where $\boldsymbol{r}_{\mathrm{L},j}$ and $\boldsymbol{r}_{\mathrm{R},j}$ still points form the CG to the left and right joints, and $\boldsymbol{\tau}_{\mathrm{L},j}$ and $\boldsymbol{\tau}_{\mathrm{R},j}$ are given by (B.1). Expression (B.2) requires only the moment of inertia about the CG, J_j, which is obtained form (A.3).

References

This model is produced from simple mechanistic principles and have no references, except maybe `http://en.wikipedia.org/wiki/Moment_of_inertia`.